

**SEASONAL EFFECT OF CLIMATE VARIABILITY ON SOIL MOISTURE AND
BIOMASS PRODUCTION: A CASE STUDY OF MAASAI MARA RANGELAND
AND NAIVASHA CROPLAND ECOSYSTEMS, KENYA**

CHARLES CHEPKEWEL KAPKWANG

**A Thesis Submitted to the Graduate School in Fulfilment of the Requirements for the
Doctor of Philosophy Degree in Agricultural Engineering of Egerton University**

EGERTON UNIVERSITY

DECEMBER, 2022

DECLARATION AND RECOMMENDATION

Declaration

I hereby declare that this thesis is my original work and has not been presented in this University or any other for the award of a degree.

Signature.- 

05/10/2022

Charles Chepkewel Kapkwang, MSc

Date

BD11/12280/16

Recommendation

This thesis has been submitted with our approval as University supervisors.

Signature. 

11/10/2022

Prof. (Eng). Japheth O. Onyando, PhD

Date

Department of Agricultural Engineering

Egerton University

Signature. 

06/10/2022

Dr. Peter M. Kundu, PhD

Date

Department of Agricultural Engineering

Egerton University

Signature. 

12/10/2022

Prof. Johannes C.B. Hoedjes, PhD

Date

Department of Water Resources

Faculty of Geo - Information Science and Earth Observation

(ITC), University of Twente, Netherlands

COPYRIGHT

©2022 Kapkwang, Charles Chepkewel

All rights reserved. No part or whole of this thesis may be reproduced, stored in a retrieval system or transmitted in any form or by any means, photocopying, scanning, recording or otherwise, without the permission of the author or Egerton University.

DEDICATION

This research work is dedicated to my late dad, William Chepkewel Kapkwang, loving mum Pauline and my dear wife Grace Jepchumba Kibet, Children Prudence, Doreen Maureen, Faith and Abraham for their unceasing prayers, encouragement and patience. Much appreciation too for their understanding and immense moral support throughout my study program and above all, the almighty God to whom glory belongs now and forever more.

ACKNOWLEDGEMENTS

First, I would like to thank the almighty God for his guidance and strength throughout the entire period of thesis writing. I convey my sincere thanks to Egerton University for giving me an opportunity to undertake this study. Special thanks go to my supervisors Prof. Japheth Ogallo Onyando, Dr. Peter Musula Kundu, and Prof. Johannes Hoedjes of International Trade Centre, Netherlands for their unceasing support, encouragement, scholarly guidance, and counsel, which steered me to undertake this research study. Their positive criticisms and scholarly advice contributed enormously to the final realization of this thesis writing.

Much gratitude goes to African Development Bank through the Ministry of Higher Education, Science and Technology, the program sponsor for their financial support without which this research could not have been accomplished. Many thanks also goes to Prof. Bob Su from the faculty of Geo-Information Science and Earth Observation (Water Resources) for the facilitation of research instruments, technical, moral and material support for their positive response and immediate help whenever any need arose. My sincere thanks too goes to my student colleagues from International Trade Centre, University of Twente, Netherlands, Donald Rwasoka, Kingley Kumah and Sammy Njuki for their contribution in the joint involvement of fieldwork, the research assistants, Mr. Henry Munyaka and Dominic Wambua (Maji House). Not forgetting, the contribution and cordial relations provided by senior administrators of Maasai Mara National Reserve and game rangers for the entire period of installation of instruments and data collection.

I am also indebted to the following organizations for their assistance, Kenya Agricultural and Livestock Research Organization, National Soil Survey Laboratories (Kabete), for some soil analysis, Water Resource Authority, Kenya Meteorological Department for providing Naivasha meteorological data. Gratitude also goes to the Ministry of Agriculture (Sub-County Office Naivasha) and private farms such as Kijabe/Ndabibi, Delamere/Minera, Engineer/Paul's, and Nunjoro for the provision of secondary data based on hay and wheat biomass and yields.

Special thanks go to my employer, University of Kabianga, Kenya, for granting me study leave to pursue my PhD degree. Finally, to all I say may our almighty God bless you abundantly in this universe throughout your entire life.

ABSTRACT

Globally, rangeland and cropland are ecosystems that rely exclusively on soil moisture influenced by dynamic interaction of eco-hydrologic variables caused by climate variability and soil for sustainable biomass/yield production. There are challenges of up to date variable measurements within adequate information of spatio-temporal soil moisture variation and biomass in the selected Kenyan ecosystems. The specific objectives under the study were the determination of spatio-temporal soil moisture storage and retention capacities in the ecosystems; Simulation of the influence of bi-seasonal soil moisture variability on rangeland and cropland biomass yield using coupled Hydrus-1D and Agricultural Production Systems Simulator. Finally, to analyse the impact of bi-seasonal soil moisture variation on land use land cover in rangeland and cropland vegetation. Remote sensing and Geographical Information System derived land use land cover classification maps from Normalized Difference Vegetation Index values for real-time monitoring were obtained and processed via MODIS and Proba-V imagery satellite data. Random undisturbed core soil samples collected from ten (10) sampling points with five varying replication depths of P1 (0-5cm), P2 (5-10cm), P3 (15-20cm), P4 (35-40cm) and P5 (75-80cm) for ground based (in-situ) installed 5TM-ECH₂O probes. Time series variation shows that volumetric water content of spatially distributed probes in wet season ranged between 0.11 and 0.32m³m⁻³ (0.16m³m⁻³) and in dry between 0.04 and 0.17m³m⁻³(0.11m³m⁻³) across the rangeland respectively. Cropland volumetric water content in wet season ranged between 0.13 to 0.37m³/m³ (0.22m³m⁻³) and dry between 0.06 to 0.22m³m⁻³(0.14m³m⁻³) respectively. Water retention shown that field capacity of soil water content at -3 bars ranged between 0.16cm³H₂O/cm³soil and 0.22cm³H₂O/cm³soil across the rangeland. APSIM model simulated cropland and rangeland above ground biomass reasonably well, where rangeland model performance gave NSE = 0.988, r = 0.000, RMSE = 0.103tonha⁻¹ and R² was 0.988. In overall, the rangeland covers approximately 717.203km²(46.75%) with total above ground grass biomass in dry and wet season of 35.094 tonha⁻¹(≈2,516,952.208 and 42.123 tonha⁻¹ (≈3,021,074.197) tonnes per season respectively. Land use land cover change indicates gradual encroachment of livestock and commercial wheat farms into the grassland in the last decade (2009-2019). This has decreased (closed, evergreen broadleaved) forest cover while conversion of Naivasha cropland from rain fed to irrigated cropland is also gradually increasing. In conclusion, soil moisture, biomass and change in land use land cover vary seasonally as influenced by climate variability.

TABLE OF CONTENTS

DECLARATION AND RECOMMENDATION	ii
COPYRIGHT	iii
DEDICATION.....	iv
ACKNOWLEDGEMENTS	v
ABSTRACT.....	vi
LIST OF FIGURES	xii
LIST OF TABLES	xvii
LIST OF ABBREVIATIONS AND ACRONYMS	xx
LIST OF SYMBOLS	xxiii
CHAPTER ONE	1
INTRODUCTION.....	1
1.1 Background Information	1
1.2 Statement of the Problem	2
1.3 Research Objectives	3
1.3.1 Broad Objective	3
1.3.2 Specific Objectives	3
1.4 Research Questions	3
1.5 Justification	3
1.6 Scope and Limitations	4
CHAPTER TWO	5
LITERATURE REVIEW	5
2.1 Climate Variability	5
2.1.1 Temperature and Wind Speed	5
2.1.2 Solar Radiation	6
2.1.3 Evapotranspiration.....	6
2.2 Bowen Ratio Theory	7
2.2.1 Latent Heat Flux	7
2.2.2 Sensible Heat Flux (H)	8
2.2.3 Soil heat Flux.....	8
2.2.4 Net Radiation.....	8
2.2.5 Surface Energy Balance.....	9
2.2.6 Water Vapour	10
2.3 Soil Water Dynamics	10

2.3.1 Soil Water Storage.....	11
2.3.2 Soil Water Retention	13
2.3.3 Surface Runoff.....	15
2.3.4 Soil Infiltration and Hydraulic Conductivity.....	15
2.3.5 Drainage.....	16
2.4 Modelling Application for Prediction and Decision Support.....	17
2.4.1 Model Calibration.....	17
2.4.2 Soil Moisture Dynamic Models.....	17
2.4.3 Vadose Zone Modelling Approaches	18
2.4.4 Bucket Model	19
2.4.5 Richards Model.....	20
2.4.6 SWAT Model	21
2.4.7 Variable Infiltration Capacity Model	21
2.4.8 Hydrus Model.....	22
2.5 Temporal and Spatial Soil Moisture Measurements	23
2.5.1 Penetration Depth in the Soil.....	24
2.5.2 Calibration of Cosmic Ray Neutron Sensor	25
2.6 Models for Biomass and Yield Prediction	26
2.6.1 Crop Yield Prediction.....	28
2.6.2 Agricultural Production System Simulator.....	29
2.6.3 Model Parameterisation and Calibration	29
2.7 Detecting and Quantifying Land Use and Land Cover Change.....	29
2.7.1 Crop Area Estimation	30
2.7.2 Ground Survey.....	31
2.7.3 Area Frame Sampling.....	31
2.8 Satellite Imagery Data.....	32
2.8.1 Project for On-Board Autonomy - Vegetation (Proba V)	32
2.8.2 Project for On-Board Autonomy – Vegetation (PROBA-V) Data Products.....	34
2.8.3. Geometric Processing	35
2.8.4. Radiometric Processing	35
2.8.5 Mapping and SWIR Mosaicking	36
2.8.6 Cloud and Cloud Shadow Detection	36
2.8.7 Atmospheric Correction	36
2.9 Sentinel 2A.....	37

2.9.1 Normalized Difference Vegetation Index.....	39
2.10 Net Primary Productivity	39
2.11 Model Sensitivity Analysis	40
CHAPTER THREE.....	41
MATERIALS AND METHODS	41
3.1 The Study Area.....	41
3.1.1 Maasai Mara National Reserve Rangeland and Ecosystem	41
3.1.2 Naivasha Cropland and Ecosystem	42
3.2 Determination of Spatio-Temporal Soil Moisture Storage and Retention Capacities in Maasai Mara National Reserve Rangeland Ecosystem.....	44
3.2.1 Soil Physical and Chemical Properties of Maasai Mara Rangeland Ecosystems....	46
3.2.2 Cosmic Ray Probe Soil Water Content Determination	48
3.2.3 Neutron Intensity Method.....	49
3.2.4 Molar Fraction Based Method (Hmf-Method)	49
3.2.5 Field Calibration and Validation of Cosmic Ray Soil Moisture Sensor.....	50
3.2.6 Calibration of Cosmic Ray Soil Moisture Sensor by Gravimetric Sampling.....	51
3.2.7 Calibration by Soil Moisture and Temperature Capacitance Probes.....	55
3.3 Soil Moisture Storage Measurements	55
3.3.1 Gravimetric Water Content	56
3.3.2 Soil Moisture Content.....	57
3.3.3 Spatial Variability of Soil Moisture.....	57
3.3.4 Temporal Variability of Soil Moisture	57
3.4 Soil Moisture Retention Capacity	59
3.4.1 Statistical Analysis	60
3.5 Simulation of the Influence of Soil Moisture Variability on Rangeland and Cropland Biomass Production Using Coupled Hydrus-1D and Agricultural Production System Simulator (APSIM) Model.....	61
3.5.1 Calibration and Validation of Hydrus -1D model	61
3.5.2 Parameterisation and Calibration of APSIM Model.....	61
3.6 Field Clipping Campaign of Aboveground Grass Biomass.....	62
3.6.1 Satellite Estimation of Aboveground Biomass.....	63
3.7 Evaluation of Land Use Land Cover Change in Rangeland and Cropland Ecosystems	65
3.7.1 Direct Expansion and Regression for Area Estimation	65
3.7.2 Relative Efficiency	67

3.7.3 Analysis of Land Use Land Cover Changes in Maasai Mara National Reserve Ecosystem.....	67
3.7.4 Moderate Resolution Imaging Spectro-Radiometer (MODIS)	68
3.7.5 On Level II (National and Sub-National Level - 100 m Ground Resolution).....	69
3.7.6 MODIS Imagery Selection	69
3.7.7 Data Pre-Processing.....	69
3.7.8 MODIS Imagery Enhancement	70
3.7.9 Accuracy Assessment of Classification.....	71
3.7.10 Evaluation of Model Performance.....	74
3.7.11 Sensitivity Analysis	76
3.8 Data Analysis	77
CHAPTER FOUR.....	78
RESULTS AND DISCUSSION	78
4.1 Determination of Spatio-Temporal Soil Moisture Storage and Retention Capacities in Maasai Mara Rangeland Ecosystem	78
4.1.1 Rainfall Characteristics.....	78
4.1.2 Air Temperature and Humidity	79
4.1.3 Vapour Pressure Deficit.....	80
4.1.4 Wind Speed.....	81
4.2 Spatial Physical and Chemical Properties Soil Sampling Campaign.....	85
4.2.1 Soil Texture	85
4.2.2 Total Organic Carbon	87
4.2.3 Bulk Density	92
4.2.4 Particle Density.....	93
4.2.5 Maasai Mara National Reserve Rangeland Ecosystem Soil Chemical Properties ..	96
4.2.6 Infiltration Rate and Saturated Hydraulic Conductivity.....	97
4.3 Moderated Neutron Counts	111
4.3.1 Biomass Water Equivalent	112
4.3.2 Root Biomass Density	113
4.4 Moisture Retention Characteristics	115
4.4.1 Soil Moisture Retention Curves from Soil Profile Data.....	122
4.4.2 Statistical Analysis	124
4.5 Simulate the Influence of Soil Moisture Variability in Biomass Production Using Coupled Hydrus-1D and Agricultural Production Systems Simulator (APSIM) Model. ..	125

4.5.1 Simulation Results of Hydrus - 1D.....	126
4.5.2 Hydrus-1D Model Calibration.....	128
4.5.3 Sensitivity Analysis	133
4.6 Measured Aboveground Standing Grass Biomass at Maasai Mara Rangeland Ecosystem.....	135
4.6.1 Observed and Simulated Output Results Obtained from APSIM Model.....	139
4.6.2 Statistical Evaluation of Model Performance.....	143
4.7 Naivasha Cropland Rainfall Characteristics	145
4.7.1 Soil Information for Naivasha Cropland Ecosystem.....	146
4.7.2 Soil Moisture Characteristics.....	147
4.7.3 Soil moisture variability in selected Naivasha cropland	148
4.7.4 Wheat Biomass and Yield Production in Naivasha Cropland Ecosystem.....	150
4.7.5 APSIM Simulation Results of Wheat Crop.....	152
4.7.6 Model Sensitivity Analysis.....	156
4.8 Normalized Difference Vegetation Index (NDVI).....	156
4.8.1 Naivasha Cropland Ecosystem	161
4.8.2 Time Series Analysis of Minimum and Maximum NDVI	165
4.8.3 Linear Correlation between Mean Monthly NDVI and Mean Maximum Monthly Rainfall	165
4.8.4 Time Series Analyses of Mean Monthly Rainfall for 2017-2019 Period in Maasai Mara Rangeland Ecosystem	165
4.8.5 Time Series Analyses of Maximum Mean Monthly Temperature	166
4.8.6 Time Series Analyses of Mean Monthly NDVI for the 2017- 2019 Period.....	166
4.8.7 Statistical Analysis of Total Aboveground Standing Biomass Quantities	167
4.9 Land Use Land Cover Change in Maasai Mara National Reserve Rangeland and Naivasha Cropland Ecosystems	167
4.9.1 Maasai Mara National Reserve Rangeland Ecosystem	167
4.9.2 Naivasha Cropland Ecosystem	178
4.10 Estimation of Land Cover and Land Use Change.....	183
4.10.1 Area Estimation through Direct Expansion.....	184
4.10.2 Other Land Use and Land Cover in Naivasha Cropland.....	187
4.10.3 Land Classification Accuracy Assessment.....	187
4.10.4 Common Characteristics of Rangeland and Cropland	191
4.11 Contribution of the Study to the Scientific World and the Economy	191

4.11.1 Contribution to Knowledge	191
4.11.2 Contribution to Planning and Policy	192
CHAPTER FIVE	194
CONCLUSIONS AND RECOMMENDATIONS.....	194
5.1 Conclusions	194
5.2 Recommendations	195
REFERENCES.....	197
APPENDICES	222
Appendices A: Plates	222
Appendices B: Tables.....	225
Appendices C: Graphs.....	297
Appendices D: Research Permit.....	302
Appendices E: List of Publications	303

LIST OF FIGURES

Figure 2.1: Schematic diagram of soil moisture dynamics.....	11
Figure 2.2: Soil water retention curves adjusted by the cubic polynomial model at depths of 20, 40, 60, and 80 cm.....	14
Figure 2.3: Schematic representation of climate-soil-vegetation system interaction	18
Figure 2.4: Schematic representation of the vertically averaged bucket model	20
Figure 2.5: Schematic representation of the one-dimensional Richards model.....	21
Figure 2.6: Soil moisture sensors.....	24
Figure 2.7: Schematic representation of coupled VIC and CropSyst model	27
Figure 2.8: Schematic of the yield prediction workflow	28
Figure 2.9: PROBA-V product processing chain flowchart	34
Figure 2.10: Flowchart of the collection 1 cloud detection algorithm.....	36
Figure 3.1: Maasai Mara National Reserve rangeland ecosystem.....	42
Figure 3.2: Naivasha cropland ecosystem	43
Figure 3.3: Automatic meteorological station at Maasai Mara National Reserve. From left to right: Cosmic Ray Neutron sensor, Standard rain gauge, Eddy covariance, Bowen’s ratio with tipping bucket rain-gauge and CNR4 Net radiometer	44
Figure 3.4: The cosmic-ray probe measurement footprint.....	50
Figure 3.5: Calibration procedure for gravimetric soil sampling	52
Figure 3.6: Soil moisture and temperature capacitance (5TM-ECH ₂ O) probes	55
Figure 3.7: Schematic flowchart for satellite biomass estimation.....	63
Figure 4.1: 30 minutes’ rainfall pattern in Mara rangeland ecosystem for the period of (a) Oct - Nov 2018 and (b) March - April 2019.....	78
Figure 4.2: 30 minutes’ variation of air temperature (red) in relation to relative humidity (blue) in Mara Ecosystem for the period of March – April 2019	79
Figure 4.3: Hourly behaviour of vapour pressure deficit as observed in Maasai Mara rangeland ecosystem for the period of Oct – Nov 2018	80
Figure 4.4: General trend of wind speed in Mara rangeland ecosystem as observed by Bowen’s Ratio system.....	81
Figure 4.5: General 30 minutes’ wind rose behaviour in Mara rangeland ecosystem as observed by Bowen’s Ratio System	82
Figure 4.6: General weekly 30 minutes’ wind rose pattern as observed by Bowen’s ratio system for the period of March 2019.....	82
Figure 4.7: Soil texture classification	87

Figure 4.8: Total organic carbon and soil organic matter at three sampled 5TM-ECH ₂ O stations	91
Figure 4.9: General trend of bulk and particle densities in variation to soil depth across Maasai Mara rangeland ecosystem	95
Figure 4.10: Selected spatial behaviour of total soil porosity in variation to soil depths	95
Figure 4.11: Infiltration rate at sampling sites of Maasai Mara National Reserve rangeland ecosystem during the dry season.....	97
Figure 4.12: Time series trend of rainfall correlation to volumetric water content between Nov 2017 and April 2018.	105
Figure 4.13: Trend of Nice bridge volumetric water content with respect to soil layers for 2018-2019	106
Figure 4.14: Trend of monthly soil moisture and temperature variation per depths at Kissinger 5TM-ECH ₂ O site: 2018-2019.....	107
Figure 4.15: Variation of Ashnil site soil moisture and temperature at different soil profiles ...	108
Figure 4.16: Time series of daily rainfall and moderated neutron counts during the period 2017 and 2018 at Maasai Mara National Reserve.	110
Figure 4.17: CRNS temporal simulation trend of soil moisture content receding after rainfall event.....	111
Figure 4.18: Root density distribution of grass vegetation in Mara ecosystem soil profile	113
Figure 4.19: Weighted average distribution of near surface 5cm depth volumetric moisture content according to respective site's soil texture	120
Figure 4.20: Characteristics of soil water potential for (a) 5cm and (b) 10cm depth at Maasai Mara rangeland	124
Figure 4.21: Variation of (a) matric potential and (b) volumetric water content with depths....	126
Figure 4.22: Variations of (a) flow and (b) hydraulic conductivity with depth in different periods.....	127
Figure 4.23: Variation of (a) surface layer input flow and (b) water fluxes in different periods	128
Figure 4.24: Soil moisture characteristic curve	131
Figure 4.25: Variation of (a) Pressure heads in different periods (b) relation between volumetric water content and matrix potential	133
Figure 4.26: Box plot of selected trend of Mara main aboveground biomass per quadrat during dry and wet season.....	137
Figure 4.27: Observed and Simulated aboveground grass biomass in dry season	142
Figure 4.28: Simulated and observed aboveground grass standing biomass wet season	142

Figure 4.29: Observed and simulated aboveground standing aboveground grass biomass for respective soil moisture sites	143
Figure 4.30: Automatic Weather Station at Kijabe Farm Naivasha Cropland	145
Figure 4.31: Trend of Monthly rainfall for Naivasha Cropland: 2010-2019.....	146
Figure 4.32: Soil moisture and temperature variation per depth profile for Kijabe/Ndabibi 5TM- ECH ₂ 0 site: 2017-2019.....	148
Figure 4.33: Soil moisture and temperature variation at Nunjoro farm site: 2018.....	149
Figure 4.34: General trend of annual wheat crop production in Naivasha cropland	150
Figure 4.35: Trend of pasture crop production between 2013 and 2019 in Naivasha cropland .	151
Figure 4.36: Correlation of wheat crop per stage biomass to extractable water content.....	151
Figure 4.37: Comparison between observed and simulated annual aboveground biomass for Naivasha cropland from 2017 to 2019.....	153
Figure 4.38: Comparison between observed and simulated annual wheat grain yield for Naivasha cropland from 2017 to 2019.....	154
Figure 4.39: Measured and simulated aboveground biomass of wheat crop.....	154
Figure 4.40: Vegetation NDVI trend from PROBA-V satellite imagery data for Maasai Mara Rangeland wet and dry season acquired on (May and Dec 2017).....	158
Figure 4.41: Vegetation NDVI trend from PROBA-V satellite imagery data for Maasai Mara Rangeland wet and dry season acquired on (May and Dec 2018).....	159
Figure 4.42: Vegetation NDVI trend from PROBA-V imagery satellite data for Maasai Mara Rangeland wet (a) and dry (b) season acquired on (May and Dec 2019).....	160
Figure 4.43: Vegetation NDVI trend derived from PROBA-V imagery satellite data for Naivasha cropland (a) wet (May) and (b) dry season (Dec) acquired on 2017.	161
Figure 4.44: Vegetation NDVI trend derived from PROBA-V imagery satellite data for Naivasha cropland (a) wet (May) and (b) dry season (Dec) acquired on 2018.	162
Figure 4.45: Vegetation NDVI trend derived from PROBA-V imagery satellite data for Naivasha cropland (a) wet (May) and (b) dry season (Dec) acquired on 2019.	163
Figure 4.46: Graphical representation of NDVI trend between January – December in Naivasha cropland ecosystem during wet and dry season in 2017.....	164
Figure 4.47: Graphical representation of NDVI trend of Naivasha Cropland ecosystem between January and December wet and dry season for the period 2017, 2018, and 2019	164
Figure 4.48: Annual precipitation and temperature during the seasons.....	166
Figure 4.49: Land use/cover classification maps using MODIS imagery data of Maasai Mara National Reserve from January 2009 through December 2011	170

Figure 4.50: Land use/cover classification maps of Maasai Mara National Reserve from 2013 through 2015 using MODIS imagery data.....	171
Figure 4.51: Land use/cover classification maps of Maasai Mara National Reserve in 2017 through 2018 from MODIS imagery data.....	172
Figure 4.52: Land use Land cover classification representation in percent for Maasai Mara rangeland ecosystem in 2019.....	173
Figure 4.53: General Land use land cover distribution of Naivasha Sub-County.....	178
Figure 4.54: Land Use Land Cover Change for Naivasha Cropland in 2009 and 2011.....	179
Figure 4.55: Land Use Land Cover Change for Naivasha Cropland in 2013 and 2015.....	180
Figure 4.56: Land cover Land use changes for Naivasha cropland in 2017 and 2018.....	181
Figure 4.57: Land use land cover maps and percent representation of Naivasha Cropland ecosystem for the period 2019.....	182

LIST OF TABLES

Table 2.1. Some examples of constant infiltration rates for different soil types	16
Table 2.2: PROBA-V spectral, radiometric, and geometric characteristics, L_{ref} refers to the Top-Of-Atmosphere (TOA) irradiance at the respective spectral band, Geometric mean accuracy values obtained over the period 16 December 2016-15 December 2017. FWHM = Full Width at Half Maximum, SNR = Signal to Noise Ratio	33
Table 2.3: Technical Characteristics of Sentinel 2	38
Table 3.1: Design of Confusion/Error Matrix applied in accuracy assessment of land cover classification	72
Table 3.2: Quantification of Cohen's Kappa coefficient as measure of agreement	74
Table 3.3. Sensitivity Index Classes	77
Table 4.1: Spatially distributed soil moisture, soil temperature and soil sampling stations	83
Table 4.2: 5TM-ECH ₂ O sensors measurement detail including site name, geographic location, elevation vegetation cover/land use, aboveground biomass, and textural class	84
Table 4.3: Spatially distributed soil textural classes varied with depths across the Maasai Mara National Reserve rangeland ecosystem	86
Table 4.4: Maasai Mara National Reserve sites total organic carbon concentration measured according to soil depths.	88
Table 4.5: Sampled Ashnil site particle size distribution, total organic carbon, soil organic matter and texture class.....	90
Table 4.6: Maasai Mara National Reserve sites soil bulk density in with soil depths.....	92
Table 4.7: General particle densities of Maasai Mara National Reserve according to soil profiles	94
Table 4.8: Laboratory soil analysis of Maasai Mara National Reserve rangeland ecosystem	96
Table 4.9: Analysis of variance (ANOVA) on spatial distribution of volumetric water content with depth at 10 m concentric distance to CRNS in Maasai Mara rangeland ecosystem (Main station).....	99
Table 4.10: Analysis of variance on spatial distribution of volumetric water content with depth at 25 m concentric distance to CRNS in Maasai Mara rangeland ecosystem (main station).....	100
Table 4.11: Spatial distribution of volumetric water content with depth at 75 m concentric distance to CRNS in Maasai Mara rangeland ecosystem (Main station).....	101

Table 4.12: Analysis of variance on spatial distribution of volumetric water content with depth at 175 m concentric distance to CRNS in Maasai Mara rangeland ecosystem (Main station).....	102
Table 4.13: Weighted average volumetric water content of spatially distributed 5TM-ECH ₂ O Probes.....	103
Table 4.14: Analysis of variance on volumetric water content as per 5TM-ECH ₂ O Soil Moisture, Temperature Capacitance Probes	104
Table 4.15: Cosmic ray volumetric water content according to soil layers at Mara Main station.....	109
Table 4.16: Calibrations, dates, gravimetric soil moisture, bulk density, neutron counts and calculated No values.	112
Table 4.17: Root density of soil samples as collected from MMNR main sampling site.....	114
Table 4.18: Soil moisture variations across rangeland ecosystem according to soil layers	117
Table 4.19: Soil moisture characteristics of Maasai Mara rangeland sites for various soil texture denoted as SL – Sandy Loam, SC – Sandy Clay, SCL – Sandy Clay Loam, C - Clay ..	116
Table 4.20: Spatial soil water characteristics at 0-5 cm soil depth and soil water retention	118
Table 4.21: Spatial soil water characteristics at 5-10 cm soil depth and soil water retention	119
Table 4.22: Charactersitics of Soil moisture retention with depth across Maasai Mara rangeland ecosystem, 2019	122
Table 4.23: Lower and upper bound of four van Genuchten model parameters	129
Table 4.24: Estimated Van Genuchten physical and empirical parameters based on soil constituent particles	130
Table 4.25: Measured and simulated soil water content using Hydrus 1D across Maasai Mara National Reserve Rangeland Ecosystem	130
Table 4.26: Hydrus-1D statistical evaluation of measured and predicted/simulated modelled soil water/moisture content across the rangeland ecosystem.....	132
Table 4.27: Statistical indicators comparing performance of three approaches applied to describe the measured soil water content across the rangeland ecosystem	132
Table 4.28: Observed aboveground standing Biomass, Meta Plains – Main Mara, 12/12/2017_Dry season	135
Table 4.29: Observed aboveground standing biomass, Mara – Meta Plains – Main Mara, 05/05/2018_Wet season.....	136
Table 4.30: Comparison of distributed above ground standing biomass in Maasai Mara catchment sites during dry and wet season	138

Table 4.31: Measured and simulated aboveground standing grass dry matter (biomass) during dry season.....	140
Table 4.32: Measured and simulated aboveground standing grass dry matter (biomass) during wet season at Maasai Mara rangeland ecosystem.....	141
Table 4.33: Overall APSIM Model Performance of observed and simulated aboveground standing grass biomass in MMNR rangeland ecosystem during dry season.....	144
Table 4.34: Overall APSIM Model performance of observed and simulated aboveground standing grass biomass in MMNR rangeland ecosystem during wet season.....	144
Table 4.35: APSIM simulation trend of wheat crop seasonal stages on aboveground biomass at Kijabe/Ndabibi Farm.....	152
Table 4.36: Statistical model evaluation performance of observed and simulated aboveground biomass of wheat.....	155
Table 4.37: Statistical model evaluation performance of observed and simulated grain yield of wheat.....	155
Table 4.38: Description of land cover classes in Maasai Mara rangeland ecosystem.....	169
Table 4.39: Maasai Mara National Reserve Land Use Land Cover classification between 2017- 2019 according to FAO land cover classes	174
Table 4.40: Maasai Mara National Reserve Land Cover and Land Use Statistics for 2017- 2019.....	175
Table 4.41: Maasai Mara National Reserve Rangeland Accuracy Assessment Report for Classification of MODIS images 2017, 2018, and 2019	177
Table 4.42: Description of land cover classes in Naivasha Cropland.....	178
Table 4.43: Naivasha Land Use Land Cover classification between 2017 and 2019 according to FAO land cover classes.....	183
Table 4.44: Naivasha Cropland Land Cover and Land Use Statistics for 2017 - 2019.....	185
Table: 4.45: Cropping systems in Naivasha cropland with Land Use Land Cover sizes.	187
Table 4.46: Naivasha Cropland Accuracy Assessment Report for Classification of MODIS image 2017, 2018, and 2019.....	189

LIST OF ABBREVIATIONS AND ACRONYMS

AEZ	Agro Ecological Zones
AfDB	African Development Bank
AFS	Area Frame Sampling
AGB	Above Ground Biomass
ANNP	Annual Net Primary Productivity
ANOVA	Analysis of Variance
AOT	Aerosol Optical Thickness
APSIM	Agricultural Production Systems Simulator
AVHRR	Advanced Very High Resolution Radiometer
AWC	Available Water Capacity
BR	Bowen Ratio
BREB	Bowen Ratio-Energy Balance
BWE	Biomass Water Equivalent
CESBIO	Centre d'Études Spatiales de la Biosphère
CI	Confidence Interval
CRNS	Cosmic Ray Neutron Sensor
CZCS	Coastal Zone Color Scanner
COSMOS	Cosmic Ray Soil Moisture Observing System
CropSyst	Cropping Systems Simulation Model
CV	Coefficient of Variation
DLL	Drainage Lower Limit
DUL	Drainage Upper Limit
ECMWF	European Center for Mid-Range Weather Forecast
GDD	Growing Degree Days
GDP	Gross Domestic Product
EC	Eddy Covariance
EOS	Earth Observing System
ESA	European Space Agency
ET	Evapotranspiration
ET _o	Reference Evapotranspiration
EU	European Union
FAO	Food and Agricultural Organization of the United Nations

FC	Field Capacity
GCM	General Circulation Models
GHG	Greenhouse Gases
GLSDEM	Global Land Surface Digital Elevation Model
HIRS	High Resolution Infrared Radiation Sounder
ITC	International Trade Centre
ITCZ	Intertropical Convergence Zone
KALRO	Kenya Agricultural and Livestock Research Organization
KWSTI	Kenya Wildlife Service Training Institute
KMD	Kenya Meteorological Department
LAI	Leaf Area Index
LSD	Least Significant Difference
LULC	Land use Land cover
MCNPX	Monte Carlo N-Particle eXtended
MMNR	Maasai Mara National Reserve
MODIS	Moderate Resolution Imaging Spectrometer
MSE	Mean Square Error
MVC	Maximum Value Composite
NARL	National Agricultural Research Laboratories
NACOSTI	National Commission for Science Technology and Innovation
NDVI	Normalized Difference Vegetation Index
NIR	Near Infra-Red
NOAA	National Oceanic and Atmospheric Administration
NPP	Net Primary Productivity
NRMSE	Normalized Root Mean Square Error
NSE	Nash-Sutcliffe Efficiency
NWP	Numerical Weather Prediction
PDF	Probability Density Function
PPMCC	Pearson Product Moment Correlation Coefficient
PROBA-V	Project for On-Board Autonomy - Vegetation
PWP	Permanent Wilting Point
RCBD	Randomized Complete Block Design
REV	Representative Elementary Volume
RMSE	Root Mean Square Error

SA	Sensitivity Analysis
SAR	Synthetic Aperture Radar
SD	Standard Deviation
SE	Standard Error
SeaWiFS	Sea-viewing Wide Field of View Sensor
SSE	Sum of Square Error
SM	Soil Moisture
SMAC	Simplified Model for Atmospheric Correction
SMC	Soil Moisture Content
SWR	Soil Water Retention
SWC	Soil Water Content
SWRC	Soil Water Retention Curve
5TM-ECH ₂ O	Soil Moisture, Soil Temperature sensors
TOMS	Total Ozone Mapping Spectrometer
USDA	United States Department of Agriculture
VIC	Variable Infiltration Capacity
VPD	Vapour Pressure Deficit
VWC	Volumetric Water Content
WGS84	World Geodetic System 1984
WRA	Water Resource Authority

LIST OF SYMBOLS

Rh	Relative humidity	N_o	Neutron intensity
e	Actual vapour pressure	ω_{lat}	Lattice water
e^o	Saturation vapour pressure	ω_{SOM}	Soil organic matter water
θ	Volumetric water content	N_{corr}	Corrected neutron counts
h	Pressure head	S_p	Water absorption potential
K_{sat}	Saturated hydraulic conductivity	σ'	Plant uptake local rate
β	Soil parameter	e'	Evaporation local rate
λE	Latent heat flux	Z_r	Root zone depth
H	Sensible heat flux	η	Porosity
Rn	Net radiation	ρ_p	Particle density
ΔT	Change in temperature	ρ_b	Bulk density
S	Average saturation over the root zone	Δe	Vapour pressure difference
G_0	Soil heat flux	ρ_F	Fluid density
Z_s	Depth of soil layer	C_p	Specific heat of constant pressure
K	Net short wave radiation	ρ_{bd}	Dry bulk density
L	Net long wave radiation	ρ_{air}	Air density
$R_s \uparrow$	Outgoing short wave radiation	λ_s	Soil thermal conductivity
$R_L \downarrow$	Incoming long wave radiation	T_s	Surface temperature
α	Surface albedo	ϵ_o	Surface emissivity
θ	Solar incidence angle	τ_a	Atmospheric transmissivity
∂r	Relative earth-sun distance	τ	Weight fraction of lattice water
ρ_{nir}	Near infrared band reflectance	ρ_{red}	Red band reflectance
T_{max}	Maximum daily temperature	T_{min}	Minimum daily temperature
R_{corr}	Corrected rainfall	ΔSG	Heat storage change
J_g	Energy storage within soil profile	g	Gravitational acceleration
v	Settling velocity	ρ_s	Solid density

J_v	Energy storage within the soil canopy	δ	Solid diameter
μ	Fluid viscosity		
∂T	Air temperature and aerodynamic temperature difference		
R^2	Coefficient of determination/correlation		

CHAPTER ONE

INTRODUCTION

1.1 Background Information

FAO (2015) estimates that out of the earth's 132 million square kilometres of land, about 25 million square kilometres is used for cattle pasture and about 15 million square kilometres is used for agriculture. According to research conducted by Huyghe *et al.* (2014a), permanent grasslands account for 33% of Europe's agricultural land, whereas temporary grasslands account for 6%. Furthermore, land usage and cover differs from nation to country due to low and unpredictable precipitation. Kenya's rangeland ecosystems are characterised by fluctuating supply of fodder for wildlife and livestock feeds (Smith *et al.*, 2010). Around 10 million people reside in the Kenyan rangelands, which also produce nearly to 70% of the nation's cattle and around 90% of its yearly tourism revenue. Most of these areas have abundant fodder of different quality during typical wet seasons (Mbatha & Ward, 2010). Ontitism *et al.* (2000), further stated that forage is scarce and generally of low quality during dry seasons. According to Reid *et al.* (2004), rangeland is any area that is used for grazing cattle and wildlife in its natural environment and is dominated by grasses, grass-like plants, forbs, or shrubs. Biomass refers to all plant life in the watershed, including grasses, shrubs, trees, agriculture wastes, and human and animal waste. About 80% of Kenya's dry and semiarid terrain consists of rangelands. When plants have limited access to water, their stomata conductance decreases so that they can preserve water; this, in turn, slows photosynthesis and reduces the amount of carbohydrates the plant can store. However, the availability of soil moisture as required for plant growth is a major limitation on the capacity of an agro-ecological system to produce biomass. Accurate observations of root zone soil moisture over vast spatial extents are necessary for model validation and run-time assimilation due to soil moisture being a state variable in many hydrological, meteorological, and agricultural models (Brocca *et al.*, 2010a; Grayson & Western, 1998). Factors that affect soil moisture include (1) precipitation history, (2) soil texture (which determines water holding capacity), (3) land surface slope (which influences runoff and infiltration), and (4) vegetation and land cover (which influences evapotranspiration and deep percolation) at any given time. Agricultural expansion is blamed for the decline of wildlife in rangelands because it causes the loss of habitat and the fragmentation of wildlife migration corridors. Mulinge *et al.* (2015) discovered that the rate of severe deterioration in Kenya increased from 23 to 30 percent between 1997 and 2000. According to Waithaka (2004), the Kenya Maasai Mara National Reserve (MMNR) is one of the most productive natural terrestrial ecosystems

because it supports more than 1.3 million wildebeest, 200,000 zebras, and thousands of Thomson's gazelles. It supports roughly 237 herbivores per km², making it unique in the world.

The Mara rangelands have shown remarkable durability throughout the years, accommodating an exceptionally high biomass of both permanent and seasonal herbivores (Lamprey & Reid, 2004). However, wildlife populations have declined as a result of the loss of habitat caused by the conversion of vast swaths of rangelands in the Loita plains (to the north of the national reserve) to large-scale commercial farms (Homewood *et al.*, 2001; Lamprey & Reid, 2004; Serneels & Lambin, 2001). The impact of shrub and tree invasion on various soil attributes varies greatly depending on plant species, regional climate, and soil type in areas where herbaceous plants are the dominant vegetation type (Barger *et al.*, 2011; Schuman *et al.*, 2002). Degradation leads to desertification and the introduction of invasive species if it is not properly managed. As water is a finite resource, any shifts in its distribution are likely to have far-reaching consequences for a region's agricultural output and social make-up, as argued by Smith *et al.* (2014). The ecosystem of the Naivasha croplands is under pressure from nearby infrastructural construction and industrial activity. Naivasha's subsistence farmers are making the switch to water-saving industrial horticulture techniques like drip irrigation and greenhouse construction because of the region's limited availability of surface water caused by rains.

1.2 Statement of the Problem

Climate variability with change in land use, land cover may lead to the alteration of soil matrix and thus poor infiltration. This phenomenon is accompanied by excess runoff downstream in form of storm water resulting to less moisture storage and retention for vegetation growth and healthy blossom of biomass in an ecosystem. The decrease in soil porosity and increase in bulk density minimizes storage and retention capacities of soil moisture dynamics suitable for vegetation development. Economic and social motives have led to increased rates of change of cropland use and rangeland encroachment of livestock herds and, as a consequence, continuous displacement of free-ranging animals. The ecosystems are currently threatened by ecological problems associated with climate variability, land use changes, land degradation, socio-economic problems, breakdown of traditional governance structures and shared habitats. Due to this, there is need for research in understanding soil moisture variability on ecosystems nature and its continual influence on vegetation growth and biomass productivity.

1.3 Research Objectives

1.3.1 Broad Objective

The overall objective was to evaluate the seasonal effect of climate variability on soil moisture and biomass production under rangeland and cropland ecosystems.

1.3.2 Specific Objectives

The specific objectives of the study were:

- i). To determine the spatio-temporal soil moisture storage and retention capacities in rangeland and cropland ecosystems.
- ii). To simulate the influence of bi-seasonal soil moisture variability on rangeland and cropland biomass yield using coupled Hydrus-1D and Agricultural Production Systems Simulator Model.
- iii). To analyse the impact of bi-seasonal soil moisture variability on land use change in rangeland and cropland vegetation cover.

1.4 Research Questions

- i). How do spatio-temporal soil moisture storage and retention capacities vary in rangeland and cropland ecosystem?
- ii). How does simulation of bi-seasonal soil moisture variability influence biomass yield in rangeland and cropland ecosystems using coupled Hydrus-1D and Agricultural Production Systems Simulator models?
- iii). How does bi-seasonal soil moisture variability impact on land use change in rangeland and cropland vegetation cover?

1.5 Justification

Soil moisture variability on spatial and temporal scale affects the distribution of biomass yield in both rangeland and cropland ecosystems. Weather conditions over time consecutively combine to form climate variability, which affects soil moisture variability and in turn influences vegetation growth and development. This variation is caused by long-term changes of atmospheric air, soil physical and chemical properties coupled with climatic variables such as rainfall patterns, temperature, humidity, wind speed, and direction among other weather variables. Notably, the majority of rangelands are constrained by water inputs, whether due to meteorological drought caused by low rainfall or agricultural drought caused by management practices that reduce the soil's ability to infiltrate and store water, thereby limiting crop or forage production (Mishra & Singh, 2010; Rockstrom, 2003). The study was informed by the migratory reasons of wildebeest, zebras, and habiting herbivores depending on biomass as feedstock. This seeks to address the effect of climatic variability attributes to soil moisture

variation on biomass build-up in ecosystems. Stressed plants result in low biomass production/yields due to limited soil moisture storage and retention for plants utilization. The need of understanding ecosystems and conservation policies on soil moisture content and monitoring clearly shows how aboveground biomass production (AGB) of vegetation allows for proper management and conservation in both ecosystems. The findings of the predicted biomass quantity and land cover in the study will permit ecosystem's planners, policy formulators, and managers' to schedule and fairly distribute, upscale or downscale their livestock/wildlife adjustment per unit area (carrying capacity) and allows the restoration of both environmental and economic exploitation. The productivity estimates of rangelands biomass and croplands yield trend provides the state of art practical experience and measures for management and assessment of vegetation vigour and growth capacity.

1.6 Scope and Limitations

The study focused on temporal and spatial soil moisture variability as the common denominator and its effect on biomass yield during bi-seasons (wet and dry) as influenced by climate variability; however, soil physical properties, with chemical properties were also evaluated on both ecosystems. The research also dealt with MMNR and Naivasha cropland ecosystem behaviour in view of soil moisture trends and biomass using selected models. The study took 2^{1/2} consecutive years that were used on instruments installation, soil sampling, soil analysis and setup of data collection tools for calibration and validation. The limitation of the study was attributed by large extent of spatio-temporal soil moisture and biomass collected from different soil moisture, soil temperature probes (5TM-ECH₂O) sites used to calibrate the cosmic ray soil moisture sensor (CRNS). Further, destructive clipping of grass AGB samples was experienced with inadequate drying of quadrat harvested green matter due to cloudy daily weather conditions during the research period. Most importantly, there was no noticeable weight loss in the use of in-situ solar and oven drying of clipped grass biomass.

CHAPTER TWO

LITERATURE REVIEW

2.1 Climate Variability

Changes in the mean state of the climate and other climate statistics (such as the frequency with which extremes occur and the size of their standard deviations) are all included in the broader concept of climate variability, which extends to all time and space scales beyond those of individual weather events. The behaviour of the ever-changing atmosphere can be seen on a daily or weekly basis, and is known as weather variability. Herrero *et al.* (2010) claimed that climate is the most influential predictor in rain-fed agricultural systems, and its impact is considerably greater in arid and semi-arid regions (ASALs). Worldwide, regionally, topographically, and locally, precipitation has been used to explain why semi-arid regions have such a wide range of yields (O'Connor *et al.*, 2001; Shan & Chen, 1993). Several studies in the last decade have shown that precipitation and soil moisture are strong indicators of total net aboveground primary productivity (NAPP) (Briggs & Knapp, 1995). Climate variability and change are realities that have an impact on rural livelihoods in West Africa today, as well as in many other parts of Africa and around the world, as observed by Jalloh *et al.* (2013). However, Mora *et al.* (2015) showed that the number of ideal growing degree-days would drop by as much as 11 percent worldwide if other limiting climatic factors including temperature, water availability, and solar radiation were taken into account. Significant climatic variables that influence the spatial and temporal availability of soil moisture include precipitation, relative humidity, air temperature, solar radiation, and wind speed.

Roughly sixty percent of the world's rangelands fall under the "dry" category. Galvin *et al.* (2008) and the fact that there isn't enough water during certain months of the year (Plisnier *et al.*, 2000; Scholes *et al.*, 1997) put at risk any local human populations that depend on ecosystem services that is often lessened by migration. According to Western *et al.* (2003), mean annual rainfall is not the only factor that affects pasture production; the seasonality of rainfall does so as well. Although rainfall estimates for the West African region are imprecise due to ambiguity in assessing potential vegetation-climate linkages (Intergovernmental Panel on Climate Change [IPCC], 2013), climate projections show that the rainfall differential between wet and dry regions and wet and dry seasons would rise.

2.1.1 Temperature and Wind Speed

Numerous ecological processes, including net primary production, root biomass, and soil respiration, are influenced by changes in temperature and precipitation patterns (Knapp *et al.*,

2008). Plants' photosynthesis and respiration are affected by temperature (Peng *et al.*, 2013), and temperature is the key determinant in determining when the growth season begins and ends (Piao *et al.*, 2005; Piao *et al.*, 2008). The dispersion and movement of atmospheric contaminants can be calculated using accurate wind speed observations. This includes not just the rate at which the wind is blowing but also its direction and how turbulent or gusty it is. Reduced crop yields are anticipated in some regions of the developing world, most notably Sub-Saharan Africa and portions of Asia, due to changes in temperature, precipitation, and extreme weather events caused by climate change (Gornall *et al.*, 2010). Environments vary in terms of temperature, radiation, and water availability, all of which interact to place complex and unique limits on plant growth and development (Nemani *et al.*, 2003).

2.1.2 Solar Radiation

Absorption of solar radiation is the energy source for photosynthesis since it provides the raw material for the process of electronic excitation. Soil moisture is a better indicator of plant-available water than precipitation alone (Liu *et al.*, 2013). Crop yield decreases of up to 50% in West Africa due to warmer temperatures were projected by scientists (Roudier *et al.*, 2011; Tamiru & Fekadu, 2019) due to the effects of global warming on temperature and precipitation. This in turn affects the soil moisture status and ground water level. Additionally, once the temperature rises by more than 2 degrees Celsius, the detrimental impacts of this temperature increase cannot be compensated for by any hypothetical increase in rainfall (Sultan *et al.*, 2013). Changes to the landscape are likely due to rising levels of drought, warmth, wildfire, and invasive species, which will make many formerly productive agricultural and wildlife areas unusable.

2.1.3 Evapotranspiration

As much as 70% of precipitation is thought to be returned to the atmosphere by evapotranspiration (ET), which includes soil evaporation, plant transpiration, and canopy intercepted rainfall evaporation (Kalma *et al.*, 2008; Trenberth *et al.*, 2011). When calculating latent (evaporative) and sensible heat fluxes, eddy covariance (EC) makes use of high-frequency measurements of water vapour concentration, air temperature, and vertical wind speed. In particular, evaporation is limited by the amount of water in the soil (Seneviratne *et al.*, 2010), meaning that it affects plant stress and response. Actual evapotranspiration (ET_a) is determined by subtracting losses from sensible heat flux (energy needed to heat the air) and ground heat flux from net surface radiation (energy stored in the soil and vegetation). The major 'sink' term in Equation (2.1) is evapotranspiration, or water

uptake by plants, which indicates the quantity of soil moisture that is utilized through crop consumption.

$$\int_0^Z \theta_2 z dZ = \int \theta_1 z dZ + RF_1 + CR_1 - DP_1 - DR_1 - ET_1 \quad (2.1)$$

where, θ_2 , is the volumetric soil moisture content of the root zone depth Z on day 2 ($\text{cm}^3 \text{cm}^{-3}$), θ_1 is the volumetric SMC on day 1 ($\text{cm}^3 \text{cm}^{-3}$), and Z is the root zone depth (cm). Effective precipitation, capillary rise, deep percolation, surface runoff/drainage out of the field, and crop evapotranspiration on day 1 are represented by RF_1 , CR_1 , DP_1 , DR_1 , and ET_1 , respectively (cm). Comparing the eddy covariance and catchment water balance methods, Wilson *et al.* (2011) found that annual evapotranspiration was similar between the two methods. Pauwels and Samson (2006) examined the estimates of latent heat fluxes from BREB and EC-based models in wet sloping grassland and found considerable agreement between the two approaches. The comparison between the BR-DTS and the reference approaches revealed a very strong correlation between the sensible heat flow at seven data points (slope of 0.93, zero offset of 4.7Wm^{-2} and R^2 of 0.88).

2.2 Bowen Ratio Theory

Determining the latent heat flow and real land surface evaporation is as easy as using the Bowen ratio (BR) method of surface energy balance. Measurements of the air's temperature and vapour pressure gradient are used to determine the Bowen ratio. Latent heat fluxes can be calculated using the Bowen ratio in conjunction with net radiation (R_n) and the soil heat flux (G_o). Shi *et al.* (2008) calculated latent heat transfer inside a temperate mixed forest of broad-leaved and coniferous trees in north-eastern China's Changbai Mountains. The author used three different techniques during the growth seasons (May to September) of 2003 – 2005: EC, BREB, and Penman–Monteith (PM). He found that the patterns of diurnal and seasonal variations in latent heat fluxes were similar across the three approaches.

2.2.1 Latent Heat Flux

The rate of latent heat loss from the surface as a result of evapotranspiration is known as latent heat flux (λE). Equation (2.2) allows for the following representation of the latent heat: (2.2)

$$\lambda E = R_n - G_o - H \quad (2.2)$$

A single remote sensing data point used to assess land surface fluxes, namely evapotranspiration, is the estimation of evaporative fraction (Λ), which is the ratio of latent heat

flux over available energy. It's common knowledge that during days with a 12-hour daylight period in fair weather, the evaporative percentage exhibits diurnal behaviour (Bastiaansen *et al.*, 1996). Niaghi (2019) assessed ET in the upper Midwest in 2018 using the EC, BREB, and soil water balance methodologies throughout the corn-growing season. The author found that when comparing the estimated λE by the EC system's residual approach to the determination by the BREB system across the whole growing season, the EC system's estimate was 29 percent higher.

2.2.2 Sensible Heat Flux (H)

Rate of heat loss to the air by convection and conduction due to a temperature differential, denoted by the sensible heat flux (H), is given by the following formula:

$$H = \rho_{air} C_p \frac{dT}{r_{ah}} \quad (2.3)$$

Where ρ_{air} is the density of air (in kilograms per cubic meter), C_p is the specific heat of air (1004 Jkg⁻¹K⁻¹), dT is the difference between the temperature of the air and the temperature of the air near the surface, ($dT = T_a - T_s$), and r_{ah} is the resistance of air to movement. Using a modified Bowen ratio approach, Foken (2015) discovered that sensible and latent heat fluxes could be determined with uncertainties of about 10% for the former and about 20% for the latter techniques.

2.2.3 Soil heat Flux

The rate at which a soil stores heat due to temperature gradient between its surface and its uppermost layer is known as the soil heat flux G_0 , and it is measured in watts per square meter (Wm⁻²). G_0 Measurements of under field conditions are possible if the thermal conductivity of the soil is known, as shown below:

$$G_0 = \lambda_s \frac{\Delta T_s}{\Delta z} \quad (2.4)$$

where, λ_s = the thermal conductivity of the soil, ΔT_s = temperature difference between T_0 and T_1 and Δz = depth difference between z_0 and z_1 .

2.2.4 Net Radiation

Atmospheric conditions must remain constant for there to be a net radiation balance between incoming and outgoing short wave and long wave radiation.

$$R_n = R_s \downarrow + R_s \uparrow + R_L \downarrow - R_L \uparrow \quad (2.5)$$

where, R_n is the net radiation ($\text{W}\cdot\text{m}^{-2}$), $R_s \downarrow$ is the incoming short-wave radiation ($\text{W}\cdot\text{m}^{-2}$), and $R_s \uparrow$ is the outgoing short-wave radiation ($\text{W}\cdot\text{m}^{-2}$), while $RL \downarrow$ is the incoming long-wave radiation ($\text{W}\cdot\text{m}^{-2}$), and $RL \uparrow$ is the outgoing long-wave radiation ($\text{W}\cdot\text{m}^{-2}$). The net short-wave radiation can be written as follows:

$$\sum R_s = (1 - \alpha) R_s \downarrow = (1 - \alpha) (S_c \times \cos \theta \times d_r \times \tau_a) \quad (2.6)$$

Where α is the surface albedo, S_c is the solar constant (Wm^{-2}), θ is the angle at which the sun hits the surface, d_r is the distance between the Earth and the Sun, and τ_a is the amount of light that can pass through the atmosphere. The atmosphere's downward thermal radiation flux is responsible for the entering long-wave radiation. It is possible to determine the emissivity of a cloudless atmosphere by determining the relationship between the amount of water vapour, the pressure, and the temperature.

$$R_L \downarrow = e_{sky} \times \sigma \times T_a^4 \quad (2.7)$$

Where e_{sky} is the emissivity of air, σ is the Stefan-Boltzmann constant (in $\text{Wm}^{-2}\text{K}^{-4}$), and T_a is the air temperature (K). The Stefan-Boltzmann equation is used to calculate the long-wavelength radiation that is emitted.

$$R_L \uparrow = \varepsilon_o \times \sigma \times T_s^4 \quad (2.8)$$

where, ε_o is the surface emissivity and T_s is the surface temperature (K).

2.2.5 Surface Energy Balance

The energy entering the surface must match the energy leaving during the same time. The energy balance equations must take into account all energy fluxes. The equation for a surface in the process of evaporation is:

$$R_n = k + L = \lambda E + H + G_o \quad (2.9)$$

Where R_n is net radiation, k net short-wave radiation, L net long-wave radiation, λE latent heat flow (Wm^{-2}), H sensible heat flux (Wm^{-2}), and G_o soil heat conduction are variables (Wm^{-2}). The distribution of daytime net radiation among sense heat flux, latent heat flux, and soil heat conduction is determined by the surface's composition. Evaporation potential is the primary factor in determining the relative importance of sensible and latent heat fluxes. Veenendaal *et al.* (2004) investigated seasonal variations in energy fluxes and carbon dioxide exchange in a broad-leaved semi-arid savannah (Mopane forest) in Southern Africa. They found that throughout the rainy season, the Bowen ratio (b) was frequently just below unity,

and that sensible and latent heat fluxes were linearly proportional to incoming solar radiation (I). During the dry season, when solar radiation is low (about 150Wm^{-2}), b is normally around 1, but it rises dramatically with I, reaching values of 4 or 5 around solar noon. As a result, under these dry conditions, practically all of the available energy was lost as sensible heat rather than latent heat.

2.2.6 Water Vapour

A volume of air's relative humidity is expressed as a percentage based on the difference between its actual vapour pressure and its saturation vapour pressure. It's also utilized to calculate the deficit in vapour pressure that's having an effect on plant growth.

$$Rh = \frac{e}{e^o} \quad (2.10)$$

Where Rh is the relative humidity on a certain day, e is the actual vapor pressure on a particular day (kPa), and e^o is the saturation vapor pressure on a particular day (kPa).

The rate of evaporation is directly related to the pressure differential between the surface and the surrounding air. The gap between the two is known as the vapour pressure deficit.

$$vpd = e^o - e \quad (2.11)$$

where vpd is the actual vapor pressure on a given day kPa , e^o is the saturation vapor pressure for that day kPa , and e is the vapor pressure deficit for that day (kPa). The higher the value of, the quicker the rate of evaporation. The quantity of heat energy needed to vaporize liquid water (by dissolving its hydrogen bonds) is known as its latent heat of vaporization.

2.3 Soil Water Dynamics

This refers to soil's ability to control the availability of fresh water on land by filtering, retaining, or storing precipitation for plant use. In addition, it comprises the movement of these contaminants along flow pathways to both groundwater and surface water sources. Therefore, soil hydrologic processes are vital to the survival of nearly all land and freshwater organisms (O'Geen *et al.*, 2010). Numerous elements influence the water dynamics in soil, which vary vertically with depth, laterally across landforms, and temporally in shorter time span reaction to long-term climate change (Swarowsky *et al.*, 2011). Furthermore, dynamic elements like rainfall, evapotranspiration, drainage, lateral flow, and the presence of water tables affect the geographical and temporal distribution of soil moisture (Reynolds, 1970; Takagi & Lin, 2011). Estimating soil moisture is important for hydrology and agriculture because it affects how much water is available for plants to grow (Rodriguez-Iturbe, 2000)

and how deep aquifers are refilled (Hodnett & Bell, 1986); and (ii) the saturation of soils, which affects how rain is split between runoff and infiltration (Hodnett & Bell, 1986; Rodriguez-Iturbe, 2000).

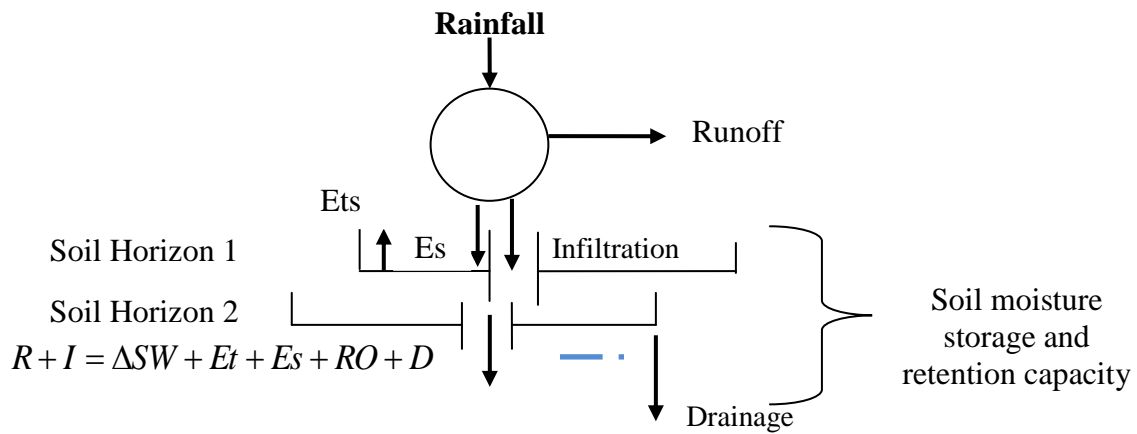


Figure 2.1: Schematic diagram of soil moisture dynamics (Swarowsky *et al.*, 2011)

2.3.1 Soil Water Storage

Bullied and Entz (1999) suggest that soil water storage is the amount of water that a plant's roots store in the soil. An increase in rooting depth suggests that there is more water in the soil, providing the crop with more moisture in between rains. In water-limited areas, plant productivity often rises linearly with mean annual precipitation or actual ET, provided that all other conditions remain unchanged (Chong *et al.*, 1993). Soil moisture is a dynamic feature that shifts over time and space as a result of usage and redistribution via subsurface movement and in response to climatic and topographical conditions (Western *et al.*, 1999). The amount of water present in the soil at any one time is known as its water content, and it can be measured either volumetrically or gravimetrically. In a wet basis context, water content (WC) measures the total amount of liquid water in a soil sample, while moisture content (MC) measures the total amount of water vapour and other volatile components. Water content and moisture are measured in the following ways;

$$\text{Water content in wet basis, } \%mc_{wb} = \frac{W_w - W_d}{W_w} \times 100 \quad (2.12)$$

$$\text{Moisture content in dry basis, } \%mc_{db} = \frac{W_w - W_d}{W_d} \times 100 \quad (2.13)$$

where, W_w = the wet weight, (g)

W_d = the weight of soil solids, (g)

The ability of soil to store water is affected by factors such as particle size, the proportion of organic matter in the soil, and the depth of the soil. The spatial and temporal variability of

soil-water characteristics is high (Gomez-Plaza *et al.*, 2000). In semi-arid and dry environments, for example, spatial and temporal changes in soil moisture have traditionally been major challenges in vegetation regeneration and water resource management (Brevik *et al.*, 2015; Yu *et al.*, 2015). The amount of soil water that is accessible depends heavily on the soil's texture, and the soil's ability to store water can rise by as much as 3.7% for every 1% increase in soil organic matter (Bot & Benites, 2005). Water movement in soil is controlled by particle size and packing, both of which are in turn governed by the size and shape of pores. Soil structure, aggregate stability, particle size distribution, and land use system all have an impact on the features of soil moisture, which are important soil hydrological qualities (Fu *et al.*, 2000). A soil's bulk density can be calculated by dividing its mass after drying it for 16 hours or more at 105 degrees Celsius by its initial volume, as stated by Easton *et al.* (2015). Similar to how bulk density is calculated, particle density is calculated by dividing the mass of the dry soil by the volume of the solid soil components while ignoring the pore space. Particle density in soil refers to the average weight of the individual mineral grains that make up a given volume of soil.

$$\rho_m = \frac{M_m}{V_m} \quad (2.14)$$

where, M_m is the mineral grain's mass and V_m is its volume. Value is usually calculated based on the soil's mineral content rather than measured. Because quartz, one of the most common minerals in soils, also has a density of 2.65 g/cm³, most soils have a particle density of roughly 2.65 g/cm³. Soils that contain a lot of either clay (2.83 g/cm³) or organic matter (0.8 g/cm³) would have a different particle density than the estimated 2.65 g/cm³ because of these additional components. The soil's dry density is known as its bulk density.

$$\rho_b = \frac{M_m}{V_s} = \frac{M_m}{V_a + V_w + V_m} \quad (2.15)$$

where, V_s is the total volume of the soil sample, which is the sum of the volume air, V_a liquid water, V_w and mineral components, V_m of the soil respectively.

Soil aggregation, texture, root penetration, and other biological activity like burrowing insects and worms all have a major impact on soil porosity. The presence of organic matter improves soil porosity by encouraging the formation of aggregates. Measuring the time it takes for a certain volume of water to completely permeate the soil's microscopic pores is a scientific method for determining its porosity. The permeability is caused by;

$$n = \frac{V_a + V_w}{V_s} = \frac{V_s - V_m}{V_s} = 1 - \frac{M_m / V_s}{M_m / V_m} = 1 - \frac{\rho_b}{\rho_m} \quad (2.16)$$

n value for is typically calculated by measuring and making reasonable assumptions about ρ_m . Soil types can have a n value anywhere from about 0.25 to 0.75. Niu *et al.* (2015) showed that the soil moisture condition in semi-arid sandy soils is affected by the land use. Soil moisture levels varied depending on the type of land use, with grassland having the greatest levels, followed by cropland, poplar land, inter-dunes, and shrub land. The temporal fluctuations in soil moisture across different land uses were not always consistent with the rainfall due to the dry sequence. One measure of soil moisture is its saturation, which is defined as;

$$S_d = \frac{\theta}{n}, \quad (2.17)$$

Intensity of saturation might be either 0 or 1. A soil sample of known volume is first weighed, followed by oven drying at 105°C, reweighing, and calculation to determine the volumetric moisture content;

$$\theta = \frac{M_s^{wet} - M_s^{dry}}{\rho_w V_s} \quad (2.18)$$

where M_s^{wet} and M_s^{dry} is the initial and final masses before and after drying, respectively, and is the density of water (1000 kg/m³). Soil moisture can be measured using this gravimetric technique.

2.3.2 Soil Water Retention

A soil's matrix potential describes the energy state of the water film and the volumetric water content is the quantity of water retained in the soil's pores (Liu *et al.*, 2012). Particle size distribution, clay mineralogy, organic content, and hysteresis all play important roles in the water retention function (Van Genuchten, 1980). While the matrix potential is high (less negative number) and the water film is thick in a moist soil, it is low (more negative number) and the water film is thin when the soil dries out (Brady & Weil, 2010). Desorption at low and high pressure (0 and 0.1 bar, respectively) is used to reach a conclusion (0.3, 1, 3, 5 to 15 bar). The 0.3 bar determination is commonly known as field capacity in agricultural settings, while the 15 bar determination is called the wilting point. The relationship between soil moisture tension and soil moisture content is known as the moisture retention curve or soil moisture characteristic. If the tension is written as the logarithm of cm of water, the resulting

graph is called a pF-curve (Figure 2.2). An index of available moisture in soils (the quantity of water that can be absorbed readily by plant roots) and soil types can be determined with the help of moisture retention curves. Both undisturbed and disrupted samples are used to establish moisture properties.

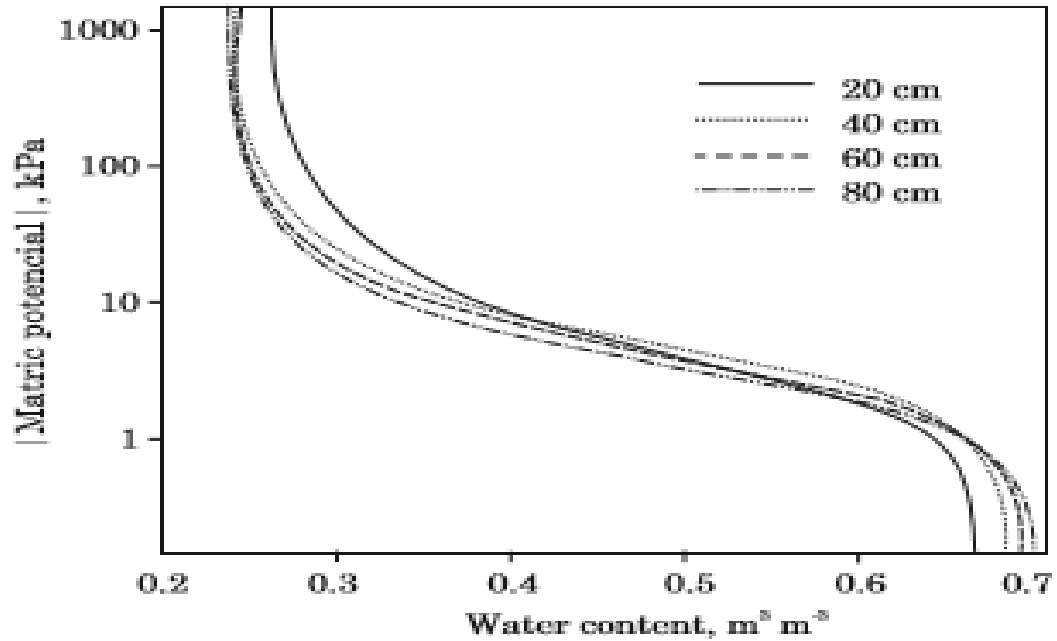


Figure 2.2: Soil water retention curves adjusted by the cubic polynomial model at depths of 20, 40, 60, and 80 cm (van Genuchten, 1980)

Sand, loam, and clay have volume percent values of 6, 20, and 17 respectively, which may vary depending on the soil type. By gradually increasing the pressure head and measuring the moisture content, we can develop a curve for the pressure head, h , versus the soil-water content, θ . Pressure heads range between 0 (for saturation) and 10^7 cm (for oven-dry conditions). pF, like pH, is the logarithm of the tension or suction in centimetres of water. Thus,

$$pF = \log|h| \quad (2.19)$$

The soil moisture retention curve (pF curve) depicts the relationship between suction and content of soil moisture (Van Genuchten, 1980). When a soil reaches F.C. (field capacity) or a pF-value of 2, it has been saturated by rainfall for approximately two to three days. When a soil dries out and plants are unable to absorb water, the soil reaches W.P (wilting point) or has a pF = 4.2. Available water is the amount of water held by a soil in the root zone between F.C. and W.P. that can be used by plants (F.C. - W.P. = Available Water Content). These values are constant depending on the type of soil since no soil is 100% pure. This is always the amount of water retained in the soil profile between FC (or DUL), which is the drainage

upper limit and PWP (or DLL), as the lower limit usually can be determined in the laboratory. Mathematically it can be expressed as:

$$AW = (\theta_{DU} - \theta_{LL})Z \quad (2.20)$$

The conversion of SMC from volumetric units into equivalent depth of water can be obtained as:

$$d = \theta Z \quad (2.21)$$

where, d is depth of water per unit of soil profile (cm); θ is volumetric soil moisture content ($\text{cm}^3 \text{cm}^{-3}$); and Z is depth of soil profile under interest (cm). In practice, soil is never allowed to dry out to PWP (or DLL), but is kept above a certain soil moisture before reaching a critical soil moisture level to avoid severe yield losses.

2.3.3 Surface Runoff

Overland flow or surface runoff is the result of water that does not penetrate the ground. At the scale of hill slopes, interactions between vegetation patches and runoff become significant. According to Ludwig *et al.* (2005), plant patches and other surface obstructions can capture and retain surface runoff through a process known as runoff-run-on. Rain that does not soak into the ground and instead flows off into bodies of water is called surface runoff (Perlman, 2016). In contrast, it decreases when soil moisture increases. The surface depressions start to fill when the rate of application exceeds the rate of infiltration. If the application rate is still higher than the infiltration rate after all depressions on the surface have been filled, runoff will occur on the surface. Perlman (2016) notes that the amount of water that flows off the land as runoff varies with the season and location, with the other two-thirds either evaporating, transpiring, or infiltrating the soil.

2.3.4 Soil Infiltration and Hydraulic Conductivity

Water enters the soil via infiltration when it drains or seeps downward from the surface (Thompson *et al.*, 2010; Zhang *et al.*, 2010). As water infiltration is essential for plant water supply and erosion prevention via overland flow, double-ring infiltrometers are commonly employed to assess the hydraulic conductivity of soils in situ (Ashraf *et al.*, 1997; Ben-Hur & Assouline, 2002; Bouwer, 1986; Dirk *et al.*, 1999). The presence of vegetation can greatly enhance infiltration because it slows overland flow, extending the time that water spends infiltrating the soil. Vegetation cover is essential for maximizing infiltration as it decreases soil compaction, buffers the force of rainfall hitting the soil surface, boosts porosity through root development, and boosts soil organic matter to encourage aggregation (Li *et al.*, 2011).

Table 2.1: Some examples of constant infiltration rates for different soil types

Soil Type	Constant infiltration rate (mm/hr)
Sand	>30mm
Sandy Loam	20-30
Loam	10-20
Clayey Loam	5-10
Clay	1-5

Source: (Bouwer, 1986)

Soil hydraulic conductivity at or near saturation can be inferred from infiltrometry test results by fitting the volume of infiltrated water versus time. Ward and Robinson (1990) reported that the soil water retention $\theta(h)$ and hydraulic conductivity $K(h)$ functions describe the soil's hydraulic properties. These functions describe how water moves through the vadose zone and how it is split between infiltration and runoff. Testing with infiltrometry can be done in a laboratory or on-site to get an estimate of the hydraulic conductivity (K_{sat}). Oguike and Onwuka (2018) tested a variety of land use systems in Ubakala Umuahia, Abia State, Nigeria, and found that the slowest saturated hydraulic conductivity (K_{sat}) was between 0 and 20 centimetres deep (0.71 and 0.62 cm min⁻¹). Under cassava-cultivated land, infiltration rates (Ir) were observed at 0.63 cm min⁻¹, while the quickest Ksat (0.80 and 0.77 cm min⁻¹) were recorded under 4-year bush fallow. Forests were the areas with the highest Ir (0.73 cm min⁻¹). In all types of ecosystems, increasing soil depth increased field capacity and accessible moisture content while decreasing permanent wilting point.

2.3.5 Drainage

Richards' equation directs soil water seepage to depths beyond the root zone. Setting the bottom border of the soil column far enough down means it will have little impact on the root zone's soil moisture dynamics. It is assumed, as in Laio *et al.* (2001b), that the unsaturated hydraulic conductivity has an exponential shape, and the leakage rate in the root zone is equal to this value.

$$L(S) = K_{sat} \frac{e^{\beta(S-S_{fc})} - 1}{e^{\beta(1-S_{fc})} - 1} \quad (2.22)$$

where, K_{sat} is the saturated hydraulic conductivity, and β is a parameter of the soil. The field capacity S_{fc} is the saturation at which the rate of gravity drainage becomes negligible relative to evapotranspiration.

2.4 Modelling Application for Prediction and Decision Support

According to Ma *et al.* (2011), mechanistic models' incorporation of biophysical processes enables them to anticipate system behaviour across a wide range of situations. The models are empirical in nature; therefore, they need to be calibrated initially using specific inputs and circumstances before being extrapolated to other soil, climatic, and management settings. Users must choose a model or models based on their goals and decision support criteria before defining the confidence intervals for model acceptance. The model(s) must then be calibrated using the experimental data that is currently available.

2.4.1 Model Calibration

In order to get accurate predictions from a model, Imnek and Hopmans (2002) define model calibration as "the act of fine-tuning a model for a specific situation by adjusting the input parameters (e.g., soil hydraulic parameters) on boundary conditions within appropriate ranges until the simulated model outputs closely match the observed variables" (e.g., pressure heads, water contents, concentrations, various fluxes). Model calibration often involves selecting an objective function that may be used to quantify the degree to which observed data agrees with those predicted by the model and that is linked in some way to the parameters under study. The optimal fitting parameters are then selected by minimizing this objective function. Models can be calibrated either by trial and error or with the use of computerized minimization or parameter estimation strategies. For a model to be considered, calibrated it must be able to recreate data with an accuracy that is deemed satisfactory (Konikow & Bredehoeft, 1992). Model calibration is sometimes known as "history matching," "parameter optimization," or "parameter estimation" (Imnek & de Vos, 1999).

2.4.2 Soil Moisture Dynamic Models

The study of the interplay between climate, soil moisture dynamics, and plant life is called eco-hydrology, and it is a relatively new scientific discipline (Rodriguez-Iturbe, 2000). Many elements, including fire, grazing, and nutrient availability, affect plant growth and survival, but so far researchers have focused primarily on water-controlled ecosystems (Laio *et al.*, 2001a; Ridolfi *et al.*, 2000; Rodriguez-Iturbe *et al.*, 1999). Predictability varies with time and location, making seasonal forecasting a challenging subject of study and application. Furthermore, the predictable signal is often masked by natural fluctuation (Stockdale *et al.*,

2010). These issues undermine the importance of this study and the justification for conducting presently, when the climate is highly unpredictable. Since precipitation is inherently unpredictable, and the processes of infiltration, evaporation, transpiration, and drainage are all nonlinear, soil moisture displays a wide range of complex variations.

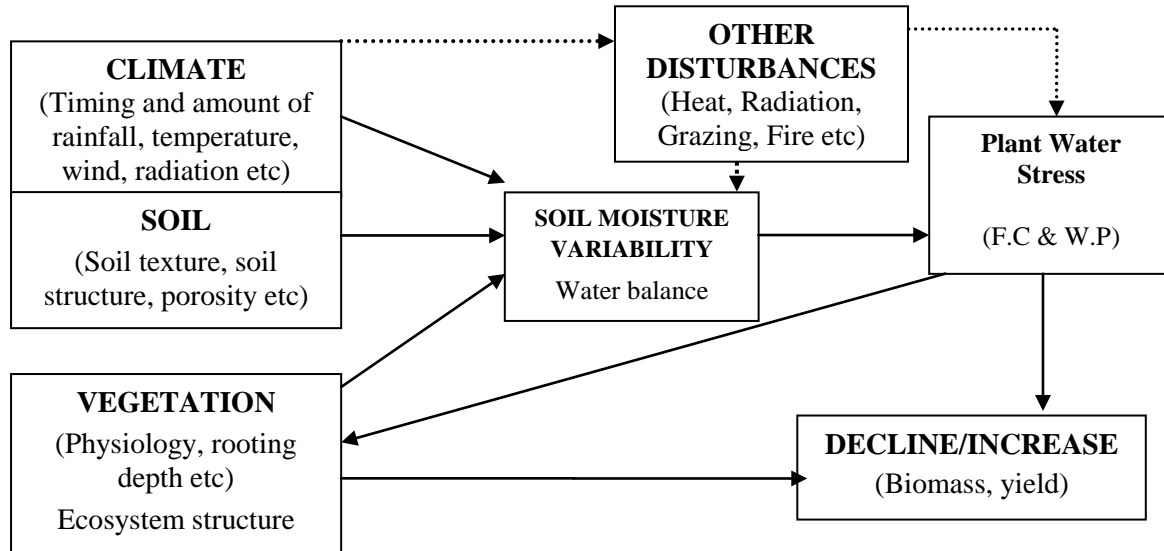


Figure 2.3: Modified schematic representation of climate-soil-vegetation system interaction (Porporato & Rodriguez-Iturbe, 2002)

As a result, the dynamics of soil moisture have a major bearing on the pressures experienced by plants and the degrees to which different plant species are adapted to a given environment. This simplification served as the foundation for a model created by Rodriguez-Iturbe *et al.* (1999), who analytically determined the steady state probability density function (pdf) of soil moisture. D'Odorico *et al.* (2000) used these models to investigate the impact of seasonal climate variability on soil moisture.

2.4.3 Vadose Zone Modelling Approaches

The American Petroleum Institute (API) defines the vadose zone as the geological layer between the land surface and the regional water table (API, 1996). Because of the presence of air and water in its pore space, the vadose zone is also known as the unsaturated zone and, less frequently, the zone of aeration. Between the ground's surface and its water table is what's called the vadose zone. In porous media like soils, water movement is frequently described using the Darcy equation, which states that flow is proportional to the product of hydraulic potential times the hydraulic conductivity:

$$q = -K \frac{\Delta H}{\Delta z} \quad (2.23)$$

where, q is the flow rate, K is the saturated hydraulic conductivity (length per time), ΔH is the hydraulic conductivity head differences, and Δz is the distance. The permeability is a

spatially variable property of soils (over several orders of magnitude over short distances). It is dependent on the soil texture, but also on the structural characteristics of the soil. Hydraulic conductivity is highly dependent on saturation level and thus on soil water tension. The Richards equation was developed based on this functional relationship by combining the Darcy equation and the continuity equation to describe flow in unsaturated porous media:

$$\frac{\partial \theta}{\partial t} = \frac{\partial}{\partial z} \left[K(h) \left(\frac{\partial h}{\partial z} + 1 \right) \right] \quad (2.24)$$

where, $K(h)$ and θ represent the unsaturated hydraulic conductivity and the moisture content respectively. Because of their capillary properties, both equations perform admirably in soils with low variability. The Richards equation has a long history of use in vadose zone hydrology for describing the flow of water. This equation relies on the mass conservation formula,

$$\frac{\partial \theta}{\partial t} = - \frac{\partial q_i}{\partial x_i} - S(h), \quad (2.25)$$

is combined with Darcy's law,

$$q_i = -K(h) \left[\frac{\partial (h + x_3)}{\partial x_i} \right], \quad (2.26)$$

which results in,

$$\frac{\partial \theta}{\partial t} = \frac{\partial}{\partial x_i} \left[K(h) \frac{\partial}{\partial x_i} (h + x_3) \right] - S(h) \quad (2.27)$$

where, θ is the soil's moisture level, q_i is the water flux, h is the soil's matric potential, K is the soil's hydraulic conductivity, t is time, S is a sink term to account for plant roots sucking up water, and x_i is Cartesian coordinates. Specifically, x_3 it denotes the vertical axis of a coordinate system. To solve equation (2.25), it is necessary to define the moisture retention characteristic, $\theta(h)$ the hydraulic conductivity function, $K(h)$, as well as the beginning and boundary conditions.

2.4.4 Bucket Model

The bucket model approximates the dynamics of soil moisture using a volume balance equation applied to the root zone of a plant (Rodriguez-Iturbe *et al.*, 1999):

$$nZ_r \frac{\partial S}{\partial t} = I(S, t) - L(S) - T(S) - E(S) \quad (2.28)$$

where, S represents the average saturation over the root zone, n represents the porosity, Z_r represents the depth of the root zone, $I(S, t)$ represents the infiltration rate to the root zone,

$L(S)$ represents the rate at which water is lost from the root zone, and $T(S)$ and $E(S)$ represent the transpiration and evaporation rates, respectively.

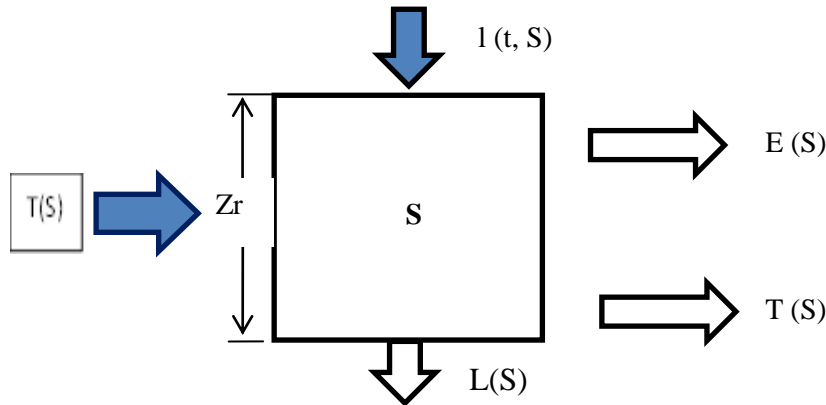


Figure 2.4: Schematic representation of the vertically averaged bucket model (Rodriguez-Iturbe *et al.*, 1999)

In this simplistic model, the soil moisture content across the root zone is simply represented as a single saturation value, with wetting front propagation disregarded. Root zone saturation is the only determinant of leakage and evapotranspiration losses. Figure 2.4 is a schematic representation of the bucket model, and Rodriguez - Iturbe *et al.* (1999) and Laio *et al.* (2001b) provide detailed explanations.

2.4.5 Richards Model

The Richards model resolves the soil column in the vertical dimension, and Richards' equation describes the soil moisture dynamics:

$$\frac{\partial(ns)}{\partial t} - \frac{\partial}{\partial z} K \frac{\partial h}{\partial z} + \frac{\partial K}{\partial z} = -e' - \sigma' \quad (2.29)$$

where, s , is the local saturation, h is the water pressure head in lengths, z is positive downhill, and K is the unsaturated hydraulic conductivity in lengths per second. Local evaporation and plant uptake rates are given by the functions e' and σ , respectively. Water is lost by evaporation at a depth of Z_e and taken up by the plant at a depth of in the root zone, Z_r . The volume balance for layer i becomes, for a uniformly discretized soil column,

$$\Delta z \frac{\partial(ns)_i}{\partial t} - K_{i+\frac{1}{2}} \left(\frac{h_{i+1} - h_i}{\Delta z} \right) - K_{i-\frac{1}{2}} \left(\frac{h_i - h_{i-1}}{\Delta z} - 1 \right) = -e_i - \sigma_i \quad (2.30)$$

where, Δz , is the level of spatial discretization, e_i and σ_i are the (depth-per-time) rates of evaporation and plant uptake from layer i . The Richards model is depicted in a simplified form in Figure 2.5. When it comes to finding knowledge gaps and choosing the appropriate

process-based modules, Derner *et al.* (2012) stressed the importance of validating models with well-designed experimental data.

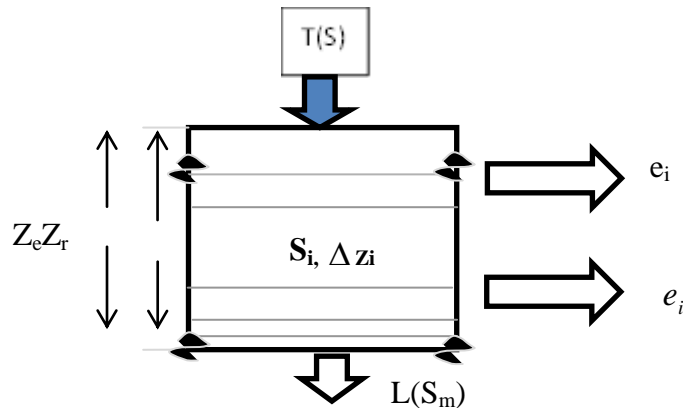


Figure 2.5: Schematic representation of the one-dimensional Richards model (Rodriguez-Iturbe *et al.*, 1999)

2.4.6 SWAT Model

Soil and water analysis (SWAT) tool, is a watershed model created by Dr. Jeff Arnold in the early 1990s for the Agricultural Research Service of the United States Department of Agriculture (ARS). To predict long-term effects of land management strategies on water, sediment, and agricultural chemical yields in large, complex watersheds with varied soils, land use, and management circumstances. SWAT uses a cascading method to simulate changes in soil water content. When hourly precipitation data is available, it uses the Curve Number (CN) method to compute infiltration, and otherwise it uses the Green-Ampt method. Using SWAT (version 2012), Mwangi *et al.* (2016) evaluated the effect of land use change and climate variability on watershed hydrology in the Mara River Basin, East Africa. Their simulations indicated that agro- forestry in the watershed would decrease surface runoff, primarily as a result of the expected improvement of soil infiltration. The module works under the premise that soil moisture is continuously dispersed throughout its various levels. According to Brocca *et al.* (2012), additional study is necessary to optimize the framework of SWAT and other hydrologic models in order to maximize the benefits of including an increasing number of large-scale soil moisture observations.

2.4.7 Variable Infiltration Capacity Model

Variable Infiltration Capacity (VIC) is a process-based, regional hydrologic model created by Liang *et al.* (1994). With the variable infiltration capacity curve developed by Zhao *et al.* (1980) and the base flow formula developed by Franchini and Pacciani (1991), VIC can simulate infiltration and surface runoff. Liang *et al.* (1996) added multiple soil moisture layers to the mode while (the original version only had two). Water and energy fluxes are well represented in the VIC model, and the model can be run at sub-daily time steps, both of

which are necessary for comprehending land-atmosphere interactions and atmospheric coupling. This is because the VIC model was developed to be coupled to regional and global-scale atmospheric models. Using historic land surface hydrology simulations from the VIC model, Sheffield *et al.* (2004) created a soil-moisture-based drought index.

2.4.8 Hydrus Model

Water flow across one-, two-, and three-dimensional variably saturated porous media can be simulated using the Hydrus (1D, 2D/3D) Windows-based computer programs. A California University is responsible for developing the software (Simunek *et al.* 2012; van Genuchten, 1985). Soil moisture dynamics are represented by the two-dimensional mode equations (2.29), (2.30), which are based on Richard's equation. Chen *et al.* (2014) utilized Hydrus-1D to replicate soil moisture in two sub-basins of the Goulburn River in Australia for three years. As a result of their inverse modelling efforts, they found that the soil properties changed, with r becoming less significant and s and K_s becoming more significant. In addition to soil texture, the aforementioned authors state that the amount of macropores generated by roots or fractures, the kind of vegetation, organic matter, and human activities are all taken into account when calculating calibrated hydraulic parameters. Gupta *et al.* (2012) provided software that gives numerical solution to the Richards' equation for unsaturated water and the advection-dispersion equation for solute transport based on the Fickian approximation. Soil water flow in one dimension is described by Hydrus-2D, which uses numerical solutions to Richard's equation.

$$\frac{\partial \theta}{\partial t} = \frac{\partial}{\partial x} \left(K(\theta) \left(\frac{\partial h}{\partial x} + \cos \alpha \right) \right) - S \quad (2.31)$$

$$\frac{\partial \theta}{\partial t} = \frac{\partial}{\partial x} \left[K \left(K_{ij}^A \frac{\partial}{\partial x_j} + K_{iz}^A \right) \right] - S \quad (2.32)$$

where, θ is the volumetric soil water content ($\text{m}^3 \text{m}^{-3}$), t is time (s), K is the unsaturated soil hydraulic conductivity (mms^{-1}), h is water pressure head (L), α is angle between the flow direction and the vertical axis (for vertical movement of water in soil $\alpha = 0$, for horizontal movement $\alpha = 90$ and $0 < \alpha < 90$ is for other direction). S is the roots water uptake term ($\text{L}^3 \text{L}^{-3} \text{T}^{-1}$) and x is spatial coordinate (L) (positive upward). Roots water uptake (S) term in equation 2.38) is determined as the volume of water taken from the soil by plants per unit volume per unit time. In this model, S is based on Feddes relationship and defined as:

$$S(h) = \alpha(h) S_p \quad (2.33)$$

where, $\alpha(h)$ is water stress function and S_p is water absorption potential. Over the years, Hydrus-1D model has been successfully applied in various studies worldwide for predicting soil moisture content and water movement under different conditions (Chen *et al.*, 2014; Da *et al.*, 2015; Gabiri *et al.*, 2018). Honar *et al.* (2011) analysed water flow and infiltration in a sprinkler irrigation system to depth using the HYDRUS-1D model; their findings revealed that field capacity could be maintained with irrigation and flow rate. Corn farming in France was simulated using this program, and it was utilized in another study to model agricultural water and soil conditions using actual data. Hydrus-1D is a physically based model, hence it requires data that can be gathered through experiments, such as weather data for surface boundary conditions, soil physical conditions, and physical parameters (saturated hydraulic conductivity and a soil water retention curve) (Honari *et al.*, 2017; Simunek *et al.*, 1999; Tinet *et al.*, 2015). Specifically, Hydrus 1D was chosen for this investigation due to its reliability and the fact that the study's input parameters were all directly related to estimating soil moisture.

2.5 Temporal and Spatial Soil Moisture Measurements

The CRNS is one instrument that can be used to safely and effectively track soil moisture levels over time. Prior use of observed neutron intensities to enhance predictions of soil moisture profiles using a land surface model were limited by the fact that the model's parameters were calibrated based on known soil moisture conditions (Han *et al.*, 2015a; Rosolem *et al.*, 2014; Shuttleworth *et al.*, 2013). According to Köhli *et al.* (2015), the cosmic-ray neutron probe can bridge the gap between remote sensing and point-scale measurements by delivering average soil moisture readings over a 240m radius as the maximum footprint. Soil moisture sensors come in a wide variety (Figure 2.6), but the cosmic-ray probe is a novel method for measuring integral soil moisture on a field or small catchment scale (Zreda *et al.*, 2008, 2012). Soil moisture at the field scale may be accurately measured using cosmic-ray neutron sensors in a wide range of environments and areas (e.g. Bogena *et al.*, 2013; Franz *et al.*, 2012a; Hawdon *et al.*, 2014; Rivera Villarreyes *et al.*, 2011). They could also be used to check the accuracy of data collected by remote sensing (Crow *et al.*, 2012; Dong *et al.*, 2014; Hornbuckle *et al.*, 2012). Information on soil moisture is helpful in many fields, including hydrology and agriculture. Many studies have shown that soil moisture data may be extrapolated from satellite imagery (Albergel *et al.*, 2012; Njoku *et al.*, 2003).

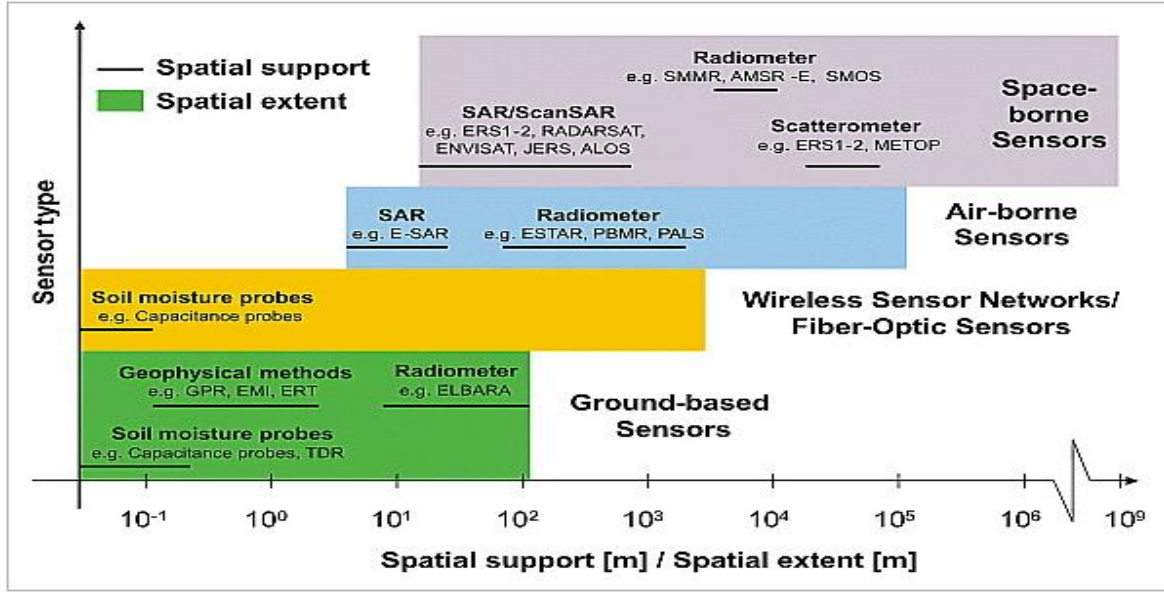


Figure 2.6: Soil moisture sensors (Bogena *et al.*, 2006)

Because hydrogen atom is the most effective slowing agent for fast neutrons, the amount of fast neutrons detected by the probe can be related to soil moisture. The neutron counts detected by the probe are converted to volumetric soil moisture (θ_v) using the equation from Hawdon *et al.* (2014),

$$\theta_v = \left[\frac{0.0808}{\left(\frac{N_{corr}}{N_o} \right) - 0.372} - 0.115 - \omega_{lat} - \omega_{SOM} \right] \rho_{bd} \quad (2.34)$$

where, N_o is the neutron intensity over dry soil, and N_{corr} is the corrected neutron counts. The neutron counts are corrected for air pressure, atmospheric water vapour, and incoming neutron intensity using the method outlined in Zreda *et al.* (2012).

2.5.1 Penetration Depth in the Soil

The probed soil layer's thickness is a significant advantage of the CRNS method over most remote sensing products. Cosmic-ray neutrons can pass almost undetected through the first decimetres of soil, whereas electromagnetic signals interact in the upper 0-5 cm. Franz *et al.* (2012b) showed that the effective representation of the penetration depth, $z^*(\theta)$, is a reciprocal function of soil moisture, but it is unclear how it varies with the distance from the probe. The cosmic-ray neutron probe has substantial potential; unfortunately, the effective measuring depth for the majority of soils is less than 30 centimetres, necessitating depth scaling to reflect the whole root zone. Soil moisture has a negative relationship with the

effective depth of measurement, which is defined as the depth of soil from which 86% of neutrons counted originates from as shown in (Equation 2.35). The effective depth was observed by Zreda *et al.* (2008) to vary non-linearly from 12 cm (wet soil, water content $0.40 \text{ m}^3 \text{ m}^{-3}$) to 76 cm based on MCNPX simulated results (dry soil, the water content of 0).

$$z = \frac{5.8}{\rho_{bd} \times \tau + \theta + 0.0829} \quad (2.35)$$

where, ρ_{bd} is the dry bulk density of soil (gcm^{-3}), τ is the weight fraction of lattice water in the mineral grains and bound water (very small), θ is volume of soil moisture and z is effective depth (cm). The effective measurement depth (z^*), an important factor for depth scaling, varies with changes in volumetric water content. The relationship determined by Franz *et al.* (2012b), with the inclusion of soil organic matter, is

$$z^* = \frac{5.8}{\rho_{bd} \times (\omega_{lat} + \omega_{SOM}) + \theta_v + 0.0829} \quad (2.36)$$

Here, integrating neutron counts over one hour and averaging soil moisture over the previous twelve hours helps to smooth out the data signal (Zreda *et al.*, 2012). To verify the cosmic-ray neutron probe, six (6) randomly chosen locations within the footprint had gravimetric soil samples obtained from a depth of 0-30cm cm on May 30, June 6, June 9, and August 9, 2018. The method outlined by Kohli *et al.* (2015) was utilized to compute a distance-weighted average. Using data collected over the course of two years from a prairie pasture in central Saskatchewan, Canada, Peterson *et al.* (2016) assessed the efficacy of depth-scaling approaches for determining field-scale volumetric water content and moisture variations. The scientists found that employing cosmic-ray neutron probe data was the most accurate way for assessing soil moisture in the root zone.

2.5.2 Calibration of Cosmic Ray Neutron Sensor

Cosmic ray probes have become increasingly popular in recent years for measuring soil moisture. Currently, there are a number of approaches that can be used to estimate soil water content from fast neutron fluxes, including (i) a site-specific shape-defining function (N_0 - method) (Desilets *et al.*, 2010), (ii) a universal calibration function (hmf-method) (Franz *et al.*, 2013b), and (iii) a cosmic-ray Soil Moisture Interaction Code (COSMIC operator).

Chrisman and Zreda (2013) created a universal calibration function to avoid the necessity for local calibration campaigns in the event of logistical or practical issues and to permit measurements with a cosmic-ray probe in motion. Soil water content can be estimated with

computational simplicity using the site-specific -method, which needs substantial soil sample for determining a single calibration parameter.

2.6 Models for Biomass and Yield Prediction

Accurate estimates of terrestrial biomass, crop growth, and yield are necessary for global-scale modelling of climate-related issues such as potential food production shortfalls (Tan & Shibasaki, 2003), drought risk (Alcamo *et al.*, 2007), carbon balance (Bondeau *et al.*, 2007), or greenhouse gas emissions (Stehfest *et al.*, 2007). According to Nicole Frost (2014), rising winter temperatures and carbon dioxide levels may result in enhanced pasture growth rates; nevertheless, total annual productivity is anticipated to drop as a result of diminished water availability. Roger Blench and Florian Sommer (2015) reported that population growth in many semi-arid countries, along with the development of innovative irrigation methods, is pushing arable farming into hitherto unfeasible peri-urban and peri-rural settings. Consequently, this place more stress on pastoralists, foragers, and the vegetation of rangelands. *Pennisetum purpureum* grass regularly generates up to 10-12 t/ha dry matter under rain-fed conditions, making it a popular choice for the cut-and-carry method of feeding grass to stall-fed cattle in eastern Africa's smallholder dairy business (Boonman, 1993). Although major questions have been raised concerning the long-term effects of 'overgrazing,' the short-term effects of severe pressure on rangelands can cause them to produce insufficient biomass for livestock and wildlife over time.

a) CropSyst

CropSyst was designed as a tool for analysing the impacts of climate, soil, and management on cropping systems over a number of years and crops (Stöckle *et al.*, 2010). The model takes into account daily and hourly time steps and spans multiple crop cycles. For simulating a wide range of management and meteorological scenarios, CropSyst is a cropping system model. All aspects of the environment's ecosystem, including water, nitrogen, and soil, can be accounted for in this model. The usefulness of a model as a research instrument depends on its capacity to make accurate predictions.

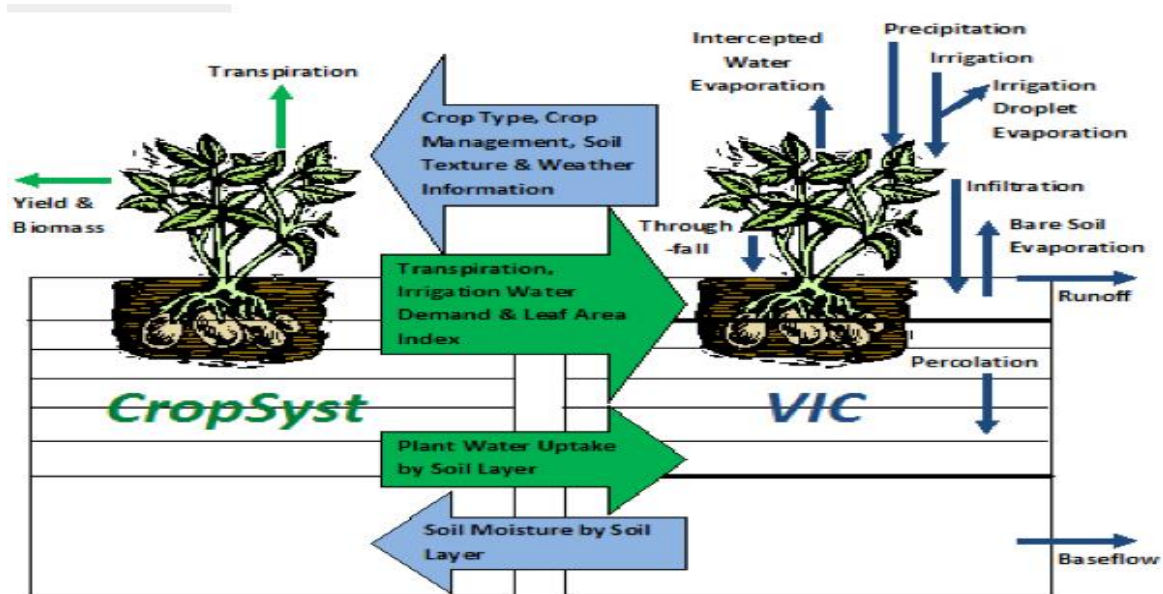


Figure 2.7: Schematic representation of coupled VIC and CropSyst model (Malek *et al.*, 2017)

b) VIC-CropSyst

The tightly coupled dynamics between hydrologic and biogeochemical processes, as well as producer decisions, may be simulated in rain-fed/irrigated and dry land agricultural regions with the fully integrated VIC-CropSyst model. As shown in Figure 2.7, model integration can look like what was reported by Malek *et al.* (2017); in this case, VIC replicates all hydrologic processes apart from transpiration, which is provided by CropSyst. In this application of VIC, root zone dynamics are captured by employing a large number of thinly spaced soil moisture layers. In addition to simulating evaporation losses from bare soil and canopy-interception, VIC has been tweaked to model the evaporation of raindrops as they fall, based on the technologies used to collect them. How much rainwater really reaches crops and how much is lost to evaporation, surface runoff, and deep drainage can be estimated more accurately with this information. VIC-CropSyst not only models crop yields, but also carbon and nitrogen fluxes.

c) AquaCrop

The Food and Agricultural Organization (FAO) created AquaCrop, a crop water productivity model, after consulting with experts from top universities and research facilities as well as international governments. Since water is often the limiting component in agricultural productivity, the AquaCrop model was developed by Steduto *et al.* (2009) as a means of simulating the yield response of herbaceous crops to changes in water availability.

Using the conservatism of biomass water productivity, AquaCrop bases crop growth and yield on the quantity of water lost during photosynthesis (or biomass water use efficiency).

2.6.1 Crop Yield Prediction

This is the methodology of predicting crop yields (at various scales: from farms to counties, to countries and to global scale) prior to harvest.

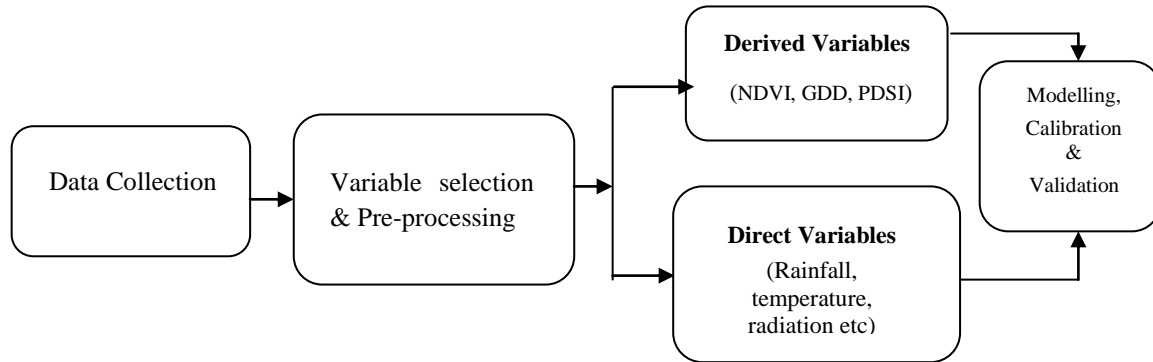


Figure 2.8: Schematic of the yield prediction workflow

a) Growing Degree Days

According to the International Association of Hydrological Sciences, "growing days" are "the period (in days) during the year when precipitation (P) exceeds half the potential evapotranspiration (PET) plus a period required to evapotranspire up to 100 mm of water from excess precipitation considered stored in the soil profile" (FAO, 1978). Agronomists use a concept called Growing Degree Days (GDD) to describe the correlation between temperature and plant growth (Gibson, 2015). The range of 50F (1°C) to 86F (30°C) is ideal for maximum growth (3°C). Fischer *et al.* (2000) noted that during the growing season, the average daily temperature must be above 5°C; if temperatures fall outside of this range, it has been seen that growth rates decline. Using heat accumulation, GDD is a heuristic phenological approach for estimating future growth rates. Calculating GDD is:

$$GDD = \frac{(T_{\max} + T_{\min})}{2} - T_{base} \quad (2.37)$$

where, T_{\max} indicate the maximum daily temperature (86F or 3°C) when temperature exceed beyond 86°F, T_{\min} indicate the minimum daily temperature (50F or 1°C) when temperature falls below 50F (1°C), T_{base} indicate the base temperature required to trigger the optimum.

b) Palmer Drought Severity Index

The Palmer Drought Severity Index (PDSI) measures the availability of moisture after precipitation and recent temperature changes. The PDSI has also been used to perform spatial soil, and temporal correlations analysis (Fuchs, 2015).

2.6.2 Agricultural Production System Simulator

Sub-models (or modules) can be linked together in Agricultural Production Systems Simulator (APSIM), a computer application that simulates agricultural systems (McCown *et al.*, 1996). Daily rainfall, maximum and minimum temperatures, solar radiation, and measurable soil physical properties for different soil strata are required by APSIM. The bulk density, the saturated water content, the field capacity, and the wilting point are all examples of such characteristics. The dynamic, daily-time-step modelling available in APSIM, which combines biophysical and managerial modules into a single engine to mimic cropping systems, made it the ideal choice for this research. Keating *et al.* (2003) created APSIM-wheat to mimic biophysical processes in agricultural systems, particularly when the economic and ecological ramifications of management approaches in the face of climate hazards are of concern.

2.6.3 Model Parameterisation and Calibration

Effective model calibration and evaluation calls on complete and trustworthy data sets. Modellers have specified priorities or minimal data needs for model calibration and evaluation, but ideal data would span various aspects of the soil-plant-atmosphere continuum (Hunt & Boote, 1998). Thomas *et al.* (2013) claim that while consumers may have difficulty with model selection, model parameterization is significantly more difficult. Most grazing land models are empirically parameterized in practice. Half of users who employed crop models relied on trial and error to determine the best parameter values, which they did on average after three tries. The use of iteration to choose parameters that are suitable for both the calibration and validation data is common even among those who profess to keep the two datasets separate (Seidel *et al.*, 2018). Based Independent observations of soil hydraulic characteristics, as well as site-specific measurements of variables including bulk density, organic carbon, C/N ratio, and pH, are used to parameterize the model for each data set. However, estimates for other model parameters necessitated actual data from simulation or experiment. Ma *et al.* (2015) discovered that optimizing net ecosystem exchange, gross primary production, ecosystem respiration, and evapotranspiration across 12 experimental sites in Europe produced the best results when compared to parameters obtained from selected sites when calibrating the Pasture simulation model.

2.7 Detecting and Quantifying Land Use and Land Cover Change

Teixeria *et al.* (2014) argue that analysing land use change through time can help explain what's behind the shifts and what might be causing them. Land-use change in pastoral ranches next to the Maasai Mara National Reserve has been blamed by Ogutu *et al.* (2009)

for the dwindling populations of various species of wild animals, including giraffe, waterbuck, and impala. Land usage is the practice of putting one's land to various uses (Comber, 2006). Land use creates a causal link between land cover and human actions in the natural world. Transferring data on land cover and land use from producers to consumers provides an important starting point for "land" analysis. What people do, where they do it, and what they put into a specific sort of land cover is what we call "land use," and it's the relationship between people and their environments. When defining cover characteristics for an area substantially larger than the sampled area, sampling is often used. Samples should be collected carefully to ensure they are representative of the entire habitat and devoid of bias. In this study, a rectangular quadrat frame (50cm x 50cm) was employed to define the sampling region; however, a quadrat can also be a fixed area inside a site. The most common quantitative sampling techniques are the segment or quadrat method and the transect approach. The quadrat method was selected since it allows the user to set a specific area for analysis. For this purpose, it is necessary to use an experimental design that allows for the random placement of the frame or permanent quadrat. Surveying smaller quadrats is considerably more manageable than larger ones, but the results may not be as trustworthy. Extrapolating or projecting to the actual size, or making use of remote sensing technology, are all viable options for determining the optimum size of the quadrat. However, more time and effort is needed to thoroughly analyze the larger quadrats. Consequently, it is necessary to strike a balance between the theoretical and the actual.

2.7.1 Crop Area Estimation

The estimation of crop area is the "backbone" of agricultural activity. Not only that, but it is a vital factor in yield forecasting. By collecting data over wide areas at a high rate of revisit, remote sensing can significantly contribute to giving a current and accurate picture of the agriculture industry (Atzberger, 2013). For effective agricultural planning and decision-making, it is essential to have a reliable and timely estimate of crop acreage. Goldewijk *et al.* (2011) found that the proportion of land used for farming increased from 5.9% to 10.6% between 1900 and 2000. Forests and grasslands have historically been the principal targets for agricultural conversion (Carmona & Nahuelhual, 2012; Mao & Cherkauer, 2009). There are primarily three remote sensing methods that can be used for estimating crop areas:

- a) Pixel counting is the quickest and easiest way, but it might produce inaccurate findings for a number of reasons. This area estimation bias can be the result of the same omission errors.
- b) Regression, calibration, and estimation of tiny regions - These techniques are based on a combination of remote sensing data and accurate sample information. The regression

estimator of survey estimates is a widely used technique for estimating the mean of a variable Y known for n samples using an auxiliary variable X known for all n components of the population and connected with Y (Carfagna *et al.*, 2005; Latham 1981/82/83). The calibration estimator is a statistical technique family in which the erroneous pixel-counting estimator is adjusted using a confusion matrix computed on samples. When the sample size is too small to provide reliable results, small area estimate can be used to extrapolate the results to a larger population using supplementary data (Carfagna *et al.*, 2005).

c) Surveys of area frames. The area frame can benefit from satellite imagery in a few different ways: the imagery can help define the sample unit for stratification; and ii) the imagery can be used as visual documentation for ground surveys and quality control. Gallego (2008), in particular, underlined the cheap cost and efficiency of stratification based on coarse photo-interpretation of satellite pictures.

2.7.2 Ground Survey

"Ground truthing" refers to the practice of using primary sources to verify and validate the results of a remote sensing study, and is commonly employed in this field. However, this practice rarely has an immediate bearing on how we categorize landforms based on satellite or airplane imagery. Observations and maps made in the field are the backbone of the time-honoured practice of conducting field surveys to learn about the biological features of a given piece of land.

2.7.3 Area Frame Sampling

A sample frame can be a list or a map that details every member of the population of interest (Perry, 1979). Each member of the population must be able to be positively identified; hence a map or list of that nature is necessary. Persons from the population whose characteristics are being studied make up the sampling units. Most commonly, a geo-information system is used to combine many sets of frame components into a single sampling frame (GIS). Among the most important aspects of an efficient area frame sampling (AFS) are its durability and its aesthetic appeal. "divide the complete area to be surveyed into N small blocks (Segments) without any overlap or omission, additionally choose a random sample of n small blocks, and acquire the needed data for reporting units of the population that is in the sample blocks" is how area frame sampling is described (Madana, 2002). When conducting a probability survey with a specified probability of selection, Cotter and Tomczak (1994) stressed the importance of area frames to achieve full coverage and accurate representation of geographical areas. Unless the population rapidly grows in areas where this frame does not apply, it will not become out-dated anytime soon.

2.8 Satellite Imagery Data

2.8.1 Project for On-Board Autonomy - Vegetation (Proba V)

PROBA-V was launched on May 6, 2013, to fill the void in space-borne vegetation measurements between the Sentinel-3 satellites, the first of which has been in orbit since February 16, 2016, and the second of which was launched on March 30, 2018, and SPOT-VGT, which operated from March 1998 to May 2014. A swath width of 2295 kilometres is possible because to the VEGETATION instrument's 1020-degree field of view. At this swath width, we can guarantee daily coverage of 90% of the Earth and every two days we'll cover the entire planet. The primary camera looks out over a 517- kilometre radius with a resolution of 100 meters, providing five-day worldwide coverage at a minimum. By comparing Proba-V (PV) NDVI with VGT NDVI for operational crop monitoring and yield forecasting activities, Meroni *et al.* (2015) assessed producer quality, offering some level of user or fitness for assessment purpose. The scientists performed an analysis of paired observations obtained by the two instruments during the overlap time while both satellite systems were active. Between late October 2013 and late May 2014, there was a period of overlap that coincided with the time when North African countries track crop growth (January to May) to make accurate yield predictions for major grain crops (barley, soft and durum wheat). The authors found the largest discrepancies in the anomalies maps, where a comparison of SPOT-VGT and PROBA-V's agreement coefficients (ACs) showed that while no significant systematic differences exist, there is significant scatter due to unexplained unsystematic variability (AC = 0.55, ACs = 0.98, ACu = 0.56). When the NDVI collected across cropland is averaged by administrative units to construct temporal profiles, a high degree of agreement is shown between the sources (AC = 0.94), suggesting that the ad hoc variability is greatly decreased. Finally, the scientists found that the spatial quality differential between the two sensors (PROBA-V offering more geographical detail) significantly impacted yield prediction in an arid location with rapid transitions between agriculture and desert, despite having the same nominal spatial resolution. A total of four spectral bands can be observed using PROBA-V. Based on the research of Francois *et al.* (2014), the spectral centres of BLUE (0.463 m), RED (0.655 m), NIR (0.837 m), and SWIR (1.603 m). Resolutions for the VNIR and SWIR channels range from 100 to 180 meters at nadir to as much as 350 meters and 660 meters at the swath's edges, respectively.

Table 2.2: PROBA-V spectral, radiometric, and geometric characteristics, Lref refers to the Top-Of-Atmosphere (TOA) irradiance at the respective spectral band, Geometric mean accuracy values obtained over the period 16 December 2016-15 December 2017. FWHM = Full Width at Half Maximum, SNR = Signal to Noise Ratio

Band name	Centre wavelength (μm)	Spectral range @ FWHM (μm)	SNR@ Lref ($\text{Wm}^{-2} \text{sr}^{-1}$ μm^{-1}) at 300m resolution
BLUE	0.464	0.440 - 0.487	177@111
RED	0.655	0.614 - 0.696	598@110
NIR	0.837	0.772 – 0.902	574@106
SWIR	1.603	1.570-1.635	720@20
Radiometric Performance			
Absolute accuracy (%)		< 5	
Inter-channel accuracy		< 3	
Stability (%)	< 3		
Geometric Performance			
Mean Geo-location	BLUE: 77.6 (92.6)		
accuracy (standard	RED: 73.2 (79.0)		
deviation (m)	NIR: 69.2 (77.9)		
	SWIR: 71.4 (78.7)		

i) Segment Products (Level 1C and Level 2A, Level 3, Both Consisting of TOA and TOC Reflectance's)

Raw segmented observations, along with calibration data, can be found in the Level 1C product, whereas projected segment data can be found in the Level 2A (L2A) goods. P-products was the term used to describe these later data sets during the time of SPOT-VGT. These products include cloud, shadow, and snow/ice filtered observations for TOA reflectance on a daily basis (S1, available at all resolutions) and on a multi-daily basis (S5 for 100 m and S10 for 300 m and 1 km). Top-of-Canopy (TOC) reflectance and Normalized Difference Vegetation Index (NDVI) data are additionally corrected for air reflectance factors such aerosols and gaseous absorption. The S-products of SPOT-VGT synthesized back in the day. The next processing stages that are carried out to generate the Level-1C result are shown in the upper portion of figure 2.9, which contains the Level 1 algorithm and data (the "Level

1 processor"). Geometric processing and radiometric processing are the two basic types of processing.

2.8.2 Project for On-Board Autonomy – Vegetation (PROBA-V) Data Products

The PROBA-V products are similar to the ones of SPOT-VGT in terms of file structure and comprise the following elements:

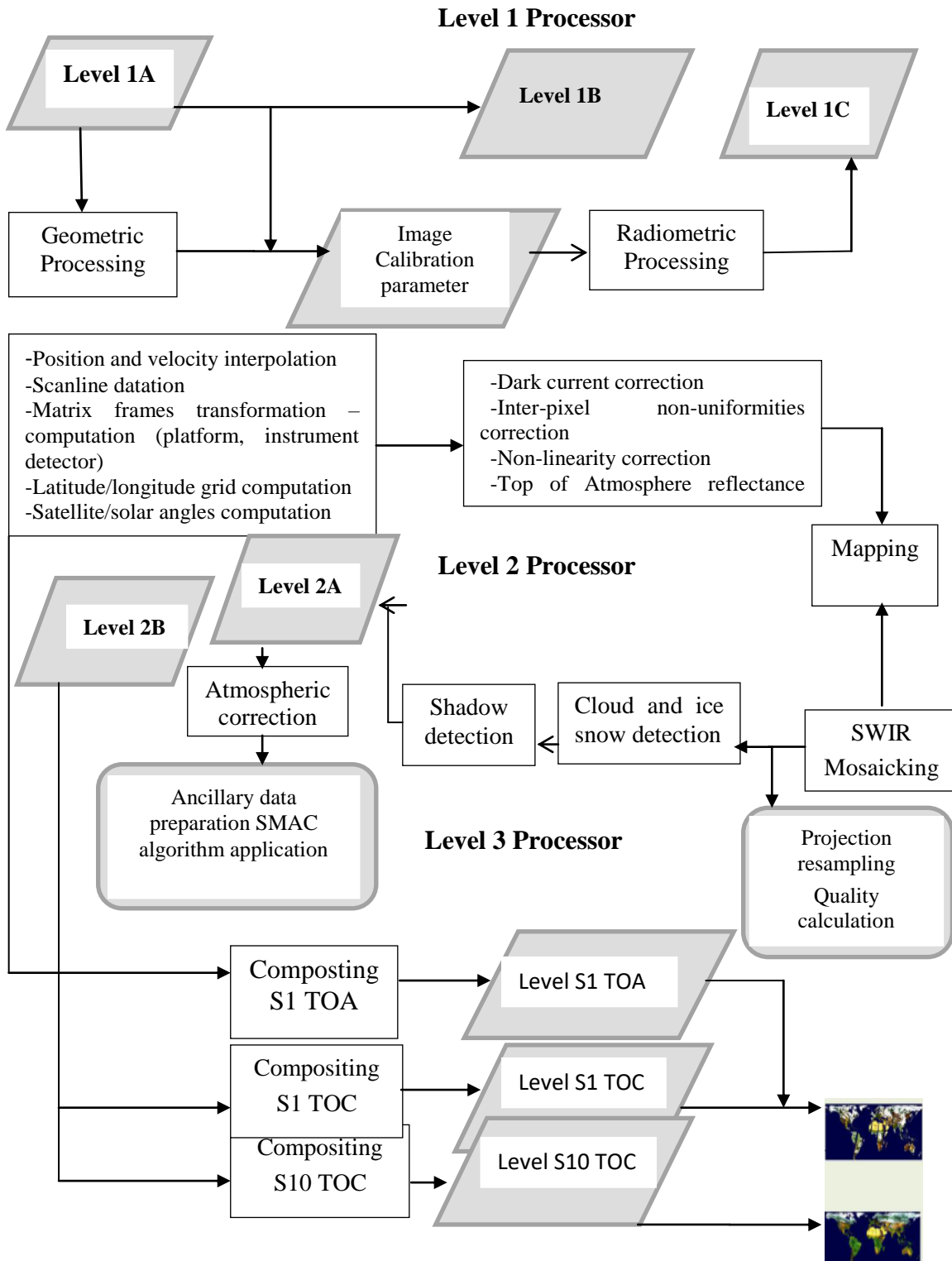


Figure 2.9: PROBA-V product processing chain flowchart

2.8.3. Geometric Processing

Using the Level 1A raw and uncompressed data, the latitude and longitude of each observed pixel were calculated and used to geo-locate each satellite position. Satellite positions and velocities are interpolated along each scan line using a model of propagation across space. Utilizing the geometric Instrument Calibration Parameters (ICP) file enhances the precision of the geo-location (figure 2.9). The ICP file details how the eclipse's length and the Sun's beta angle affect the detector's field of vision. The viewing and solar zenith angles (VZA and SZA), which are necessary for further processing, are also computed by the geometric processing model. Data at Level 1B is the result of the geometric processing. Sterckx *et al.* (2014) offer additional information regarding the geometric processing.

2.8.4. Radiometric Processing

Radiometric processing changes the number of digital numbers in a certain spectral band (DN) into physical values for TOA reflectance. As a first step, the DN value is calibrated to account for detector non-linearities, dark currents, and pixel-to-pixel variations. Second, the band-specific calibration coefficients from the radiometric ICP file are used to convert the numbers to sensor radiance L ($\text{Wm}^{-2}\text{sr}^{-1}\text{m}^{-1}$). At last, we transform the TOA radiance L for a specific spectral band into reflectance at that band by using:

$$R_{TOA} = \frac{\pi \times d^2 \times L}{E_o \times \text{Cos}(\theta_s)} \quad (2.38)$$

With R_{TOA} the obtained TOA reflectance value (-), d the Earth – Sun distance (AU), E_o the mean exo-atmospheric irradiance at the specific spectral band ($\text{Wm}^{-2}\mu\text{m}^{-1}$), with values from Thuillier *et al.* (2003), and $\text{cos}(\theta_s)$ the solar zenith angle (o). The outputs of the radiometric processing are the Level 1C data.

a) Level 2 Algorithm and Data

The Level 1C data are used as input for further processing in the Level 2 processor, which consists of the following steps, and the compositing procedure for the 300m and 1km products is slightly different from the Level 2 procedure in certain steps.

- i). Mapping and SWIR mosaicking
- ii). Snow/ice detection
- iii). Cloud and cloud shadow detection
- iv). Atmospheric correction

2.8.5 Mapping and SWIR Mosaicking

The Level 1C data is projected onto a World Geodetic System (WGS 84) geographic latitudes/longitudes grid according to a method developed by Riazanoff (2004). Pixel-specific Level-1 (p, l) coordinates are reconstructed from Level-2 (x, y) coordinates using an inverse model, where x and y represent longitude and latitude, respectively; p and l represent the pixel-in-line and line number, respectively; and l is the line number.

2.8.6 Cloud and Cloud Shadow Detection

When clouds are present, satellite measurements of the land's surface are hindered and cannot be used to retrieve the land's original properties. Thus, appropriate cloud screening is crucial for pre-processing the various value-added products. It has been found through extensive research and user feedback that the PROBA-V cloud identification system in Collection 0 has various flaws. Collection 0 uses a static threshold technique for the BLUE and SWIR spectral bands. Among the method's key flaws was its tendency to incorrectly detect clouds over bright surfaces like deserts and salt lakes, as well as its tendency to incorrectly classify thick ice clouds as snow/ice. A new algorithm for PROBA-V reprocessing was created and deployed to address these constraints (Collection 1). Collection 1's updated and functional cloud detection algorithm overcomes the major shortcomings of Collection 0's by employing a more thorough and complex battery of cloud testing. A supervised training of a classification method was created to take the role of the defunct Collection 0 algorithm;

- i). Contextualization maps are constructed with high-resolution surface albedo data.
- ii). A Comprehensive battery of threshold tests and similarity checks determines whether a pixel should be labelled "cloud" or "clear."

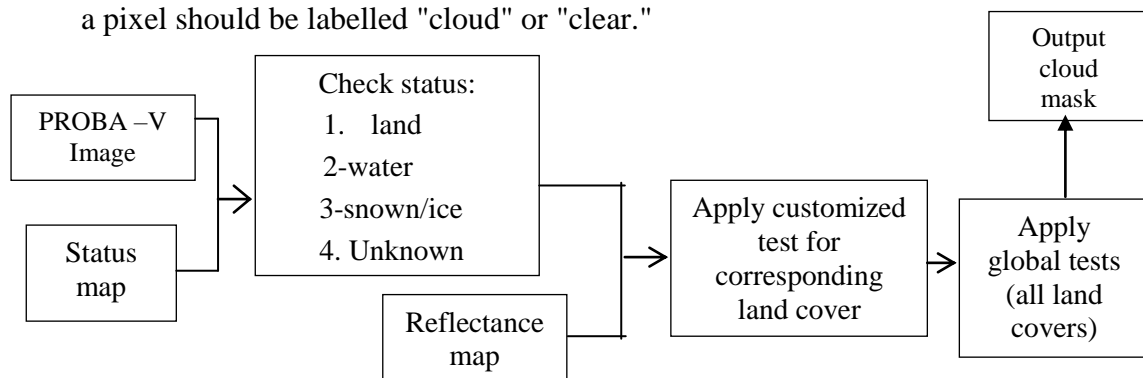


Figure 2.10: Flowchart of the collection 1 cloud detection algorithm

2.8.7 Atmospheric Correction

Surface reflectance and scattering, absorption, and multiple reflections inside the air column underneath the satellite combine to provide the TOA reflectance observations at Level 2A. (clouds, gases, aerosols). According to Rahman *et al.* (1994, pp. 123-143) the

directional TOC reflectance values are calculated using the Simplified Model for Atmospheric Correction (SMAC) (Level 2B data). This model extrapolates the TOA reflectance to the TOC reflectance using data on water vapour, ozone, and surface pressure. The humidity is courtesy of the European Centre for Medium-Range Weather Forecasts (ECMWF). The Numerical Weather Prediction (NWP) model offered by MeteoServices is bi-linear in space and linear in time. The Centre d'Études Spatiales de la Bio-sphère (CESBIO) climatology is utilized for ozone. It was calculated using data collected by the Total Ozone Mapping Spectrometer (TOMS) over a period of 10 years. By utilizing the Global Land Surface Digital Elevation Model (GLSDEM), a height-to-pressure conversion formula was proposed by Plummer *et al.* (2003). By comparing the TOA NDVI and the SWIR/ BLUE TOC reflectance ratio, the aerosol optical thickness (AOT) can be estimated empirically. Only pixels with enough vegetation ($NDVI > 0.2$ and $TOC\ SWIR > 0.4$) can apply this aerosol retrieval method; for those that do not, a straightforward AOT, as a function of latitude is applied instead (Berthelot *et al.*, 1997).

2.9 Sentinel 2A

When a high temporal resolution is required, agricultural monitoring and applications commonly make use of satellite pictures with a high temporal frequency (daily) but a low spatial resolution ($>250m$). Images of Earth's surface are taken by Sentinel-2A/MSI in 13 spectral bands at spatial resolutions of 10 meters (20 meters), 30 meters (60 meters), and 60 meters (200 meters) (Drusch *et al.*, 2012). The GDD-based technique proposed by Franch *et al.* (2015) is utilized as a proxy to forecast an NDVI peak utilizing the historical link between NDVI and GDD, hence improving peak NDVI estimate. The GDD is computed by subtracting the average daily maximum T_{max} and minimum temperatures T_{min} from a base temperature. Large-scale applications of remotely sensed satellite data for crop area and yield estimation have been adopted in both the United States and the European Union (Latham, 1981-83; Wigton *et al.*, 2009).

Table 2.3: Technical characteristics of Sentinel 2

Launched	2014	
Instruments on board	Sentinel-2 is a polar-orbiting, multispectral high-resolution imaging mission	
Processing	Level 1 Pre-processing includes:	<p>a) Radiometric corrections: stray-light/crosstalk correction and defective pixels' exclusion, denoising, de-convolution, relative and Level 1 image processing includes: absolute calibration</p> <p>b) Geometric corrections: co-registration inter-bands and inter-detectors, ortho-rectification.</p> <p>c) Cloud screening</p> <p>d) Atmospheric corrections: including thin cirrus, slope and adjacency effects correction</p>
	Level 2 image processing include:	a) Geophysical variables retrieval algorithms: e.g. fAPAR, leaf chlorophyll content, leaf area index, land cover classification
	Level 3 provides spatio-temporal synthesis	Simulation of cloud corrections within a Level 2 image
Pixel size	< 1 ha MMU (Minimum Mapping Unit) fully achievable with 10 m 4 bands at 10 m, 6 bands at 20 m and 3 bands at 60 m spatial resolution (the latter is dedicated to atmospheric corrections and cloud screening).	
Spectral bands	Optical payload with visible, near infrared and shortwave infrared sensors comprising 13 spectral bands) 0.4-2.4 μm (VNIR + SWIR).	
Scene size	Swath width of 290 km.	
Data characteristics	Revisit time of five days at the equator (under cloud-free conditions) and 2–3 days at mid-latitudes.	
Info	https://earth.esa.int/web/sentinel/user-guides/sentinel-2-msi/resolutions/spatial	

2.9.1 Normalized Difference Vegetation Index

The NDVI, or Normalized Difference Vegetation Index, is a common index used to generate a green image (relative biomass). When it comes to anticipating seasonal shifts in ET and soil moisture status, NDVI has been found to be quite helpful, as was mentioned by Nemani *et al.* (1989). Using a multispectral raster dataset, this index takes use of the difference between the red band absorptions of chlorophyll pigments and the high reflectivity of plant components in the near infrared (NIR) band. The following formula is used to calculate it using the measured intensities of the red (R) and near infrared (NIR) spectral regimes.

$$NDVI = \frac{(\rho_{nir} - \rho_{red})}{(\rho_{nir} + \rho_{red})} \quad (2.39)$$

where, ρ_{nir} indicate the near-infrared band reflectance, ρ_{red} indicate the red band reflectance, red = Intensity/brightness of reflected light in the red filter (ca. 0.6–0.7 μm), nir = intensity/brightness of reflected light in the near infrared filter (ca. 0.8–0.9 μm).

SENTINEL - 2A Band 3 (red band) and Band 4 (green band) reflectance data are used to calculate the NDVI values in bands 4 and 8 of the Sentinel-2A MSI camera. Sentinel is made up of several different missions, each of which is equipped with a different suite of instruments for monitoring our planet, such as radar and multi-spectral imaging devices. Agriculture is the focus of Sentinels 1 and 2, while the other missions (Sentinels 3, 4, and 5) monitor things like ocean and land colour, air quality, and temperature (Sentinel 4-5).

2.10 Net Primary Productivity

The rate at which carbon dioxide is turned into biomass (all plant life forms) each year is known as the net primary productivity (NPP). The rate of production of goods or services in an economy or ecosystem is its productivity, and it is quantified by the amount of material produced per unit of time and space. Above- and below-ground biomass contributes to NPP (plant shoots and roots). The annual net primary production (NPP) of rangelands varies widely in space, from practically nothing to about 3,000 gm^{-2} (Running *et al.*, 2004). Primary productivity on rangelands is primarily affected by a number of different types of change, including (but not limited to) i) land-use change (including soil-related changes), ii) climate change (precipitation and temperature changes), iii) changes in atmospheric composition (CO_2), and iv) changes in biodiversity. When the amount of precipitation falls and the temperature rises, as it typically does, NPP falls, as stated by Sala (2001). Precipitation may increase or decrease in many parts of the world as predicted by climate change models.

2.11 Model Sensitivity Analysis

The output of a simulation model can be subjected to a Sensitivity Analysis (SA) in order to learn more about how different changes to the model's input parameters affect the accuracy of its predictions. One of the simplest ways to express local sensitivity is through the first-order partial derivatives of the output to the factors. Define a model $y = f(x)$, where y is the output of the model; x is factor of the model. The sensitivity of the factor (S_i) is defined as:

$$S_i = \frac{\Delta y_i}{\Delta x_i} \quad (2.40)$$

where, i is the i^{th} factor of the model.

Instead of model output, y the model error is used such as Root Mean Squared Error or Mean Absolute Error). Higher value of S_i indicates higher sensitivity of the factor and is called Sensitivity Index (SI). Local SA also termed the “one factor at a time” (OAT) or deterministic approaches quantify the exact local response of output (Y) to a particular input factor (x_i) at a selected point (x_0) within the full input parameter space for the model. The most common form of a local sensitivity is:

$$\left[\frac{\partial Y}{\partial x_i} \right]_{x^0} = \frac{Y(x_1^0, \dots, x_i^0 + \partial x_i, \dots, x_l^0) - Y(x^0)}{\partial x_i} \quad (2.41)$$

where, $i = (1, \dots, I)$, and I indicate the number of total input parameters. The local sensitivity index measures the partial derivatives of Y with respect to x_i at point x^0 . The method of sensitivity auditing (Saltelli *et al.*, 2013; Saltelli & Funtowicz, 2014) involves doing a sensitivity analysis in order to ascertain the applicability and credibility of model-based reasoning employed in the formation of policy (European Commission, 2015). Touhami *et al.* (2013) report that measurements of weather data and soil parameters, two common types of inputs to models, show substantial temporal and spatial variability. A plethora of research has relied heavily on sensitivity analysis to zero in on the best set of calibration parameters. Due to the location-specific nature of all experiments and the mostly empirical nature of the models' descriptions of certain processes, there is a relationship between calibrated parameters and experimental sites (Behrman *et al.*, 2014).

CHAPTER THREE

MATERIALS AND METHODS

3.1 The Study Area

3.1.1 Maasai Mara National Reserve Rangeland and Ecosystem

The Maasai Mara rangeland and ecosystem (Figure 3.1) is located in southwest Kenya ($1^{\circ} 29' 35''$ N and $035^{\circ} 08' 57''$ W). The experimental sites sample were represented by the following coordinate points ($1^{\circ} 29' 35.9520''$ S, $35^{\circ} 8' 57.0480''$ E), ($1^{\circ} 33' 32.004''$ S, $35^{\circ} 14' 11.904''$ E), ($1^{\circ} 27' 10.476''$ S, $35^{\circ} 4' 19.74''$ E) and ($1^{\circ} 32' 17.988''$ S, $35^{\circ} 2' 10.14''$ E) within the MMNR. The total area of the MMNR is around 1,530 sq. km, although less than 10% of that is protected land inhabited by the agro-pastoral community and conservancies. The MMNR rangeland ecosystem, located at an elevation of roughly 1,600 meters above sea level, consists of undulating savanna/woodland that is intersected by multiple drainage lines and divided by the Mara River (Olson *et al.*, 2000). Dense woodland, bush land, grassland, group ranches, agricultural fields, urban areas, and marsh are all found in the Mara River Basin (MRB) (Dessu & Melesse, 2010, 2012; Mati *et al.*, 2008). Rainfall in MRB is highly variable because to the movement of the Inter-Tropical Convergence Zone (ITCZ). The ITCZ's southbound migration causes the short rainfall from October to December, whereas its northward migration provides the long rainfall from March to May. The beginning, length, and intensity of rainfall in the MRB are all influenced by yearly fluctuations in Indian Ocean sea surface temperatures, which in turn are affected by El Nino southern Oscillation and La Nina episodes (Dessu *et al.*, 2007, 2013). Rainfall patterns are caused by the monsoonal winds of the Inter-Tropical Convergence Zone (ITCZ) (Ongoma & Chen 2017; Yang *et al.* 2015). The majority of the region's precipitation comes during the summer monsoon, but the impact of climate change on this pattern is still unclear (Morgan *et al.*, 2015). There is a gradient from northwest to southeast that results in a temperature range of 12 to 28° degrees Celsius and an annual rainfall average of 800 to 1,200 millimetres. There are two main dry periods: one lasting from about mid-June to about mid-October, and the other lasting January and February.

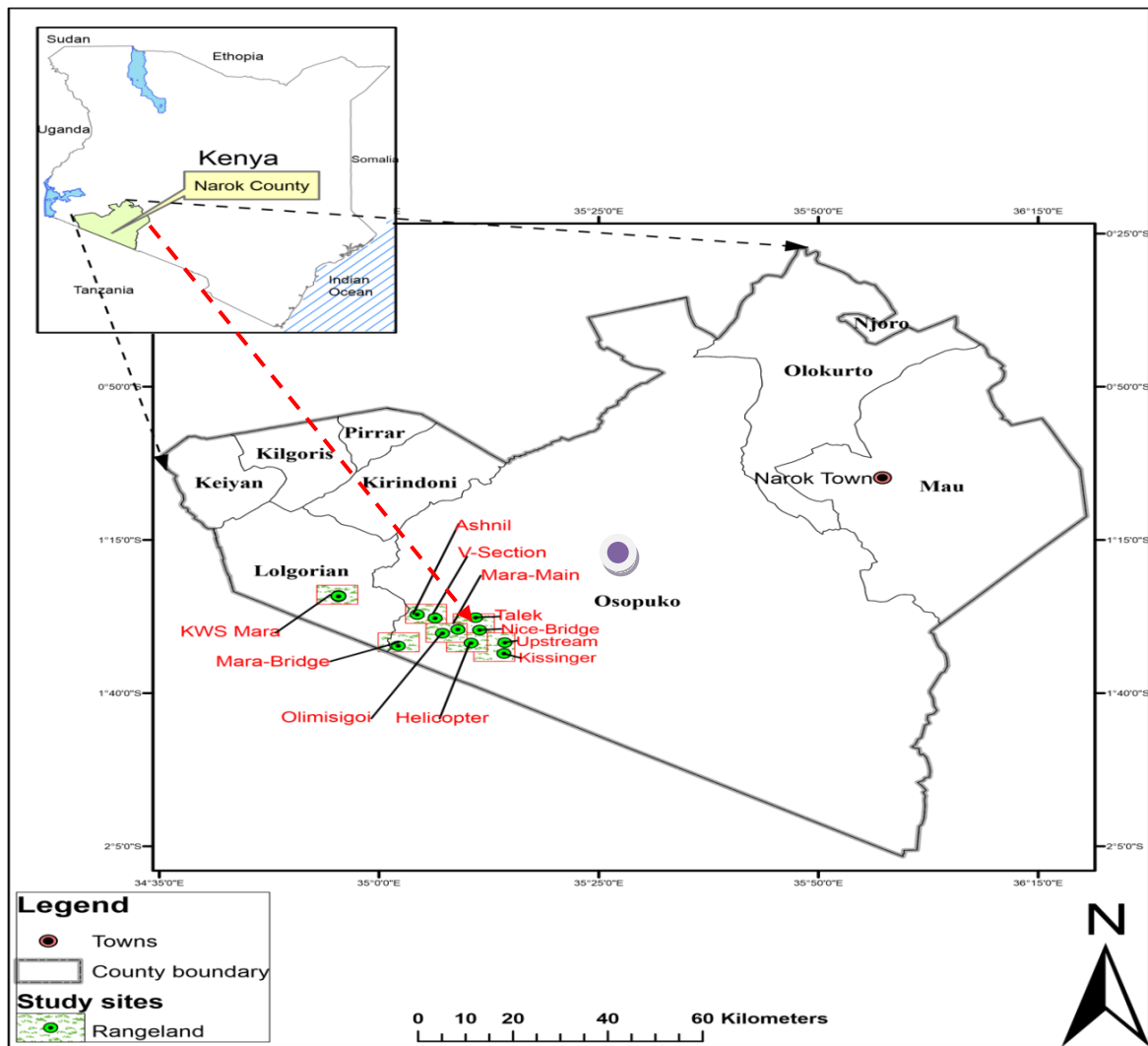


Figure 3.1: Maasai Mara National Reserve rangeland ecosystem

3.1.2 Naivasha Cropland and Ecosystem

The geographical location of Naivasha Sub County lies in the floor of the Great Rift Valley and borders five other sub counties namely: - Gilgil to the North, Kajiado and Kiambu to the East, Narok to the south and North Kinangop to the North East. The experimental sites were located within the following sample coordinate points (0° 35' 59.28"S, 36° 33' 59.76"E), (0° 45' 13.68"S, 36° 11' 27.24"E), (0° 38' 38.04"S, 36° 28' 45.48"E), (0° 44' 12.12" S, 36° 27' 3.6" E), (0° 38' 38.148" S, 36° 28' 45.48" E) within Naivasha Sub county which covers an area of 1,685.8 km². The sub county is located in the medium potential agro-ecological zone (Zone 111). The annual rainfall of the area has been determined to be between 600 - 700mm with an annual average of 650mm. Bimodal rainfall pattern are made of short rains that falls between October to December and long rains between March to May. The altitude ranges between 1520 and 2700 metres above the sea level. Lake Naivasha lies in the basin. Again, the climate within Lake Naivasha basin is

heterogeneous across locations and is dominated by semiarid conditions, while cooler, but humid conditions can be found upstream in the higher altitude areas. Average annual precipitation in the basin varies greatly from about 650 millimeters at Lake Naivasha to 1300 millimetres in the mountain forests of the Aberdares, demonstrating the basin's spatial diversity. The Naivasha Sub County station measures an annual pan evaporation rate of 1790 mm, which contributes to the lake basin's semiarid environment. A reduced rate of evaporation is observed at higher elevations. Average monthly lows at Lake Naivasha are in the 6°C to 10°C range, while average monthly highs are in the 26°C to 31°C range. Temperatures typically hover in the range of 15.9 to 17.8 degrees Celsius on a monthly basis (De Jong, 2011). The warmest months are December, January, and February, while the coolest are June and July, with an average temperature of 12.3 degrees.

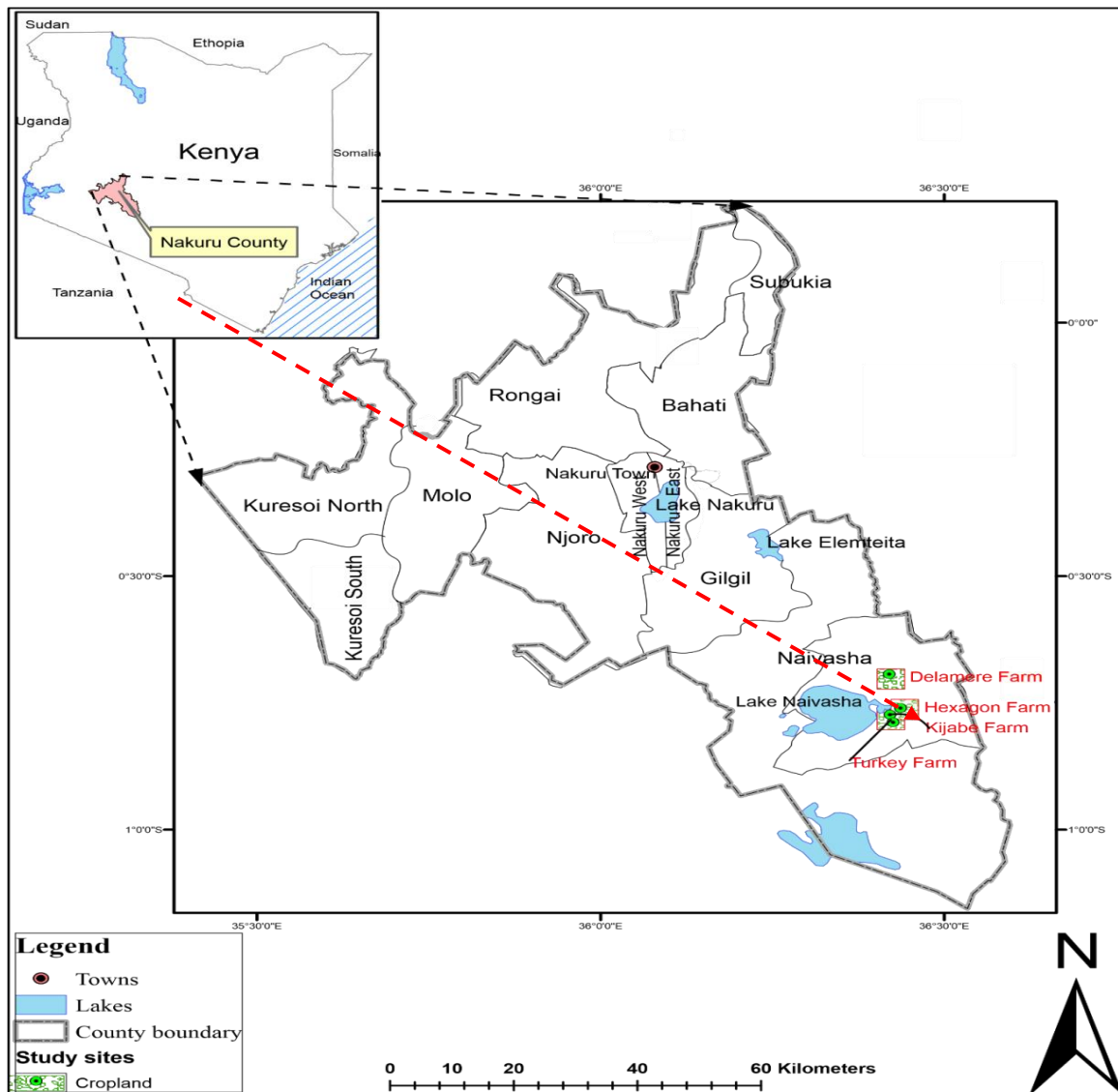


Figure 3.2: Naivasha cropland ecosystem

3.2 Determination of Spatio-Temporal Soil Moisture Storage and Retention Capacities in Maasai Mara National Reserve Rangeland Ecosystem

a) Meteorological Data

Rainfall, wind speed, relative humidity, and air temperature were measured from a set-up of installed automatic weather station at meta-plains of Maasai Mara National Reserve and the datasets were recorded at every 15min to half-hourly timescale as shown in figure 3.3. The main data logger was connected to the automatic weather station cables, which enabled data streaming for various parameters of the catchment atmospheric conditions.

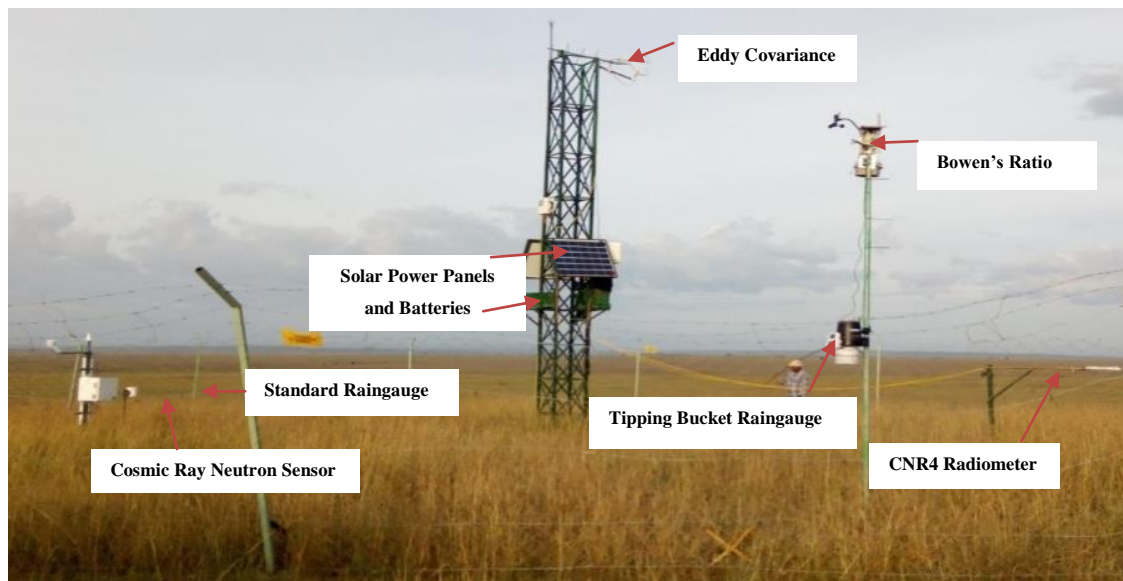


Figure 3.3: Automatic meteorological station at Maasai Mara National Reserve. From left to right: Cosmic Ray Neutron sensor, Standard rain gauge, Eddy covariance, Bowen’s ratio with tipping bucket rain-gauge and CNR4 Net radiometer

Rainfall was measured using a tipping bucket (resolution:0.2mm per tip) rain gauge installed at the MMNR main weather station which also helped in the calibration of the standard rain gauge installed to collect the rainfall data. The rain gauge was placed closer to the cosmic ray neutron sensor. The standard rain gauge readings (R , in mmh^{-1}) were corrected for catching, wetting, and evaporation losses according to WMO (2009).

$$R_{cor} = 1.2R^{0.92} \quad (3.1)$$

b) Carbon and Water Vapour Fluxes

In the study, a CO_2 and H_2O Flux Eddy Covariance measurement system was installed in a tower at an open homogeneous ground surface of MMNR Meta Plains, which acted as the Main Weather station. The instruments equipped were an open path infrared $\text{CO}_2/\text{H}_2\text{O}$ gas analyzer (Licor 7500, LI-COR Biosciences, USA) and a 3-D sonic anemometer (CSAT3, Campbell Scientific, UK). The EC’s tower at MMNR main station complex was 8 meters

high and the Licor-CSAT3 sensor separation distance was 5.5 cm. Wind direction was measured in three directions (x, y and z) while the vertical wind velocities and specific humidity was measured with 10Hz frequency. All the sensor's data loggers were set to record data in temporal resolution of between 15 and 30min intervals, which were finally averaged to daily and monthly values for easy handling by respective models as input parameters.

a) Evapotranspiration

The Eddy Covariance (EC) was used to measure the land surface exchange fluxes within the Main Mara station where the Automatic Weather Station was established with mainly homogeneous natural grassland dominated environment. The site was chosen for the installation of the instruments because it would allow for accurate measurements of the transfer of heat, energy, and momentum between the land and the atmosphere without compromising the integrity of the ecosystem. An EC exchange flux was defined as the covariance between the vertical wind speed and the scalar of interest. Therefore, if we apply this to the LE flux (Wm^{-2}), we get,

$$LE = \lambda \rho q' w' \quad (3.2)$$

where, λ (Jkg^{-1}) and ρ (kgm^{-3}) are the heat of vaporization and the density of air, respectively. The symbol q (kg kg^{-1}) stands for the specific humidity of the air, and w (ms^{-1}) denotes the vertical wind speed. The term $q' w'$ is the covariance between the fluctuations of the two quantities. The EC data have undergone all necessary corrections, such as the correction of the sonic temperature for the effect of moisture according to Webb, Pearman, and Leuning (WPL), the correction of the water vapour flux for air density effects (Webb *et al.*, 1980), and the correction of the coordinate rotation. Net radiation, air temperature, and humidity were measured with a Bowen's ratio system for use in adjusting the Eddy Covariance (EC) system's accuracy. Since the majority of the land in the area is grassland, a Bowen Ratio (BR) system (Campbell Scientific Inc., CSI) was erected near the northernmost end of the primary weather station. It included a net radiometer Q-7.1 (CSI), a dew-point hygrometer "Dew-10" (General Eastern, MA, USA), three soil heat flux plates (HFT3, CSI), four soil thermocouples (TCAV, CSI), and two fine-wire thermocouples (FW05, CSI). Every 30 minutes, the data was logged into a data recorder for later analysis. The built-in sensors scanned data once every second with basic processing, like wind correction of net radiation. At the end of each quarter, the processed data was downloaded to a desktop computer where it could be stored and used in subsequent calculations and analyses. Eddy covariance (EC) data for the study region was gathered using a Campbell Scientific data

logger (CR3000, Campbell Scientific, Logan, UT, USA) and analysed according to standardized eddy covariance techniques, as described in Reed *et al.* (2014; 2016) and Desai *et al.* (2009). Open source EddyPro 3.0 software (LI-COR Biosciences, Lincoln, NE) analysed the 10Hz frequency wind velocities, CO₂ and H₂O flux concentrations, and calculated the 30-minute fluxes. Energy balance was described by the following ways: The method of Leuning *et al.* (2012) was followed using equation 3.3, where energy balance for the field site was defined with net radiation (R_n), measured latent (LE) and sensible (H) heat fluxes. Soil heat flux, G_0 was also scanned via heat plates at depth (G) and energy storage within the soil profile (J_g) and energy storage within the canopy (J_v) at each 30 min time scale.

$$R_n = LE + H + G + J_g + J_v \quad (3.3)$$

In this method, the net radiation was considered positive for energy flux towards the surface; the other values are positive for energy leaving the surface.

b) Ground Heat Flux

Three soil heat flux plates at 6cm and 8cm depths were also set up. The hydraulic gradient at the water balance domain's base was calculated using data from five sensors placed at various depths (two matrix potential sensors at 40cm and three more at 80cm). A distance of 100cm was chosen as the horizontal distance between sensors. Using the measured soil heat flux and the heat storage change (equation 3.4) between the land surface and the plates, we were able to determine the ground heat flux (Foken, 2008b).

$$\Delta S_G = \frac{C_v \times \Delta T \times L}{\Delta t} \quad (3.4)$$

where, C_v ($Jm^{-3} \circ C^{-1}$) indicate the volumetric heat capacity of the soil, ΔT ($\circ C$) represents the soil temperature change during the period of time, Δt , measured, and $L(m)$ is the thickness of the soil layer above the soil heat flux plates.

3.2.1 Soil Physical and Chemical Properties of Maasai Mara Rangeland Ecosystems

a) Soil Texture

Soil texture for 24 selected sampling points at bearing angles of (0, 60, 120, 180, 240 and 300) degrees and radii distance of (10, 25, 75 and 175) m in the study area denoted as A, B, C and D rings were collected, labelled and taken for laboratory analysis (appendix A.4). For each field test, 144 soil samples were collected from the 24 sample points at depths of midpoint range 0-5cm, 5-10cm, 10-15cm, 15-20cm, 20-25cm, and 25-30cm for biophysical soil properties characterization, which included texture, bulk density, particle density, soil

moisture. The mixture of all soil profile depth samples were used for soil chemistry analysis such as pH, soil organic matter, or total organic carbon including other macro and micronutrients for soil in MMNR rangeland and Naivasha cropland ecosystems.

The soil was dispersed with sodium hexametaphosphate and mixed with water, then subjected to the conventional procedure of screening and sedimentation analysis based on Stokes' Law (hydrometer method) to evaluate its texture on soil suspension (Karkanis *et al.*, 1991). This study on particle size distribution was conducted at the National Agricultural Research Laboratories of the Kenya Agricultural and Livestock Research Organization (KALRO), in Kabete (NARL). Particle diameter and the gravitational, buoyant, and drag forces acting on soil particles were used to calculate the settling velocities of individual particles. The Stokes' law written as in equation (3.5) gave the free fall velocity as;

$$v = \frac{1}{18} \left(\frac{(\rho_s - \rho_f)gd^2}{\mu} \right) \quad (3.5)$$

where, v = settling velocity, g = gravitational acceleration, $g = 9.80 \text{ m/s}^2$, ρ_s = density of dropped object d = diameter of dropped object, ρ_f = density of fluid μ = viscosity of fluid. Soil mixture was finally classified according to soil textural triangle, where determined percentage distributions of sand, silt and clay particles were characterised to give the soil's textural classes (Saxton *et al.*, 1986), Figure 4.7).

b) Bulk Density

Blake and Harge (1986) used gravimetric coring method to determine the bulk densities for each soil depths and a water pycnometer was employed to find the soil particle density, ρ_z (Soil Survey, 2014) (Appendix B.6)

c) Soil Organic Matter

The Organic Carbon (% OC) was analysed by Walkey and Black procedure (Nelson & Sommers, 1982). Organic matter (OM %) was calculated by multiplying OC with conventional Vanbamer factor. The values of organic carbon were multiplied by a Vanbamer factor of (58%) 1.724 to obtain values for organic matter content available in the soil. The organic matter content was measured as the Cox in % (Xingwu *et al.*, 2017). These values were converted into the organic matter in percentage using the conversion equation $OM = 1.724 \text{ Cox (\%)}$. According to Saxton and Rawls (2006), the organic matter content of the soil is critical for soil water retention. Increased soil pore volume can significantly increase infiltration, which is facilitated by soil aggregation and channels created by roots and soil organisms.

d) Macro and Microelements of Naivasha Cropland

Measurements for a wide range of chemical characteristics in the Naivasha Cropland ecosystem were analysed using the outlined methods and the findings are shown in the appendix (B.14). A 1:2.5 (w/v) soil-water suspension was used to measure the soil's pH with a pH-meter with a glass electrode (Black, 1965). Conductivity bridge was also used to measure electrical conductivity (EC) of soil by immersing an electrode in a mixture of soil and water (Hanna, 1964). In addition, Bremners' modified macro-Kjeldhal method calculated the total nitrogen (1965). Phosphorus was recovered using the Bray 1 extraction technique (Bray & Kurtz, 1945), and P content was calculated through calorimetry. The other total metal analyses for Zn, Cu, Fe, Mn, Ca, Mg, Na, K, Cr, and Pb was measured using an Atomic Absorption Spectrophotometer (AAS), nova 400 Germany, following extraction through dry ashing (Neutral Ammonium Acetate).

e) Infiltration Rate/Saturated Hydraulic Conductivity

The infiltration measurements was conducted at the ten-5TM-ECH₂O soil moisture, temperature stations using a double ring infiltrometer with inner and outer ring diameters of 30/55cm and a height of 25 cm, as described by Ayu (2013). (Appendix B.9). Charts for MMNR station illustrated infiltration rates (Figure 4.12). Based on its attractiveness as a function of computational time and cumulative infiltration, the study used Philip's two-term equation (Sharma *et al.*, 1980). They demonstrated an approximation of cumulative infiltration I over time in water-ponded circumstances by,

$$I = St^{0.5} + At \quad (3.6)$$

where, I represents cumulative infiltration L, S represents sorptivity ($L/T^{0.5}$), and A represents a constant (L/T). With more and more elapsed time, the first term becomes insignificant, and A , which stands for the bulk of the gravitational influence, becomes more pivotal (Koorevaar *et al.*, 1983). The A term represents the saturated hydraulic conductivity of the wetted zone (K_w) following a significant amount of infiltration time (Bouwer, 1986).

3.2.2 Cosmic Ray Probe Soil Water Content Determination

Continuous monitoring of soil moisture was done via cosmic ray soil sensors (Model CRS-1000 from Hydroinnova LLC, Albuquerque, NM, USA) and (Decagon Devices, Inc.) connected to a data logger. The CS 616 sensors (Figure 3.1, 3.5) were buried underneath the soil at 5cm depth concentrically in three-degree angles of 120°, 240° and 360°,0° with equidistance footprint of 7m. During the seasonal field visits, undisturbed soil samples were collected from the periphery of 5TM-ECH₂O (soil moisture, soil temperature) stations at

specific profile depths (P1, P2, P3, P4 and P5) of respective (0-5cm, 5-10cm, 10-15cm, 15-20cm, 20-25cm, and 25-30cm, 35-40cm and 75-80cm) represented by 2.5cm, 7.5cm, 12.5cm, 17.5cm, 22.5cm and 27.5cm, 37.5cm and 77.5cm. Sample collections were spatial distributed in distances of 10m, 25m, 75m, and 175m from the CO₂ flux collars using core-sampling rings (5cm diameter, 5cm height) which allowed measurements for further soil properties under controlled laboratory conditions. The soil water content was determined according to the described methods as follows;

3.2.3 Neutron Intensity Method

Desilets *et al.* (2010) developed a shape-defining function, hereafter called N_o -method, to determine volumetric soil water content θ_{vol} (cm³cm⁻³) directly from corrected neutron flux:

$$\theta_{vol} = (a_o \times \rho_{bd}) \times (N_{pih}/N_o - a_1)^{-1} - (a_2 - \rho_{bd}) \quad (3.7)$$

where, the parameters $a_o = 0.0808$, $a_1 = 0.372$, $a_2 = 0.115$ are dimensionless and N_o is a site-specific calibration parameter. The assumptions made were that the variables, a_o , a_1 and a_2 are independent of the chemical makeup of the soil and are stable throughout time (Desilets *et al.*, 2010; Zreda *et al.*, 2008). The N_o is a continuous calibration parameter that varies with time and depends heavily on local variables.

3.2.4 Molar Fraction Based Method (Hmf-Method)

An approximation of the relationship between hydrogen molar fraction (hmf) and neutron flux is given by Franz *et al.* (2013) as,

$$\frac{N_{pih}}{N_s} = 4.486 \exp(-48.1 \times hmf) + 4.195 \exp(-6.181 \times hmf) \quad (3.8)$$

where, N_s is a time-constant site-specific calibration parameter (cph) and N_{pih} is the neutron flux corrected for pressure, incoming radiation and air humidity.

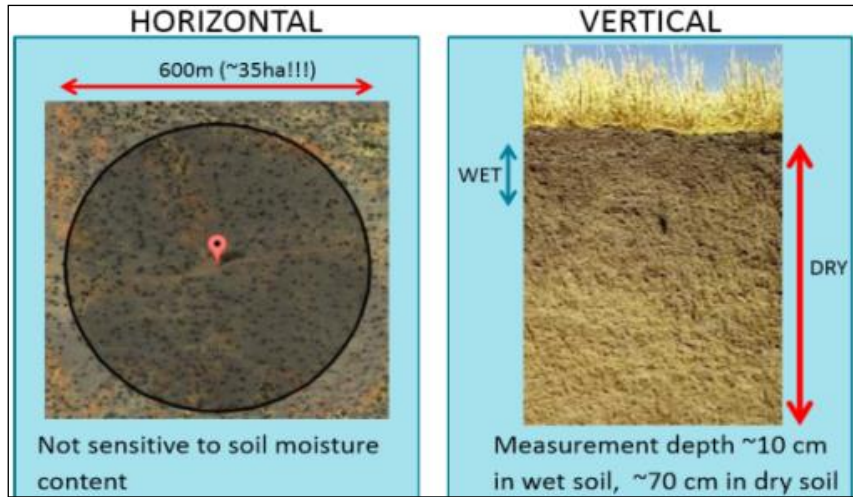


Figure 3.4: The cosmic-ray probe measurement footprint

N_s was calibrated for each probe with the average measured neutron flux N_{pih} of a 12 h time window at the time of calibration and the calculated hydrogen molar fraction were based on sampling campaign results.

3.2.5 Field Calibration and Validation of Cosmic Ray Soil Moisture Sensor

There were ten calibration campaigns conducted between 2017 and 2019 over the field study's biannual period. The first incident occurred in February, at the height of the rainy season, when the soil was exceptionally saturated. Zreda *et al.* (2012) created the recommended sampling pattern for the calibration of CRNS, which was slightly changed by Franz *et al.* (2012b). The prescribed sample plan involved four concentric circles with radii of 10, 25, 75, and 175m around the CRNS (Figure 3.5). From the sensor, six straight lines pointing to the following bearings (0 degrees, 60 degrees, 120 degrees, 180 degrees, 240 degrees, and 300 degrees) intersected each of the four circles uniformly. All of the junctions were sampled, and the samples were taken from the exact centre of the intersections. Due to the exponentially decreasing sensitivity of the CRNS with increasing distance, the sampling design ensured that each sample contributed equally to the spatial mean of soil moisture measured by CRNS. Soil cores were taken from the ground at 18 different locations within the sensor's footprint, each one 30 centimetres in length. The cores were then cut into six equal sections, each 5 centimetres in thickness: 0-5cm (0.25cm), 5-10cm (7.5cm), 10-15cm (12.50cm), 15-20cm (17.50cm), 20-25cm (22.5cm), and 25-30cm (27.5cm). We collected 108 soil samples total, 10 from each of the 10 calibrations, and transported them in a cooler box full of ice to the chemical department at Maasai Mara University for analysis and gravimetric determination of water content (GWC). The water content and bulk density were

calculated by immediately weighing the samples, drying them in an oven at 105 degrees Celsius for 24 hours, then reweighing them.

Five depth-representative soil samples were taken to Kabete for analysis of texture, particle density, total organic carbon, and root biomass at the National Agricultural Research Laboratories (NARL). The 108 samples (from the most recent calibration campaign in November) were divided into strata according to their sampling depth. Two grams were taken from each of the 18 samples taken at each depth range (0-5cm, 5-10cm, 15-20cm, 35-40cm, and 75-80cm), then these were combined to make a single bulk sample. This was followed by a search of the scholarly literature to determine the lattice water value. When calculating SOM, dried soil samples were weighed and re-dried at 400 degrees Celsius for further 24 hours. This was done using the "loss on ignition" method as described by (Ball, 1964; Davies, 1974) as the organic material is destroyed throughout the process. Extracting the root biomass and organic matter from the soil was done. After being weighed, samples were re-heated in an oven for 24 hours at a temperature of roughly 1000 degrees Celsius to calculate the fraction of soil organic matter and root biomass. Afterwards, 0.556 was multiplied the weight of the soil organic matter and root biomass, which is the ratio of 5 times the molecular weight of water, to obtain the equivalents of water. The molecular weight of cellulose was considered using the same method as Hawdon *et al.* (2014), which means that the fact that cellulose ($C_6H_{10}O_5$) has 10 hydrogen atoms per molecule whereas water (H_2O) has only two was taken into account. To lessen the impact of measurement noise, the sensor's neutron counts were smoothed with a 12-hour moving window (Bogena *et al.*, 2013). The neutron counts were then corrected for variations in (a) pressure, (b) incoming neutron flux, and (c) water vapour in the air using equation (3.7) as presented by Desilets *et al.* (2010).

3.2.6 Calibration of Cosmic Ray Soil Moisture Sensor by Gravimetric Sampling

The recommended gravimetric soil-sampling method for the calibration of CRNS produced by Zreda *et al.* (2012) was followed and significantly modified for use in calibration campaigns as described in detail by Franz *et al.* (2012b). At each of the 24 calibration locations, 144 soil samples were taken from 0-5cm, 10-15cm, 15-20cm, 35-40cm, and 75-80cm depths using a core ring (5cm in diameter and 5cm in height) at concentric sampling (coordinate) points at four radial rings at 60, 120, 180, 240, 300, and (0, 360) degrees. Pits or trenches 50 centimetres (cm) wide and 100 centimetres (cm) deep were dug for core sampling to the bottom of the pit or trench during calibration.

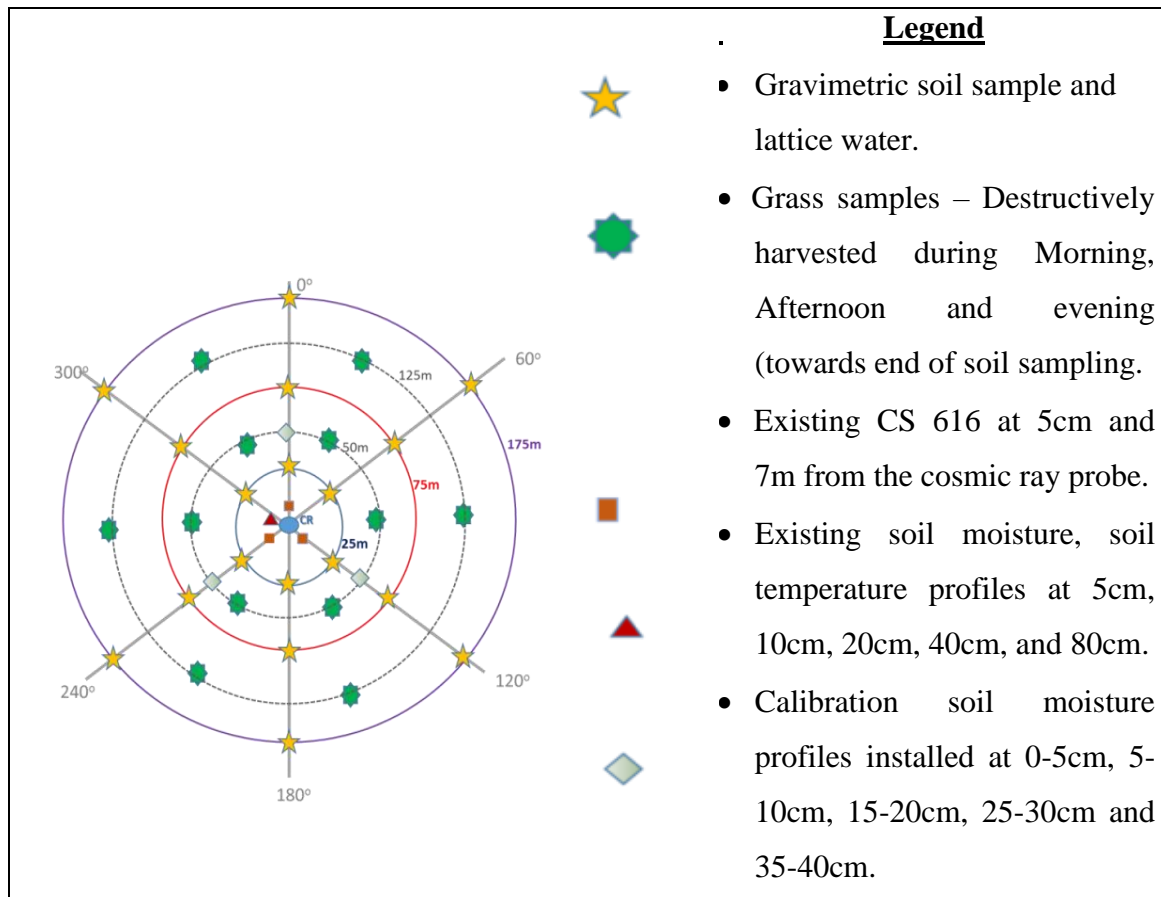


Figure 3.5: Calibration procedure for gravimetric soil sampling

Soil samples were taken on 20th May 2018 to calibrate neutron intensity (N_o) and determine site-specific parameters. The excavated soil samples were placed in plastic bags and transported to a laboratory within 10 hours. The damp dirt from the field was collected, weighed, and then dried at 105 degrees Celsius for 48 hours in a well-ventilated oven. The samples were weighed and reweighed until the final weights were consistent within measurements. In order to get the volumetric water content, we multiplied the gravimetric water content by the bulk density, which is based on the mass balance. In order to convert the gravimetric soil moisture content to the volumetric water content for use in the CRNS calibration, a representative bulk density measurement is required. In contrast, CRNS measures the soil's volumetric moisture content, which is expressed as the ratio of the soil sample's water volume to its total volume (m^3/m^3). In order to calculate the rangeland's bulk density, rings of undisturbed soil were taken from a number of different depths and places. After some computation, we found that the average bulk density was $1.34g/cm^3$. Although the rangeland is a natural ecosystem, its high bulk density value can be linked to a number of factors, including the dense grass cover, low organic matter content, low platy soil structure, low porosity, high proportion of sandy clay loam (SCL) soil, and compaction brought on by

wildlife trampling, tourist track traffic, and invasion by Maasai herds. Here, the calibration target was to determine the average N_o value (site-specific calibration parameter), which is the theoretical neutron intensity (counting rate) in air above dry soil (no moisture).

The CRNS primarily sends data through satellite link once per hour. The procedure for calibrating was based on one developed by Franz *et al.* (2014, 2015). The neutron count corrections were the first step in the initial calibration method. The neutron correction factors were calculated using the following formulae.

$$N_{corr} = \frac{N' \times CP \times CWV}{CI \times CS} \quad (3.9)$$

where, N_{corr} is the corrected neutron counts per hour, N' is the raw moderated neutron counts, CP is the pressure correction factor, CWV is the water vapour correction factor, CI is the high-energy intensity correction factor, and CS is the scaling factor for geomagnetic latitude.

$$CP = \exp\left(\frac{P_0 - P}{L}\right) \quad (3.10)$$

where, L is the mass attenuation length for high-energy neutrons (g/cm^2), P is the atmospheric pressure (mb) at a specific site and P_0 is the reference atmospheric pressure (mb).

$$CWV = 1 + 0.0054 (P_{vo} - P_{vo}^{ref}) \quad (3.11)$$

where, P_{vo} is the absolute humidity of the air (g/m^3) and P_{vo}^{ref} is the reference absolute humidity of the air (g/m^3).

$$CI = \frac{I_m}{I_{ref}} \quad (3.12)$$

where, I_m is the selected neutron monitoring count rate at any particular point in time and I_{ref} is the reference count rate for the same neutron monitor from an arbitrary fixed point in time. The neutron flux data was obtained through the neutron-monitoring database (www.nmdb.eu), which provides real-time data from a global network of monitoring stations.

$$CI = f(x, y, z, t) \quad (3.13)$$

$$(\theta_p + \theta_{lw} + \theta_{soc}) = \frac{0.0808}{\frac{N}{N_o} - 0.372} - 0.115 \quad (3.14)$$

where, x, y, z is location and elevation, and t is time. The following calibration function was then used to determine the N_0 value for each calibration

Rearranging the calibration function to determine,

$$N_0 = \left(\frac{N}{\frac{0.0808}{(\theta_p + \theta_{lw} + \theta_{soc}) + 0.115} + 0.372} \right) \quad (3.15)$$

where θ_p is the gravimetric water content (g/g), θ_{LW} is lattice water content (g/g), θ_{SOC} is soil organic carbon water content (g/g), θ_{bd} is dry soil bulk density (g/cm³), N is the corrected neutron counts per hour, and N_0 is an instrument-specific calibrated parameter.

$$WVC = \left(\frac{0.0808}{\left(\frac{N}{N_0} \right) - 0.372} - 0.115 - (\theta_p + \theta_{LW} + \theta_{SOC}) \rho_{bd} \right) \quad (3.16)$$

Notably, here soil moisture is often expressed in units of volume percent, $WVC(\%) = \theta_p \times \rho_{bd} \times 100$. θ_{soc} was not determined, but was given a value of 0.01 g/g based on published values. θ_{lw} was determined to be 0.154 g/g. This was a 50-g representative soil sample sent to Activation Laboratories in Canada for θ_w determination by combustion at 1000°C (Franz *et al.* (2014, 2015). Correction for biomass was also computed using equation 3.17.

$$(\theta_p + \theta_{LW} + \theta_{soc}) = \frac{0.0808}{\frac{N}{N_0(BWE)} - 0.372} - 0.115 \quad (3.17)$$

where, BWE is the biomass water equivalent (mm). Vegetation types whose biomass varies with their growing stage are often the focus of the biomass computation, but since short grasslands of varying species predominated in MMNR, this was not the case (appendix A.9). Thus, the water equivalent of biomass was rather high. The neutron count (N) for each calibration was calculated by averaging the neutron count during the period when soil samples were collected for that calibration. Using the rearranged calibration Equation 3.15, we were able to calculate the N_0 value for each calibration from these counts.

3.2.7 Calibration by Soil Moisture and Temperature Capacitance Probes

In the study, 10 (ten) 5TM-ECH₂O (soil moisture, soil temperature) campaign sensor stations were installed at various spatially distributed points in the ecosystem of MMNR and similar probes were installed in Naivasha cropland for moisture monitoring as demonstrated in figure 3.6.



Figure 3.6: Soil moisture and temperature capacitance (5TM-ECH₂O) probes

Five combined 5TM-ECH₂O soil moisture sensors at each point were horizontally placed in soil profiles as follows; first layer was ranged between **P1**(0 - 5cm), second layer between **P2** (5 - 10cm), third layer at mid-point of **P3**(15 - 20cm), fourth layer between **P4**(35 – 40cm) and the fifth layer was finally ranged at mid of **P5**(75cm – 80cm). These were installed below the soil surface to continuously measure soil water content at temporal resolution of 15mins interval. The trench was compacted during backfilling each layer by ensuring the soil surrounding the probe is properly fixed to minimize preferential capillary flow to the sensor probes. A laboratory calibration database on gravimetric water content, soil moisture probes were used to determine and statistically verify the accuracy of the cosmic ray soil moisture sensor.

3.3 Soil Moisture Storage Measurements

Soil water content was measured using the gravimetric technique, which entails obtaining a sample of the soil, weighing it before any water is lost, and then weighing it again after it has dried in an oven. Drying water mass was a direct indicator of soil moisture. The root zone water content (W_{rz}) was calculated as the sum of volumetric water content, θ_v at each depth, multiplied by the depth of soil layer represented by the water content.

$$W_{rz} = \theta_{v1}d_1 + \theta_{v2}d_2 + \theta_{v3}d_3 + \theta_{v4}d_4 + \theta_{v5}d_5 \quad (3.18)$$

where, θ_{v1} , θ_{v2} , θ_{v3} , θ_{v4} and θ_{v5} are volumetric water contents at five soil depths representing the root zone, d_1 , d_2 , d_3 , d_4 and d_5 are the thickness of each of the five soil layers sampled; and W_{rz} has the units of d . Five soil layers were used in this study.

3.3.1 Gravimetric Water Content

Gravimetric analysis was used to calculate the volumetric water content of soil samples taken from various locations near and far from the central weather station, where cosmic ray neutron sensor and soil moisture, soil temperature (5TM-ECH₂O) capacitance probes were installed (Appendix B.1). For this study, 144 samples of soil were collected geographically utilizing sampling core rings during field visits, then stored in a cooler box and oven dried at 105 degrees Celsius for 24 hours. The soil was taken from in-field locations using core rings (5cm in diameter and 5cm in height), with additional samples gathered concentrically at varying distances from the primary weather station (60, 120, 180, 240, 300 and 360). Different profile depths are shown by the horizontal distances of 25, 50, 75, 150, and 175m from the centre of the cosmic ray probe footprint radii (0-5, 5-10, 15-20, 35-40, and 75-80cm). The depth-averaged SMC for each site and measurement time was determined in this study using equation (3.19), based on 144 samples of shallow depth SMC data.

$$SMC_j = \frac{1}{n} \sum_{n=1}^n SMC_n \quad (3.19)$$

where, n is the number of measurement layers at the site j , and SMC_n is the mean soil moisture content in layer n calculated by five sampling profiles. The temporal-averaged shallow SMC of each site was also calculated by using equation (3.20):

$$SMC_n = \frac{1}{n} \sum_{j=1}^n SMC_j \quad (3.20)$$

where, n is the number of measurement times at the site j .

Samples were also evaluated for bulk density (dB), soil textural categorization, particle density, Total organic matter (TOC), surface hydraulic conductivity (infiltration rate) and soil chemistry (pH) at incremental depths up to 80cm as tabulated in the appendix (B.1 to B.7) (B.1 to B.7). The gravimetric soil moisture content is commonly reported by weight as the ratio of the quantity of water present to the dry weight of the soil sample (g/g). Capacitance probe sensors were placed at five distinct soil levels across the watershed. Decagon Devices Corporation, USA-made 5TM-ECH₂O sensors were used to take the measurements and their

signals were recorded in 15-minute time series using Decagon data recorders for accuracy and reliability. To make the soil moisture data more manageable as input to the simulation models, a weighted average was calculated for each station on a daily time-step. The locations of the sites were spread out across the catchment using the coordinates given in table 4.1 and the satellite view of the area provided by Google Earth (Appendix A.5).

3.3.2 Soil Moisture Content

Locations of ten soil moisture and temperature capacitance probes were recorded using a Garmin GPS60 and are shown in table below (4.1). Diverse soil probes were placed at varying depths (Appendix A.6). At P1 (0-5cm), P2 (5-10cm), P3 (15-20cm), P4 (35-40cm), and P5 (75-80cm) depths, we used a data logger to take direct measurements of volumetric water content as soil moisture. The instruments were connected to a remote computer via USB so that all the data could be transferred and analysed there.

3.3.3 Spatial Variability of Soil Moisture

Pearson's product-moment correlation coefficient (PPMCC), non-point mean near-surface soil moisture, was used to examine spatially variable site features. Maximum surface depth of water; percentage of coarse, sand, and fine soil fractions; altitude; percentage of seasonally active vegetation cover; and water equivalent at maximum surface depth were some of the features analysed. Dorigo *et al.* (2015) compared the soil moisture data reported by the validation ground stations network to the ESA CCI soil moisture composite product. For the most recent merger period (July 2012-December 2014), the median correlation coefficient across all stations was 0.89 with a 95% confidence interval of 0.96 to 0.79. (third and first quartiles of the series of correlation coefficients obtained in each station). When a given site characteristic has no influence on the spatial distribution of soil moisture at that site, then reject the null hypothesis that soil moisture is related to any single site characteristic index or value. The statistical significance of r was calculated at a significance level of $= 0.05$ for both positive (+) and negative (-) correlations. These methods were used in this investigation.

3.3.4 Temporal Variability of Soil Moisture

Grant *et al.* (2004), Grayson and Western (1998), and Vachaud *et al.* (1985) all recommend using time stability analysis to determine how much each measurement site varies from the average soil moisture in a watershed. Here, time stability analysis was required for each sample location on each sampling date, calculation of soil water storage (S_{ij}) at the greatest common depth (80 cm) and the relative difference (ij) in soil water

storage capacity and catchment mean near-surface soil water storage (S_j). Soil water storage at each sample location i , at time j , was calculated as:

$$S_{ij} = \theta_{ij} z_{ij} \quad (3.21)$$

where, θ_{ij} and z_{ij} represent measured near-surface soil moisture content and the thickness of the sampled soil profile (5 cm) respectively at location i , time j . The relative difference (δ_{ij}) between soil water storage (S_{ij}) at a location, i and the catchment mean near-surface soil water storage (\bar{S}_j) observed at time j was computed as;

$$\delta_{ij} = \frac{S_{ij} - \bar{S}_j}{S_j} \quad (3.22)$$

The mean relative difference ($\bar{\delta}_i$) for all sample times was calculated as:

$$\bar{\delta}_i = \frac{1}{m} \sum_{j=1}^m \delta_{ij} \quad (3.23)$$

where, m is the number of sampling times. Time stability between successive measurement dates was determined by a Spearman correlation coefficient (rs) described by Vachaud *et al.* (1985):

$$rs = 1 - \frac{6 \sum_{i=1}^n ((R_i(j_2)) - (R_i(j_1)))^2}{n(n^2 - 1)} \quad (3.24)$$

where, n is the number of observations, $R_i(j_2)$ is the rank of S_{ij} at location i , time j_2 , and $R_i(j_1)$ is the rank of S_{ij} at location i , time j_1 . The time stability between two sampling dates becomes more stable as rs approaches 1, with perfect time stability occurring where $rs = 1$ (Vachaud *et al.*, 1985). In addition to time stability between successive sampling times, we are interested in the tendency for locations to retain their relative wetness ranks throughout the year. Grayson and Western. further suggested that the standard deviation of the relative difference for a sample location $\sigma(\delta_i)$ is an indicator of time stability, reasoning that locations with low values retain similar relative differences through time. The standard deviation is calculated as:

$$\sigma(\delta_i) = \sum_{j=1}^n \left(\frac{\delta_{ij} - \bar{\delta}_i}{m-1} \right)^{1/2} \quad (3.25)$$

where, m is the number of sample times. It is possible that extreme wet or dry locations have high $\sigma(\delta i)$ values while retaining stable wetness ranks. To identify these locations, rank change index (RCI) was used. The RCI for a location i is the sum of the absolute values of the differences in rank between successive measurements:

$$RCI_i = \sum_{j=1}^n \left(|R_j - R_{j-1}| \right) \quad (3.26)$$

where, m is the number of sample dates, and R is the rank of the location's soil moisture content relative to all locations on date j .

3.4 Soil Moisture Retention Capacity

The soil water potential was measured with a tensiometer at between 0-0.05m, 0.05m-0.1m, 0.15-0.20m, 0.25-0.30m, up to 0.35-0.40m, where the porous ceramic cup was vertical inserted into the soil layers on the spatial selected sites where soil was heterogeneous and due to the length of the tensiometer which was 0.43m. Soil samples of undisturbed structure were also collected in volumetric rings from spatially distributed twenty-four (24) different trenches/pits surrounding the cosmic ray probe at various concentric points with profile depths of 0-5, 5-10, 15-20, 35-40 and 75-80 cm. This determination was critical due to the soil moisture variation in the soil profile and rooting depths, the grassland physical properties of the subsurface layers were significant in the computation of plants available water content on the plant root systems under respective conditions. In the study, the volumetric water content (θ) data obtained for samples with undisturbed structure, soil water retention curves (SWRC) for each replicate from similar sample soil depths were adjusted. The adjustments were based on two distinct models. First, by the van Genuchten (1980) model, described in equation (3.27) with the Mualen restriction $m = 1 - \left(\frac{1}{n} \right)$, by means of software RETC (van Genuchten et al., 1991), calculating the modulus of the potential at the inflection point of SWRC (h_{IP}) and the corresponding water content (θ_{IP}), as described by Dexter and Bird (2001), as presented in equations 3.27 and 3.28.

$$\theta = (\theta_{sat} - \theta_{res}) \left[1 + (\alpha h)^n \right]^{-m} + \theta_{res} \quad (3.27)$$

where, θ is the soil water content ($\text{cm}^3 \text{cm}^{-3}$); h is the modulus of the potential or the soil water tension (kPa); θ_{sat} is the water content of the saturated sample ($\text{cm}^3 \text{cm}^{-3}$); θ_{res} the water content ($\text{cm}^3 \text{cm}^{-3}$) at 1500 kPa tension, and m , n , α are the adjustment parameters of the model.

$$h_{IP} = \frac{1}{\alpha} \left(\frac{1}{m} \right)^{\frac{1}{n}} \quad (3.28)$$

$$\theta_{IP} = (\theta_{sat} - \theta_{res}) \left[1 + \frac{1}{m} \right]^m + \theta_{res} \quad (3.29)$$

Subsequently, the cubic polynomial model, between θ and the logarithm of matric potential in cm H₂O (pF), for calculating h_{IP} and θ_{IP} as proposed by Mello *et al.* (2002), is shown in equations 3.30, 3.31, 3.32 and 3.33:

$$\log(h) = \alpha + b \times \theta^2 + d \times \theta^3 \quad (3.30)$$

$$\frac{d(\log h)}{d\theta} = b + 2 \times c \times \theta + 3 \times d \times \theta^2 \quad (3.31)$$

$$\frac{d(d \log h) / d\theta}{d\theta} = 2 \times c + 6 \times d \times \theta \quad (3.32)$$

Equating equation (3.32) to zero, we had the water content at the inflection point:

$$\theta_{IP} = \frac{-c}{3d} \quad (3.33)$$

where, h = the matric potential modulus, $\log h$ = logarithm of matrix potential; θ_{IP} = water content corresponding to the inflection; a, b, c and d are adjustment parameters.

3.4.1 Statistical Analysis

Significant impacts of soil moisture, bulk density, particle density, and total organic carbon on biomass production were identified by analysis of variance (ANOVA) using the PROC GLM program in SAS. The treatment means were independently analysed using Fisher's protected least significant difference (LSD). SAS's PROC REG technique was used to do the study of regression (SAS Institute 2008). Statistical measures (mean, variance, maximum and lowest value, standard deviation, and coefficient of variation) were used to characterize the soil moisture content at various locations (Table 4.9 to 4.14). They were computed and employed to gauge the degree of data dispersion. The calculation of Spearman's rank correlation coefficient aimed to correlate the soil water content at various times and its relationship to other soil parameters. The relative mean difference (δ_{ij}) was calculated and presented graphically in order to show the rank of wettest, driest and mean points in the area for each year. This method ranks the measurement sites by their deviation from the spatial average (Vachaud *et al.*, 1985). These steps were taken to determine the average relative difference;

$$\delta_{ij} = \frac{\Delta_{ij}}{S_j} \quad (3.34)$$

where, Δ_{ij} is calculated by the difference between the measurements at each point (i) on day (j) and the mean measurement for day (j), and S_j represents the field mean soil water storage for a particular day (j). For each location, the average and standard deviation of δ_{ij} , were calculated and graphically presented.

3.5 Simulation of the Influence of Soil Moisture Variability on Rangeland and Cropland Biomass Production Using Coupled Hydrus-1D and Agricultural Production System Simulator (APSIM) Model

3.5.1 Calibration and Validation of Hydrus -1D model

The infiltration rate, hydraulic conductivity, and moisture content were calculated with Hydrus 1D after calibration of the model. The weather data, soil hydraulic characteristics, geometry, and timing data were used as input parameters. This natural grassland ecosystem soil was profiled at several depths from 0 to 80 centimetres down to reveal the pre- and post-processed data inputs for each layer. Through trial and error, we were able to calibrate to levels that were consistent with the observed data (table 4.23). This research used a gravimetric approach to acquire a fifth set of parameters (P5) based on the water content of reference soil samples taken at 80cm. Therefore, in order to validate the reference parameters, comparisons were made between the four sets evaluated (P1-P4) and the reference parameters (P5). Each soil sample was tested for its ability to retain water using a series of five pressure heads (-33, -100, -300, -1,000, and -1500kPa), and a moisture retention curve was calculated for each.

3.5.2 Parameterisation and Calibration of APSIM Model

This model's simulation runs used a trial-and-error approach to calibration, with an initial value determined from field experimental data relevant to the parameter to be estimated via calibration. After a model was developed using parameters gleaned from a review of the relevant literature, a field experiment was carried out to collect data for use in refining the model. Rainfall, temperature, organic matter concentration, and carbon to nitrogen (C: N) ratio were just some of the input variables used to calibrate the model against the experimental dataset of soil and climate conditions. It was necessary to calibrate the model after parameterization to confirm that the predicted values were consistent with the observed ones. The procedure was repeated multiple times, ultimately culminating in a statistically insignificant mean difference. Since it was assumed that elements such soil moisture, C:N

ratio, temperature (soil and air), and other environmental factors defining model input parameters were tied to plant-specific materials, these factors were not used during the adjustment of the model calibration. Adjustment of the parameter values was performed manually, with numerous permutations tested until the optimal fit was found. The procedure consisted of a series of iterations that were changed up in order to increase the likelihood of success. Under the Naivasha farmland as a distinct regime, the model was parameterized and assessed for various conditions of climate variables, soil type, plant species (wheat). Naivasha cropland was utilized as an independent dataset to quantitatively compare observed biomass and yield with simulated outcomes in order to verify the APSIM model.

3.6 Field Clipping Campaign of Aboveground Grass Biomass

At both the wet and dry seasons' ends, destructive hand shear cuts to the ground level through a metal square frame measuring 50cm x 50cm quadrat were used to collect aboveground grass biomass (AGB) (Appendix A.7). Both traditional field methods and remote sensing were employed to obtain biomass estimates. The MMNR rangeland ecosystem was sampled using a randomized complete block design to gather AGB from ten (10) evenly spaced 5TM-ECH₂O sampling stations with six (6) replications for each site. The treatments inside the Automatic weather station's walled perimeter served as a control group, while the stations located outside served as trial plots while being open to wildlife for the purposes of feeding and interfering. Independently distributed on radial rings of 10m, 25m, 75m, and 175m at bearing degrees of (0, 360), 60, 120, 180, 240, and 300, 24 replicate plots were sampled radially for each quadrat of dominant grass species. Litter and standing sections of each grass were sorted by hand after harvest, their wet weights recorded using a digital scale, and they were dried in the sun for seven days or oven dried at 60 degrees Celsius for further 72 hours. This helped establish the dry matter content of the plants by stopping their metabolism. In order to calculate the total aboveground grass biomass, we added together the dry litter and the standing sections. Over a total of 30 months, beginning from May 2017, researchers monitored the dominating grassland's per quadrat biomass performance twice: once between January and December 2017 and again between May and December 2018. (2018 - 2019). Using the approach outlined by Fonseca *et al.* (2007), the standing AGB grass biomasses were trimmed and weighed at the beginning and conclusion of each wet and dry growth cycle. Grass biomass was measured "in situ," or in the field, to serve as a reference for verifying and calibrating satellite readings. Garmin Global Positioning System coordinates were acquired for each quadrat of aboveground grass biomass clipped area with 5TM-ECH₂O soil moisture probes attached (GGPS). Each

quadrat's worth of wet grass cuttings was weighed on a computerized balance, and the results were recorded and bagged up for later analysis. After collecting the samples, we dried them in an oven at the lab (Appendix A.8) to ensure accurate results. The grass biomass dry matter was determined, henceforth termed derived aboveground grass biomass. Dry and wet season total aboveground biomasses were spatially calculated in situ for the entire rangeland ecosystem over the course of three years (January 2017 to December 2019). Tons per hectare were derived from the average of the aboveground grass biomasses that were measured.

3.6.1 Satellite Estimation of Aboveground Biomass

The NDVI data values were derived from MODIS and PROBA-V mission vegetation instrument that were processed for the same period of months and years that the “in situ” data of aboveground biomass campaigns were destructively harvested. At the sampling points (coordinates), the NDVI images were used from Global Land Service of Copernicus products for each pixel. The data was downloaded from the Vegetation website (<http://free.vgt.vito.be>) where the satellite images are available in ten (5TM-ECH₂O) capacitance probes spatially predefined regions of interest. The satellite images were selected for the points/regions of interest in the study area as provided in the 5TM-ECH₂O coordinates for the experimental sites. The relative resolution of the MODIS satellite images was 600m for the selected points.

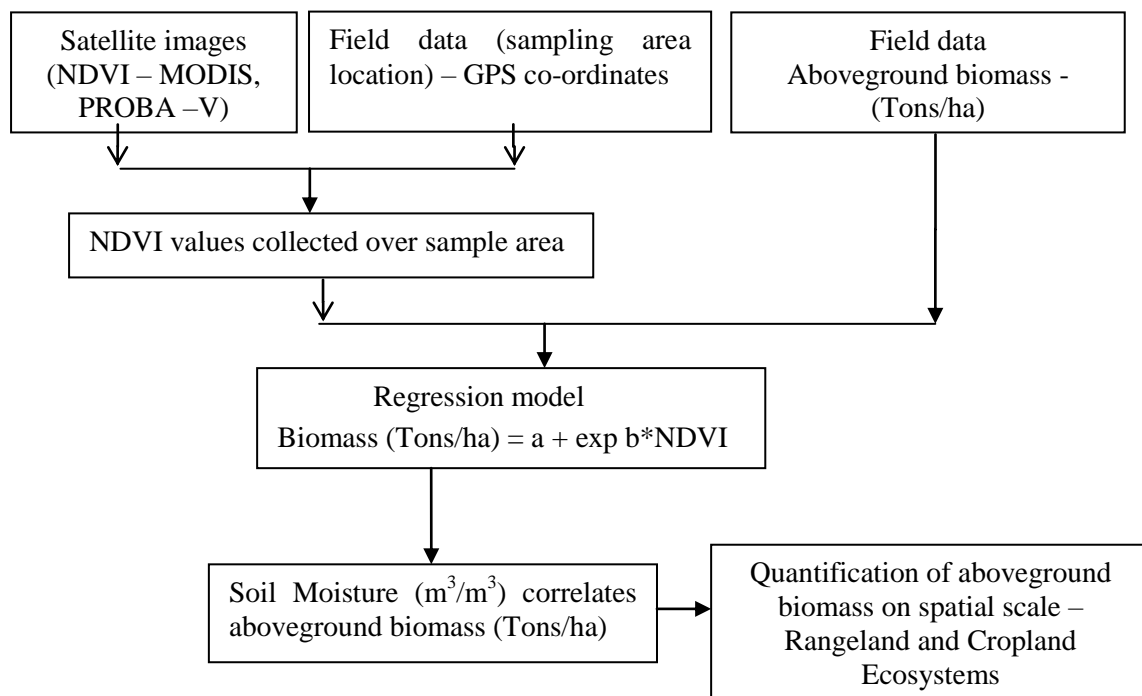


Figure 3.7: Schematic flowchart for satellite biomass estimation

a) Extraction of NDVI images

MODIS, PROBA-V, and SENTINEL-2 were used to process the NDVI time series. The Level 2 (100m) products' foundational input layers (normalized difference vegetation index, aerosol optical thickness, and fractional aerosol photon extinction rate) came from the Proba-V satellite until the end of the year. The Proba-V satellite was turned off in June of 2020. Level 2 input layers for NDVI, albedo, and fAPAR began using data from the Copernicus Sentinel-2 mission in January 2020. To create the initial 10-day MVC synthesis, NDVI pictures from December 2017 through May 2019 were chosen. Copernicus Open Access Hub (Sci-Hub) downloads of Global Land Service of Copernicus vegetation image files with baseline processing versions between 02.01 and 02.04 were conducted. The initial step was to schedule biomass-sampling campaigns around when the instruments were available for taking samples. This process was carried out multiple times, once for each data file used in the NDVI time series' creation. The NDVI images for dry and rainy seasons were derived over a 36-month time period, from January 2017 through December 2019. Once all data was extracted, NDVI images and status maps were made. The yearly average NDVI value is a rough measure of growth efficiency and a proxy for net primary productivity.

b) Dimensionless Model Balance Equations

In the relationship of soil moisture variability to biomass, the model took the characteristic water budget parameters as $(K_s \alpha)^{-1}$ and α^{-1} which were respectively the time and length scale carrying capacity C_i of each species scales and the related biomass density N_i . The dimensionless form of the proposed eco-hydrological model consists of the following set of balance equations for groundwater depth (h), soil moisture (w), the first (and eventually dominant) plant biomass density (n_1), and the second plant biomass density (n_2). The spatially explicit model is defined in $1D$ as a function of space x and time, t :

$$\frac{\partial h}{\partial t} = \frac{\partial}{\partial x} \left(h \frac{\partial h}{\partial x} \right) + q_v \quad (3.35)$$

$$\frac{\partial w}{\partial t} = \frac{w}{(z_s - h)} \frac{\partial h}{\partial t} + \frac{1}{(z_s - h)} \cdot (i - e - \gamma e_1(w_{r1})n_1 + e_2(w_{r2})n_2 - q_v) + v_w \frac{\partial w}{\partial x} + d_w \frac{\partial^2 w}{\partial x^2} \quad (3.36)$$

$$\frac{\partial n_1}{\partial t} = g_1 \cdot n_1 \cdot [l_1(w_{r1}) - n_1] + d_1 \frac{\partial^2 n_1}{\partial x^2} \quad (3.37)$$

$$\frac{\partial n_2}{\partial t} = g_2 \cdot n_2 \cdot [l_2(w_{r2}) - n_2 - \beta \gamma n_1] + d_2 \frac{\partial^2 n_2}{\partial x^2} \quad (3.38)$$

The dimensionless groups in the model (equation 3.37) are:

$$i = \frac{IW_s}{K_s}, q_v = \frac{Q_v W_s}{K_s}, e = \frac{EW_s}{K_s}, e_{1,2} = \frac{E_{1,2} C_{1,2} W_s}{K_s} f_{1,2}, \gamma = \frac{C_1}{C_2}, \quad (3.39)$$

$$V_w = -\frac{dz}{dx}, d_w = 1, g_{1,2} = \frac{G^0_{1,2}}{\alpha \cdot K_s}, m_{1,2} = \frac{M_{1,2}}{\alpha \cdot K_s}, d_{1,2} = \frac{D_{1,2} \alpha}{K_s} \quad (3.40)$$

The parameters q_v , e , v_w , and d_w characterizes the hydrological functioning of the ecosystem.

The two dimensionless functions e_1 and e_2 link the biological growth to the hydrologic regime whereas g_1 and g_2 represented the ratios between the characteristic timescale of soil moisture dynamics and that of biomass dynamics.

3.7 Evaluation of Land Use Land Cover Change in Rangeland and Cropland Ecosystems

3.7.1 Direct Expansion and Regression for Area Estimation

Grassland, sparsely scattered shrub-lands, rain-fed cropland, irrigated farmland, and varied forest covers (closed and open evergreen or deciduous, broad-leaved) were all estimated for both ecosystems, while in Naiveté cropland, mainly rain-fed and irrigated croplands were investigated. Cochran's (1977) stratified random sample method was used to the estimation of regions with varying land cover and use, yielding the following equation (3.41).

$$\hat{T} = \sum_{i=1}^h \hat{T}(i) \quad (3.41)$$

where, $\hat{T}(i) = D(i) \bar{y}(i)$, $\bar{y}(i) = \left[\frac{1}{n(i)} \right] \sum_{j=1}^{n(i)} y(i, j)$,

$$\hat{V}(\hat{T}) = \sum_{i=1}^h \hat{V}(\hat{T}(i)) = \sum_{i=1}^h D^2(i) \hat{V}(\bar{y}(i))$$

and $\hat{V}(\bar{y}(i)) = \left[1 - \frac{n(i)}{N(i)} \right] \left[\frac{1}{n(i)} \right] \left[\frac{1}{(n(i)-1)} \right] \times \sum_{j=1}^{n(i)} \left[y(i, j) - \bar{y}(i) \right]^2$ here, h , is number of

land use strata, \hat{T} , estimated total of land cover study zone, $\hat{T}(i)$ estimated total of study zone area for i^{th} stratum, $N(i)$, number of elementary area frame units in the i^{th} stratum, $n(i)$, number of segments sampled in the i^{th} stratum, $D(i)$, surface of the i^{th} stratum, $\bar{y}(i)$. The average proportion of land cover area per segment in i^{th} stratum, $y(i, j)$, proportion of cover area in the j^{th} sample in the i^{th} stratum as deduced from digitization, $\hat{V}(\hat{T})$, estimated

variance of $\bar{y}(i)$, $\hat{V}(T(i))$, estimated variance of the total for the i^{th} stratum and $\hat{V}(y(i))$, estimated variance of $\bar{y}(i)$. It was paramount to note that in the direct expansion method, only the information deduced from the digitization of the segments are used.

The regression estimators consist of the corrections to estimated average variable Y as a function of the results obtained from an auxiliary variable X . In this study, for a given vegetation or crop cover, for each segment in the sample, Y is the proportion occupied by the crop/vegetation as deduced from digitization of the ground survey and X was the proportion of pixels of the satellite image classified as being of the given crop/vegetation cover. A linear regression was fitted in each stratum between the two variables. The linear model and the entire satellite image classification were used for regression estimation. The formulas found in Cochran (1977) was used to estimate the total T using the following estimator,

$$\hat{T}_{reg} = \sum_{i=1}^h D(i) \bar{y}_{reg}(i), \text{ where, } \bar{y}_{reg}(i) = \bar{y}(i) + \hat{b}(i) \left[m_x(i) - \bar{x}(i) \right] \text{ and,} \quad (3.42)$$

$D(i)$, surface of the i^{th} stratum, $\bar{y}(i)$, the average proportion of land cover per segment in i^{th} stratum, $\hat{b}(i)$, the estimated regression coefficient for the i^{th} stratum when regressing proportion of ground reported cover on proportion of classified pixels for the $n(i)$ sample units in the i^{th} stratum,

$$\hat{b}(i) = \frac{\sum_{j=1}^{n(i)} \left[y(i, j) - \bar{y}(i) \right] \left[x(i, j) - \bar{x}(i) \right]}{\sum_{j=1}^{n(i)} \left[x(i, j) - \bar{x}(i) \right]^2} \quad (3.43)$$

$m_x(i)$, the proportion of pixels classified as specific cover in the i^{th} stratum,

$\bar{x}(i)$, the average proportion of pixels classified as specific cover per segment in the i^{th} stratum, $x(i, j)$, proportion of pixels classified as specific cover in the j^{th} sample unit in the i^{th} stratum, The estimate variance for the regression estimator is given as;

$$\hat{V}(\hat{T}_{reg}) = \sum_{i=1}^h D(i)^2 \hat{V}(\bar{y}_{reg}(i)) \text{ where, } \hat{V}(\bar{y}_{reg}(i)) = V(\bar{y}(i)) \left[1 - \hat{r}(i)^2 \right] \quad (3.44)$$

and $\hat{r}(i)^2$, sample coefficient of determination between the variables $y(i, j)$ and $x(i, j)$ in the i^{th} stratum,

$$\hat{r}(i)^2 = \frac{\left\{ \sum_{j=1}^{n(i)} [y(i, j) - \bar{y}(i)] [x(i, j) - \bar{x}(i)] \right\}^2}{\left\{ \sum_{j=1}^{n(i)} [y(i, j) - \bar{y}(i)]^2 \right\} \left\{ \sum_{j=1}^{n(i)} [x(i, j) - \bar{x}(i)]^2 \right\}} \quad (3.45)$$

Note that,

$$\hat{V}(T_{reg}) = \sum_{i=1}^h D(i)^2 \hat{V}(\bar{y}(i)) \left[1 - \hat{r}(i)^2 \right] = \sum_{i=1}^h \hat{V}(T(i)) \left[1 - \hat{r}(i)^2 \right] \text{ and so,}$$

$$\lim \hat{V}(T_{reg}) \rightarrow 0, \text{ as } \hat{r}(i)^2 \rightarrow 0 \quad (3.46)$$

If the coefficient of determination is large for most strata, it lowers the estimated variance for the regression estimator.

3.7.2 Relative Efficiency

Relative efficiency was computed, and accuracy with the regression estimator was measured. The ratio of the variances was used to characterize the RE of the regression estimate in comparison to the direct expansion estimator.

$$RE = \frac{\hat{V}(T)}{\hat{V}(T_{reg})} \quad (3.47)$$

An $RE = 2$ means that the same precision would have been obtained if the ground data sample size had been doubled and the satellite image had not been used.

3.7.3 Analysis of Land Use Land Cover Changes in Maasai Mara National Reserve Ecosystem

The next section details the steps taken to analyse LULC shifts, including the acquisition of MODIS-processed satellite images via the Copernicus training data and operational workflow, with a few tweaks made to account for variations in spatial resolution and the delivered land cover classes and their classification used to create land cover maps. The complete MMNR rangeland and the Naivasha agricultural region's Land Use/Land Cover information was extracted from MODIS photos. Satellite data has made it possible to monitor shifts in land use and land cover at a variety of spatial scales. Previously, ground surveys or aerial images could only be used to gather data from very small areas to determine land use/cover. Land cover change in bigger watersheds can now be evaluated over varying time scales thanks to satellite data, which has greatly increased the scope of ground observation and increased the frequency of observations (Al-doski *et al.*, 2013; DeFries & Eshleman,

2004). Copernicus, the European Commission's Earth Observation initiative, provided the photos for the Level 1 land cover products. In 2009, the European Union authorized the Earth Observing Satellite Mission, which is being cooperatively managed by the organization www.landcover.org. Time series data on decadal reflectance is used in Land Cover Classification, as is seasonal phenology data from the Crop Calendar. Another method for pinpointing irrigated regions involves using an index that accounts for both average seasonal rainfall and actual evaporation loss. A 2015 version of the worldwide CGLS-100m land cover map was used as the foundation for both levels 1 and 2, while the cropland class was further subdivided annually into irrigated, rain-fed, and fallow. The applied classification was based on the FAO-created Land Cover Classification System (LCCS). Co-created data subcomponent with the FRAME Consortium. The Level 2 (100m) products' foundational input layers (normalized difference vegetation index, aerosol optical thickness, and fractional aerosol photon extinction rate) came from the Proba-V satellite.

3.7.4 Moderate Resolution Imaging Spectro-Radiometer (MODIS)

Terra, the first Earth Observing System (EOS) satellite, was launched on December 18, 1999, carrying five remote sensors. By combining the ability to detect electromagnetic radiation across a wide spectrum range with continuous, all-day measurements at three spatial resolutions and a wide field of view, MODIS stands out as the most all-encompassing EOS sensor. This constant, all-encompassing coverage allows MODIS to complete an electromagnetic image of the world every two days. For example, while Landsat's Enhanced Thematic Mapper Plus displays the Earth in higher spatial depth, it only captures an area's image once every 16 days, which isn't often enough to catch many of the rapid biological and meteorological changes detected by MODIS. The MODIS instruments were developed to acquire information in wavelength ranges that were formerly reserved for satellite sensors.

MODIS adds to what we already know by combining data from older sensors like NOAA's Advanced Very High Resolution Radiometer. The Coastal Zone Color Scanner (CZCS) and Sea-viewing Wide Field of View Sensor (SeaWiFS) are used to monitor ocean biological activities; Landsat is used to monitor terrestrial conditions; and NOAA's High Resolution Infrared Radiation Sounder (HIRS) is used to monitor atmospheric conditions. Land cover maps show not only whether an area is vegetated, but also what type of vegetation is present, distinguishing between coniferous forests, deciduous forests, cropland, and grassland; these maps are a product of the on-going data collection that MODIS contributes to in order to understand both long-term and short-term change in the global environment. The maps not only classify MODIS's high-resolution images according to the

types of vegetation present, but also discriminate between other types of non-vegetated surfaces, such as bare soil, water, and urban land cover types. Scientists can also use daily data to track changes in land cover and land use, such as the conversion of grassland to farmland, the recovery of burned land, and the reforestation of previously forested areas.

3.7.5 On Level II (National and Sub-National Level - 100 m Ground Resolution)

While discriminating between the productivity of land and water for irrigated and rain-fed agriculture in a subset of countries and river basins, we track the growth of a number of important crops. The output per unit area of land is measured in kilograms per hectare, while the output per unit of water is measured in kilograms per cubic meter. Actual evapotranspiration is the unit of measure for the quantity of water expended in agricultural output; this metric distinguishes between natural (or "green") evapotranspiration and artificial (or "blue") evaporation. Following is a synopsis of the primary steps required to classify land cover.

- i) Selection of MODIS imagery
- ii) Pre-processing of MODIS imagery
- iii) MODIS imagery enhancement
- iv) Assessment of classification accuracy
- v) Composition of final land cover maps

3.7.6 MODIS Imagery Selection

Image statistics is usually most important for extracting land cover information, and choosing MODIS images can reduce pattern mistakes caused by things like crop phenology and sensor distortion. Images captured during the dry season (often between December and March) were prioritized for this study because to the clear contrast they provide between forested and undeveloped areas. Images with distinct changes over time were chosen, and this was spaced out over a period spanning 5-10 years to reflect vegetation and other features cropup/propup, but according to Campbell (2002), this was shown to lessen image pre-processing that always cause loss of information. Therefore, images from January 2010 to December 2019 were chosen. MODIS imagery (from the MODIS earth observation satellite sensor) was used in this procedure. The global website www.landcover.org is a great resource for learning about the primary essential design criteria of MODIS images and their subsequent implementation.

3.7.7 Data Pre-Processing

When examining numerous ten-day MODIS and PROBA-V NDVI images, it is immediately apparent that they are impacted by residual atmospheric disturbances during

periods and places of heavy cloud cover (Huete *et al.*, 2002). Consequently, the NDVI data set was corrected using the algorithm proposed by White *et al.* (1997), with some tweaks to take into consideration the modern data. This technique was designed on the hypothesis that cloud influences cause sudden drops in NDVI followed by relatively rapid recoveries (within two to three 10-day intervals). Eliminating these drops would need some sort of temporal moving-average operation. Benedetti *et al.* (1994) state that 23 NDVI photos from 2001 were created using this method and all of them shared a great deal of information with one another. This information was summarised using a principal component (PC) analysis, which yielded a small set of PC images. The CORINE land-cover map was then pre-processed by removing the forest class. The original vector file was rasterised at a resolution of 50 m, which created a forest/non-forest mask for the whole region. According to Maselli (2001), a forest-fraction (or abundance) image was created by superimposing 250-meter-resolution MODIS data with a mask created by spatially contracting the mask using pixel aggregation.

3.7.8 MODIS Imagery Enhancement

The most useable technique in image enhancement involves the principal component analysis (PCA) used to improve the interpretability of MODIS images before it's applied in actual land use land cover classification. It is meant to reduce the number of bands for the creation of new ones accounting to variance of image pixel dataset. This was used to assist in features extraction, studying and sorting unique areas and objects seen on the ground and relating the same information to the classified image through matching. For example, cases such as the emergence of small-scale agriculture, agro-forestry, and managed grass in a small parcel of land. Here, differentiating mixed types of land cover was done through improved selection of Landsat images that felt in the dry season and use of enhancement techniques. In this study, PCA was applied to compress redundant data in just a few bands. This results into new images with the same bands as the original images and with reduced data dimensions. The quality of new images in terms of interpretability was highly improved due to the following corresponding components such as brightness, greenness, and wetness. The difference accounted between the classified images and pre-processing of multi-date images in PCA are made less tedious according to Collins and Woodcock (1996). The PCA output files with digital numbers (DN) range (0-255) in ERDAS IMAGINE are displayed through stretching process to unsigned 8-bit window, which makes it easy to analyse. According to Collins and Woodcock, the multi-date PCA can be efficient and effective representation of the weak tie to the interpretation of the results. A MODIS image has pixels each with 256 DN that indicates the capacity of electromagnetic energy reflected from the earth surface their 7

bands. Filtering functions were replaced by the central pixel value in window with the major filtering employed using neighbourhood function to analyse pixels in relation to others in their neighbourhood. A kernel size window, which may affect the interpretation of the images and here size of 3x3 was found suitable for filtering images of 2000 and 2015 and 5x5 as appropriate for MODIS images of 2019. The role of filtering removes “salt and pepper” redundancies in land cover types and general appearances by smoothing effect of the class edges.

3.7.9 Accuracy Assessment of Classification

During the process of MODIS imagery classification, matrix errors mostly occur from the selection of training data. It was therefore needful to conduct an accuracy assessment on the derived land cover maps. This indicates the validity of the produced land cover maps because the classified maps and the ground truth are accounted for simultaneously. Baldyga (2005) shown that accuracy assessment of a given region, future efforts of information were directed towards quantifying the dynamics of land cover. According to Congalton (1991), the most commonly techniques used accuracy assessment of land cover classification for remotely sensed images in inter-rater reliability of error matrix (called confusion matrix, contingency tables, covariance matrix, or correlation matrix). The design of error matrix entails the comparison of classified data from land cover maps and the reference data (ground truth). The derived MODIS imagery provided two options of comparison between the generated reference data using points generated randomly and the use of ground truth data taken from the field. The choice of MODIS image of 2000 was used to test the classification accuracy because the other options of EMT+ 2000 was far too old for comparison of the current reference data obtained. The table indicates the statistical techniques used to calculate the accuracy assessment of error matrix classes or components. The output of the correctly classified images is an accurate thematic map. Foody (2002) stated that there are several equations that can be used to calculate the level of error statistically including producer accuracy, user accuracy, overall accuracy and Kappa index. A standard error matrix was used to assess the accuracy of the two classifications (rangeland and cropland) using collected ground-truth data. Kappa statistics and overall accuracy were used to determine the performance of the selected methods of heterogeneous region (Table 3.1).

Table 3.1: Design of Confusion/Error Matrix applied in accuracy assessment of land cover classification

		Classified Data						
Reference data		Class	A	B	C	n	Row Total
Reference data	A		$N_{1,1}$	$N_{1,2}$	$N_{1,3}$	$N_{1,n}$	N_{1+}
	B		$N_{2,1}$	$N_{2,2}$	$N_{2,3}$	$N_{2,n}$	N_{2+}
	C		$N_{3,1}$	$N_{3,2}$	$N_{3,3}$	$N_{3,n}$	N_{3+}

	n		$N_{n,1}$	$N_{n,2}$	$N_{n,3}$	$N_{n,n}$	N_{n+}
	Column Total		N_{+1}	N_{+2}	N_{+3}	N_{+n}	N_{OA}

In reference to the description of Congalton (1991) and Jansen (1996), of error matrix components the accuracy assessments of the land cover classification were explained as follows;

- i). Rows – The ground truth map corresponds to these thematic groupings (training set)
- ii). Columns – The images have been categorised according to these broad categories.
- iii). Diagonal Values – These are the proportion of instances where a given class label was correctly assigned to a pixel (the proportion of ground-truth instances labelled with a given class name that were classified as belonging to that class).
- iv). Off-diagonal values – represents the number of pixels from the ground truth that were incorrectly assigned a class during the classification process.
- v). Commission Error (or inclusion) – This is a representation of the other classes' ground truth pixels that were incorporated into a given categorization (off-diagonal column elements).
- vi). Omission Error (exclusion) – Pixels from the ground truth belonging to a specific class that were incorrectly assigned to another class during classification are indicated below (off-diagonal rows elements).
- vii). Producer's accuracy - This is the proportion of ground-truth-class pixels that were correctly classified. Here, the accuracy was determined by dividing the number of correctly categorized pixels by the total number of ground truth or test pixels of that class, one by one, across each row of ground truth data.

$$ACC = \frac{N_{1,1}}{N_{1+}} * 100\% \quad (3.48)$$

where, ACC is the producer's accuracy, $N_{1,1}$ is the total number of the correctly classified pixels in that class and N_{1+} is the total number of ground truth pixels of that class (summation of the pixels in that row).

viii). User's accuracy (inter-rater reliability) - This reflected the proportion of correctly labelled pixels relative to all labelled pixels in the categorized image. A confidence interval was calculated for each column of classified images by dividing the number of correctly categorized pixels by the total number of classified pixels in that class.

$$Rel = \frac{N_{1,1}}{N_{+1}} * 100\% \quad (3.49)$$

where, Rel is user's accuracy(reliability), $N_{1,1}$ is the total number of the pixels classified in that category and N_{+1} is the total number of pixels that were classified as this category or class (summation of the pixels in that column).

ix). Overall accuracy – It is a tally of how well the classified data matches up with the data in the training set. The major diagonal components are included, but the errors of commission and omission are left out. A common expression is as follows.

$$OA = \frac{D}{N} * 100\% \quad (3.50)$$

where, OA is the overall accuracy, D is the total number of correctly classified pixels (diagonals values i.e. $N_{1,1} + N_{2,2} + N_{3,3} + \dots + N_{n,n}$ and N_{OA} is the total number of the set (reference) pixels.

x). Overall kappa statistic – This is the KAPPA-derived measure of agreement or precision. Its primary application is in comparing the classified data to the reference data (ground truth data) to find statistically significant differences. This idea can be stated as;

$$\hat{K} = \frac{N_{OA} \sum_{i=1}^n N_{i,i} - \sum_{n=1}^n N_{i+} * N_{+i}}{N_{OA}^2 - \sum_{i=1}^n (N_{i+} * N_{+i})} \quad (3.51)$$

where, \hat{K} is the overall Kappa statistic coefficient, n is the number of rows in the error matrix, $N_{i,i}$ represents the total number of correct pixels in a class (value in row i and column i), N_{i+} is the total number of rows i , N_{+i} is columns total i and N_{OA} is the

total number of the pixels in error matrix. The values greater than 0.7 indicates that the inter-rater reliability of classified and ground data were satisfactory. On the other hand, values less than 0.4 means fair agreement while 0.6 to 0.8 indicates substantial agreement. A typical guidance used was as shown on the table 3.2:

Table 3.2: Quantification of Cohen's Kappa coefficient as measure of agreement

Kappa Value	Interpretation
< 0	Less than chance agreement
0 to 0.2	Slight agreement
0.2 to 0.4	Fair agreement
0.4 to 0.6	Moderate agreement
0.6 to 0.8	Substantial agreement
0.8 to 1.0	Almost perfect agreement

Source: (Cohen, 1960)

x) Conditional Kappa statistics – This represents the measure of agreement or rather accuracy based on KAPPA analysis based on each class category. It is normally expressed as;

$$\hat{K}_i = \frac{N_{OA}(N_{i,i}) - (N_{i+} * N_{+i})}{N_{OA}(N_{i+} * N_{+i})} \quad (3.52)$$

where, \hat{K}_i is the conditional Kappa statistics for individual class category and the other symbols are defined as in earlier expressions.

3.7.10 Evaluation of Model Performance

In the study, the following indicators were used to evaluate the models; Nash-Sutcliffe Efficiency (*NSE*), Pearson product moment correlation coefficient (*r*), Root Mean Square Error (*RMSE*) and Coefficient of determination (*R*²).

i) The Nash-Sutcliffe efficiency (NSE) is a normalized statistic used to estimate the relative amount of the residual variance ("noise") in relation to the measured data variance ("information") (Nash & Sutcliffe, 1970). The normalized residual error (NSE) showed how well the 1:1 line fitted the plot of observed versus simulated data. The following equation was used to determine NSE, which is the most widely used and critically significant performance measure in hydrology.

$$NSE = 1 - \left[\frac{\sum_{i=1}^n (y_i^{obs} - x_i^{sim})^2}{\sum_{i=1}^n (y_i^{obs} - y^{obs\ mean})^2} \right] \quad (3.53)$$

where, y_i^{obs} is the i^{th} observation for the constituent being evaluated, x_i^{sim} is the i^{th} simulated value for the evaluated constituent, y^{obs}_{mean} is the mean of observed data for the constituent being evaluated, and n is the total number of observations. Applying this formula to raw data from any model yields the same result as using the square of the linear regression. NSE may be negative for non-linear models. The ideal value of NSE is 1, yet it can be found in the range of $-\infty$ to 1.0 (1 inclusive). In general, scores between 0.0 to 1.0 are considered satisfactory, whereas scores below 0.0 indicate poor performance due to the mean observed value being a better predictor than the simulated value.

ii) The Pearson product-moment correlation coefficient, often known as Pearson's r , Pearson's r -squared, or the PPMCC, is a measure of the linear correlation (dependency) between two variables x and y , with values ranging from +1 to -1, where 1 denotes a perfect positive correlation, 0 denotes no correlation, and -1 indicates a perfect negative correlation. In the sciences, it is commonly used to assess the closeness of the relationship between two variables. A linear link between two variables can be measured with the use of the Pearson product moment correlation coefficient, which is defined as

$$r = \frac{\sum_{i=1}^n ((x_i - \bar{x})(y_i - \bar{y}))}{\sqrt{\sum_{i=1}^n (x_i - \bar{x})^2 \sum_{i=1}^n (y_i - \bar{y})^2}} \quad (3.54)$$

where, $\bar{y} = \frac{\sum_{i=1}^n y_i}{n}$ and $\bar{x} = \frac{\sum_{i=1}^n x_i}{n}$; where, y_i denotes the measured value, x_i refers to the predicted value. The Pearson's production-moment correlation coefficient measures how strongly two variables are associated linearly. For numerical data on an interval or ratio scale when each variable follows a normal distribution, the r coefficient of correlation is used.

iii) The RMSE represents a measure of the overall or mean deviation between observed (y_i) and simulated (x_i) values. Since the RMSE has the same unit as the simulated variable, the closer the value is to zero, the better the model's ability to simulate that variable. To obtain the same unit order, the square root of Mean Squared Error (MSE) is taken multiple times. The term for this error is Root Mean Squared Error. For each prediction, the agreement between the predicted moisture content $\theta_i(p)$ and measured moisture content $\theta_i(m)$ are expressed in terms of the root mean square errors (RMSEs), given by

$$RMSE = \sqrt{\frac{1}{n} \sum_{i=1}^n (y_i - x_i)^2} \quad (3.55)$$

iv) Mean Square Error (MSE) or mean squared deviation measures the average of the squares of the errors, the average squared difference between the estimated and actual value. MSE is a risk function that corresponds to the expected squared error loss value. MSE unit order is always higher than the error unit as the error is squared. $RMSE = \text{SQRT}(MSE)$

$$MSE = \frac{1}{n} \sum_{i=1}^n \left(Y_i - \hat{Y}_i \right)^2 \quad (3.56)$$

where,

MSE = Mean squared error

n = number of data points

Y_i = Observed values

\hat{Y}_i = Predicted values

v) The coefficient of determination-squared (R^2) is a statistic that explains the amount of variance accounted for in the relationship between two (or more) variables. It is the fraction of the total variance in the dependent variable that can be explained by changes in the independent variable as indicated by the regression equation (s). When R^2 equals 1, it can be concluded that the fitted regression equation fully describes the distribution of the dependent variable's values in the data set. Conversely, if R^2 equals 0, it means that no variance is explained by the regression equation.

$$R^2 = 1 - \frac{\sum_{i=1}^n \left(y_i - x_i \right)^2}{\sum_{i=1}^n \left(y_i - \bar{y} \right)^2} \quad (3.57)$$

where, y_i denotes the measured value, x_i refers to the predicted value, \bar{y} represents the average of the measured values of y .

3.7.11 Sensitivity Analysis

One-at-a-time (OAT) parameter variations were used to conduct the local sensitivity analysis of soil-related factors for the soil moisture simulation model. A dimensionless sensitivity index was used to indicate the degree to which model results varied in response to shifts in input parameters. The base value was changed by $\pm \Delta x$ with $\Delta 1 = x_0 - \Delta x$ and $x_2 = x_0 + \Delta x$. The mathematical model output resulting from the implementation of these values are y_1 and y_2 . The sensitivity index was computed as follows:

$$I' = \frac{y_2 - y_1}{2\Delta x} \quad (3.58)$$

This index I' should be normalised to be dimensionless

$$I = \frac{(y_2 - y_1)/y_0}{2\Delta x/x_0} \quad (3.59)$$

The sensitivity of the model output to each tested input parameter was ranked in accordance with Table 3.3, as indicated by Lenhart *et al.* (2002), with the sensitivity index being averaged across the whole simulation period. To conduct the sensitivity analysis, we utilized SimLab 2.2, the latest version of the program given in (Giglioli *et al.*, 2000). (SA). SimLab 2.2 includes a pre-processor module that lets the user select from multiple combined parameter generation methods, a model execution module that lets the user run an internal or external model with the parameter combination, and a post-processor module that executes uncertainty and sensitivity analysis.

Table 3.3. Sensitivity Index Classes

Class	Index	Sensitivity
I	$0.00 \leq I < 0.05$	Small to negligible
II	$0.05 \leq I < 0.2$	Medium
III	$0.2 \leq I < 1.00$	High
IV	$ I \geq 1.00$	Very high

3.8 Data Analysis

Soil water storage and retention capacities as it changed monthly rainfall and water consumption with yearly biomass production of vegetation were analysed statistically using MINITAB 18.0 (Khan, 2013). Confidence interval, simple regression, quality control and APSIM and HYDRUS-1D were used as general linear models to simulate and compute the trend of biomass production and soil moisture variability which explained the difference in growth and development of vegetation biomass in the natural grassland and cropland ecosystems with varying soil moisture and soil properties as influenced by climate variables. Satellite images of normalized difference vegetation index were derived via PROBA-V and MODIS to analyse land use and land cover changes in rangeland and cropland ecosystems. The results of the study were presented in form of written text, tables, figures, plates, charts and graphs.

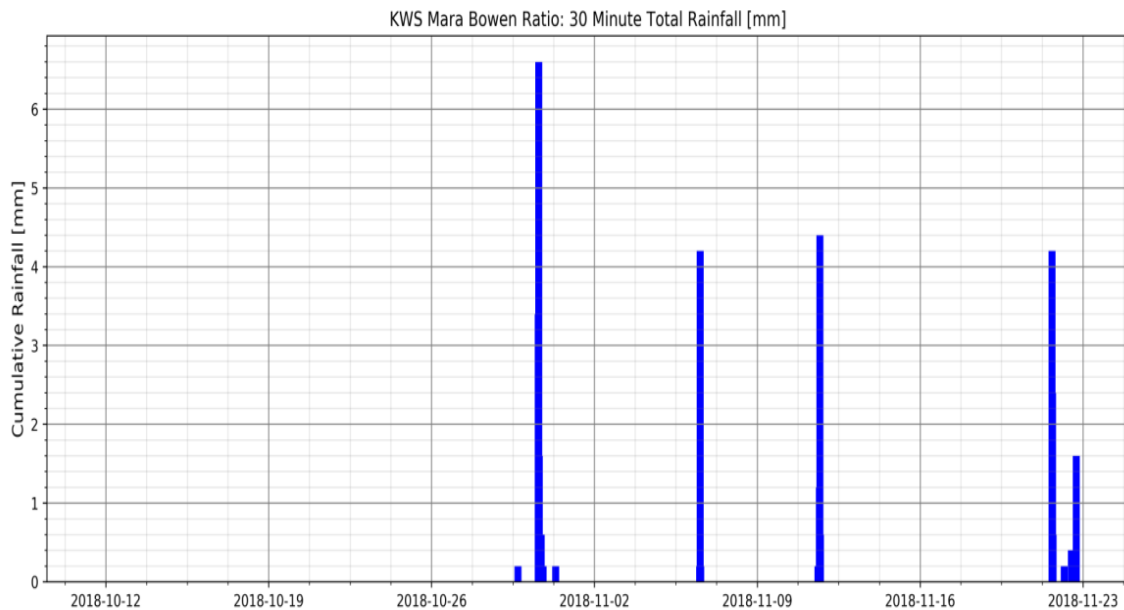
CHAPTER FOUR

RESULTS AND DISCUSSION

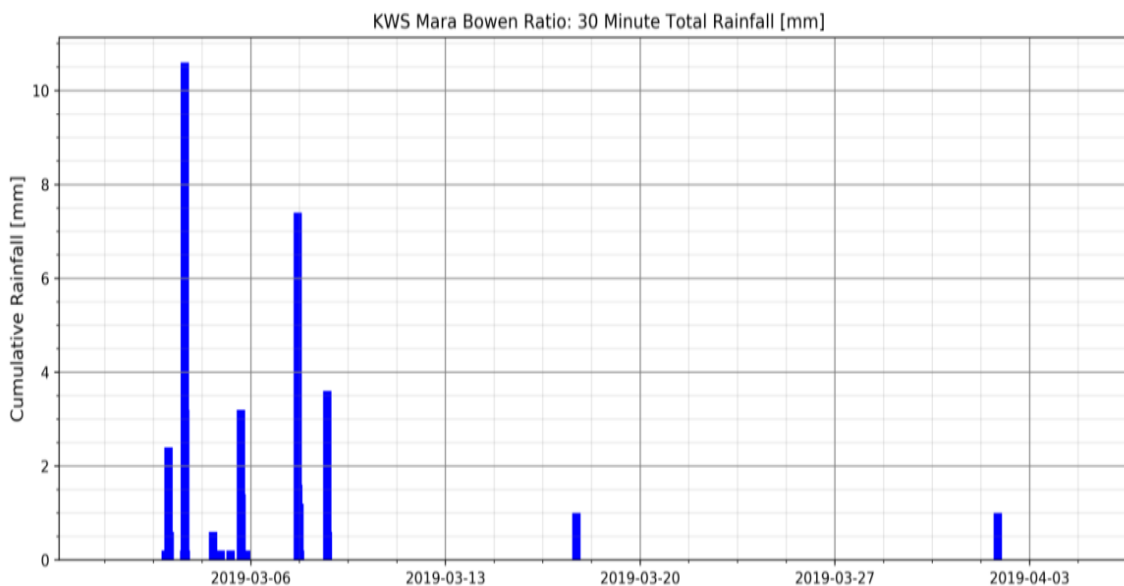
This chapter presents the results and discussion of each objective and the outcome highlighted and presented in tables, graphs, charts and written text in the subsequent order.

4.1 Determination of Spatio-Temporal Soil Moisture Storage and Retention Capacities in Maasai Mara Rangeland Ecosystem

4.1.1 Rainfall Characteristics



(a)



(b)

Figure 4.1: 30 minutes' rainfall patterns in Mara rangeland ecosystem for the period of (a) Oct - Nov 2018 and (b) March - April 2019

Rainfall events in most parts of MMNR were quite erratic as a phenomenon of semi-arid regions with extreme rainfall occurring as high at some period in a season. As observed from figure 4.1, there was heavy rainfall of 6.6mm experienced in late October with slight drop towards the end of November and little rainfall close within the period. The rainfall shows spatial distribution with inconsistency of high, medium to low rainfall phenomenon. During the season, rainfall ranged from as low as 0.2mm to as high as 6.6mm in 30min cumulative rainfall. The temporal resolution of 30 minutes' rainfall, which could be averaged on daily time step, indicates intermittent behaviour of rainfall pattern experienced in semi-arid rangelands ecosystem depicted by MMNR. During the period of March to April 2019, high intensity of 10.5mm rainfall was received with continuous rains within the same week followed by erratic rainfall. This area received a 30-minute rainfall from low to high that ranged between 0.4mm and 10.2mm in the wet season. The rangeland ecosystem due to seasonality was characterised by increased soil moisture content during the rainy periods and a decline in dry season caused by low rainfall levels; however, precipitation here is one main climatic factor that determines the soil moisture and surface water levels in the ecosystem.

4.1.2 Air Temperature and Humidity

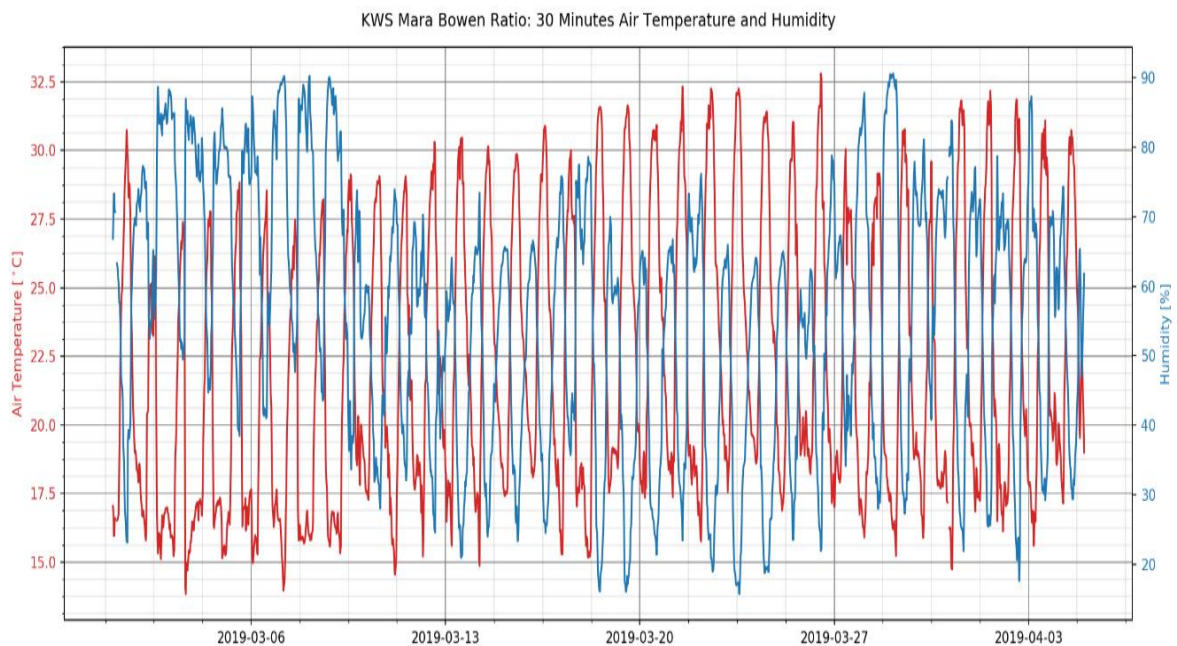


Figure 4.2: 30 minutes' variation of air temperature (red) in relation to relative humidity (blue) in Mara Ecosystem for the period of March – April 2019

Figure 4.2 shows the relationship between temperature and humidity with respect to evaporation in 2019. The conditions were quite typical in that the mean daily temperatures oscillated between 14°C and 32.8°C. In dry season, there was gradual increase in air

temperature especially in the days with average daily temperature above 30°C, which were recorded at the station towards the end of March 2019. During the last week of March, the season had the highest temperatures. Similarly, some periods in early March had gradual increase in air temperature to a maximum not exceeding 30°C while the humidity conditions significantly decreased since high air temperatures affects evaporation rates. The percentage humidity during the period also oscillated between 16% and 91%. It was observed that towards the end of February 2019, there was high humid period above 80% that gradually decreased until the end of March when it increased subsequently under decreased air temperature and the vice-versa.

4.1.3 Vapour Pressure Deficit

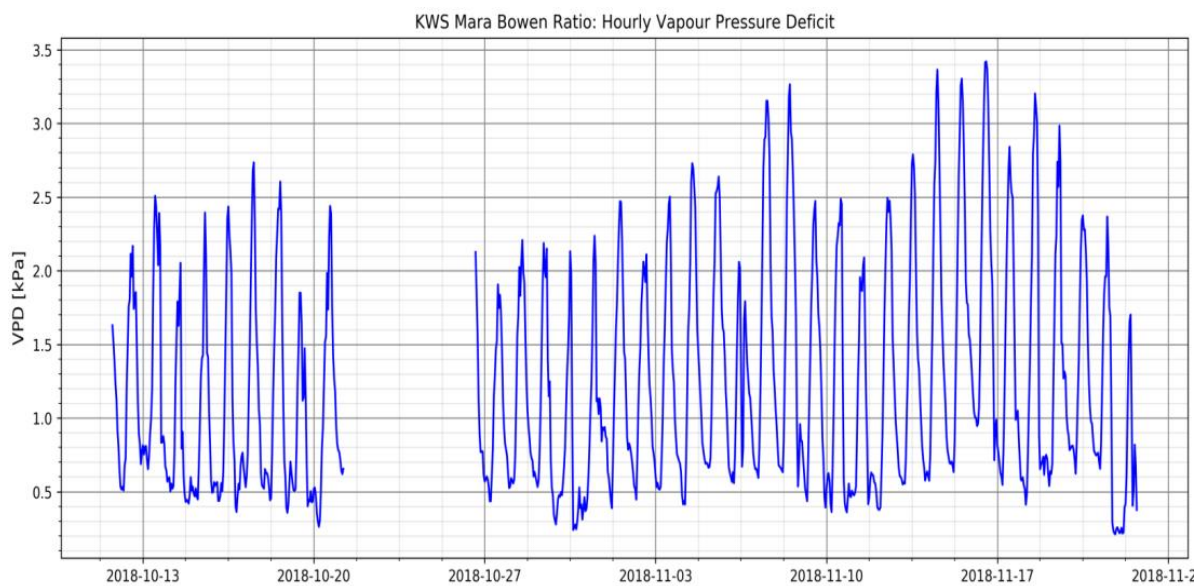


Figure 4.3: Hourly behaviour of vapour pressure deficit as observed in Maasai Mara rangeland ecosystem for the period of Oct – Nov 2018

In the period under analysis, vapour pressure deficit (VPD) oscillated from as low as 0.3 kPa to as high 3.4 kPa, in the annual pattern of VPD in 2018, during the mid-month of October vapour pressure deficit varied below 0.5kPa to a maximum of 2.7 kPa. During the same period on early week of November there was a gradually increase of 3.3kPa and slight drop before it gradually increased (figure 4.3). The intermittent behaviour and gradual drop of VPD towards the last week of November was characterised by conditions similar to those of saturated air with water vapour. The gap experienced between 20/10/2018 and 27/10/2018 vapour pressure deficit indicates extremely very low humidity attributed by high temperature or failure of instrument taking the signals however, the missing data could be interpolated. During the same week in mid-November 2018, an occurrence of very high vapour pressure

deficit was experienced. The hourly data was cumulated into daily time step for ease of graphical presentation.

4.1.4 Wind Speed

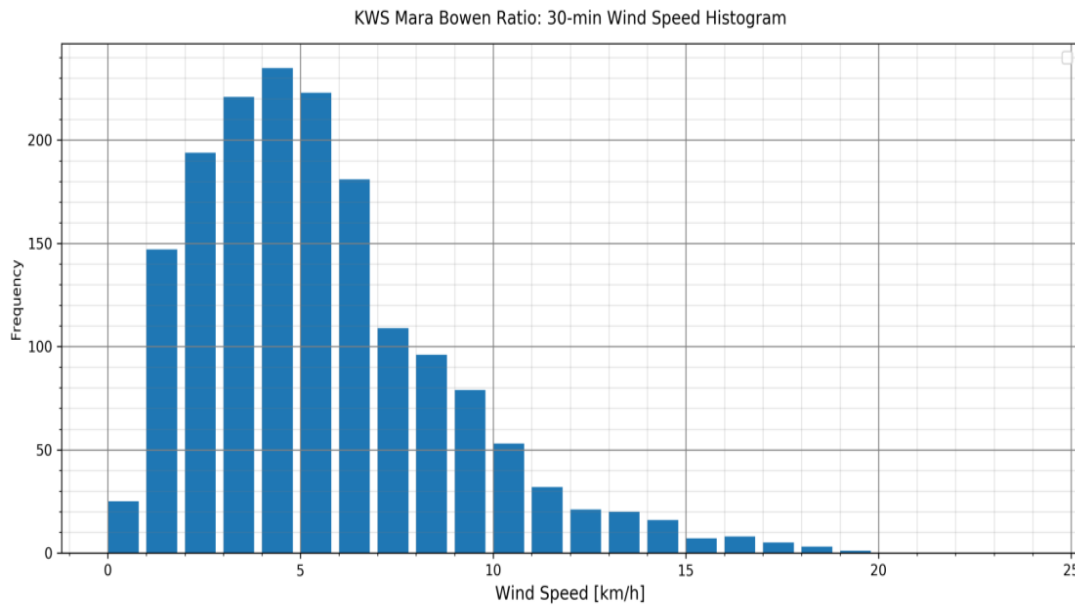


Figure 4.4: General trend of wind speed in Mara rangeland ecosystem as observed by Bowen’s Ratio system.

Generally, the wind velocity frequency was high at fivekmh⁻¹ with above 200 hz in a 30 mins wind speed measured via a Bowen’s Ratio system and declines gradual with as low frequency at 19 kmh⁻¹ during most of the periods in this region. During the period the rate of evaporation was highly influenced by wind velocity, it was observed that with daily average wind velocity of five kmh⁻¹ high wind speeds mainly prevailed and this was experienced during the normal annual dry seasons (Figure 4.4). The daily average wind velocity oscillated around fourkmh⁻¹ and the maximum rarely exceeded 19kmh⁻¹ though the highest frequency runs for several days at the minimum wind speeds of less than five kmh⁻¹. The general trend for the wind frequency and strength of Mara between the 9th to 13th week in 2019 had constant wind frequency and strength experienced probably because of the dynamics of weather pattern which indicates the consistency of climate parameters that influenced the vegetation’s environment in the ecosystem as characterised in table 4.1 and 4.2.

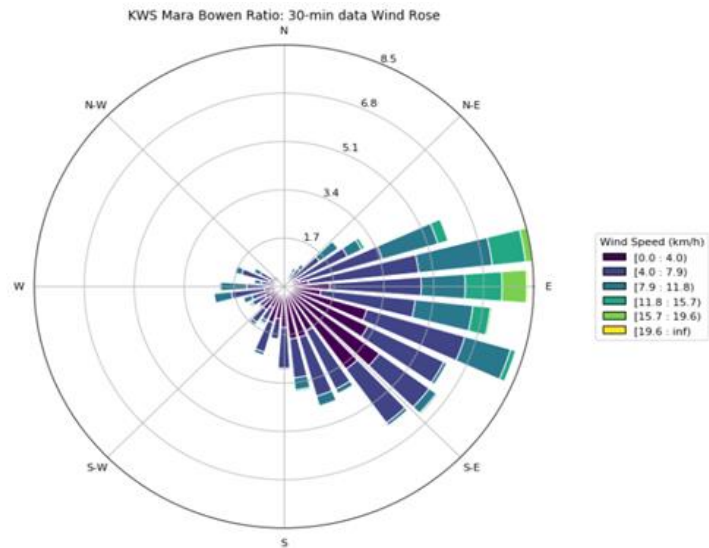


Figure 4.5: General 30 minutes' wind rose behaviour in Mara rangeland ecosystem as observed by Bowen's Ratio System

Figure 4.6 shows the strength and wind speed within Maasai Mara ecosystem mainly range between 4.0 to 7.9 km/hr and at some point wind moves at high speed of a maximum of between 15.7 to 19.6km/hr of which in most cases the wind blows from North West (NW) direction to the East (E) and to the South-East (SE). The measurements are taken using Bowen's Ratio system on hourly basis however; this could be averaged into daily basis dataset.

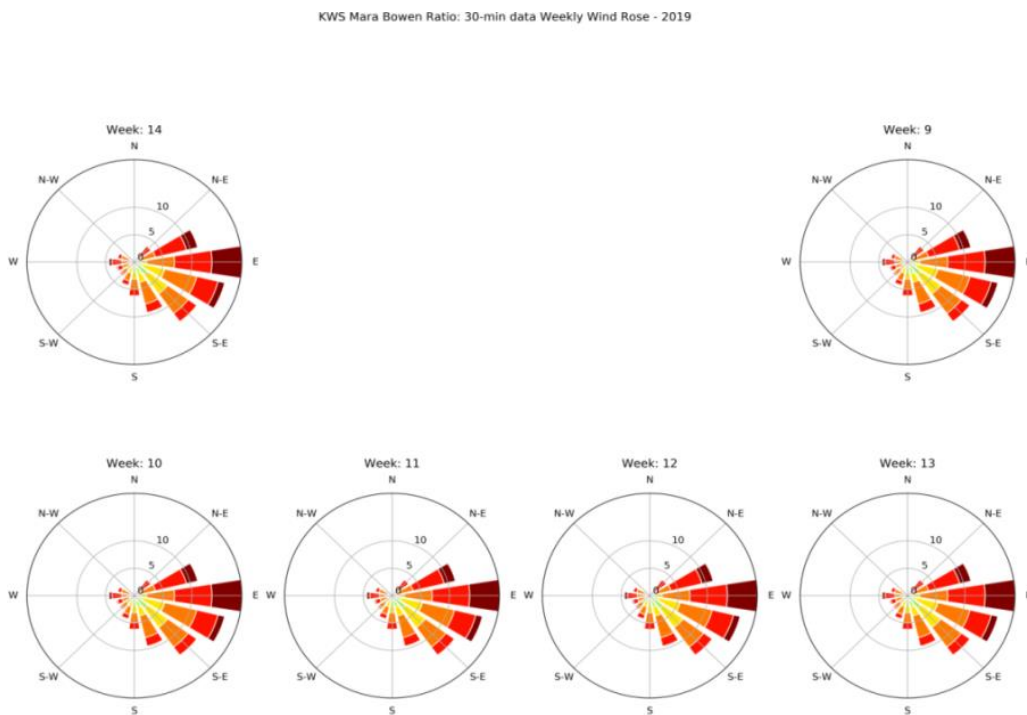


Figure 4.6: General weekly 30 minutes' wind rose pattern as observed by Bowen's ratio system for the period of March 2019

Table 4.1: Spatially distributed soil moisture, soil temperature and soil sampling stations

Station ID	Coordinates		Slopes	Date installed	Installation time	Decagon logger-1D	20m radius	5TM-ECH ₂ O Profile depths
	Latitudes	Longitudes						
Mara Main	-1.49332	35.14918	Upper-Plateau	27-7-2017	1040	5G106354	Grassland	5,10,20,40,80
Kissinger	-1.55889	35.23664	Upper-Plateau	30-12-2017	1540	EM37042	Grassland	5,10,20,40,80
Ashnil	-1.45291	35.07215	Upper-Plateau	30-12-2017	1100	5G106351	Isolated shrubs	5,10,20,40,80
Mara-Bridge	-1.53833	35.03615	Upper-Plateau	25-12-2017	1700	5G106361	Grassland	5,10,20,40,80
Helicopter	-1.53042	35.17422	Lower slope	25-6-2018	1330	EM27041	Grassland	5,10,20,40,80
Olimisigioi	-1.50384	35.12008	Mid-slope	22-6-2018	1750	EM37044	Grassland	5,10,20,40,80
Talek	-1.46117	35.18276	Mid- slope	27-6-2018	1035	5G0D2637	Shrubs, Grassland	5,10,20,40,80
Upstream	-1.52919	35.23824	Mid-slope	28-6-2018	1320	EM42521	Grassland	5,10,20,40,80
V-section	-1.46249	35.10616	Mid-slope	25-6-2018	1100	5G106363	Grassland	5,10,20,40,80
Nice - Bridge	-1.49519	35.19034	Lower slope	24-6-2018	1700	5G0D2640	Grassland	5,10,20,40,80

Table 4.2: 5TM-ECH₂O sensors measurement detail including site name, geographic location, elevation vegetation cover/land use, aboveground biomass, and textural class

Site	Lat/Long	Elevation (m)	Vegetation Cover/Land Use	Wet season AGB (kgm ⁻²)	Dry Season AGB(kgm ⁻²)	Mara Rangeland Textural Class
Mara main	-1.49332/35.14920	1540	Open grassland/grazing	0.409	0.328	SCL
Kissinger	-1.55889/35.23664	1660	Open grassland/grazing	0.589	0.366	SCL
Ashnil	-1.45291/35.07215	1540	Trees/sparse shrubs/grazing	0.437	0.371	SC
Mara Bridge	-1.53833/35.03615	1600	Open grassland/grazing	0.308	0.264	SCL
Helicopter	-1.53042/35.17422	1540	Open grassland/grazing	0.413	0.389	SCL
Olimisiogioi	-1.50384/35.12008	1520	Mixed grassland and shrubs/grazing	0.397	0.365	SC
Talek	-1.46117/35.18276	1540	Mixed grassland and shrubs/grazing	0.412	0.357	SCL
Upstream	-1.52919/35.23824	1600	Open grassland/grazing	0.423	0.354	SC
V-section	-1.46249/35.10616	1520	Open grassland/grazing	0.411	0.355	SCL
Nice Bridge	-1.49519/35.19034	1540	Open grassland/grazing	0.414	0.366	SCL

Tables 4.1 and 4.2 shows the geographical location of 5TM-ECH₂O probes distributed across rangeland. The ecosystem is occupied by mainly dominant grass vegetation and distributed sparse shrubs; the soil texture on the top 5cm depth layer was mainly homogeneous sandy clay soil because 30% of the sites texture was sandy clay (SC) while 70% is made of sandy clay loam (SCL) at the bottom soil layer.

The mean particle fraction observed across the rangeland was distributed as 67% sand, 25.3% clay and 7.7% silt. The 5TM-ECH₂O probe sites were distributed to represent the distribution of soil moisture over the natural grassland entirely occupying approximately 70% grass cover and about 20% shrubs, 10% tall trees along the streams of Mara and Talek river catchment. The effective rooting depth for the Mara grassland was between 0.3 and 0.45m due to compacted layer, which was observed mainly at around 0.45m depth and this was due to decreased total organic matter concentration from the surface layer.

4.2 Spatial Physical and Chemical Properties Soil Sampling Campaign

This section shows the result of soil samples excavated from ten 5TM-ECH₂O soil moisture stations and laboratory analysis to determine; their soil texture, total organic carbon (TOC), soil organic matter, particle density, and bulk density, which were subsequently used to calculate gravimetric water content. The laboratory analysis performed was meant for the calibration of the CRNS and subsequent determination of soil moisture storage capacity. Volumetric water content was spatially determined from different spatial moisture and concentrically distributed 5TM-ECH₂O probe stations with varied profile depths as indicated in tables 4.10 to 4.13.

4.2.1 Soil Texture

Table 4.2 shows a range of soil types of MMNR rangeland ecosystem and it was observed that almost homogeneous sandy clay loam (SCL) in locations and profiles dominant with 62% (SCL) and should add up to 38% distributed as 28% (SC), 8% (SL), 2% (C) and appears different as depth increases from the top soil surface to the bottom level. The soil type at the top 2.5cm with distance of 10m away from the centre of the cosmic ray neutron sensor are sandy loam (SL) attributed to high organic content with the mean particles size distribution 76.6% sand, 16.3% clay and 7% silt. This was tested within six sample locations concentrically distributed at angles of 60 degrees as A60, A120, A180, A240, A300 and A360, 0. Classifications for the unconsolidated parent material were made according to USDA texture classes, with coarse (S, LS, SL or approximately sand > 50% and clay 20%), medium (L, SCL, CL, Si, SiL, SiCL), and fine (SC, SiC, C or approximately clay > 40%) textures being used. The spatially distributed distance from the centre of the cosmic ray neutron sensor were at intervals of 10m, 25m, 50m, 75m, 150m and 175m. The soil type at 25m distance from the CRNS at the profile depth of 12.5cm were made of sandy clay loam (SCL) with mean particles size distribution percent of 67% sand, 25.3% clay and 7.7% silt (Appendix B.3). Soil samples were also collected from 10 spatially distributed soil moisture, soil temperature stations with varying depths profile ranging from 10cm to 80cm depth. Soil

type at the Mara main station were sandy clay loam (SCL) within the top soil depth range of 0-10cm while below 10cm and between 10-80cm depth, the soil is sandy clay with mean particle size distribution of 71% sand, 22% clay and 7% silt and 55% sand, 39% clay and 7% silt respectively.

Table 4.3: Spatially distributed soil textural classes varied with depths across the Maasai Mara National Reserve rangeland ecosystem

Key: SC – Sandy Clay, SCL – Sandy Clay Loam, SL – Sandy Loam, C- Clay

S. No.	Station	Soil Depth (cm)	0-5	5-10	15-20	35-40	75-80
1.	Mara Main	Soil Texture	SCL	SCL	SC	SC	SC
2.	Kissinger	„	SCL	SCL	SCL	SCL	SCL
3.	Ashnil	„	SCL	SL	SCL	SCL	SCL
4.	Mara Bridge	„	SCL	SL	SCL	SCL	SCL
5.	Helicopter	„	SL	SL	SCL	SCL	SCL
6.	Olimisiogioi	„	SCL	SCL	C	SCL	SC
7.	Talek	„	SCL	SCL	SC	SC	SC
8.	Upstream	„	SCL	SC	SC	SC	SC
9.	V-section	„	SCL	SCL	SC	SC	SC
10.	Nice-Bridge	„	SCL	SCL	SCL	SCL	SCL

The area like Olimisiogioi has varied soil layers from top 0-10cm with sandy clay loam, clay soil at 20cm, sandy clay loam at 40cm while at 80cm the soils are sandy clay. The soil texture of most of the soil moisture, temperature stations namely, V-section, Nice Bridge, Talek, Helicopter, Olimisiogioi, Upstream, Kissinger, Ashnil and Mara Bridge are made of sandy clay loam for the first layer 0-10cm depth. The layers below from 20-80cm have variable soil types with mainly sandy clay except nice bridge with uniform sandy clay loam from top to bottom layer. The results of soil texture grade indicate that in this natural grassland vegetated ecosystem, the soil surface layers across the catchment are mainly sandy clay loam with dominant grass species for suitable for grazing wildlife over many decades.

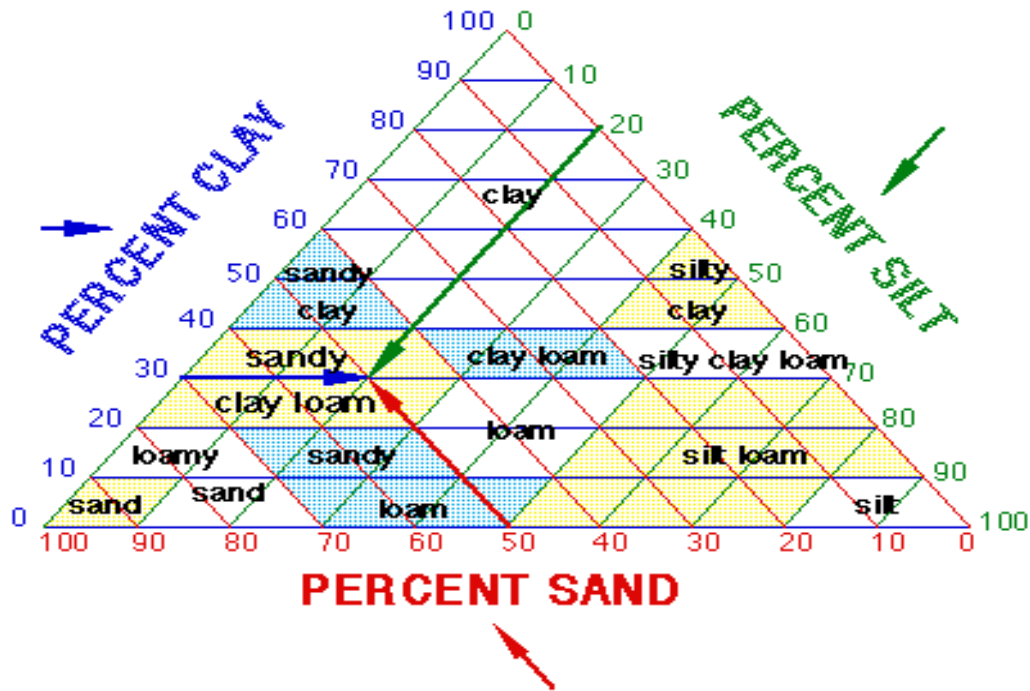


Figure 4.7: Soil texture classification (Saxton, 2006)

The mean particle size distribution ranged between 60-77% sand, 20-27% clay and 6-15% silt for the top layer depth range of 0-10cm while for sub soil layers below 10cm to 80cm most soils are sandy clay with mean particle size distribution ranging from 54-68% sand, 22-38% clay, and 6-10% silt soil. Aliku *et al.* (2016) conducted a study in Nigeria and found that the clay and sand contents of Savannah and Derived savannah soils increased with depth, while those of rainforest soils decreased and increased, respectively, with depth. The clay concentration varied from 6.75 to 14.9 percent in Savannah, 19.07 to 35.35 percent in derived savannah, and 26.2 to 17.3 percent in rainforest from the surface down to a depth of 60 centimetres. However, in the rainforest, the sand content increased from 64.2 to 78.4%, while in the savannah and derived savannah, it declined from 92.2 to 84.2% and 76.6 to 61.3%, respectively. The author discovered that the soils in the three-agro ecological zones of Nigeria ranged from loamy sand to sandy clay on the surface, but only slightly between sandy clay loam and sandy clay in the subsurface.

4.2.2 Total Organic Carbon

The total organic carbon (TOC) % decreases downwards with soil depths with much of the concentration found in the soil surface layer starting from 0-5cm, 5-10cm, 15-20cm, 35-40cm and 75-80cm with Mara main site with the highest TOC concentration as 2.25%, 2.00%, 1.49%, 1.13% and 1.04% (Table 4.4). This was followed by Ashnil sites having 2.11%, 1.81%, 1.47%, 1.11%, and 0.42% with depth respectively. The collected soil samples from

the 5TM-ECH₂O sensor stations were analysed through dry combustion following Walkey and Black procedure (Nelson & Sommers, 1996).

Table 4.4: Maasai Mara National Reserve sites total organic carbon concentration measured according to soil depths.

Site TOC (%)	Soil Depth (cm)				
	Port 1 (0-5cm)	Port 2 (5-10cm)	Port 3 (15-20cm)	Port 4 (35-40cm)	Port 5 (75-80cm)
Mara Main	2.25	2.00	1.49	1.26	1.04
Kissinger	2.39	1.95	1.58	1.32	0.82
Talek	2.28	1.84	1.75	1.16	0.98
Nice Bridge	2.29	1.98	1.72	0.92	0.46
Upstream	1.85	1.62	1.41	0.92	0.53
Helicopter	1.85	1.66	1.34	0.8	0.52
Ashnil	2.11	1.81	1.47	1.11	0.42
Olimisiogioi	2.3	2.13	1.86	1.2	0.64
V-Section	1.95	1.64	1.26	0.99	0.74
Mara Bridge	1.81	1.62	1.31	1.1	0.92
Sample Mean	2.11	1.83	1.52	1.08	0.71

Kissinger site has the least concentration of TOC ranging from the top soil surface content of 2.39% and the least 0.82% as compared to the other sites in the catchment. Most of the TOC concentration varied according to the nature of the surrounding vegetation, presence of dead and living organisms, which gradually decomposed increasing the levels of litter quality and organic matter caused by increased temperature and soil moisture influence in rangeland ecosystem. Here, lower temperature resulting from increases soil moisture content on the surface layers would cause less microbial activity and enzymatic oxidation of organic matter to produce soil respiration. Vather *et al.* (2018) found that soils with an organic matter level of 6–10% have a greater potential to retain water. Soil texture, together with organic-matter content, affects water-holding capacity and erodibility and provides oxygen to plant roots.

Table 4.5 shows that the rangeland ecosystem consistently tends to increase in soil porosity from the surface layer as hydraulic conductivity decreases downwards and that increase in infiltration, aeration, percolation of water and their canopy cover reduces runoff and erosion hazards. According to Howard and Howard (1990), organic matter content of less

than 1% is considerably low and are limited to desert areas while organic matter of more than 20% by weight are mainly peat soils which on low or high extremes reduce soil productivity. The normal estimates of OM from loss-on-ignition (LOI) method are transformed to SOC usually assuming that 58% (1.724) of OM as composed by carbon (Ball, 1964). The average ideal soil consists of only 5% organic matter mainly composed of carbonaceous substances with soil biomass and remains of dead and living organisms. This implies that the soil at Maasai Mara rangeland due to its adaptive suitable favours the growth of grass vegetation with gradual topography, dominant flat surface, and homogeneous soils aggregated due to cyclic restorations of dead and living organisms.

Table 4.5: Sampled Ashnil site particle size distribution, total organic carbon, soil organic matter and texture class

Depth (cm)	Sensor Horizon	pH (H ₂ O)	Total Organic Carbon (%TOC)	%SOM (%0C*1.724)	Mean Particle Size Distribution			Porosity (%)	Hydraulic Conductivity (Ks)	Textural Class
					%Sand	%Clay	%Silt			
0-5	Port 1	5.53	2.11	3.64	68	23	9	40.5	40.18	SCL
5-10	Port 2	6.26	1.81	3.12	67	25	8	40.7	39.61	SCL
10-20	Port 3	5.81	1.47	2.53	58	35	8	42.0	30.51	SCL
35-40	Port 4	5.72	1.11	1.91	60	34	6	41.8	33.30	SCL
75-80	Port 5	5.86	0.42	0.72	59	34	8	41.8	31.41	SCL

The total organic carbon concentration for most soil shows that the percentage carbon for the top soil is higher than the bottom soil layer where most of the stations had >2.0% (2.11) upper layer while for the lower layer total organic carbon was <1.0% (0.42). Following the method by Howard and Howard (1990), the SOM was computed by multiplying the organic carbon concentration with Conventional Vanbammeller factor of 1.724. This indicates that soil organic matter the Maasai Mara rangeland ecosystem constitutes between 0.5 to approximately 4% by weight of the topsoil in upland soils.

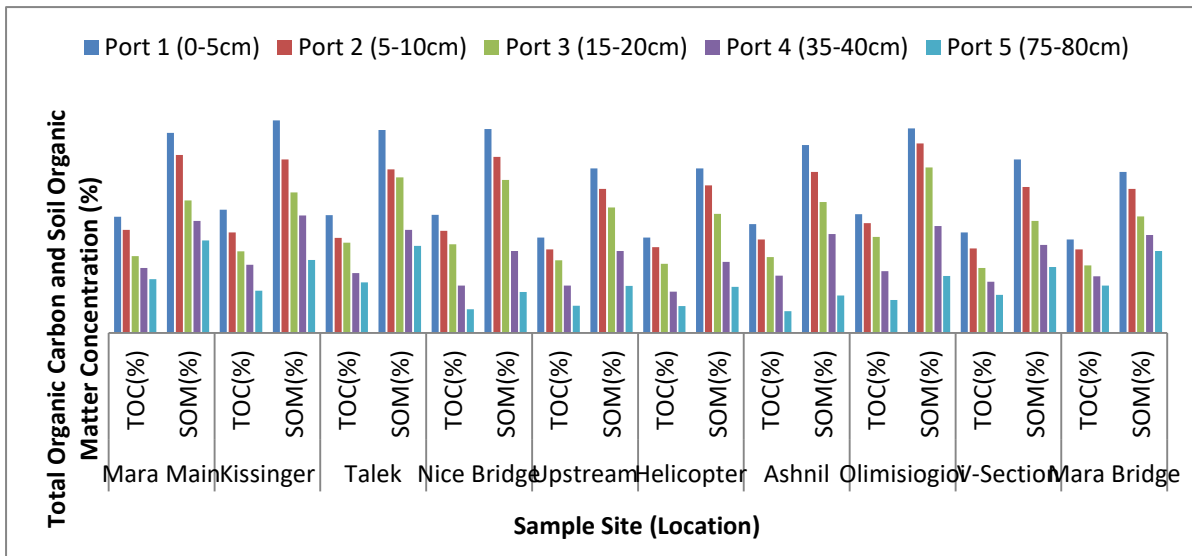


Figure 4.8: Total organic carbon and soil organic matter at three sampled 5TM-ECH₂O stations

Figure 4.8 shows similar characteristics of TOC with depth applicable to all sites across the entire ecosystem with decreased TOC concentration. In the analysis of variance, it was found that total organic carbon had significant difference in concentrations with depth at different sites in reduced concentration. The TOC and SOM concentration respectively decreased with increased depth near the soil surface, high concentration of TOC accumulated and spatially spread across the ecosystem. However, the effective rooting depth of the vegetated grassland was approximately 0.45m in depth. The concentrations were significantly higher at Mara main site (coordinates) as compared to Kissinger and Ashnil sites, which had significantly lower concentrations. However, the concentration at P1 (0-5cm) and P4 (35-40cm) had closely similar and higher concentrations compared to other depths P2 (5-10cm), P3 (15-20cm), and P5 (75-80cm) in the three selected sites which acted as the representative samples. The Mean Square Error (MSE) was 1.675 indicating a more accurate concentration estimate percent for all sampled TOC from the ten-5TM-ECH₂O probe ecosystem sites.

Analysis of variance also shows that, total organic carbon concentration an indicator of organic matter presence in the soil and contributor to moisture retention varied between 0.028 and 0.051, its standard deviation ranged from 0.167 to 0.226 (%), standard error ranged between ± 0.053 and ± 0.071 , and coefficient of variation ranged from 0.102 to 0.319. The physical and chemical properties depicted significant difference with depth across the rangeland ecosystem but the properties did not significantly affect soil moisture variation which shown homogeneous characteristics on vegetation distribution particularly in dominant grassland.

4.2.3 Bulk Density

The samples were taken to the laboratory for the determination of the compacted soil bulk density and the results were as follows; for soils at the Main Mara station and according to the soil depth, 0-5cm, 5-10cm, 15-20cm, 35-40cm and 75-80cm, the soil bulk density were 1.40g/cm³, 1.45g/cm³, 1.34g/cm³, 1.19g/cm³ and 1.25g/cm³ respectively. This indicates that surface layer in this area have high bulk density as compared to the bottom layer density as it decreases gradually with depth.

Table 4.6: Maasai Mara National Reserve sites soil bulk density in with soil depths

Location-ID	Soil Depth (cm)				
	Port 1	Port 2	Port 3	Port 4	Port 5
	(0-5cm)	(5-10cm)	(15-20cm)	(35-40cm)	(75-80cm)
	g cm ⁻³	g cm ⁻³	g cm ⁻³	g cm ⁻³	g cm ⁻³
Mara Main	1.40	1.45	1.34	1.19	1.25
Kissinger	1.52	1.62	1.71	1.72	1.52
Talek	0.98*	1.10	1.75	1.35	1.19
Nice Bridge	1.18	1.29	1.27	1.09	1.12
Upstream	1.17	1.27	1.12	1.21	1.16
Helicopter	1.37	1.11	1.33	1.13	1.10
Ashnil	1.64	1.55	1.63	1.55	1.22
Olimisiogioi	0.84*	1.13	1.00	1.22	1.35
V-Section	1.24	1.20	1.15	0.93*	1.28
Mara Bridge	1.16	1.18	1.07	1.26	1.14
Sample Mean	1.25	1.29	1.34	1.27	1.23

*Asterisks are core ring samples Not Full (NF)

The bulk density of soil at Kissinger soil moisture, soil temperature station shows that it oscillates between 1.72g/cm³ and 1.52g/cm³ at 0-5cm and 75-80cm soil depth respectively. This indicates that soil density depends highly on soil mineral particles, which are aggregated depending on soil profiles. Most of the soils in MMNR ecosystem have bulk density depending on the soil structure and texture that varied from 1.2g/cm³ to 1.75g/cm³ across profiles (Appendix B.5) with mean range of 1.23g/cm³ and 1.34g/cm³ except for the unfilled core rings hence bulk density ranged between 0.84g/cm³ and 0.93g/cm³. The rangeland ecosystem as a whole shows no statistically significant variations in mean bulk density between depths P1 (0-5cm) and P5 (75-80cm), as determined by an analysis of variance. The

bulk density of layer P3 (15-20cm) was measured to be 1.34 gcm^{-3} , which is much higher than the bulk densities of layers P2 (1.29) and P4 (1.27). The ecosystem's bulk density drops significantly to 1.23gcm^{-3} at depth P5 (75-80 cm) compared to P1 (1.25gcm^{-3}) and P4 (1.27gcm^{-3}). Since the soil is more elastic at P1 and P2 than at P5, the considerable changes in bulk density at these depths (35–40 cm) are likely the result of compression at this level as a result of higher moisture content.

4.2.4 Particle Density

With the same soil samples that were collected from five depths or layers at Mara Main station, Kissinger and Ashnil and across the other stations within the catchment, particle density was determined based on Bouyoucos Hydrometer method and described according to Karkanis *et al.* (1991) that gave the following tabulated averaged results. Table 4.7 shows the average particle density of the soil at the Mara main station on profile depths of 0- 5cm, 5-10cm, 15-20cm, 35-40cm and 75-80cm shows that the particle density was respectively 2.46g/cm^3 , 2.37g/cm^3 , 2.5g/cm^3 , 2.38g/cm^3 and 2.53g/cm^3 . The other 5TM-ECH₂O stations, that is Kissinger, Ashnil, Mara Bridge, Talek, Nice Bridge, V-section, Olimisigiioi and helicopter has almost constant average particle densities ranging from 2.40g/cm^3 to 2.55g/cm^3 as shown in appendix B.6). At 75 –80 cm, the particle density of this site was again significantly higher at 2.53gcm^{-3} as compared to other sites. Across MMNR rangeland ecosystem, it can be observed that no significant difference in particle density signifying homogeneous total porosity across the ecosystem. The bulk density also has variance ranging from 0.016 to 0.074, standard deviation between 0.127 and 0.272 gcm^{-3} , standard error ranged between ± 0.016 and ± 0.068 , and coefficient of variation ranged between 0.013 and 0.086 across the catchment. The other properties such as particle density varied between 0.005 and 0.011, standard deviation ranged between 0.071 and 0.106 gcm^{-3} , standard error ranged from ± 0.022 to 0.034, with coefficient of variation from 0.029 to 0.043.

Table 4.7: General particle densities of Maasai Mara National Reserve according to soil profiles

Site	Soil Depth (cm)				
	Port 1 (0-5cm)	Port 2 (5-10cm)	Port 3 (15-20cm)	Port 4 (35-40cm)	Port 5 (75-80cm)
	g cm^{-3}	g cm^{-3}	g cm^{-3}	g cm^{-3}	g cm^{-3}
Mara Main	2.46	2.37	2.51	2.38	2.53
Kissinger	2.53	2.42	2.49	2.5	2.48
Talek	2.44	2.58	2.43	2.43	2.57
Nice Bridge	2.41	2.49	2.36	2.45	2.42
Upstream	2.32	2.37	2.39	2.4	2.3
Helicopter	2.57	2.47	2.31	2.3	2.31
Ashnil	2.47	2.5	2.49	2.45	2.49
Olimisiogioi	2.29	2.36	2.37	2.5	2.32
V-Section	2.27	2.57	2.33	2.31	2.56
Mara Bridge	2.5	2.44	2.38	2.31	2.53
Sample Mean	2.43	2.46	2.41	2.40	2.45

From table 4.7 and figure 4.9, the analysis of variance showed no significant differences in mean particle density at all soil moisture locations with depth profiles P1, P2, P3, P4, and P5 (0-5cm, 5-10cm, 15-20cm, 35-40cm and 75-80cm) as indicated. At 5-10 cm, MMNR main site was found to have a significant lower particle density of 2.37gcm^{-3} than P1, P3, P4, or P5 with particle densities of 2.46, 2.50, 2.38, and 2.53g cm^{-3} , respectively. The soil physical properties of an area influence the characteristics of soil water storage and retention caused by its matrix potential. A study conducted in three ecological zones of Nigeria by Aliku *et al.* (2016), found that bulk density values obtained from the laboratory analysis (1.31 and 1.41g cm^{-3}) were significantly lower ($p<0.05$) than the predicted values (1.66 and 1.55g cm^{-3}) for savannah at 0-30 cm and 30-60 cm depths. The authors also noted that bulk density values were higher in soils from 30-60 cm depth than 0-30 cm depth for all locations and no significant difference between the observed and predicted bulk density values in rainforest zone.

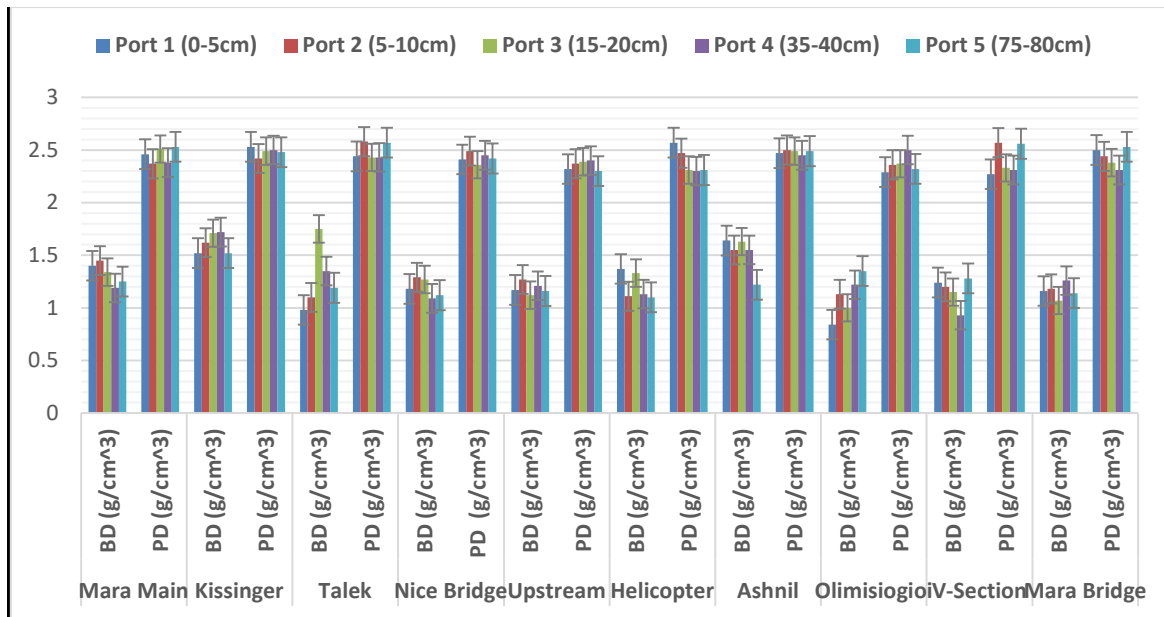


Figure 4.9: General trend of bulk densities (BD) and particle densities (PD) in variation to soil depth across Maasai Mara rangeland ecosystem

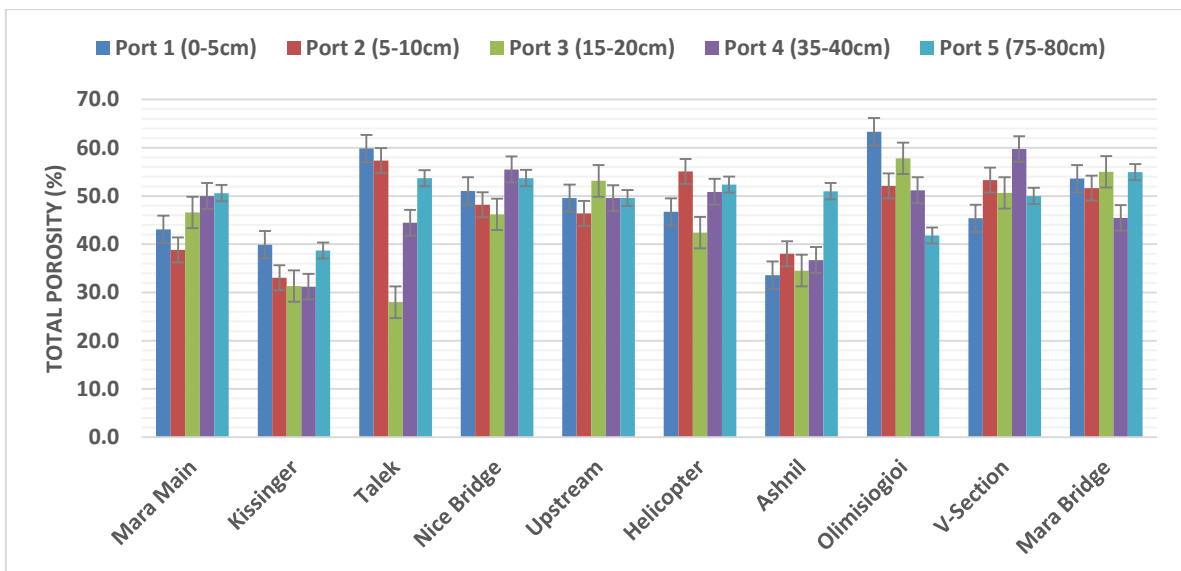


Figure 4.10: Selected spatial behaviour of total soil porosity in variation to soil depths

Figure 4.10 indicates the variation of total soil porosity for selected MMNR representative sites in relation to soil depths from 0-5cm, 5-10cm, 15-20cm, 35-40cm, and 75-80cm. The state of art ecosystem scenario of soil samples shows the subsequent characteristics. Here, sand content ranged from 60 to 80%, clay from 14 to 30% and silt content from 6 to 10%. The particle density ranged from 2.3 to 2.7g/cm³ while the total porosity varied from 30.1 to 51% across the ecosystem.

4.2.5 Maasai Mara National Reserve Rangeland Ecosystem Soil Chemical Properties

Table 4.8: Laboratory soil analysis of Maasai Mara National Reserve rangeland ecosystem

Soil depth (cm)	0-5		10-15		20-25		25-30	
Fertility results	Value	Class	Value	Class	Value	Class	Value	Class
Soil pH	5.53	Medium acid	6.26	Slight acid	5.81	Medium acid	5.72	Medium acid
Total nitrogen %	0.19	low	0.13	low	0.14	low	0.18	low
Total Org. Carbon	2.12	moderate	1.45	moderate	1.25	low	2.07	moderate
Phosphorous ppm	5	low	15	low	5	low	10.0	low
Potassium me%	1.04	adequate	0.48	adequate	1.22	low	1.28	adequate
Calcium me%	8.7	adequate	14.5	adequate	10.7	adequate	9.8	adequate
Magnesium me%	1.29	adequate	3.95	high	1.21	low	1.25	adequate
Manganese me%	0.38	adequate	0.23	adequate	0.40	adequate	1.25	adequate
Copper ppm	1.79	adequate	3.86	adequate	1.83	adequate	1.98	adequate
Iron ppm	48.9	adequate	23.6	adequate	45.0	adequate	45.8	Adequate
Zinc ppm	3.07	low	2.45	low	1.64	low	1.94	low
Sodium me%	0.16	adequate	0.39	adequate	0.98	adequate	0.77	adequate

Table 4.8 indicates that soils of MMNR rangeland ecosystem has varied potential of hydrogen ions classified according to the layers. The top surface layer was analysed as 0-5cm, 10-15cm, 20-25cm and 25-30cm with their pH ranges as 5.53 (medium acidic), 6.26 with slight acidity, 5.81 for medium acidic and 5.72 as medium acidic respectively. The soils of this rangeland are mainly homogeneous across most parts of land. The other nutrients that contribute to the suitability of mixed grasses and shrubs growth were also determined and it was found that the following macro and microelements concentrations of total nitrogen with their respective layers were 0.19%, 0.13%, 0.14% and 0.18% were low in the soil. The total organic carbon was also analysed and found present in the soil as 2.12%, 1.45%, 1.25% and 2.07% respectively (Appendix B.7).

Macro elements such as phosphorous measured in parts per million were found to be low in the soils with 5, 15, 5 and 10 ppm and potassium 1.04 me%, 0.48me%, 1.22 me% and 1.28me% which were adequate in the soil. The amount of calcium, magnesium, manganese, copper, iron, and sodium were adequate in the soil layers while zinc being low in its concentration for soils in this ecosystem probably make rangelands suitable for grass biomass production since its dominant vegetation of grass mixed with sparse shrubs vegetation.

4.2.6 Infiltration Rate and Saturated Hydraulic Conductivity

As observed from figure 4.11, the rate of infiltration was initially high and decreases with time as the soil becomes saturated. Within the initial start of infiltration, the rate in mm/min was higher and as the water recedes downwards, the rate gradually decreased over time until constant infiltration rate was achieved. The gravimetric water content in the soil receded until there was no water drainage because of wetting front effect where field capacity (water holding capacity) was attained after 13 mins with the soil infiltration rate of 2.17cm/hr or (21.7mm/hr). As observed from the figure, cumulative soil infiltration rate was higher because the dry soil had low initial water content or no moisture, thus high saturation hydraulic conductivity.

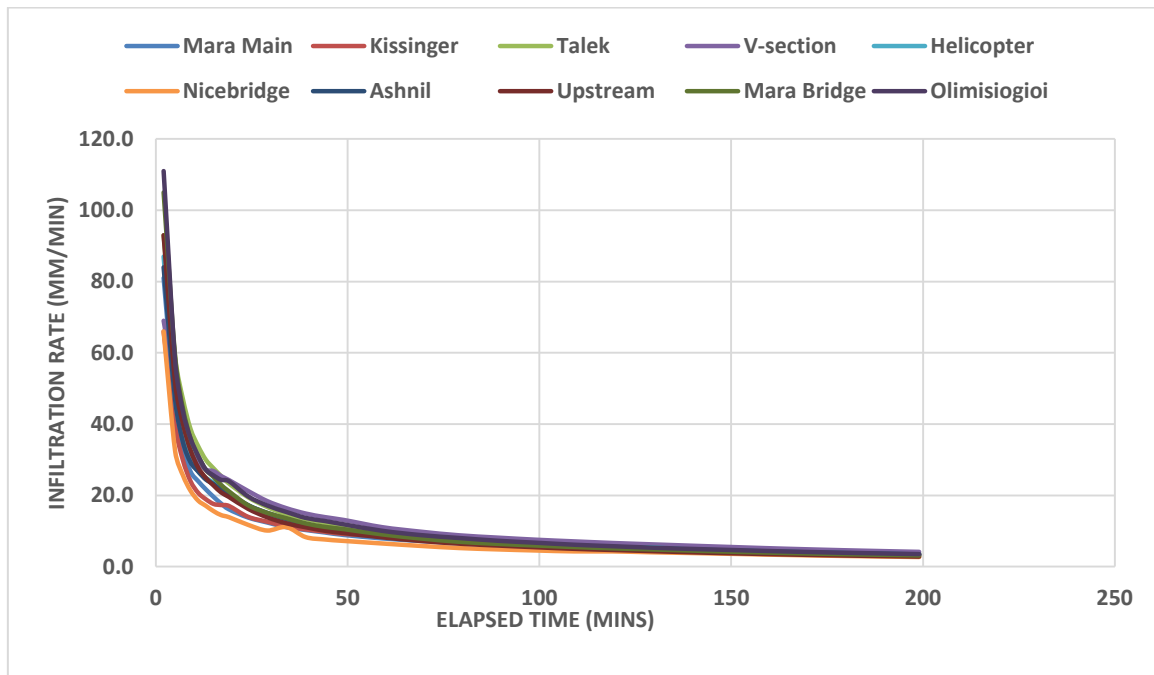


Figure 4.11: Infiltration rate at sampling sites of Maasai Mara National Reserve rangeland ecosystem during the dry season

Similar studies conducted by Rietkerk *et al.* (2000) and Li *et al.* (2004) shown that vegetation covered soil surface has a higher infiltration rate than bared soil reasons being plant roots tend to increase infiltration better because of its enhanced soil water retention. The

initial rate at which water entered into the soil depended upon the soil texture, organic matter, and cation exchange capacity and soil conditions. The variation in the cumulative infiltration into the soils depicted different water intake rates within the study locations. Generally, dry soil permitted faster infiltration rates because of low initial soil moisture content than when if the soil moisture was high.

The homogeneous description of soil in the study area indicates that the soils mainly sandy clay loam on the top 0-5cm layer were made of decomposed grass residues over time that contributed to organic matter forming similar rangeland soil characteristics. The vegetation covers similarly characterized as grassland were made of short and densely growth species of grasses, which protected the soil surface from excessive runoff and infiltration rate, however low moisture retention due surface exposure to evaporation. MMNR being natural grassland with sparse shrubs, the results indicate that infiltration rates are slightly higher in medium covered surface as compared to extremely bare surface with sparsely vegetated surfaces and moderate moisture content. These implies that the overall soil condition and vegetation cover in this rangeland ecosystem is dominated with naturally dense grass species that caused low surface runoff, high infiltration rate and vice-versa with moderate evaporation characterized with homogeneous vegetation cover. Again, the rangeland characteristics was influenced by the surface soil texture with high soil porosity due to fine textured soils, low bulk density and high particle density including high surface organic matter content. This ecosystem is however made of coarse textured soils such as sandy clay loam (SCL), sandy clay (SC), sandy loam (SL) and clay (C) based on FAO/USDA classification system of soil textural classes.

Table 4.9: Analysis of variance (ANOVA) on spatial distribution of volumetric water content with depth at 10 m concentric distance to CRNS in Maasai Mara rangeland ecosystem

Soil Depth (cm)	Volumetric Water Content (m ³ /m ³) @ 10m from CRS footprint						Mean VWC (m ³ /m ³)	Variance	Standard Deviation (m ³ /m ³)	Standard Error	Coefficient of Variation
	0 ⁰ , 360 ⁰	60 ⁰	120 ⁰	180 ⁰	240 ⁰	300 ⁰	Spatial Mean	V	SD	SE	CV
P1(0-5)	0.14	0.16	0.16	0.17	0.14	0.15	0.153	0.000	0.012	±0.005	0.079
P2(5-10)	0.17	0.18	0.22	0.25	0.18	0.28	0.213	0.002	0.045	±0.018	0.209
P3(15-20)	0.19	0.27	0.36	0.36	0.27	0.33	0.297	0.004	0.066	±0.027	0.223
P4(25-40)	0.25	0.39	0.43	0.41	0.30	0.36	0.357	0.005	0.069	±0.028	0.194
P4(35-40)	0.30	0.42	0.47	0.47	0.38	0.39	0.405	0.004	0.064	±0.026	0.158
P5(75-80)	0.40	0.49	0.50	0.50	0.39	0.40	0.447	0.003	0.055	±0.022	0.123
Mean	1.45	1.91	2.14	2.16	1.66	1.91					

V- Variance, **SD** – Standard Deviation, **SE** – Standard Error, **CV** – Coefficient of Variation

From table 4.9, the analysis of variance indicates that the spatial mean soil moisture was significantly different throughout the profile with the surface top soil (0-5cm) being the lowest 0.153m³/m³ and the highest soil moisture content at lower depth (75-80cm) being 0.447m³/m³ respectively. This shows that volumetric water content increases with depth, a phenomenon that surface moisture is affected by environmental factors such as surface evaporation, rainfall runoff, soil infiltration, deep percolation and plant transpiration has direct influence on water storage and retention capacity within the soil matrix. There were four treatments (control (C), warmed (W), precipitation doubling (PPT), and warmed plus precipitation doubling (W+PPT), with five replicates for each treatment), and the results were comparable to those found in this study. In all soil depths tested, the authors discovered a statistically significant change in soil moisture between treatments (C, PPT, W, and W+PPT) (0–15,

15–30, 30–60, 60–90, and 90–120 cm). As for soil moisture frequency distributions, the authors discovered that C and PPT had the wettest frequencies across all depths, whereas W+PPT and W had the driest frequencies. Under all test conditions, they also found that soil moisture increased with depth. The coefficient of variation for soil moisture was 0.000 – 0.005, while the standard deviation and error were 0.012 – 0.069 and 0.005 – 0.028, respectively.

Table 4.10: Analysis of variance on spatial distribution of volumetric water content with depth at 25 m concentric distance to CRNS in Maasai Mara rangeland ecosystem (main station)

Soil Depth (cm)	Volumetric Water Content (m^3/m^3) @ 25m from CRS footprint						Mean VWC (m^3/m^3)	Variance	Standard Deviation (m^3/m^3)	Standard Error	Coefficient of Variation
	0^0 , 360^0	60^0	120^0	180^0	240^0	300^0					
P1(0-5)	0.13	0.16	0.17	0.16	0.15	0.14	0.152	0.000	0.015	\pm 0.006	0.097
P2(5-10)	0.18	0.19	0.17	0.23	0.19	0.24	0.200	0.001	0.028	\pm 0.012	0.141
P3(15-20)	0.20	0.26	0.39	0.37	0.29	0.36	0.292	0.006	0.075	\pm 0.031	0.257
P4(25-30)	0.25	0.39	0.43	0.47	0.30	0.39	0.372	0.007	0.082	\pm 0.034	0.221
P4(35-40)	0.29	0.45	0.46	0.50	0.36	0.37	0.405	0.006	0.078	\pm 0.032	0.193
P5(75-80)	0.45	0.49	0.50	0.51	0.40	0.44	0.453	0.003	0.057	\pm 0.023	0.125
Mean	1.50	1.94	2.12	2.24	1.69	1.94					

Table 4.11: Spatial distribution of volumetric water content with depth at 75 m concentric distance to CRNS in Maasai Mara rangeland ecosystem (Main station)

Soil Depth (cm)	Volumetric Water Content (m^3/m^3) @ 75m from CRS footprint						Mean VWC (m^3/m^3)	Variance	Standard Deviation (m^3/m^3)	Standard Error	Coefficient of Variation
	0^0 , 360^0	60^0	120^0	180^0	240^0	300^0	Spatial Mean	V	SD	SE	CV
P1 (0-5)	0.15	0.16	0.16	0.17	0.14	0.16	0.157	0.000	0.010	± 0.004	0.066
P2 (5-10)	0.18	0.19	0.18	0.23	0.18	0.24	0.200	0.001	0.028	± 0.011	0.138
P3(15-20)	0.19	0.23	0.33	0.39	0.27	0.34	0.292	0.006	0.075	± 0.031	0.257
P4(25-30)	0.19	0.39	0.42	0.49	0.30	0.38	0.362	0.011	0.104	± 0.043	0.288
P4(35-40)	0.33	0.42	0.46	0.51	0.37	0.36	0.408	0.005	0.068	± 0.028	0.166
P5(75-80)	0.50	0.48	0.49	0.52	0.39	0.41	0.465	0.003	0.052	± 0.021	0.113
Mean	1.54	1.87	2.04	2.31	1.65	1.59					

Table 4.12: Analysis of variance on spatial distribution of volumetric water content with depth at 175 m concentric distance to CRNS in Maasai Mara rangeland ecosystem (Main station)

Soil Depth (cm)	Volumetric Water Content θ (m ³ /m ³) @ 175m from CRNS footprint						Mean VWC (m ³ /m ³)	Variance	Standard Deviation (m ³ /m ³)	Standard Error	Coefficient of Variation
	0 ⁰ , 360 ⁰	60 ⁰	120 ⁰	180 ⁰	240 ⁰	300 ⁰	Spatial Mean	V	SD	SE	CV
P1(0-5)	0.17	0.14	0.16	0.16	0.14	0.16	0.155	0.000	0.0122	± 0.0050	0.0790
P2(5-10)	0.17	0.19	0.18	0.25	0.16	0.26	0.202	0.002	0.0426	± 0.0174	0.2114
P3(15-20)	0.17	0.22	0.36	0.39	0.29	0.35	0.297	0.008	0.0866	± 0.0354	0.2920
P4(25-30)	0.19	0.40	0.39	0.56	0.27	0.38	0.365	0.016	0.1263	± 0.0516	0.3460
P4(35-40)	0.27	0.44	0.45	0.59	0.34	0.36	0.408	0.012	0.1113	± 0.0454	0.2724
P5(75-80)	0.50	0.51	0.49	0.51	0.35	0.34	0.450	0.007	0.8173	± 0.0334	0.1816
Mean	1.47	1.90	2.03	2.46	1.55	1.85					

Table 4.13: Weighted average volumetric water content of spatially distributed 5TM-ECH₂O Probes

Soil Depth (cm)	Weighted average 5TM-ECH ₂ Oθ (m ³ /m ³) spatially distributed sites										Mean VWC (m ³ /m ³)	SD (m ³ /m ³)	SE	CV
	Mara Main	Kissinger	Talek	Nice Bridge	Upstream	Helicopter	Ashnil	Olimisiogioi	V-Section	Mara Bridge				
P1(0-5)	0.14	0.15	0.17	0.14	0.11	0.13	0.13	0.15	0.16	0.20	0.147	0.0249	±0.00249	0.1679
P2(5-10)	0.21	0.19	0.15	0.24	0.14	0.16	0.30	0.28	0.23	0.26	0.216	0.0511	±0.01615	0.2365
P3(15-20)	0.21	0.29	0.14	0.26	0.19	0.24	0.31	0.31	0.32	0.31	0.258	0.0616	±0.01948	0.2388
P4(35-40)	0.28	0.29	0.18	0.31	0.30	0.18	0.25	0.43	0.29	0.44	0.295	0.0838	±0.02651	0.2841
P5(75-80)	0.27	0.40	0.23	0.29	0.32	0.32	0.30	0.45	0.29	0.39	0.326	0.0000	± 0.0000	0.0000
Mean	1.11	1.32	0.87	1.24	1.06	1.03	1.29	1.62	1.29	1.60				

From tables 4.9, 4.10, 4.11, 4.12 and 4.13, it can be noted that volumetric water content changes with respect to depth on spatial scale (10, 25, 75 and 175 m) spatial distance varied increasingly at near surface 0-5cm depth to deep 75-80cm depth respectively. The mean VWC ranged from 0.153m³/m³ to 0.447m³/m³ and their variance ranged between 0.000 and 0.005, standard deviation between 0.012 and 0.069m³/m³, standard error between ±0.005 and ±0.028 and coefficient of variation ranged between 0.079 and 0.223. The distribution of soil moisture with depth is a function of environmental influence caused by evaporation at near the soil surface, infiltration, runoff and percolation including the immediate soil conditions and surface vegetation cover which determines rooting depth of plants. The deeper the roots of vegetation the farther the soil moisture storage from the soil surface, plants roots response positively towards water available soil matrix and elongates as much as possible depending on extractable water content in the soil. In this rangeland ecosystem, the grass maximum rooting depth was observed to be

approximately 30cm to 45cm and grass height range between 80cm and 120cm respectively for nearly similar grass species. The grass roots were dense at near the soil surface as compared to bottom-layered soil. The standard deviation per soil moisture station was $0.104\text{m}^3/\text{m}^3$. The coefficient of variation (CV) also ranged from 0.097 to 0.257 and the significant difference at ≤ 0.05 probability level was 0.428. The soil moisture significant differed from P1 to P5 (0-5cm) to (75-80cm) depth across all the moisture stations in the rangeland ecosystem.

Table 4.14: Analysis of variance on volumetric water content as per 5TM-ECH₂O Soil Moisture, Temperature Capacitance Probes

Source	Sum of squares (SS)	Degrees of freedom (df)	Mean squares (MS)	P value	CI (%)	SD	F statistics	LSD
Between Groups	0.371	5	0.011	≤ 0.05	95	0.181	0.352	0.624
Within Groups	0.194	30	0.033					
Total		35						

P value - Significant at the 0.05 probability level, F – F ratio, CI – Confidence interval level (%), SD – Standard deviation, LSD, least significant difference between means

Mean Square of Profile (MSP) - 0.011, Mean Square Error (MSE) – 0.033, Sum of Square Error (SSE) – 0.073

Table 4.14 indicates spatial variation of soil moisture and the mean spatial volumetric water content ranged between $0.147\text{m}^3/\text{m}^3$ at the top soil profile (0-5cm) and $0.326\text{m}^3/\text{m}^3$ at below the soil depth of 75-80cm respectively. The soil moisture content decreased with depth. The standard deviation increased from the top layer to the bottom soil layer ranged from 0.0249 to $0.0838\text{m}^3/\text{m}^3$ and the standard error ranged from ± 0.0000 to ± 0.02651 while the coefficient of variation ranged from 0.0000 to 0.2841. It follows that P1(0-5cm) profile has significantly less moisture as compared to spatial means of all stations depths for P5(75-80cm) except at Kissinger which has no significantly different soil moisture at depth P3 and P4 (15-20, 35-40cm). In addition, at Talek site, the soil moisture was significantly less at all depths and significantly more as compared to Olimisiogioi location except at Kissinger location. The sum of squares of all data values (SS) was 0.371; sum of squares of the all

blocks (replicate) values was 0.194 and the sum of squares of all treatments (variety) was 0.103. The least significant difference (LSD) between means at 5% level of probability (≤ 0.05) or 95% level of confidence was 0.624 and the F ratio was 0.352 with the degrees of freedom (df) of 49, mean square error (MSE) of 0.033 and sum of square error (SSE) of 0.073. The volumetric water content variance ranged from minimal value of 0.001 to maximum value of 0.008, standard deviation from the mean ranged between 0.167 and $0.226\text{m}^3/\text{m}^3$, standard error ranged between ± 0.008 , ± 0.028 , and coefficient of variation between 0.166 and 0.295 across the rangeland ecosystem.

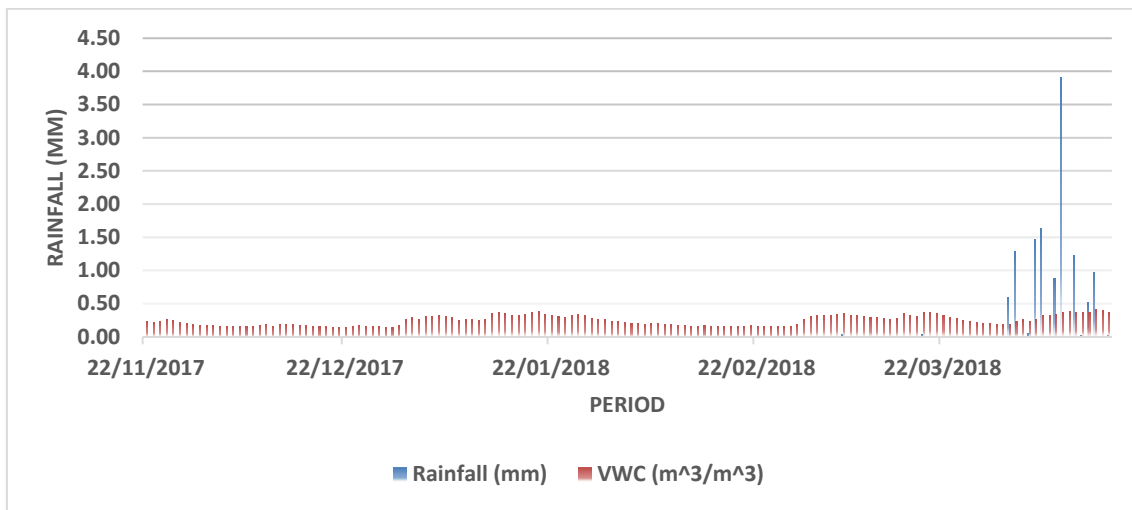


Figure 4.12: Time series trend of rainfall correlation to volumetric water content between Nov 2017 and April 2018.

Figure 4.12 shows time series variation of volumetric water content in relation to rainfall events, which occurred in 2017 and Mid-April 2018, it can be noted that rainfall was high in the month of April and May 2018 with depicting rainfall range of 0.89 to 3.91 mm with volumetric water content ranging from 0.40 to $0.436\text{m}^3/\text{m}^3$. A time series of the CRNS soil moisture data showed the dependency of the soil moisture fluctuations on rainfall. This could be deduced that the top soil moisture is low at near land surface VWC1 (0-5cm) due to the effects of runoffs, evaporation, and percolation of rainwater. Garcia-Ruiz (2010) noted in a study conducted in the Mediterranean settings of Spain that vegetation may alter the soil's physical qualities, such as bulk density, physical composition, and porosity. The pace of infiltration, amount stored, and where it goes are all affected by these shifts in the soil (Lipiec *et al.*, 2006). But the temporal change was reasonably smooth in the 80-120 cm deep soil layer, indicating a distinct lag in reaction to precipitation. Ursulino *et al.* (2019) demonstrated that soil moisture behaviour is a function of precipitation in two stations (S1 and S2) in the Tropical Experimental Basin, and their findings were consistent with those of the current

study. Soil water content was found to have increased by a maximum of 0.32 and 0.33 $\text{cm}^3\text{cm}^{-3}$ in S1 and S2, respectively, during the 15 mm rainfall episodes from May to July 2015. Soil moisture increased suddenly at the end of May 2015 due to a 61 mm rainfall event, but after that, it remained more or less constant in S1 and S2 until the conclusion of the rainy period in July. More increases are pronounced with oscillating declines in soil water content during rainfall events in 2016 as compared to 2015. During the period of prolonged dryness or no rains or little rains (blue lines), fraction of soil moisture remains in the soil (red lines) and this was depicted during the previous year in periods of 2017 and 2018 with rainfall range between 0,059 to 1.29 with VWC range between 0.25 to 0.38 m^3/m^3 . At the point where there is no element or invisible rainfall traces means that the VWC signals seen in the graph indicates retained moisture content within the soil shallow layers or that the sensor signals could read zero in case of obstruction from taking the signals especially in deeper layers. This indicates that soil moisture retention in soil enables rangeland vegetation survive under stored moisture during seasons of no rainfall for a certain period before permanent wilting threshold was attained in plants causing complete drying.

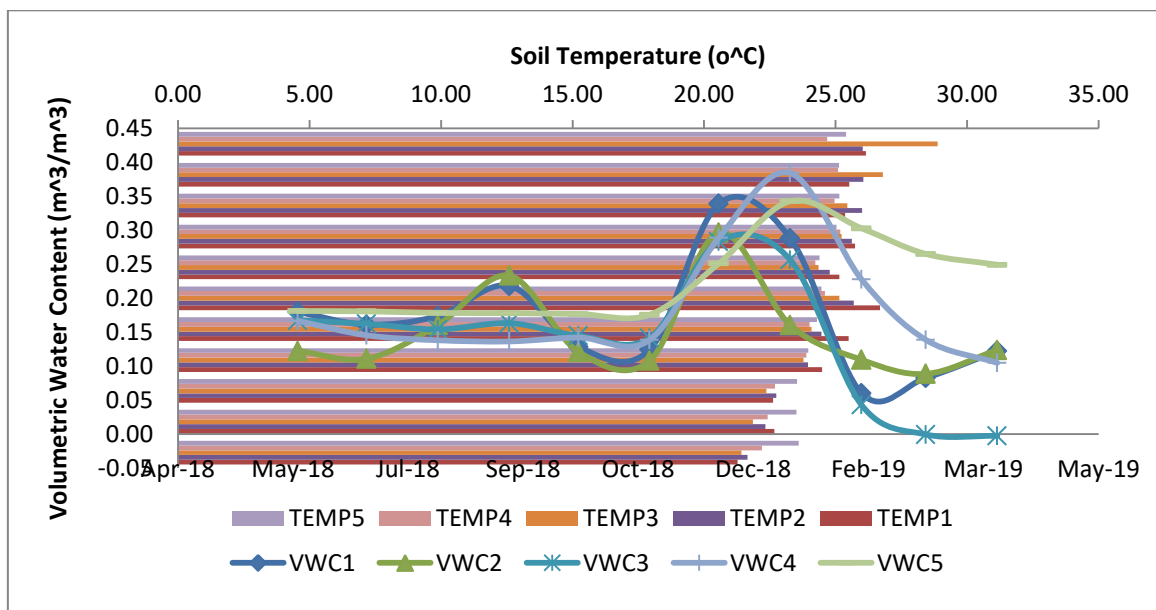


Figure 4.13: Trend of Nice bridge volumetric water content with respect to soil layers for 2018-2019

From the figure 4.13, It was evident that high moisture content was available within the VWC4 (35-40cm) soil layers during the month of July through to December 2018. This could be due to water redistribution and ground recharge before reaching the bottom VWC5 (75-80cm) layer. Again, there was subsequent low moisture at the beginning of January to April 2019 due to low rainfall and high temperature during the period. Similarly, Bell *et al.* (2010)

discovered that in a tall grass prairie experiment, soil temperatures were higher in the experimental warming treatments (W and W+PPT) than in the non-warming controls across the board (at the surface, 7.5 cm, 22.5 cm, 45 cm, 75 cm, and 105 cm) (C and PPT) down respectively. The researchers discovered no statistically significant change in soil temperature between C and PPT across any depth, and similarly found no difference between W and W+PPT. The investigation also showed that the soil temperature changed very little between the surface and 105 cm in the PPT and C plots, whereas it decreased by about 3°C in the W and W+PPT plots. The soil temperature was lowest in the W+PPT and W plots across all tiers, with the W plots maintaining their low temperature throughout.

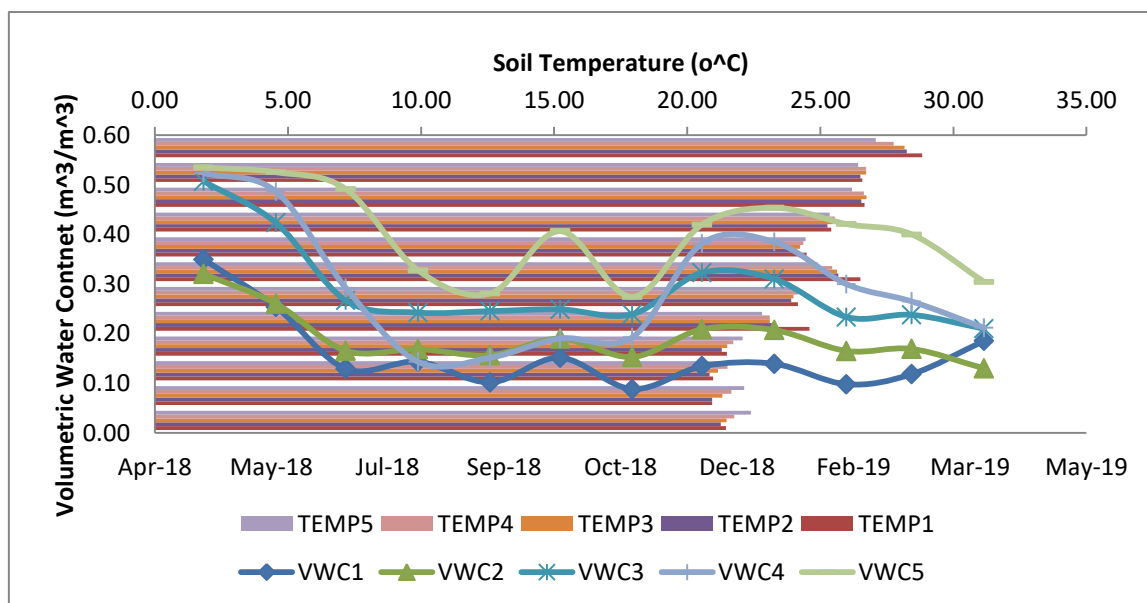


Figure 4.14: Trend of monthly soil moisture and temperature variation per depths at Kissinger 5TM-ECH₂O site: 2018-2019

Figure 4.14 shows the volumetric water content, temperature, and it can be deduced that with low temperature, soil moisture content is high and high temperature causes low moisture storage and retention, which is inversely proportion to each other. Wu *et al.* (2014) found that the relationship between the two environmental factors indicates that for soil moisture to be stored for a long period after rainfall, low temperature, infiltration rate, rainfall runoffs and deep percolation must coexist within the soil and this relies greatly on soil texture and structure. This slow decline can be traced back to the extensive evaporation and transpiration of water from the soil at that time. Crop cover was insufficient at the time to prevent further soil evaporation. This demonstrates that soil strata got soil water at different times. Only when the soil is completely saturated, or has achieved its field capacity, does any further water in the soil become available to seep downward via the soil profile. These results are

consistent with those of an experiment on water application in an irrigation scheme conducted by John Mthandi *et al.* (2014), who discovered that water had to slake the thirst of the uppermost soil profiles before it could reach the bottom layer. This finding is consistent with what has been reported in the literature, which explains that the action of surface evaporation causes higher changes of soil water contents in the lowest layers of soil profiles compared to the top layer.

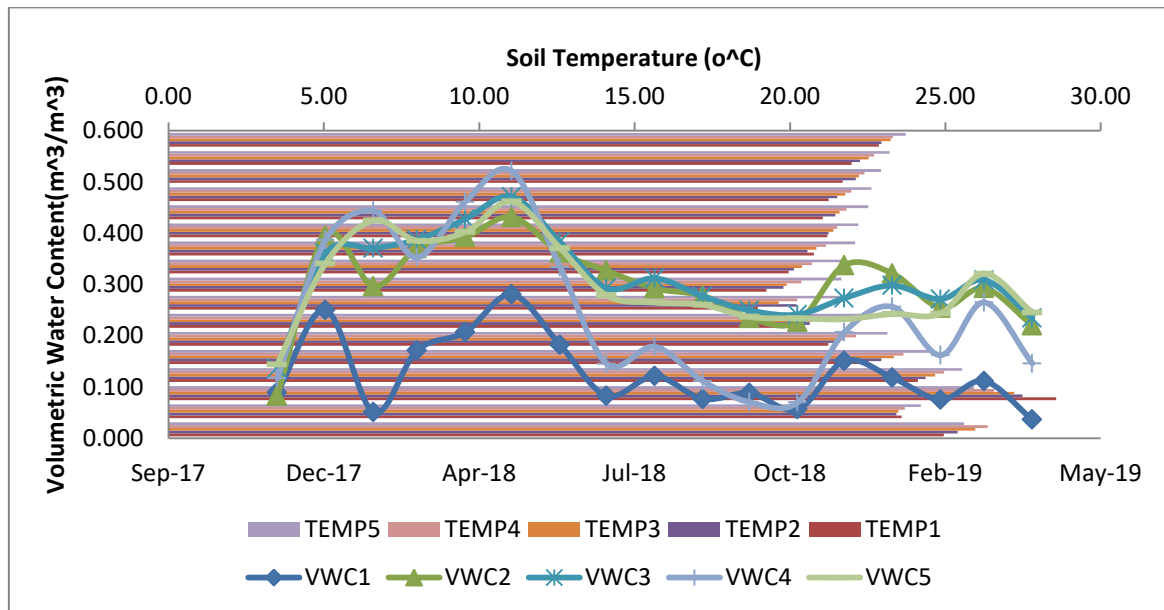


Figure 4.15: Variation of Ashnil site soil moisture and temperature at different soil profiles

Figure 4.15 shows similar behaviour in soil water and temperature relations, which indicates an inverse proportional characteristic in that during the month of September through December 2017, there was low moisture due to high temperature and oscillating variation of soil moisture with temperature. Low moisture content was also experienced at near surface layer VWC1 (0-5cm) and high below soil surface oscillating between VWC4 (35-40cm) and VWC5 (75-80cm) layer respectively. In a study done by Niu *et al.* (2015), showed that vertical soil water profile exhibited seasonal patterns for different land uses and stable layer of soil moisture was found at 80-120cm depth. Moisture showed a stable (high-low-high low) trend with wave changing type at 0-120cm in other land use except in grassland, which gradually decreased with depth from 100 to 120cm, which was not consistent with the findings of Gao *et al.* (2014).

From the selected rangeland sites, the characteristics of soil moisture behaved homogeneously with depth across the ecosystem with soil textural class of sandy clay loam (SCL) at the top soil surface VWC1 (0-5cm) layer throughout the season. It was also observed that the trend of volumetric water content spatially distributed across the ecosystem

with depth shows top soil layer P1 (0-5cm) is significantly low moisture content as compared to deep shallow layers P4 (35-40cm) and P5 (75-80cm). Zehe *et al.* (2010) observation that the length of spatial correlations changed with soil moisture levels was supported by these results. This, however, demonstrates how different controls can cause a deviation from the norm and either increase or decrease soil moisture variation (Das *et al.*, 2008; Wu *et al.*, 2012). On the other hand, dampness was observed to boost the correlation scale in grasslands but not forests. As seen from the figure 4.19, the trends have similar characteristics across sites within the ecosystem, a clear indication of dominant vegetation adapting to grassland natural environment.

Table 4.15: Cosmic ray volumetric water content according to soil layers at Mara Main station

Soil Depth (cm)	N_{corr} (ch ⁻¹)	N_0 (ch ⁻¹)	ρ_b (gcm ⁻³)	$\omega_{lattice}$ (gg ⁻¹)	SOM_{water} (gg ⁻¹)	Average VWC (m³m⁻³)	Effective Depth (cm)
0-5	565	1441	1.40	0.03	3.64	0.34	11
5-10	565	1430	1.45	0.03	3.12	0.35	11
10-15	565	1414	1.34	0.03	2.53	0.32	11
15-20	565	1388	1.19	0.03	1.91	0.29	12
20-25	565	1363	1.25	0.03	1.52	0.30	12
25-30	565	1269	1.22	0.03	0.72	0.29	12

N_{corr} – corrected neutrons, N_0 – Average neutron intensity, ρ_b – Dry bulk density, $\omega_{lattice}$ – Lattice water, SOM_{water} – Soil organic matter expressed as water equivalent.

Table 4.15 shows the average bulk density, w_{lat} , and w_{SOM} for each point in degrees of the Main Mara site where CRNS data values were collected. This indicates low moisture near the soil surface and high moisture content below the soil surface with low environmental influence on soil moisture storage and retention across the ecosystem. All vegetation relies on soil moisture storage and retention despite the rate of root zone depletion, which usually enables vegetation adaptation to suitable condition for growth and development. Long and short-term seasonal vegetation species adapt itself to a favourable environment where available water content is readily utilizable by plants at the root zone. Soil moisture content being a major sensitive parameter impacts much on vegetation biomass and yields, however climate variables, bulk density, particle density, and total organic carbon concentration influence vegetation behaviour and adaptation characteristics. The dry soil bulk density

varied from 1.19 g cm^{-3} to 1.45 g cm^{-3} . In the computation of volumetric soil moisture, the bulk density was used to convert gravimetric soil moisture content and determine the effective depth to which the CRNS probes measured the soil moisture at a given point ranged from 11 and 12cm. The effective measurement depth of CRNS over the 1-year period between Dec 2017 and April 2018 (Table 4.15) showed that the effective measurement depth ranged from 10.58 cm to 12.48 cm, with an average depth of 11.53cm. The sites had varied lattice water (water of crystallization) of 0.02 g g^{-1} at its lowest and 0.03 g g^{-1} at the highest, which maybe assumed negligible. Sandy Clay loam (SCL) majorly the top soil has the highest SOM_{water} as compared to the bottom sandy clay soil. The content varied from 0.002 to 0.03 g g^{-1} . The range of average N_0 values was between 673.48 to 899.94 counts per hour (ch^{-1}) with coefficients of variation during the dry season and 241.12 to 114.71 ch^{-1} during the wet season, for sites with its average measurement depths (z^*) ranged between 5 and 30 cm where the soil moisture was a reciprocal to the depths.

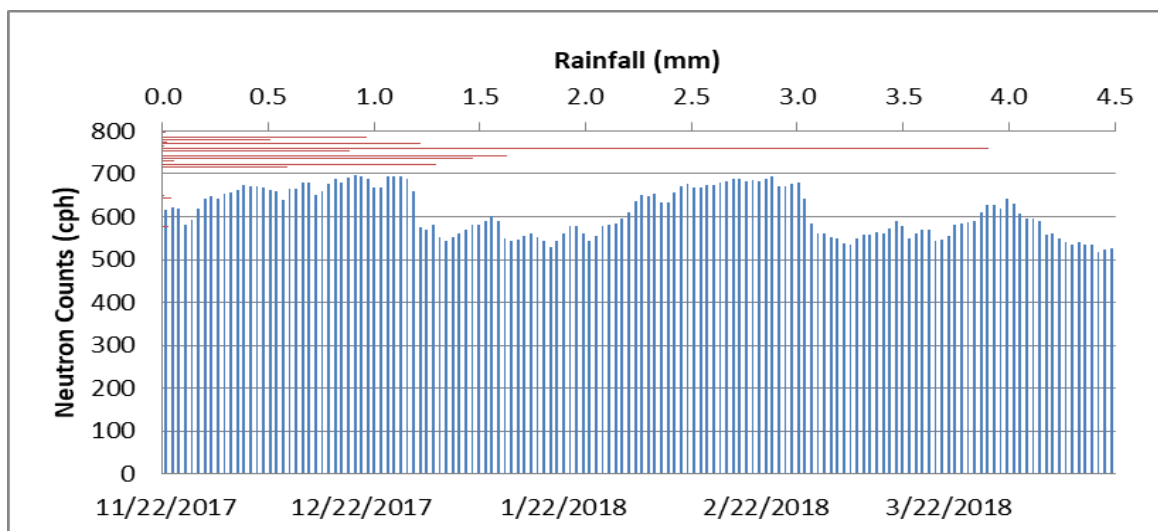


Figure 4.16: Time series of daily rainfall and moderated neutron counts during the period 2017 and 2018 at Maasai Mara National Reserve.

The minimum and maximum depths of measurement were 5cm to 80cm with soil moisture ranged from as high as $0.35 \text{ m}^3 \text{ m}^{-3}$ to $0.29 \text{ m}^3 \text{ m}^{-3}$ respectively and to $0 \text{ m}^3 \text{ m}^{-3}$ for dry soils at the 80cm bottom soil layer across the concentric distance. This shows that between 10m to 175m away from the CRNS footprint, fraction of soil moisture exists where general cover is of dominant grassland and it signifies that grassland soil does not reach complete dryness between the bi-seasons.

4.3 Moderated Neutron Counts

Figure 4.16 depicts the daily precipitation and moderated neutron counts at the study site for the years 2017 and 2018. As a result of varying precipitation, it is observable that the adjusted moderated counts reduce quickly with precipitation and climb gradually according to an exponential curve. Since the moderating effect provided to neutrons by hydrogen atoms is inversely proportionate, the predicted CRNS soil moisture increases rapidly after a rainstorm event. Time to respond is faster, and apparent soil moisture is higher in the CRNS. Soil moisture increases in proportion to increases in rainfall, but decreases progressively because of high temperature in the generated CRNS, as the soil dries out.

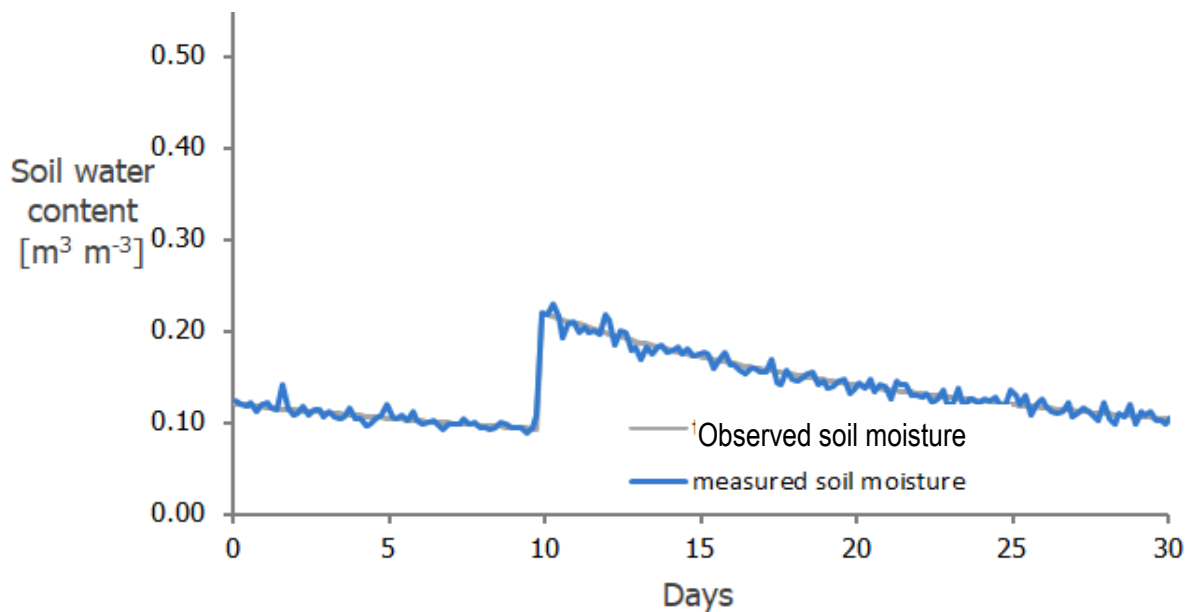


Figure 4.17: CRNS temporal simulation trend of soil moisture content receding after rainfall event

Figure 4.17 shows the CRNS simulations of soil moisture after a rainfall event and it indicates that moisture depletes with time due to evapotranspiration from $0.12\text{m}^3\text{m}^{-3}$ and receded for a period of 10 days before an additional event of rains, which eventually raised the moisture content to over $0.22\text{m}^3\text{m}^{-3}$. Due to fluctuating moisture levels, it can be noted that in dry period there was steady decline of moisture loss due to receding behaviour of rainfall event and subsequent redistribution of moisture, which gradually increased from initial moisture level for the period of 20 days from the previous rainy events (wet period). The transition of wetting front to dryness with time due to soil moisture hysteresis dynamically caused soil moisture variations.

Table 4.16: Calibrations, dates, gravimetric soil moisture, bulk density, neutron counts and calculated N_0 values.

Calibration (date)	Moisture status	Gravimetric water content (g/g)	Bulk density (g/cm ³)	Volumetric water content (m ³ /m ³)	Neutron count (count/h)	N_0
12/12/2017	Dry	0.129	1.40	0.180	665.747	1647.187
21/12/2017	Dry	0.097	1.45	0.140	697.625	1724.343
05/04/2018	Wet	0.219	1.19	0.260	589.417	1462.436
09/04/2018	Wet	0.295	1.22	0.360	540.708	1344.558
Mean						1544.631

Based on table 4.16, the calculated average N_0 value for calibrations was 1544.631. The hourly VWC was determined using the calculated N_0 value in the rearranged calibration function on equation 3.14. The hourly CRNS data (grey line) were converted into daily (blue line) average to smoothen the data for comparison with other daily-derived soil moisture products. The results show that soil moisture was higher in wet season and lower in dry season (Table 4.16) as characterized by Maasai Mara National Reserve ecosystem rainfall pattern. In the study, the conversion of the neutron count rate to gravimetric soil water equivalent θ_{grv} was performed according to Desilets *et al.* (2010) who suggested a theoretical relation that has been applied successfully by the majority of CRNS studies.

4.3.1 Biomass Water Equivalent

Site-specific calibrations implicitly took vegetation influences on the measured neutron counts into account and needed simultaneous measurements of area-averaged soil water content and neutron count. Since natural grassland predominates in the MMNR rangeland ecosystem, the experimental sites did not exhibit large variations in biomass (grassland). As a result, the biomass correction was not necessary; the variation in hydrogen biomass within the site was only 1.34mm of H₂O, which was negligible and was therefore disregarded during the calibration process (Appendix B.9). Franz *et al.* (2013a) established a method to isolate the effect of vegetation on the neutron intensity signal, and their observation and calculation of the area average biomass water equivalent were in agreement with independent measurements. Measuring N_0 levels in fields of maize (*Zea mays* L.) and soybean (*Glycine max* (L.) Merr.), Franz *et al.* (2015) similarly discovered a linear relationship, with N_0 levels

decreasing by 1% for every 1 kg/m² of biomass or water equivalent present. Water equivalent to biomass is shown here to decrease as neutron levels rise.

4.3.2 Root Biomass Density

Five cored soil samples were collected from MMNR site with homogeneous characteristics across rangeland via a core ring of volume 98.175cm³ (0.098175lts) at different soil layers of 0-5, 5-10, 15-20, 35-40 and 75-80 cm and during the lab measurements their ambient/room temperature was taken to be 24°C. The samples were used to determine the root density of the soil and it was observed that the densities decreased with increased depth. The root density at the top soil layer of 0-5cm was higher with 8.098g/l as compared to the density at the bottom layer of 75-80cm with 0.682g/l. Fine root distribution decreased with soil depth and decreased with distance from the plant stem in sandy clay loam soil. The factors that may have contributed to decline in root density depth wise consist of increased fraction of silt and clay mineral particles causing soil strength decreased with depth in soil organic matter, aeration and its fertility.

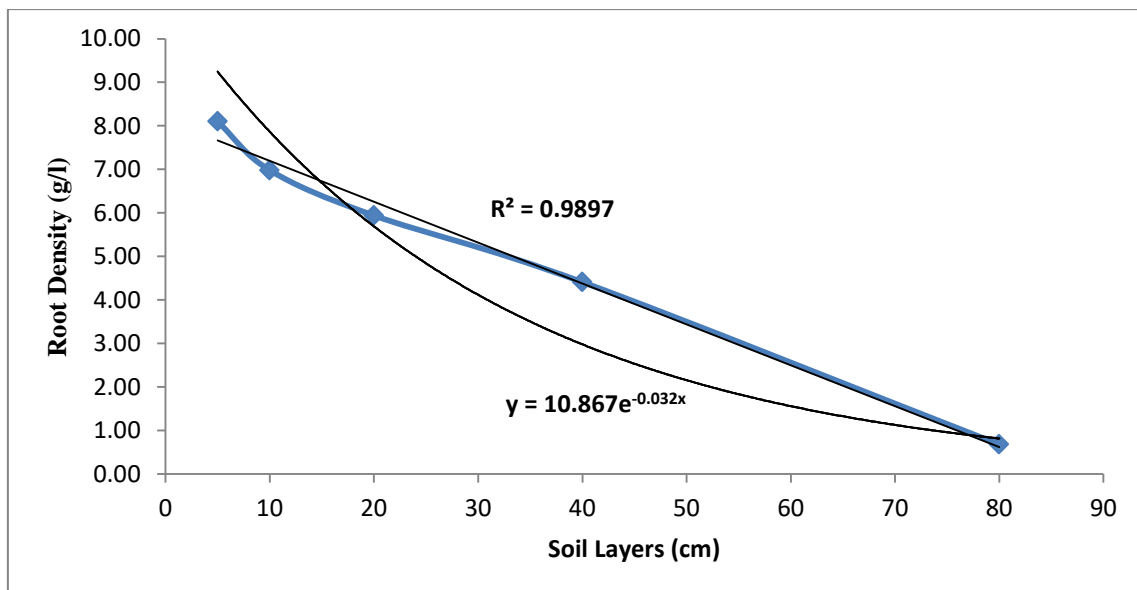


Figure 4.18: Root density distribution of grass vegetation in Mara ecosystem soil profile

Figure 4.18 displays a close association between root density distribution and soil profile, with a slope of 10.87 on the exponential function and a correlation coefficient of 0.9897. Analysis of SWC profiles and moisture temporal changes, such as those caused by infiltration and drying redistribution processes, rainfall events, and crop evapotranspiration, provided some valuable insight into the root spatial distribution, particularly with regards to root density. Due to its native nature, the grass species present within the catchment requires minimal moisture content stored within its root-zone. Root length per soil volume is a primary factor in the plant's ability to selectively absorb water.

Table 4.17: Root density of soil samples as collected from MMNR main sampling site.

Sample_ID	Initial soil sample wgt (g) + Beaker (g)	Wgt of the beaker (g)	Wgt of the beaker for measuring 1 litre of water (g)	Wgt of the 1 litre mix of soil sample (g)	Wgt of the foil (g)	Wgt of Foil + Wet weigh of roots (g)	Wgt of oven dried roots (g) + Foil (g)	Final constant wgt after oven drying.(g)	Wgt of dried roots (g)	Root Biomass (g/l)
Depth (cm)										
0-5cm	238.0	105.96	264.28	1279.6	2.19	7.31	2.98	2.98	0.80	8.10
5-10cm	268.7	105.98	264.31	1270.8	2.07	6.57	2.75	2.75	0.69	6.10
15-20cm	254.3	105.98	264.32	1184.7	2.29	6.03	2.87	2.87	0.58	5.94
35-40cm	266.7	105.99	264.33	1260.7	2.22	6.66	2.66	2.65	0.43	4.41
75-80cm	227.8	105.98	265.48	1193.5	1.98	3.90	2.05	2.05	0.07	0.68

The greatest root density is typically found a few centimetres below the surface soil, which dries earliest owing to heat exposure and evaporation. Soil water content usually changes with depth across the root zone and measurements based at different depths within the root zone. Sala *et al.* (1996) observed that soil moisture depicts low high low change in profile possibly because of the effects of bulk density and root distribution that may have contributed to soil moisture difference. Here, the volumetric water content was obtained by direct sampling of a known soil volume and use of a both 5TM-ECH₂O capacitance probes and cosmic ray neutron sensor that were used to accurately estimate, θ_v .

Table 4.18: Soil moisture variations across rangeland ecosystem according to soil layers

11	Horizon	Soil Depth (cm)	Mean Particle Size Distribution	VWC (m ³ /m ³)	Porosity (%)	(mm)	Hydraulic Conductivity (mm/hr)	b-exponent at saturation	Conductivity at Saturation	Field Capacity (m ³ /m)	Wilting Point (m ³ /m)	Soil Texture	
			% Sand % Clay % Silt										
Across sites	Port 1	0-5	68 23 9	0.35	40.0	212.6	3.863	6.507	89.3	32.69	0.276	0.128	SCL
Across sites	Port 2	5-10	67 25 8	0.35	40.1	226.0	3.255	6.824	89.93	30.83	0.281	0.135	SCL
Across sites	Port 3	15-20	58 34 8	0.35	41.0	405.3	0.944	8.264	109.5	20.80	0.314	0.171	SCL
Across sites	Port 4	35-40	60 34 6	0.35	40.7	355.5	1.148	8.258	101.8	22.04	0.309	0.168	SCL
Across sites	Port 5	75-80	59 33 8	0.35	40.9	378.7	1.090	8.104	107.1	21.73	0.310	0.167	SCL

4.4 Moisture Retention Characteristics

The moisture retained across rangeland at the soil surface to the subsoil layers was determined for Ten-5TM-ECH₂O soil moisture, soil temperature stations. The sites were spatially distributed across Maasai Mara rangeland and the results shown that there were changes in soil water content as a function of water potential (ψ). However, soil from various sites was relatively homogeneous and the bulk densities were closely similar with presence of high clay content across the rangeland. Table 4.18 shows the matrix potential across sites in the Maasai Mara ecosystem with soil depths. The mean particle size distribution ranged between 59, 68% sandy soil, 23, 34% clayey soil, and 6, 9% silt soil forming dominant sandy clay loam (SCL) soil across the ecosystem. The volumetric water content storage averaged at 0.35m³/m³ for most sites as compared with depths in the entire ecosystem. The soil porosity ranged between 40.0 to 41.0 % and its matrix potential of between 212.6 to 405.3 mm, saturated hydraulic conductivity 20.80 and 32.69 mm/hr. The distinction between saturated hydraulic conductivity ("Ks") is a quantitative expression of the soil's ability to transmit water under a given hydraulic gradient, while hydraulic conductivity (slope "K") defines

the proportional relationship between flux and hydraulic gradient, or in this case, of unidirectional flow in saturated soil. There was a wide variation in field capacity, with values between 0.276 and 0.314 m³/m and wilting point readings between 0.128 and 0.171 m³/m. Measured and anticipated field capacity values in the savannah zone increased from 13.5% to 15.0% and from 13.9% to 18.3%, respectively, in a comparable experiment conducted by Aliku *et al.* Although the projected values for savannah soils grew with depth from 22.01% to 29.59%, the measured field capacity values for savannah soils decreased from 21.34% to 18.78%.

Table 4.19: Soil moisture characteristics of Maasai Mara rangeland sites for various soil texture denoted as SL – Sandy Loam, SC – Sandy Clay, SCL – Sandy Clay Loam, C - Clay

Site_ID	%Sand	%Clay	%Silt	FC (m ³ /m ³)	WP (m ³ /m ³)	Saturation (m ³ /m ³)	Infiltration rate (m/hr)	Available Water (m ³ /m ³)	Bulk Density (g/cm ³)	Textural Class
Mara-main	61	32	7	0.270	0.182	0.479	0.216	0.089	1.40	SCL
V-section	57	32	11	0.276	0.181	0.483	0.228	0.095	1.24	SCL
Talek	62	32	6	0.269	0.182	0.479	0.213	0.087	0.98	SCL
Upstream	56	36	8	0.292	0.199	0.490	0.172	0.093	1.17	SC
Helicopter	71	25	4	0.234	0.153	0.459	0.378	0.081	1.37	SCL
Kissinger	62	30	8	0.262	0.173	0.476	0.253	0.089	1.52	SCL
Nice Bridge	68	26	6	0.241	0.157	0.463	0.348	0.084	1.18	SCL
Olimisigioi	56	36	8	0.292	0.199	0.490	0.172	0.093	0.84	SC
Mara Bridge	66	22	12	0.230	0.139	0.455	0.548	0.091	1.16	SCL
Ashnil	54	38	8	0.303	0.209	0.494	0.157	0.094	1.34	SC

Table 4.19 displays the field capacity, permanent wilting point, and water availability at several sites throughout the MMNR rangeland ecosystem. The size distribution of mineral particles in sand, silt, and clay for each soil layer across the watershed was given in table format. The available water content for the catchment sites ranged from $0.102\text{m}^3\text{m}^{-3}$ to $0.128\text{m}^3\text{m}^{-3}$ due to the presence of sand and clay mineral particles, as well as loam, caused by the accumulation of organic matter in the upper soil layer. This shows a decrease in porosity because of the cohesiveness of the aggregates comprising the soil's platy structure and its high particle density. In general, the soil moisture retention capacities in MMNR are indicative of a healthy soil structure resulting from undisturbed decomposition of organic matter (humus). According to Huntington (2007), organic matter modifications would have the greatest impact on field capacity values due to the hydrophilic nature of organic matter and its favourable influence on soil structure. Here, the high water absorption capacity is the result of a high proportion of loamy soil. The average distribution of soil textural classes was 70% sandy clay loam (SCL) and 30% sandy clay (SC) over the entire ecosystem. Aliku *et al.* found in their study that the measured wilting point (WP) values were significantly lower than the predicted values at $p < 0.05$ in all locations. The observed WP values for savannah soils from 0 to 30 cm and 30 to 60 cm depth were 1.07 and 2.80 percent, while the expected values were 7.25 and 11.25 percent, respectively. The observed WP values for derived savannah (2.81 and 5.44%) and rainforest (4.80 and 3.44%) were lower than their expected values at 0 – 30 cm and 30 – 60 cm depths, respectively.

From the observation on table 4.20, the top soil of most sites at 5cm depth is homogeneous across the whole of Mara catchment. The mineral particles have almost close range of distribution, the %sand ranges between 60 to 80, %clay between 14 to 28 and %silt between 6 and 14. The soils classified from the soil textural triangles are sandy clay loam, which constitute more of total organic matter. The infiltration rate of such soil depicts low rate of infiltration due to small pore spaces in between the particles to permit fast infiltration rate. Much of water loss led to high rainfall runoffs. The available water in the soil due to its matric potential ranges between $0.09\text{m}^3\text{m}^{-3}$ to $0.11\text{m}^3\text{m}^{-3}$, this indicates close homogeneity across catchment with mean available water of $0.10\text{m}^3\text{m}^{-3}$, mean standard deviation and error of $0.009\text{m}^3\text{m}^{-3}$ and ± 0.003 respectively. The difference is insignificant and this shows that the soil moisture is almost constant in the catchment sites.

Table 4.20: Spatial soil water characteristics at 0-5 cm soil depth and soil water retention

Site_ID	Soil Depths (cm)	%Sand	%Clay	%Silt	FC (m ³ /m ³)	WP (m ³ /m ³)	Saturation (m ³ /m ³)	Infiltration rate (cm/hr)	Avail Water (m ³ /m ³)	Bulk Density (g/cm ³)	Textural Class
Mara-main	5	70	22	8	0.225	0.140	0.453	0.534	0.086	1.450	SCL
V-section	5	64	22	14	0.232	0.139	0.457	0.556	0.094	1.439	SCL
Talek	5	68	24	8	0.234	0.148	0.459	0.431	0.086	1.434	SCL
Upstream	5	60	28	12	0.258	0.164	0.473	0.310	0.094	1.396	SCL
Helicopter	5	76	16	8	0.198	0.114	0.431	1.138	0.084	1.509	SL
Nice Bridge	5	72	22	6	0.223	0.140	0.451	0.528	0.084	1.455	SCL
Kissinger	5	80	14	6	0.186	0.105	0.420	1.531	0.081	1.536	SL
Olimisigioi	5	64	28	8	0.253	0.165	0.470	0.297	0.088	1.404	SCL
Ashnil	5	78	14	8	0.189	0.105	0.422	1.524	0.083	1.533	SL
Mara Bridge	5	68	23	10	0.231	0.144	0.456	0.482	0.087	1.440	SCL
Average	5	68	23	9	0.19	0.09	0.449	0.733	0.087	1.460	SCL

Table 4.21: Spatial soil water characteristics at 5-10 cm soil depth and soil water retention

Site_ID	Soil Depths (cm)	%Sand	%Clay	%Silt	FC (m³/m³)	WP (m³/m³)	Saturation (m³/m³)	Infiltration rate (m/hr)	Avail Water (m³/m³)	Bulk Density (g/cm³)	Textural Class
Mara-main	10	72	22	6	0.223	0.140	0.451	0.528	0.083	1.455	SCL
V-section	10	60	24	16	0.244	0.146	0.465	0.462	0.098	1.419	SCL
Talek	10	66	30	4	0.257	0.173	0.473	0.242	0.093	1.352	SCL
Upstream	10	56	36	8	0.292	0.199	0.490	0.172	0.093	1.380	SC
Helicopter	10	78	18	4	0.203	0.123	0.436	0.859	0.079	1.496	SL
Kissinger	10	78	14	8	0.189	0.105	0.422	1.524	0.083	1.533	SL
Nice Bridge	10	70	24	6	0.232	0.148	0.457	0.425	0.084	1.438	SCL
Olimisigioi	10	60	32	8	0.272	0.182	0.481	0.219	0.090	1.377	SCL
Ashnil	10	72	22	6	0.223	0.140	0.451	0.528	0.083	1.455	SCL
Mara Bridge	10	76	16	8	0.198	0.114	0.431	1.138	0.084	1.509	SL
Average	10	67	25	8	0.239	0.152	0.462	0.390	0.087	1.426	SCL

In table 4.21, it indicates that most of the spatially distributed stations have dominant sandy clay loam (SCL) below the soil surface layers followed by sandy clay (SC) with particle size distribution range of %sand from 56 to 78, %clay from 14 to 36 and %silt from 4 to 16. The mean particles distribution is %sand of 67, %clay of 25 and %silt of 8. The soil layer 5-10cm depth also shows that the mean available water content is high than the surface water content in that storage at the soil surface is highly influenced by evaporation and infiltration into the soil such that the holding capacity decreased gradually. The field capacity (FC) ranged from 0.15 to 0.22m³m⁻³ and wilting point (WP) ranged from 0.06 to 0.11m³m⁻³ with mean capacity of 0.08m³m⁻³. The soil saturation ranged 0.35 to 0.44m³m⁻³ with a mean of 0.39m³m⁻³. The infiltration rate beneath the soil surface also shows that there is an increase from 3.2 to 4.4 cm/hr or 0.032 to 0.044 m/hr due to a trade-off between the surface runoffs and evaporation with the effect of initial soil moisture. Bulk density ranged from 1.35 to 1.53g/cm³, however high density results in low water storage and vice-versa due to macropores in the soil. Within these densities, the available water ranged between 0.11m³m⁻³ and 0.15m³m⁻³ with mean of 0.12m³m⁻³. The standard deviation of the available water content of this rangeland ecosystem with homogeneous soils was 0.014m³m⁻³ and the standard error of ± 0.005 .

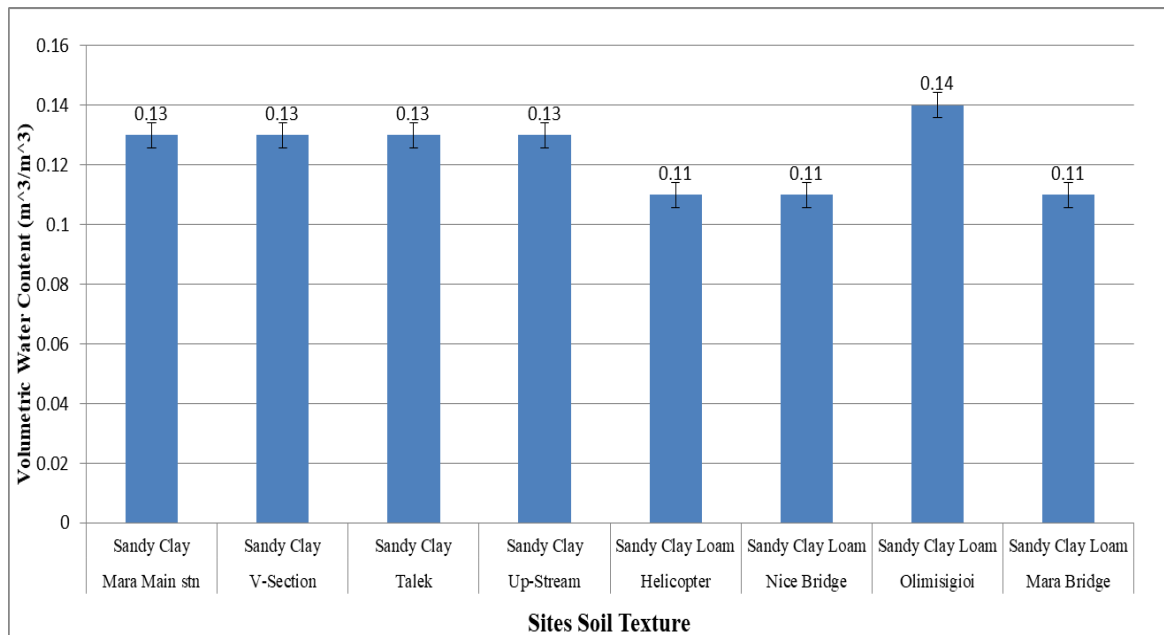


Figure 4.19: Weighted average distribution of near surface 5cm depth volumetric moisture content according to respective site's soil texture

Figure 4.19 shows the mean volumetric water content of 5cm depth was mainly 0.13m³/m³ for most of the spatially distributed 5TM-ECH₂O stations with textured soil of sandy clay. The stations with sandy clay loam soils however had volumetric water content of 0.11m³/m³

with an exception of olimisigioi site where the water content was $0.14\text{m}^3/\text{m}^3$ and the surrounding environment dominated by grassland mixed with sparse shrubs. The figure 4.19 further means that soil layers from the top surface to the bottom, the 50 moisture probes (10 5TM-ECH₂O sites) at five depths between 0-5, 5-10, 15-20, 35-40 and 75-80cm were inserted horizontally in line with the indicated segments. The averaged volumetric water content showed no significant difference since they mainly ranged between $0.10\text{m}^3\text{m}^{-3}$ and $0.12\text{m}^3\text{m}^{-3}$. The soil texture present in the moisture stations are mainly dominated by sandy clay loam (SCL) where it occupies 70% and the rest 30% sandy clay (SC) soils distributed homogeneously across the rangeland ecosystem and within the top soil layers.

The standard mean deviation of the available water to plants was $0.011\text{m}^3\text{m}^{-3}$ and its standard error was ± 0.003 . Vereecken *et al.* (2007) found that the standard deviation of soil moisture peaked between $0.17\text{cm}^3\text{cm}^{-3}$ and $0.23\text{cm}^3\text{cm}^{-3}$ for most textural classes in a study with unprecedented spatial and temporal resolution across scales such Agricultural and irrigation management practices, particularly in semiarid and arid regions. Climate and soil hydraulic characteristics interacted to determine the degree of soil moisture variation. The average moisture content at which the greatest variability relies on, are the hydraulic qualities of the soil and the vegetation in each environment. The storage capacity of soil moisture in the plant root zone highly depends on the amount of soil textural classes, rainwater, fractional amount that infiltrates, percolates into the soil and partly that goes as runoff.

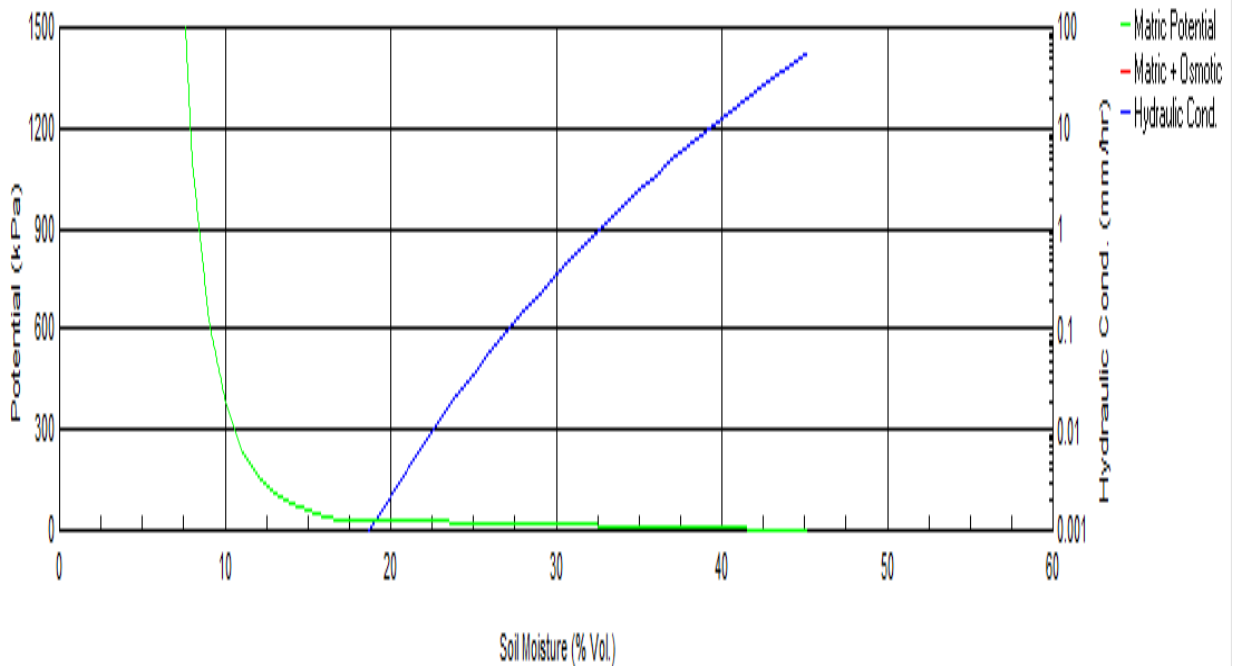
Table: 4.22: Characteristics of Soil moisture retention with depth across Maasai Mara rangeland ecosystem, 2019

Moisture sites	Sensor ID	Soil depth (cm)	pF	Average VWC(m ³ /m ³)	Average FC @ - 0.3 bars	Average WP @ - 15 bars	Textural Class
Across rangeland	P1	0- 5	0.69	0.10	0.190	0.090	SCL
Across rangeland	P2	5-10	1.00	0.11	0.239	0.152	SCL
Across rangeland	P3	15-20	1.30	0.12	0.286	0.195	SC
Across rangeland	P4	35-40	1.60	0.12	0.279	0.190	SCL
Across rangeland	P5	75-80	1.90	0.12	0.280	0.190	SCL

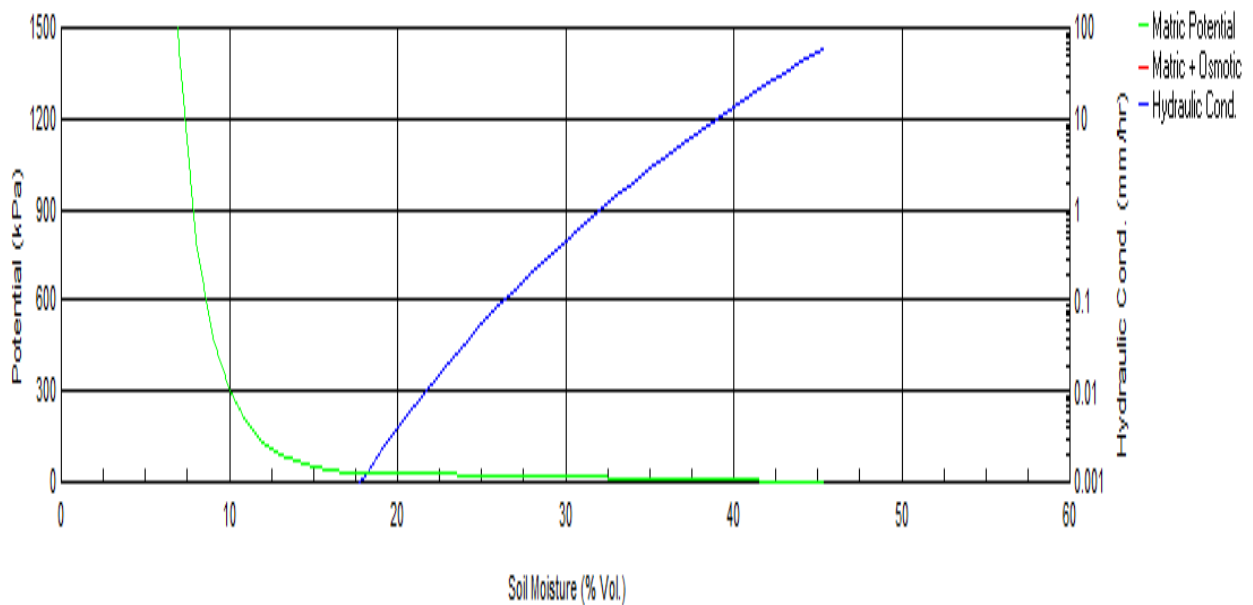
4.4.1 Soil Moisture Retention Curves from Soil Profile Data

The moisture retention curves were computed for layers within soil moisture sites in which the database for available soil moisture at field capacity and wilting points were categorised as in Table 4.22. The results were summarised and the curves for the fine, medium and coarse texture classes were well separated in terms of absolute moisture contents at given potentials, but the shapes are slightly comparable. The pressure heads for the layers in each moisture potential 5, 10, 20, 40 and 80cm were calculated for the pF (Log h) and the values were as follows 0.69, 1.00, 1.30, 1.60 and 1.90 plotted for the water content available at each layer and averaged for the spatially distributed sites. The characteristics depict homogeneous soil texture and water storage for most parts of the catchment. The dominant soil type for the area is mainly sandy clay loam followed by sandy clay, which makes it suitable for grassland environment. As observed from most parts of the sites, the field capacity at soil water content at -3 bars ranges from 0.19m³H₂O/m³soil to 0.29m³H₂O/m³soil with a mean field capacity (FC) of 0.24m³H₂O/m³soil for all parts of the rangeland. The permanent wilting point (PWP) at soil water content at -33 bars ranges from 0.10m³H₂O/m³soil to 0.12m³H₂O/m³soil at average of 0.11m³water/m³soil for most parts of the grassland.

The available water for most parts of the sites in which biomass were collected were $0.13\text{m}^3\text{H}_2\text{O}/\text{m}^3\text{soil}$ on areas with sandy clay soil and $0.11\text{m}^3\text{H}_2\text{O}/\text{m}^3\text{soil}$ for those areas dominated by sandy clay loam, which indicates that sandy clay soils retains more water than sandy clay loam (SCL). The total organic matter in the soil as determined shows that the top layer of soil within a depth of 5cm has higher total organic carbon than deeper soils. This makes the soil creates a high water retention capability than the soils with less total organic matter. The potential of retention is a result of high carbon content that creates high porosity for holding water in the soil. Figure 4.20 shows the matric potential for soil varying in depths and that water loss appears to be slightly high due to the influence of infiltration rate. It shows that in the first few days after precipitation that moisture also depletes faster at the exposed top soil surface due to evapotranspiration process occurring at -0.3 bars and -15 bars (0 to 1500kPa) volumetric field capacity. On the initial top soil layer, it is worth noting that between 0cm (soil surface) and 10cm depth, there was rapid water loss due to gravity of $0.01\text{m}^3\text{m}^{-3}$. Notably, below the depth of 10cm , there were no water loss and the moisture content nearly remained almost constant at $0.12\text{m}^3\text{m}^{-3}$ across the entire rangeland.



(a = 5cm) depth



(b = 10cm) depth

Figure 4.20: Characteristics of soil water potential for (a) 5cm and (b) 10cm depth at Maasai Mara rangeland

According to the average curve, the volumetric moisture contents at pF 4.2, 2.5, 2 and 0 are approximately 47, 33, 28, 19 and 19 v%, respectively. Statistics show that 42, 31, 21, and 15 y% are the averages of the respective measured values. This could represent optimum amount of water for plants utilization or absorption. In subsoil depths, slight variation was observed due to the influence of gravity and evaporation on the soil surface. In the subsoil depths, water retention was lower in the surface soil as compared to the subsurface since the soil moisture trends ranged between $0.11\text{m}^3\text{m}^{-3}$ and $0.12\text{m}^3\text{m}^{-3}$ respectively. Below 80cm soil layer without rains for a couple of days, there was high probability of soil water loss approaching wilting point that caused gradual dryness of grass cover in MMNR rangeland. This phenomenon occurred during the period of dryness had no further significance to vegetation growth and the blossom nature of the vegetation growth and restoration during the wet season produced suitable dry matter quality for herbivores in the entire rangeland. In the study, evapotranspiration due to the influence of temperature at a given location was highly variable from year to year and season-to-season thus largely had greater influence on biomass yield stability.

4.4.2 Statistical Analysis

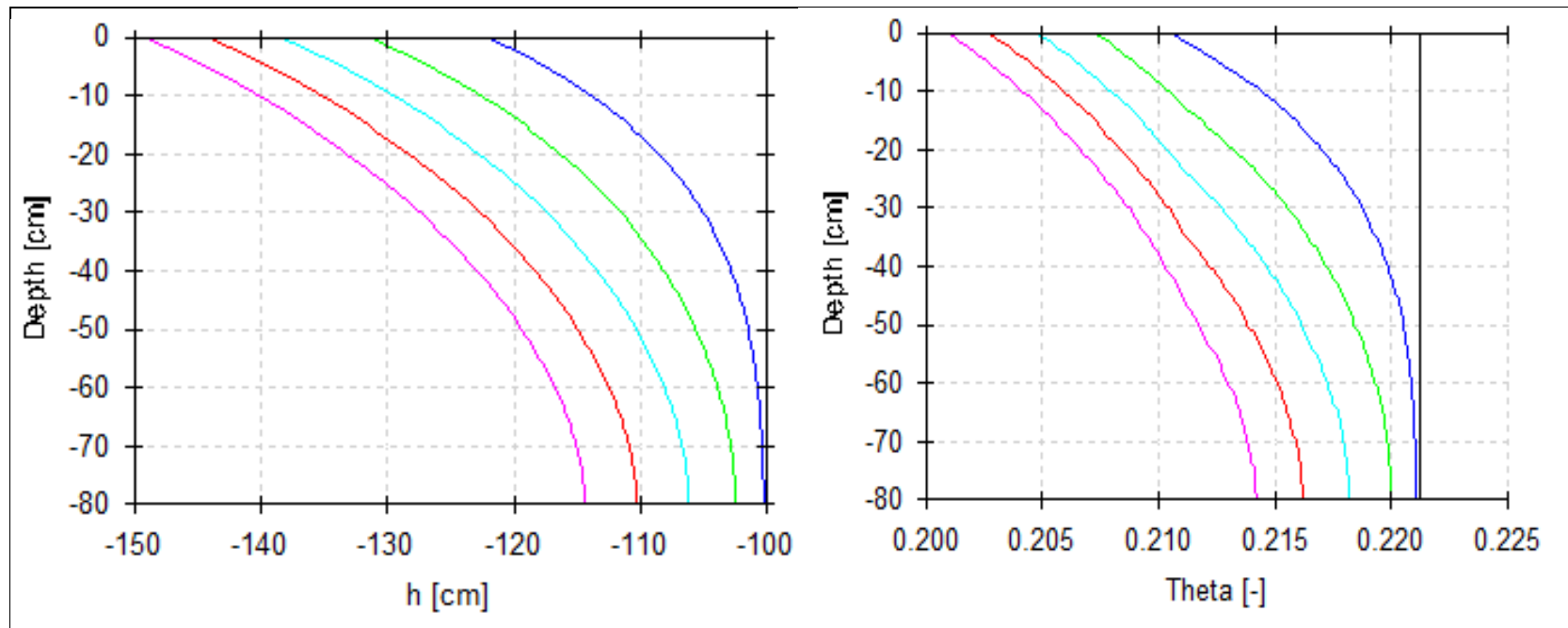
The effect of soil moisture variability on soil physical characteristics was compared using analysis of variance (ANOVA) for a randomized complete block design (RCBD) with ten (10) 5TM-ECH₂O sensors site treatments and five (5) depth replications. Least-squares-

difference (LSD) was used to distinguish significantly different means at the 5% probability level ($P \leq 0.05$). The analysis of MMNR rangeland ecosystem soil shown that, there was no significant difference in mean bulk density, particle density, and textural classes across sites with depths to soil moisture variation. Total organic carbon had no significant effect on soil moisture storage near the soil surface since the concentration of TOC was high near the soil surface and decreased gradually down the soil layers. Soil moisture storage was generally expressed as volumetric water content per unit area measured to a specific depth. This resulted in significant differences of soil moisture within depth increments where the variation in moisture was low near the soil surface and high below the surface.

4.5 Simulate the Influence of Soil Moisture Variability in Biomass Production Using Coupled Hydrus-1D and Agricultural Production Systems Simulator (APSIM) Model.

The water content simulated by Hydrus-1D on vertical profiles shown the moisture potential for vegetation growth in MMNR rangeland ecosystem. Similarly, crop simulation APSIM model was also used in the prediction of biomass production. Using similar input variables of soil properties, weather and vegetation, the output from the integrated models were displayed from graphic user interface as shown in subsequent tables and figures. The data measured for wheat biomass and crop yields were obtained from the farms of previously harvested biomass and yields (Appendix B.17 and B.18) where hay and wheat production is practiced (Figure 4.42, 4.45 and Appendix B.16). In the simulation of APSIM crop model, the dataset collected in MMNR rangeland were used for calibration while for Naivasha cropland was used as independent dataset for validation however, the MMNR climate data was partitioned for use in calibration and validation. The observed time series clipped AGB from various quadrates in dry and wet season was correlated with remotely sensed NDVI to explain the behaviour of soil moisture variability in rangeland and cropland ecosystem.

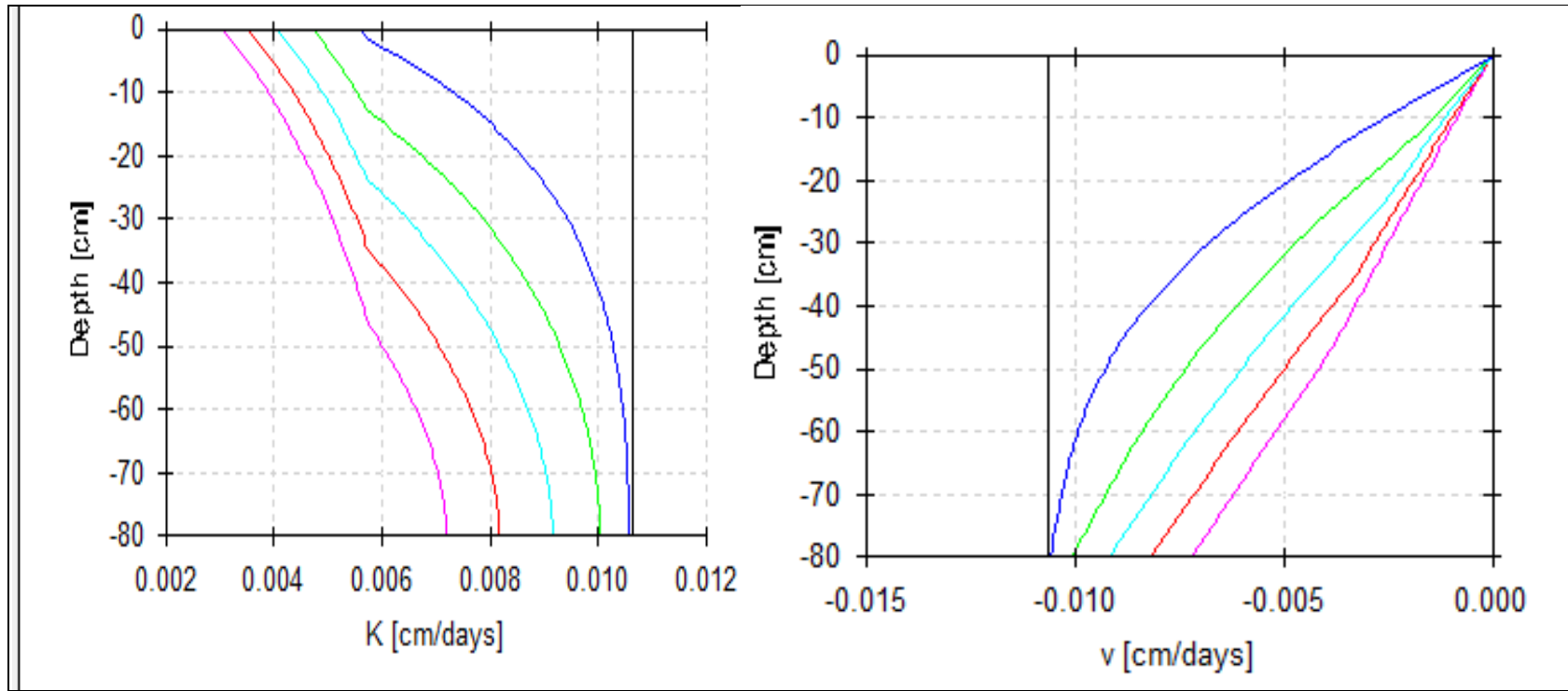
4.5.1 Simulation Results of Hydrus - 1D



(a)(b)

Figure 4.21: Variation of (a) matric potential and (b) volumetric water content with depths

Figure 4.21 shows how the Hydrus package makes use of pedo-transfer functions (PTFs) powered by neural networks to forecast van Genuchten's water retention parameters and the saturated hydraulic conductivity (K_s) from textural data. A field's capacity and the permanent wilting point are defined by the bulk density and soil water content at a pressure head (h) of -300 and -15,000 cm, respectively. In this case, the values were significantly underestimated by the Hydrus 1D package's pedo-transfer function. Consequently, the hydraulic conductivity and pressure head gradient at the soil surface are used to compute the amount of water penetrating over the soil surface (using Darcy-law), Buckingham's while any excess water is immediately eliminated as overland flows or surface runoff.



(a)

(b)

Figure 4.22: Variations of (a) flow and (b) hydraulic conductivity with depth in different periods

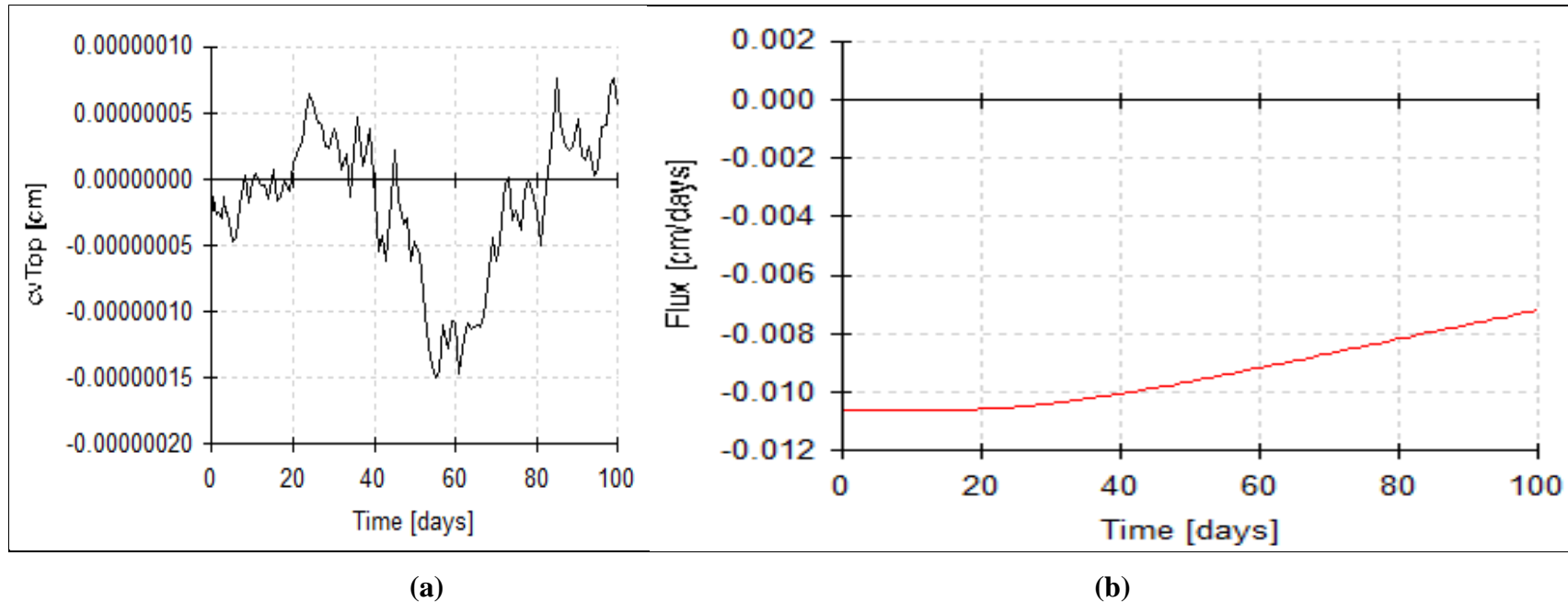


Figure 4.23: Variation of (a) surface layer input flow and (b) water fluxes in different periods

4.5.2 Hydrus-1D Model Calibration

Hydrus-1D was validated through hydraulic parameter optimization in response to a comparison of modelled and measured soil water content. We then performed a sensitivity analysis on the Mualem-van Genuchten model's hydraulic parameters. Simulated soil water contents were determined using Hydrus-1D, with a SWC percent of 2.1% on average (Table 4.26). Because of the small soil volume, the one-dimensional Hydrus-1 D model could accurately characterise the primary SPAC fluxes. Important parameters for characterizing the soil/plant water balance were the water content at saturation, the fitting parameters and n , and the slope of the fitting line. In the calibration of Hydrus-1D, five sets of hydraulic parameters, θ_r , θ_s , K_s , α , and n on depths (P1 to P5) were thought of, and these results were attained by using the Rosetta model's pedo-transfer function. Parameters, such as surface depth P1 (0-5cm), and bottom depth P5 (75-80cm), were estimated using independent

variables such the percentages of sand, clay, and silt in the five soil layers (i.e., 0-5cm, 5-10cm, 15-20cm, 35-40cm, and 75-80 cm) that were taken into account. Soil bulk density was also considered as an independent variable, along with the soil water content determined at soil water potentials of -300 cm and -15,000 cm. The lower bound and upper bounds of parameters, θ_r , θ_s , α and n of the van Genuchten Model are set and presented in Table 4.23. Further, the program has since been applied to estimate parameters of the van Genuchten model simulating the soil water retention capacity.

Table 4.23: Lower and upper bound of four van Genuchten model parameters

Parameter	θ_r	θ_s	α	n
Lower bound	0	0	0	1
Upper bound	1	1	100	100

In van Genuchten Model Parameter estimate, efficiency was determined using RETC program, here, the population size was selected as 20, and maximum number of iteration set was 20,000. In the study, final condition was done with the current iteration until it reached the maximum iteration. Different data sizes were used to set parameters for the corresponding individual soil sample. The parameters estimated via RETC program based on van Genuchten model was used to fit the measured data well and provided minimum and high values of upper and lower threshold (table 4.23).

From the observation shown in table 4.24 of most soil layers, soil texture ranged from sandy clay loam to sandy clay and again sandy clay loam with increased soil depth. Based on site results, sandy clay loam (SCL) had water content that varied from 0.18 to 0.19 (m^3/m^3) at -33 kPa and 0.06 (m^3/m^3) at -1500 kPa. However, in sandy clay textured soils, water content drastically increased from 0.18 to 0.28 (m^3/m^3) at -33 kPa and 0.07 to 0.13(m^3/m^3) at -1500 kPa. The saturated hydraulic conductivity indicated a value of 106cmd^{-1} (4.42cm/hr) for sandy clay loam textured soils and in sandy clay textured soils, it measured 31.44cmd^{-1} (1.31cm/hr). In a different study conducted by a similar evaluation of water flow and infiltration using the HYDRUS model in a sprinkler irrigation system, Honar *et al.* (2011) found similar results, with sand accounting for 22%, silt for 43%, and clay for 35% of the total dissociation. The soil was only one meter deep and consisted of a single layer. We started with 15% soil moisture, used 6.6mm/hour of sprinkler intensity, and irrigated for 12 hours.

Table 4.24: Estimated van Genuchten physical and empirical parameters based on soil constituent particles

Sensor Port Id	Soil Layer (cm)	Soil Texture	$\theta_r(cm^3cm^{-3})$	$\theta_s(cm^3cm^{-3})$	$\alpha(cm^{-1})$	n	$K_s(cm d^{-1})$
P1	0-5	Sandy Clay Loam	0.065	0.41	0.075	1.89	106.1
P2	5-10	Sandy Clay Loam	0.065	0.41	0.075	1.89	106.1
P3	15-20	Sandy Clay	0.100	0.39	0.059	1.48	31.44
P4	35-40	Sandy Clay Loam	0.065	0.41	0.075	1.89	106.1
P5	75-80	Sandy Clay Loam	0.065	0.41	0.075	1.89	106.1

From table 4.24, it can be noted that at 40m and 80m depth profiles, Kissinger station had soils mainly sandy clay and at 1540 m elevations here, two-soil sample layers were made of sandy clay and rest three profiles were sand clay loam. Observations show that there was no significant difference in textural classes since most of the sites soils had homogeneous characteristics with different depth profiles as determined from excavated various pit samples.

Table 4.25: Measured and simulated soil water content using Hydrus 1D across Maasai Mara National Reserve Rangeland Ecosystem

Depth ID	Depth (cm)	Bulk density (gcm⁻³)	Measured SWC(m³m⁻³)	Predicted SWC (m³m⁻³)	Textural Class
P1	0-5	1.40	0.214	0.222	SCL
P2	5-10	1.45	0.257	0.261	SCL
P3	15-20	1.34	0.291	0.298	SC
P4	35-40	1.19	0.316	0.323	SCL
P5	75-80	1.22	0.344	0.347	SCL
Mean		1.32	0.284	0.290	

Observed SWC – Variance, $V = 0.026$, Standard deviation, $SD = 0.0507$ and Standard Error, $SE = 0.0227$ and Predicted SWC – $V = 0.025$, $SD = 0.0497$ and $SE = \pm 0.0222$

Table 4.25 indicates the difference between the measured data and the estimated data soil water with depths of 10, 5TM-ECH₂O soil moisture, temperature, and soil textural classes across the rangeland ecosystem. From the table, we can see that the data are different in type,

bulk density, depth location and the number of data points, which indicates that the observed water content had variance of 0.026; SD of 0.0507 and SE of ± 0.0227 and the estimated water content had variance of 0.025, SD of 0.0497 and SE of ± 0.0222 respectively.

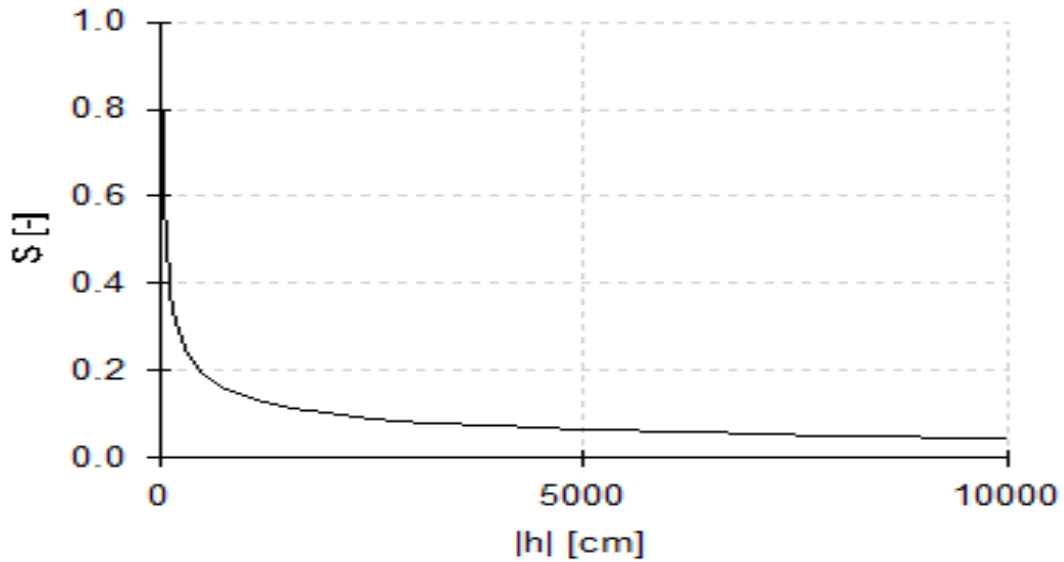


Figure 4.24: Soil moisture characteristic curve

Figure 4.24 depicts a scenario where the shape of the soil water retention curve controls the linear relationship between the mean soil moisture and its standard deviation. Heterogeneity in soil characteristics may explain for over 80% of the observed standard variation of water contents, as demonstrated by the comparison of simulated and observed soil moistures within a (0-10) cm thick topsoil layer.

Table 4.26 and 4.27 shows the statistical performance of three soil water content determination approaches and through their mean comparisons, gravimetric water content gave significantly higher performance with NSE of 0.998, $r = 0.000$, $RMSE = 0.0035 \text{ m}^3 \text{ m}^{-3}$ and R^2 was 0.998. The 5TM-ECH₂O approach gave fair prediction as compared to cosmic ray neutron sensor technique with NSE = 0.978, $r = 0.000$, $RMSE = 0.0332 \text{ m}^3 \text{ m}^{-3}$ and $R^2 = 0.933$ in relation to the overall model performance prediction results of NSE = 0.918, $r = 0.000$, $RMSE = 0.0159 \text{ m}^3 \text{ m}^{-3}$ and $R^2 = 0.923$.

Table 4.26: Hydrus-1D statistical evaluation of measured and predicted/simulated modelled soil water/moisture content across the rangeland ecosystem

Depth (cm)	NSE	R	RMSE (m^3m^{-3})	R ²
0-5	0.987	0.000	0.010	0.987
5-10	0.992	0.000	0.006	0.992
15-20	0.867	0.000	0.009	0.867
35-40	0.953	0.000	0.007	0.953
75-80	0.993	0.000	0.004	0.993

Table 4.27: Statistical indicators comparing performance of three approaches applied to describe the measured soil water content across the rangeland ecosystem

Method/Technique	NSE	r	RMSE(m^3m^{-3})	R ²
Gravimetric	0.998	0.000	0.0035	0.998
5TM-ECH ₂ O probes	0.978	0.000	0.0332	0.993
Cosmic Ray Neutron Sensor	0.779	0.000	0.0111	0.779
Overall Performance	0.918	0.000	0.0159	0.923

During both the calibration and validation years, the CRNS method yielded the most accurate predictions of root zone soil moisture at the field scale (RMSE = 0.0035 m^3m^{-3}), followed by the exponential filter (RMSE = 0.0035 and 0.0159 m^3m^{-3} for the calibration and validation years, respectively). The estimated data using the BEST approach yielded good modelling results (RMSE = 0.023 and 0.022, and R² = 0.72 and 0.81), and the optimized results (RMSE = 0.012 and 0.020, and R² = 0.83 and 0.72) were also well predicted. A second experiment was conducted by McGraw *et al.* (2015) to assess the efficacy of the CRNS approach for small watersheds in two semiarid ecosystems in the south-western United States. The watersheds were outfitted with a distributed sensor network comprised of soil moisture sensors. Over the course of the 19-month investigation, the authors observed that the CRNS approach and the distributed sensor network generated RMSE values of 0.009 and 0.013 m^3m^{-3} in a mesquite savannah in the Santa Rita Experimental and a mixed shrub land in the Jornada Experimental Range, respectively. This was primarily due to the inclusion of 5cm depth sensor observations of shallow soil moisture. As indicated, the results slightly differed with this study where the RMSE ranged between 0.0035 and 0.0332 m^3m^{-3} observed from gravimetric CRNS and distributed 5TM-ECH₂O sensor network conducted at semi-arid MMNR rangeland ecosystem. Vather *et al.* (2018) conducted research on CRP installation

and adjustment in Cathedral Peak Catchment VI, South Africa. CRP soil moisture estimates were checked against an in-situ soil moisture network made up of time-domain reflectometry and Echo probes. It was discovered that once the CRP was calibrated, it could offer spatial estimates of soil moisture that were highly correlated with the in-situ soil moisture network data set, with an R^2 value of 0.845.

4.5.3 Sensitivity Analysis

The study's parameterization approaches were evaluated for their ability to replicate soil water fluxes, and then a sensitivity analysis was performed to determine which hydraulic parameters were most sensitive in describing the soil water balance. This was done to cause perturbation on each of the five parameters namely residual water content, θ_r (m^3m^{-3}), saturated water content, θ_s (m^3m^{-3}), saturated hydraulic conductivity, K_s (cm d^{-1}) alpha, α and n (cm^{-1}) (fitting parameters) by increasing the corresponding values used in bottom layer P5 (75-80cm) by + 10% and running Hydrus-1D simulations again.

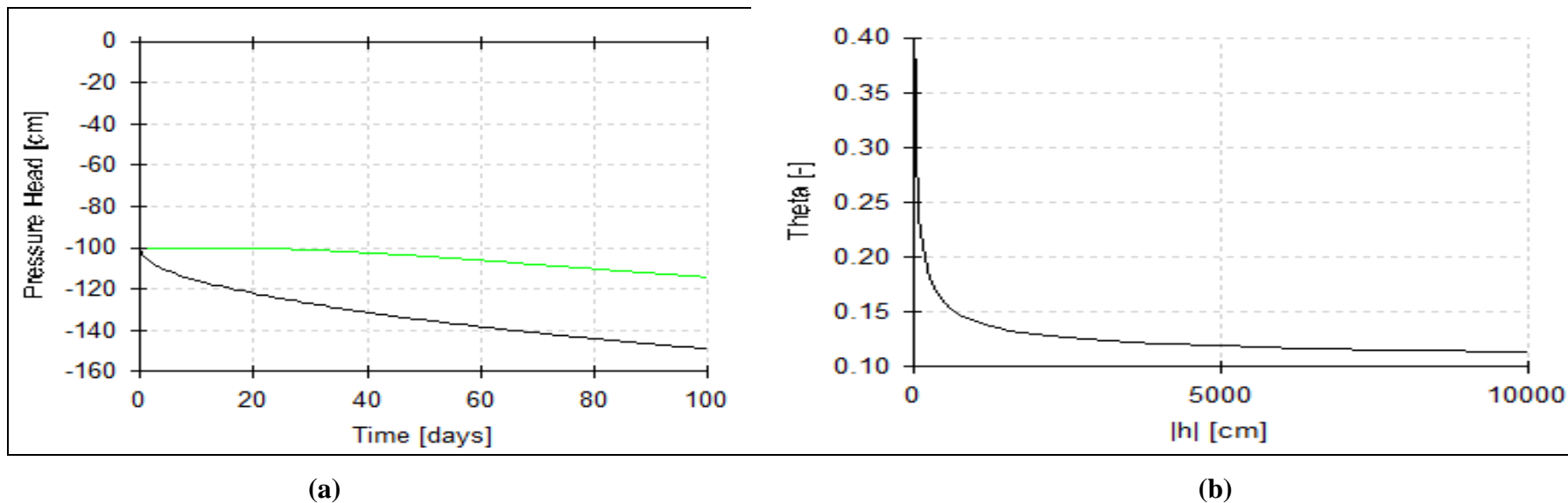


Figure 4.25: Variation of (a) Pressure heads in different periods (b) relation between volumetric water content and matrix potential

Figure 4.25 shows the soil pressure head (h) and soil water content (SWC) trends at varied depths (0 and 100 cm) in different periods. The perturbed increase of hydraulic parameters had a significant impact in the computation of the SWC both in the superficial (0-5cm) layer and in the deep layer (75-80cm). It was seen that θ_s and n were the most sensitive parameters for the shallowest layer and their +10% perturbation resulted in SWC variations that reached up to 40 and -25%, respectively. High impact on pressure head (h) occurred during dry season when there was short and low rainfall that caused strong reduction of SWC, especially in the 0-20 cm layer. The perturbation of input parameters θ_r and K_s had no significant effects while that of θ_s and n resulted in an increment of 30% while that of α in a reduction of 10%.

4.6 Measured Aboveground Standing Grass Biomass at Maasai Mara Rangeland Ecosystem

Table 4.28: Observed aboveground standing Biomass, Meta Plains – Main Mara, 12/12/2017_Dry season

Sample ID	Coordinates		Quadrat Area size (m)	Area in m ²	Wet wgt (Kg)	Dry wgt (Kg)	Projected biomass in tons/hac	Biomass in Kg/m ²
	Latitudes	Longitudes						
A	- 1.93320	35.149133	2.5m x 2.5m	6.25	2.828	2.150	3.440	0.344
B	-1.493388	35.149170	2.5m x 2.5m	6.25	2.500	2.000	3.200	0.320
C	-1.493428	35.149188	2.5m x 2.5m	6.25	2.800	2.215	3.544	0.354
D	-1.493398	35.143170	2.5m x 2.5m	6.25	1.950	1.500	2.400	0.240
E	-1.493317	35.149268	2.5m x 2.5m	6.25	3.100	2.450	3.920	0.392
F	-1.493400	35.149240	2.5m x 2.5m	6.25	2.800	2.000	3.200	0.320
Average					2.663	2.053	3.284	0.328

From table 4.28 and 4.29, it can be seen that during the dry season in 2017, the observed aboveground biomass (AGB) at this site measured an average dry biomass weight of 0.328 kg/m² or 3.28 tons/hac (Table 4.29) and this were from six replicated quadrats that had slight variations in their measurements. The non-standing biomass during clipping is also taken as part of the quadrat sample for which losses is accounted for in weighing of the biomass. The aboveground biomass from a similar site on a wet season of 2017 also varied slightly with an average weight on dry matter basis was 1.634 kg/m² or 10.208 tons clipped from 2.5m by 2.5m quadrat. The standard deviation was 0.0508 kg/m² while the standard error of the mean was ±0.0376. The following year in 2018, there was heavy rainfall, which fell almost throughout the year, and the above ground biomass harvested were dried and measured from each quadrat and the results were high as compared to 2017.

Table 4.29: Observed aboveground standing biomass, Mara – Meta Plains – Main Mara, 05/05/2018_Wet season

Sample ID	Coordinates		Quadrat Area size (m)	Area in m ²	Wet wgt (Kg)	Dry wgt (Kg)	Projected biomass in tons/hac	Biomass in Kg/m ²
	Latitudes	Longitudes						
A	-1.493320	35.149133	2.5m x 2.5m	6.25	11.575	5.910	9.456	1.513
B	-1.493388	35.149170	2.5m x 2.5m	6.25	11.125	7.015	11.224	1.796
C	-1.493428	35.149188	2.5m x 2.5m	6.25	9.200	5.455	8.728	1.397
D	-1.493398	35.143170	2.5m x 2.5m	6.25	11.550	6.187	9.899	1.584
E	-1.493317	35.149268	2.5m x 2.5m	6.25	10.350	6.489	10.382	1.661
F	-1.493400	35.149240	2.5m x 2.5m	6.25	13.100	7.225	11.560	1.850
Average					11.150	6.380	10.208	1.634

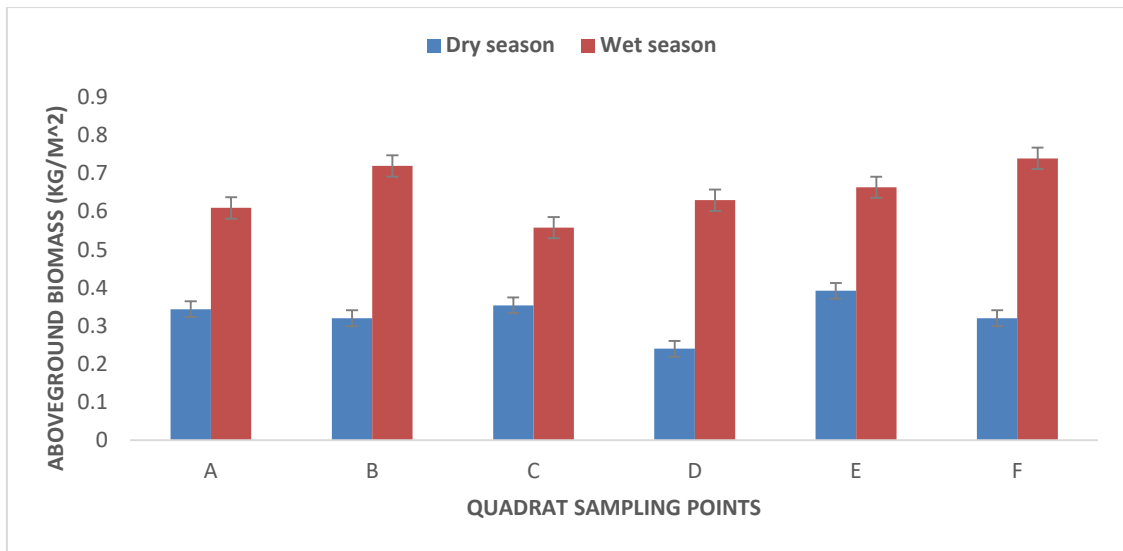


Figure 4.26: Box plot of selected trend of Mara main aboveground biomass per quadrat during dry and wet season

Figure 4.26 indicates that during the wet periods, green grass biomass was high as compared to dry season. There was better biomass coverage on the upper catchment area such as Mara main station, Olimisiogioi, Upstream and Helicopter and most of them were homogeneously distributed with green biomass cover across the rangeland with scarce scenery of mixed shrubs and tall trees along the river channels and streams passing across the rangeland. On lowlands toward Mara Bridge with low altitude (1520m), there was less vegetation/grass coverage in the western and southern periphery of the catchment while, better grass vegetation coverage was observed in the northern part of MMNR ecosystem sites. The digital scale weighed dry matter biomass was the final mass of both standing and non-standing AGB was taken to represent the weight within each quadrat sampled.

Table 4.30: Comparison of distributed above ground standing biomass in Maasai Mara catchment sites during dry and wet season

Location	Coordinates		Quadrat Area in m ²	Average Dry season wgt (Kg)	Average Wet wgt (Kg)	Dry Season Biomass in Kg/m ²	Wet Season Biomass in Kg/m ²
	Latitudes	Longitudes					
Mara Main	-1.49332	35.14918	0.255	2.053	2.663	0.328	0.654
Kissinger	-1.55889	35.23664	0.147	0.092	0.190	0.366	0.589
Ashnil	-1.45291	35.07215	0.109	0.093	0.198	0.371	0.437
Helicopter	-1.53042	35.17422	0.103	0.097	0.172	0.389	0.413
Talek	-1.46117	35.18276	0.103	0.089	0.148	0.357	0.412
NiceBridge	-1.49519	35.19034	0.104	0.092	0.185	0.360	0.414
V-section	-1.46249	35.10616	0.103	0.089	0.182	0.355	0.411
Upstream	-1.52919	35.23824	0.106	0.089	0.148	0.354	0.423
Olimisiogioi	-1.50384	35.12008	0.099	0.090	0.148	0.365	0.397
Mara Bridge	-1.53833	35.03615	0.077	0.066	0.143	0.264	0.308
Total AGB		35.094		2.850	4.177	3.509	4.458

During the dry season, low vegetation coverage class was in 2017 experienced because of low and short rainy seasons. Land generally occupied by MMNR rangeland ecosystem covers 1,534km² and the area covered as grassland were estimated to be 717.203km² (46.75%) as indicated in (Table 4.39). The total above ground biomass (AGB) for the entire rangeland ecosystem during the dry season was 35.094 tonha⁻¹ that converts to seasonal quantify of 2,516,952.208 tonnes and during the wet seasonal AGB was 42.123 tonha⁻¹, which translates into 3,021,074.197 tonnes biomass.

This conversion was based on the whole of Maasai Mara National Reserve as a rangeland ecosystem when vegetation cover density was at its maximum productivity, however the quantity may not be precise because of wildlife feeding such as the largest wildebeest population when aboveground grass biomass was being sampled. From the seasonal quantitative analysis of vegetation coverage in both seasons shown in table 4.39, there was 79.92% high vegetation coverage class in the year 2018 wet season characterized with yearly high vegetation cover classes from high to low between 2018 (79.92%) and 2017 (20.07%) consecutively.

Kariuki *et al.* (2018) found similar discoveries, noting that the home density, distance to road, grass biomass, livestock density, and wildlife density all follow normal distributions with means and standard deviations in the Amboseli and Mara habitats. In addition, the model's results show that the density of wildlife is higher in rainy years than in dry years, and that the density of wildlife is lower in private land tenure than in communal and government property.

4.6.1 Observed and Simulated Output Results Obtained from APSIM Model

The results for the measured Above Ground Biomass (AGB) from the (10) 5TM-ECH₂O stations in MMNR rangeland ecosystem were tabulated in tables (4.31 and 4.32) for both dry and wet season and their respective model performance in table 4.33 and 4.34 which indicates that the model performed reasonably well in this ecosystem simulations. Tables 4.31 and 4.32 indicates the rangeland sites quadrat aboveground biomass and water demand utilized in each growing location during dry and wet season. Despite the uniformity in quadrat area of 0.25m², the clipped biomass varied from one site to the other. This is due to the influence of environmental factors attributed to variation in climate, soil and the surrounding vegetation. The water demand for each dry matter generated during the bi-seasons (dry and wet) indicates higher water use in wet than in dry season signifying that when plants are water stressed, less biomass and subsequent yield production occurs. Most of this rangeland is dominated by standing grass of various species but they adapted well to the ecosystem natural conditions. From the tables, it can be noted that the aboveground biomass in dry season had a mean of 350.9 g/m², which was slightly lower than that of wet season, which had a mean value of 445.9g/m² which when converted becomes 3.51 and 4.46 tonha⁻¹ respectively.

Table 4.31: Measured and simulated aboveground standing grass dry matter (biomass) during dry season

Location Id	Quadrat Area in m²	Observed Above Ground Standing Biomass(g/m²)	Simulated Aboveground Standing Biomass (g/m²)	Observed Above Ground Standing Biomass(tonha⁻¹)	Simulated Aboveground Standing Biomass (tonha⁻¹)	Water Demand (mm)
Mara Main	0.25	328	332	3.28	3.32	4.444
Kissinger	0.25	366	362	3.66	3.62	4.596
Ashnil	0.25	371	367	3.71	3.67	4.464
Helicopter	0.25	389	383	3.89	3.83	4.808
Talek	0.25	357	355	3.57	3.55	4.668
Nice Bridge	0.25	360	363	3.60	3.63	4.705
V-section	0.25	355	349	3.55	3.49	4.583
Upstream	0.25	354	348	3.54	3.48	4.481
Olimisiogioi	0.25	365	361	3.65	3.61	4.584
Mara Bridge	0.25	264	258	2.64	2.58	3.981
Mean		350.9	347.8	3.51	3.48	4.531

Table 4.32: Measured and simulated aboveground standing grass dry matter (biomass) during wet season at Maasai Mara rangeland ecosystem.

Location Id	Quadrat Area in m ²	Observed Above Ground Standing Biomass (g/m ²)	Simulated Aboveground Standing Biomass (g/m ²)	Observed Above Ground Standing Biomass (tonha ⁻¹)	Simulated Aboveground Standing Biomass (tonha ⁻¹)	Water Demand (mm)
Mara Main	0.25	654	678	6.54	6.78	6.594
Kissinger	0.25	589	575	5.89	5.75	6.712
Ashnil	0.25	437	425	4.37	4.25	5.656
Helicopter	0.25	413	413	4.13	4.13	5.798
Talek	0.25	412	413	4.12	4.13	5.815
Nice Bridge	0.25	414	415	4.14	4.15	5.583
V-section	0.25	411	415	4.11	4.15	5.532
Upstream	0.25	423	428	4.23	4.28	5.556
Olimisiogioi	0.25	397	392	3.97	3.92	5.530
Mara Bridge	0.25	308	302	3.08	3.02	4.981
Mean		445.9	445.5	4.458	4.456	5.776

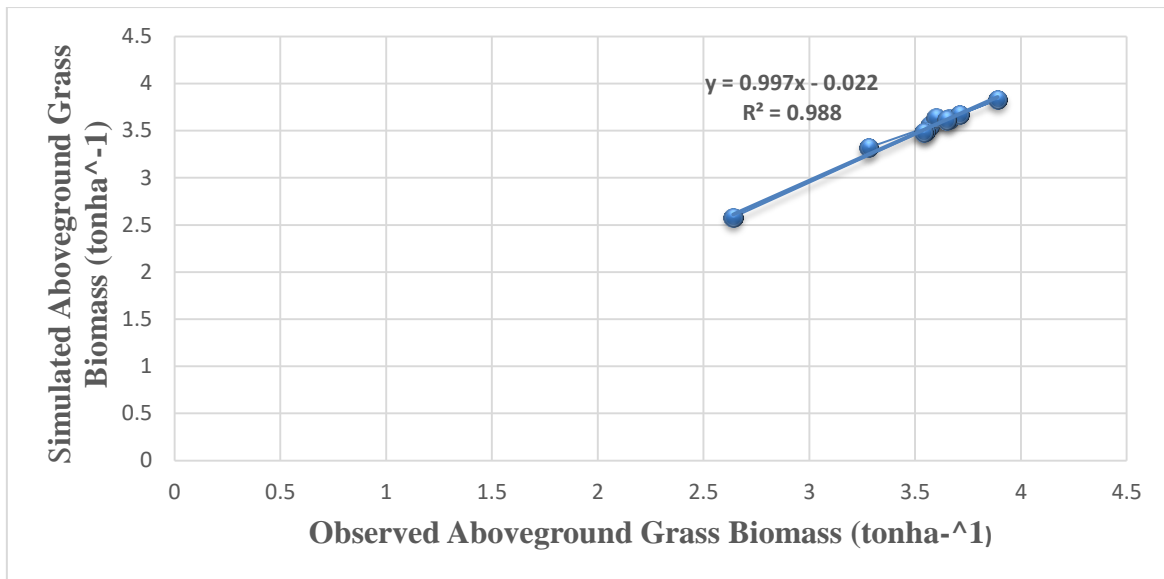


Figure 4.27: Observed and Simulated aboveground grass biomass in dry season

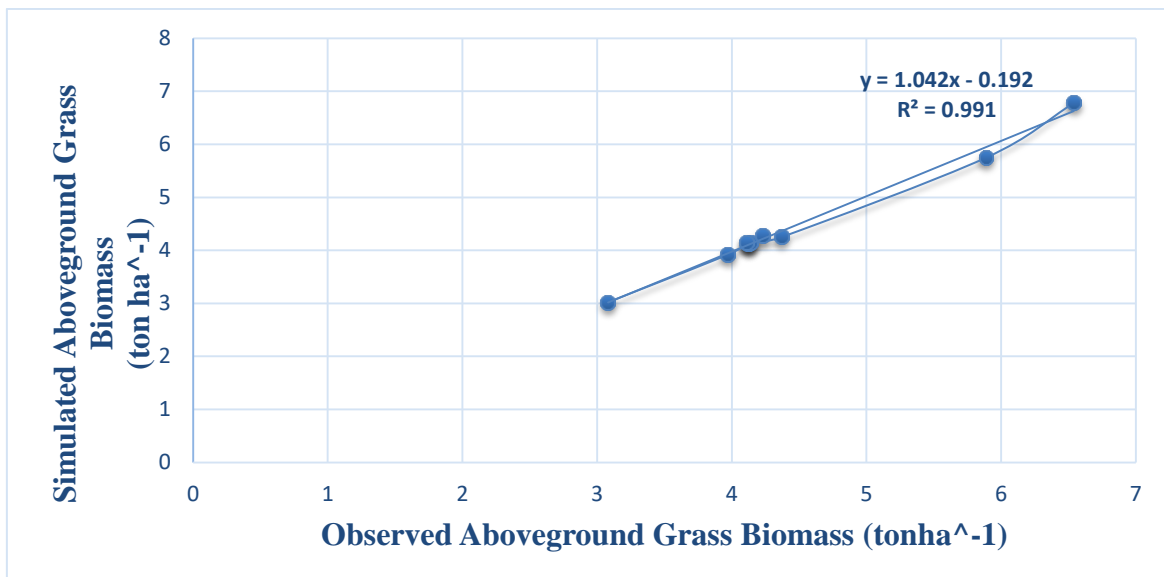


Figure 4.28: Simulated and observed aboveground grass standing biomass wet season

The figures 4.27 and 4.28 shows the model simulated well the aboveground biomass indicating the close relationship between the observed and the predicted biomass. The model underestimated the AGB for the dry season while slightly overestimated for the wet season and the results for the coefficient of correlation was $R^2 = 0.9882$ and $R^2 = 0.9914$ respectively signifying that the measured and the simulated grass aboveground biomass was closely determined to be nearly similar in their production in every season.

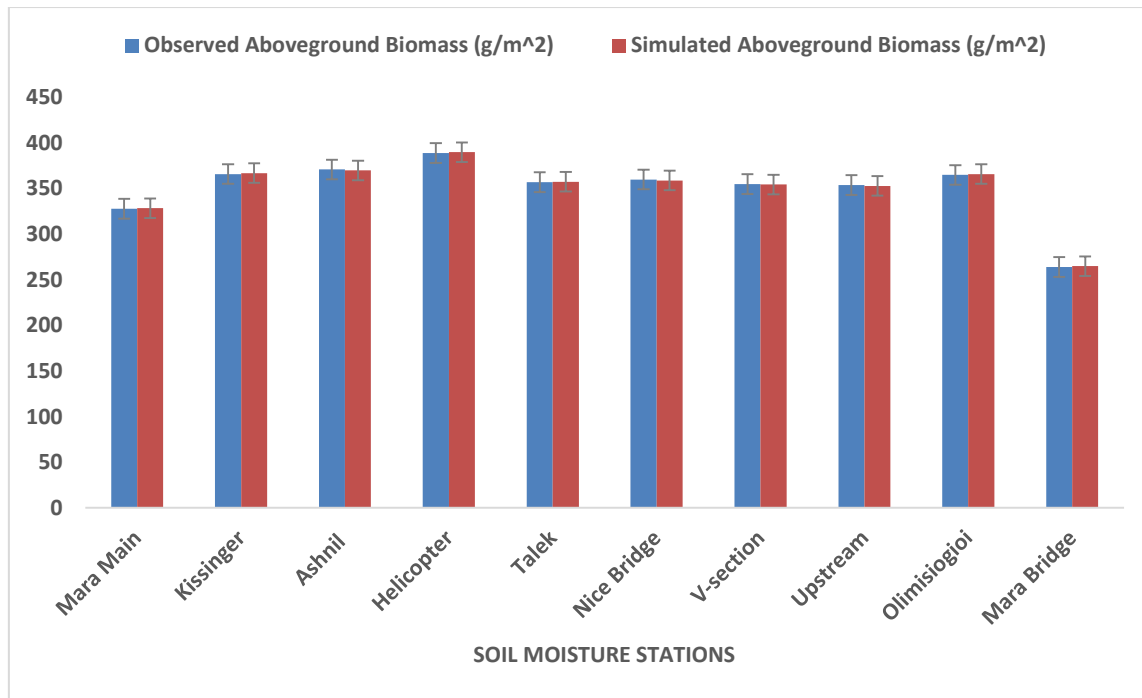


Figure 4.29: Observed and simulated aboveground standing aboveground grass biomass for respective soil moisture sites

Figure 4.29 indicates the observed and predicted standing aboveground grass biomass from various 5TM-ECH₂O sites and from the results shown in the boxplot, Helicopter had the highest production from the averaged replicated quadrats followed by olimisiogioi, which also produced much AGB than the rest of the sites. This depicts that there is a slight difference across the rangeland ecosystem and most sites such as Talek, Nice Bridge, V-section and Kissinger and Ashnil have homogeneous aboveground biomass production.

4.6.2 Statistical Evaluation of Model Performance

In this study, linear regression analysis was applied to compare paired data-points for observed and simulated aboveground standing biomass for grass in MMNR rangeland ecosystem. Model performance of the used models were also evaluated using Nash Sutcliffe Efficiency (NSE), Pearson product moment correlation coefficient (r), and the root mean square error (RMSE) as indicated in equations (3.52, 3.53 and 3.54) respectively. The slope, intercept, and coefficient of determination/correlation (R^2) of the linear regression between simulated and observed values were also determined as shown in equation (3.56). Among the indices, the R^2 and the RMSE are preferred here for model comparison. Ma *et al.* (2011) stated that for a “point” agricultural model like APSIM to be calibrated adequately the R^2 and the RMSE should be above 0.8 and <10% (0.1), respectively. The above rating scale was applied in this study.

Table 4.33: Overall APSIM model performance of observed and simulated aboveground standing grass biomass in MMNR rangeland ecosystem during dry season

Location ID	NSE	r	RMSE (gm ⁻²)	R ²
Mara Main	0.963	0.000	0.089	0.963
Kissinger	0.901	0.000	0.084	0.901
Ashnil	0.944	0.000	0.059	0.944
Helicopter	0.900	0.000	0.067	0.900
Talek	0.958	0.000	0.064	0.958
Nice Bridge	0.917	0.000	0.032	0.917
V-section	0.925	0.000	0.062	0.925
Upstream	0.927	0.000	0.077	0.927
Olimisiogioi	0.860	0.000	0.061	0.860
Mara Bridge	0.927	0.000	0.077	0.927
Overall	0.979	0.000	0.047	0.979
Performance				

Table 4.34: Overall APSIM Model performance of observed and simulated aboveground standing grass biomass in MMNR rangeland ecosystem during wet season

Location ID	NSE	r	RMSE (gm ⁻²)	R ²
Mara Main	0.934	0.000	0.251	0.934
Kissinger	0.938	0.000	0.295	0.938
Ashnil	0.970	0.000	0.181	0.970
Helicopter	0.906	0.000	0.042	0.906
Talek	0.859	0.000	0.047	0.859
Nice Bridge	0.907	0.000	0.021	0.907
V-section	0.812	0.000	0.059	0.812
Upstream	0.942	0.000	0.049	0.942
Olimisiogioi	0.840	0.000	0.061	0.840
Mara Bridge	0.970	0.000	0.068	0.970
Overall Performance	0.988	0.000	0.103	0.988

The tables 4.33 and 4.34 shows that APSIM model simulated reasonably well the observed standing aboveground biomass of rangeland ecosystem. This follows that NSE was 0.988, r =

0.000, RMSE = 0.103ton/ha and R^2 was 0.988. The NSE and R^2 gave similar simulation results though the model overestimated. The study was contrary with an experiment conducted by Archontoulis *et al.* (2014) on evaluating APSIM maize, soil water, soil nitrogen, manure, and soil temperature modules in the Midwestern United States and found that biomass production for maize gave the RMSE = 0.77 Mgha⁻¹ and grain yield RMSE = 0.53 Mgha⁻¹, however the model underestimated the results. The calibrated model was evaluated against end of season grain yield data which showed a very good performance of $R^2 = 0.87$ and biomass production, $R^2 = 0.96$.

4.7 Naivasha Cropland Rainfall Characteristics



Figure 4.30: Automatic Weather Station at Kijabe Farm Naivasha Cropland

The Naivasha cropland ecosystems during the study period had the highest annual rainfall received in 2010 with 1154mm and the lowest was 635mm in 2014, which was followed by 2016 with 773 mm. The area fell within the potential agro ecological zones of Kenya, which defines zones based on combinations of soil, landform and climatic characteristics and edaphic requirements of crops and on the management systems under which the crops are grown for production. The rainfall regimes for this cropland in the last decade has tremendously supported production of biomass such as pasture, fodder and food produce for both livestock and human consumption. The rainfall ranges for the last decade ranged between 600mm to 1200mm of annual rainfall with most falling between the months of March and June. The ecological zone to which this area falls is zone (IV) a semi-arid area due to its characteristics favourable to crop production. These are the periods when most of the

crops including non-crop plants grew since the soil moisture stored within the root zone could support plants growth.

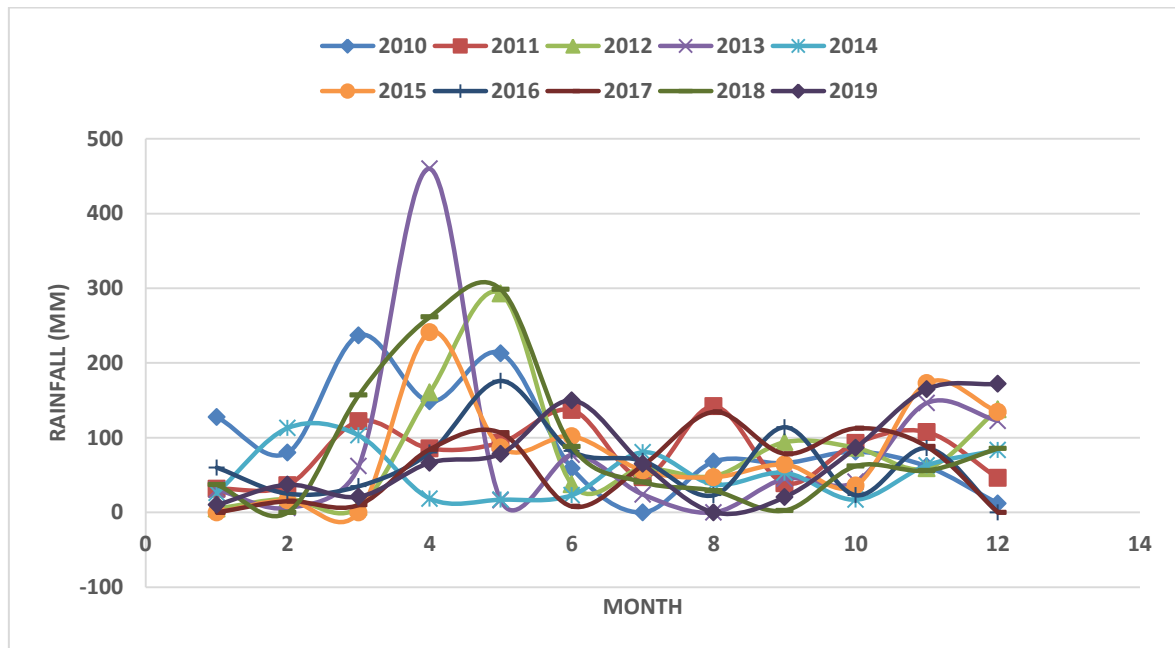


Figure 4.31: Trend of Monthly rainfall for Naivasha Cropland: 2010-2019

Figure 4.31 indicates that the Naivasha rainfall regimes for hydrological years where most of the rainy periods onset begins between March to the end of June and thereafter the area received intermittent rains that felt between July to the end of December which shown similar characteristics throughout the rainfall time series from 2010 to 2019. The highest rainfall was experienced in the month of April 2013 with 460mm, which was followed slightly with lower rainfall in the months of May to December.

4.7.1 Soil Information for Naivasha Cropland Ecosystem

a) Delamere Manera estate farm

The soil texture of this area is mainly sandy loam soils according to the soil analysed hydrometrically in 2018; the soil conditions had varied results. The soil pH (H₂O) potential of hydrogen ions was 8.74 and alkalinity has had similar value for the last three years as previously analysed. The electrical conductivity EC (salts) measured in mS/cm were determined by potentiometric method which was found to be 541 and the concentration of phosphorous (Olsen) in parts per million were 20.7 and potassium 1160(7.22%), calcium 5790(70.3%), magnesium 342(6.92%) their constituent's ratios and percentages, obtained using the colorimetric and spectroscopy methods respectively. The amount of soil organic matter present in the soil was 4.41% and total nitrogen was 0.22% determined by colorimetric technique. Other micronutrients of the chemical properties of the elements present were sulphur 99.8 ppm, sodium 1220 ppm, iron 91.5 ppm, manganese 216 ppm, boron 1.80 ppm,

copper 1.66ppm, zinc 6.45 ppm and the C.E.C in meq/100g was 41.2. The ratio of C/N ratio was 11.7, which indicated that the top soil of this area has very high pH, very low concentration of magnesium, very high sulphur, high sodium presence, high manganese, with very high C.E.C. The percentage concentration of these elements has very low percent of magnesium, high percent of sodium (ESP) and low percent of other bases including very low percent of hydrogen with very high calcium to magnesium (ca: mg) ratio in the soil. Due to high soil pH the elements calcium, magnesium, potassium, and sodium present in their respective concentrations were extracted using ammonium acetate (pH 8.0) solution. The soils are suitable for wheat, maize, and barley as cereals crop and for growing pastures such as Burma Rhodes, natural grass for human food consumption and livestock feeds.

4.7.2 Soil Moisture Characteristics

Figure 4.41 displays a time series of volumetric water content collected from field-deployed, calibrated 5TM-ECH₂O probes. Soil moisture responses were analyzed as a function of precipitation, and it was found that events with precipitation more than 15 mm elicited almost instantaneous reactions from all 10 sites. Maximum values of 0.33 and 0.37 m³m⁻³ were recorded for soil water content increase at Kijabe/Ndabibi and Delamere/Minera farm between May and July of 2018 and 2019, respectively. The soil moisture at Kijabe/Ndabibi and Delamere/Manera farms had a significant spike at the end of May 2018, likely impacted by the 261.5mm of rainfall received between March and April. However, the soil moisture remained relatively steady until the conclusion of the rainy period in July. During 2018's rainfall events, soil moisture variability was larger than in 2017's, with several sudden increases and decreases in soil water content. These spatial and temporal variations in soil moisture were most likely linked to the varying behaviour of precipitation in the three years under study (2017, 2018, and 2019). (Figure 4.31). Whereas in 2018, the rainy season began earlier in March and lasted until July, wet season was also observed in August and September. The highest rainfall was received in Naivasha cropland on April 2013 with 460mm and similarly on 298.5mm in May 2018, which eventually increase soil moisture levels that result in seasonal moisture variation.

4.7.3 Soil moisture variability in selected Naivasha cropland

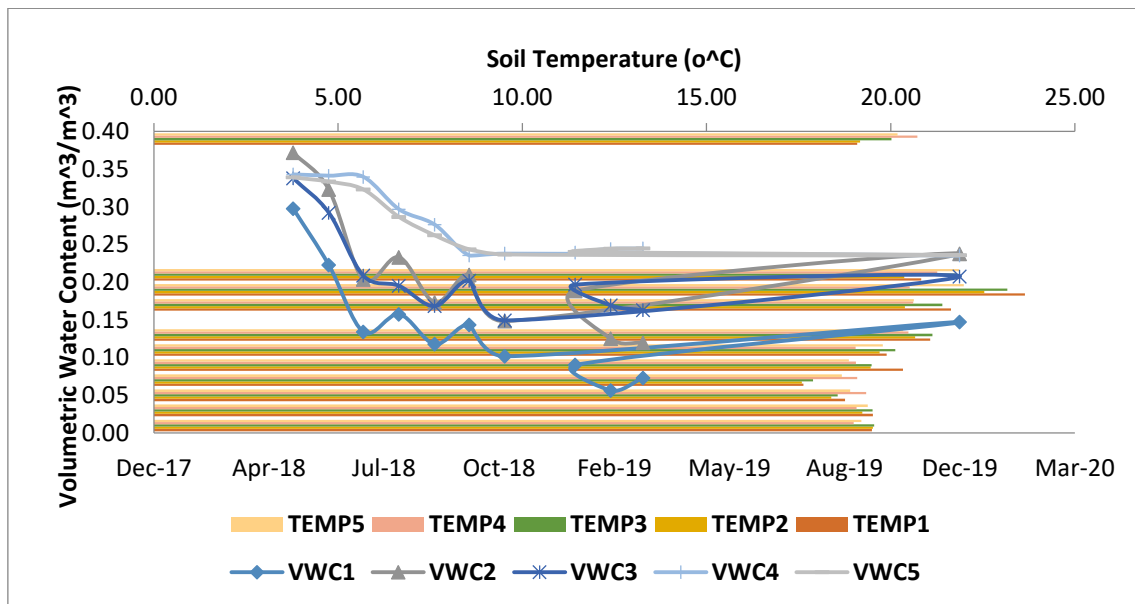


Figure 4.32: Soil moisture and temperature variation per depth profile for Kijabe/Ndabibi 5TM- ECH₂O site: 2017-2019

The volumetric water content was low at 0-5cm depth due to the influence of evapotranspiration near the soil surface and vegetation use as compared to the soil layer at 75-80cm depth since the water that infiltrated into the soil had no environmental influence. The water retained below the land surface was unexposed to changes of ground heat flux, which due to fluctuation of temperature may have had little influence on moisture below the surface. Root zone depletion of soil moisture may also have resulted from water percolation into the soil and utilization of moisture by vegetation/plants for their growth and development during transpiration process. The figure 4.32 indicates the variation of soil moisture in relation to temperature changes where during the month of April through December in 2018 and 2019, the moisture gradually decreased through from April to December due to occurrence of subsiding rainfall during the season. Soil moisture storage and retention was high due to proper soil texture and structure, however high temperature between the land surface and the atmosphere occurred due to the trade-off between latent and sensible heat fluxes. As seen from Figure 4.33, the beginning of April to December 2018, the volumetric water content decreased gradually from the top layer to the bottom layer of the soil profile. This phenomenon occurred due to the influence of moisture changes caused by varying temperature, relative humidity, wind speed, wind strength, wind direction, water vapour fluxes including average carbon dioxide concentration of 330 ppm and this altered plants growth through photosynthetic processes hence low biomass and bloomy formation during

the season. From field observation, temperature has direct effect on soil moisture variability and therefore rise in temperature in a given period causes rapid surface loss of soil moisture.

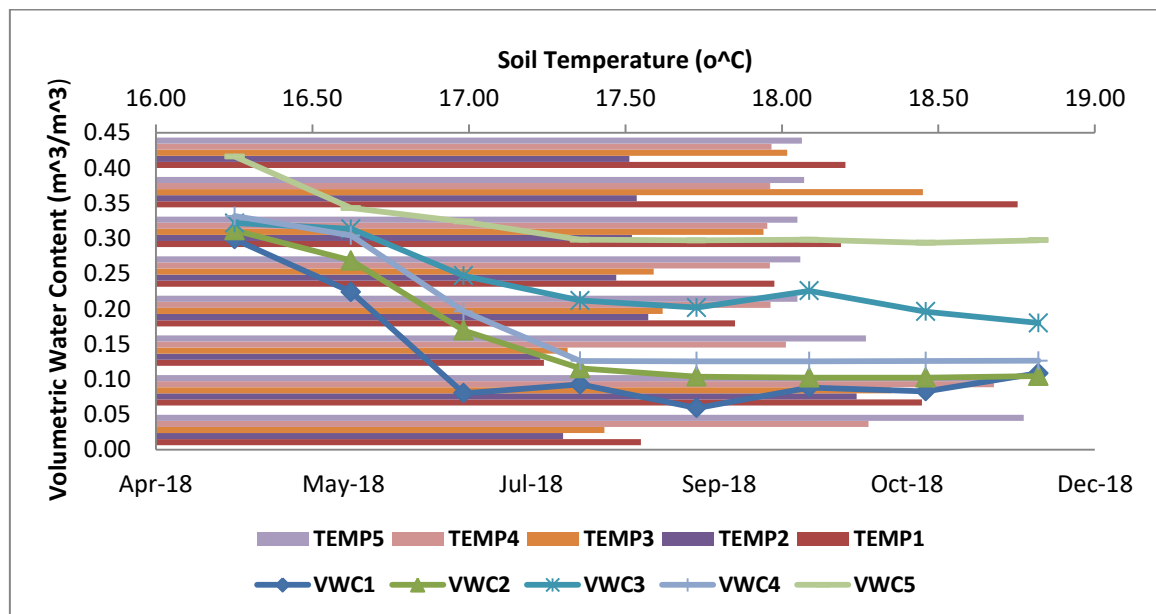


Figure 4.33: Soil moisture and temperature variation at Nunjoro farm site: 2018

Figure 4.33 shows that soil moisture varies with influence of temperature change in every season. During the period, it was observed that on April through December 2018 had declining soil moisture due to subsiding rainfall and increased temperature. Most evaporation took place because of moderate temperatures and low rains that indicate variation of soil moisture from one season to the other, however the top soil layer below 10cm experience high moisture as compared to the top layer near the surface because of evaporation prompted by heat from the sun. Here, Kijabe/Ndabibi and Nunjoro farms depict similar characteristics due to closely homogeneous soil moisture, temperature, and rainfall events. Gerten *et al.* (2007) conducted a modelling study and found that changes in soil moisture can be quite variable from one region to the next, with a general trend of decreasing soil moisture with rising temperatures. However, this study shows that soil moisture correlates with rainfall event and its intensity in a certain period, when there is low temperature; soil surfaces slightly losses ground water to the atmosphere caused by exchange of heat fluxes. In such cases, the atmospheric and soil temperature consequently remains closely variable to soil moisture for diurnal use by vegetation in the formation of food through photosynthesis. Mellander *et al.* (2004) observed that a further decrease in soil moisture could occur because of the impact of rising temperatures on plant-level processes, although this may vary depending on the circumstances (Daly *et al.*, 2004; Jones, 1992). However, in general, the amount of soil moisture increases when there is more precipitation due to climatic variability.

4.7.4 Wheat Biomass and Yield Production in Naivasha Cropland Ecosystem

Wheat being a similar vegetation species as grass in Maasai Mara rangeland ecosystem was studied as cropland produce and in Naivasha. Here, Maiella location was seen to be the most suitable wheat growing area with soil, landform, climatic characteristics and edaphic requirements as compared to other croplands. The annual production in this region for wheat crop was 2,716.2 kg/ha (2.716 tons/ha) while the rest of the area Maai Mahiu and biashara produced 0kg/ha and 1kg/ha respectively. Cereal crops such as wheat, which are in the same category as grass and pastures produced highly in this climatic zone. Again, annual maize crop production in Maiella was 1,347kg/ha (1.347tons/ha) followed by Naivasha East with 924.7kg/ha (0.925 tons/ha) and Viwandani produced 714.3kg/ha (0.7143tons/ha). As observed from annual production Maiella is the most productive zone for wheat crop in cereal production (Figure 4.34).

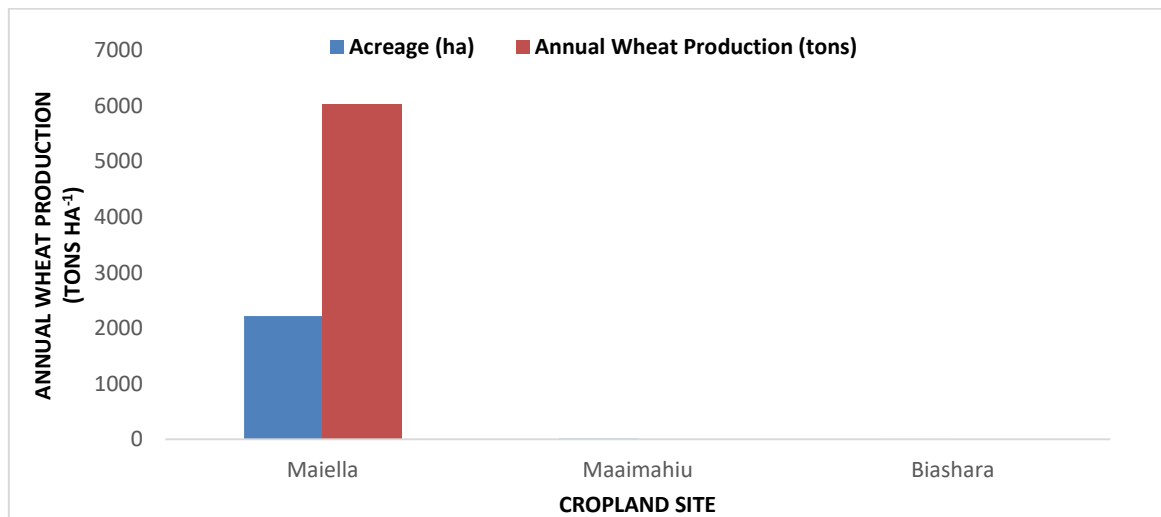


Figure 4.34: General trend of annual wheat crop production in Naivasha cropland

From figure 4.34, bales production of hay generated from wheat stovers have gradually been rising as compared to other pastures followed by wheat stovers throughout the years since 2013 to 2019. The demand of these pastures as feeds for livestock has made most subsistence and commercial farms practice the biomass production of hay and wheat stovers. The stovers concentration decreases due to moisture loss in the stalk cells and drying begins to a point where baling of stovers can be prepared as feeds for livestock. The wheat stovers however tend to harden from the release of moisture in stalks and become dry matter, which can be made into bales, stored as livestock feeds. Each harvesting was done when the crop was mature and under good quality, the amount of biomass ranged between 1260 and 1600 kilograms per acre while the average weight of a standard biomass of hay was between 18 and 20 kgs per bale.

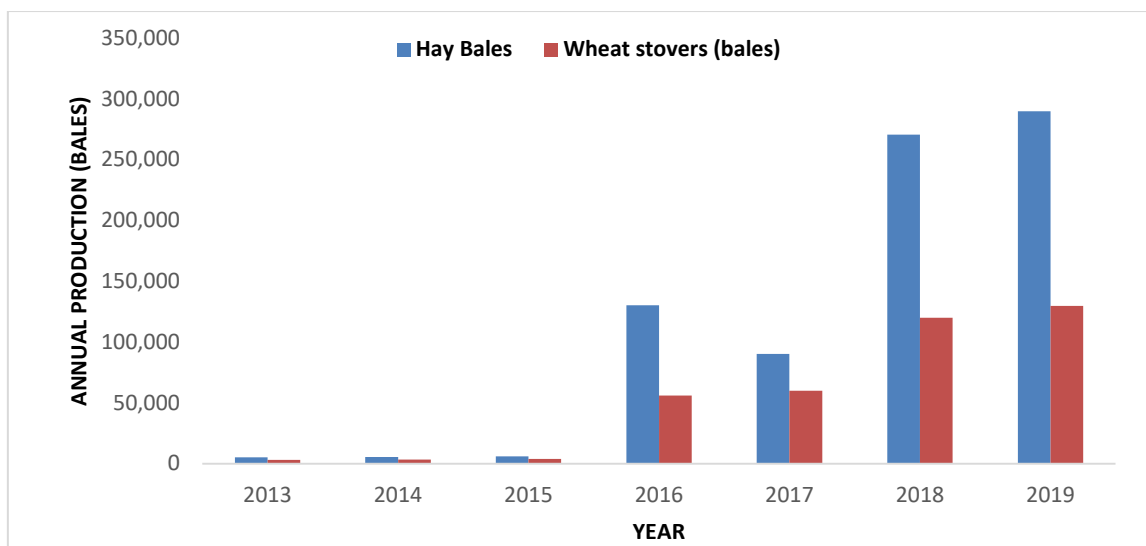


Figure 4.35: Trend of pasture crop production between 2013 and 2019 in Naivasha cropland

Figure 4.35 indicates that the corresponding wheat biomass quantity correlates with extractable water content for plants growth and development of biomass. Observation made is that during germination and emergency period little moisture was used in the germination of wheat seeds while from floral initiation stage there was progressive rainfall distribution through flowering, which requires optimal use of water to the end of grain fill and final harvest. This indicates that timely onset of rainfall matters greatly cropland as it influences the production of biomass. It can also be seen that wheat biomass production corresponds directly with extractable water content from flowering stage since it the point of grain formation and stover concentration increase in plant. The figure 4.36 shows that water is an important for effective growth of plants that is utilised in the development stage for bloom formation of quality stovers in wheat crop mainly used as bales for livestock feeds.

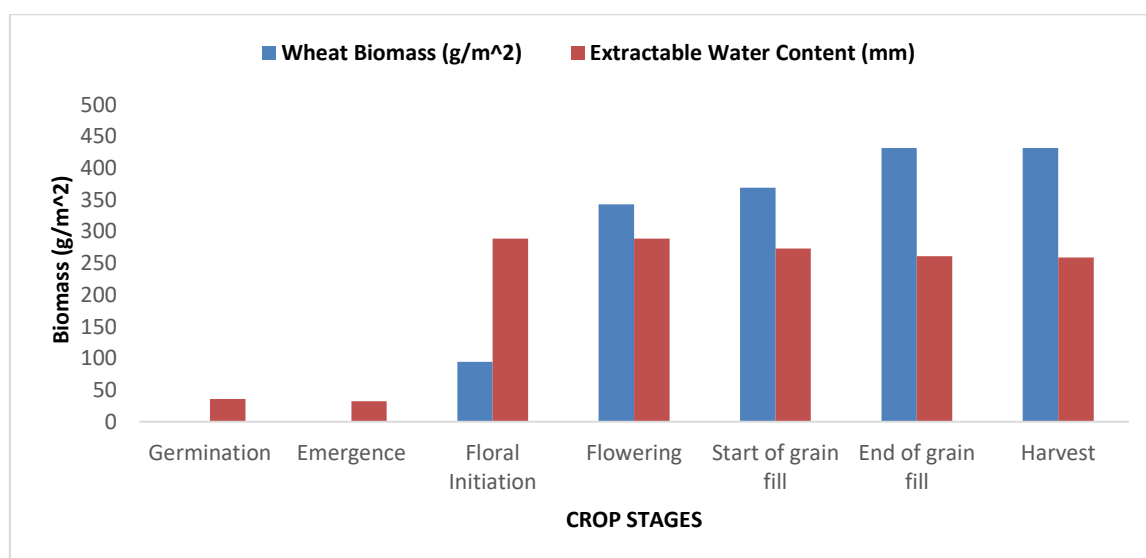


Figure 4.36: Correlation of wheat crop per stage biomass to extractable water content

4.7.5 APSIM Simulation Results of Wheat Crop

Table 4.35: APSIM simulation trend of wheat crop seasonal stages on aboveground biomass at Kijabe/Ndabibi Farm

Days after Clipping	Crop stage	Stover N Conc (%)	Leaf area Index ($m^2 m^{-2}$)	Extractable Water Content (mm)	Simulated Aboveground Biomass (gm^{-2})	Simulated Aboveground Biomass ($tonsha^{-1}$)
144	Germination	5.85	0.020	35.52	0.46	0.0046
145	Emergence	5.82	0.024	32.07	0.70	0.0070
175	Floral Initiation	3.15	1.310	288.59	94.07	0.9407
201	Flowering	1.42	0.780	288.59	342.80	3.428
208	Start of grain fill	1.23	0.329	272.77	369.00	3.690
234	End of grain fill	0.54	0.177	262.72	431.59	4.316
235	Maturity	1.23	0.00	260.65	431.59	4.316
236	Clipping/Harvest	0.54	0.00	258.88	431.59	4.316

Table 4.35 shows the physiological behaviour in crop stages of wheat crop based on the amount of extractable water content and biomass quantity produced at various stages during its growth. This indicates the number of days when biomass clipping normally begins for a wheat crop in the hay production and the quantity that can be obtained during each stage. This implies that, at the end of grain fill and maturity wheat clipping begins when biomass is at its maximum quantity of approximate amount of $431.59gm^{-2}$ ($4.316tonha^{-1}$), this corresponds to a drop in extractable water content ranging between 262.72 to 258.88 mm. During the period, crops do not use water as compared to more utilization of water during floral initialization and flowering stages when maximum water use is required. The maximum extractable water use was 288.59mm during floral period when bloomy biomass formation generally occurs.

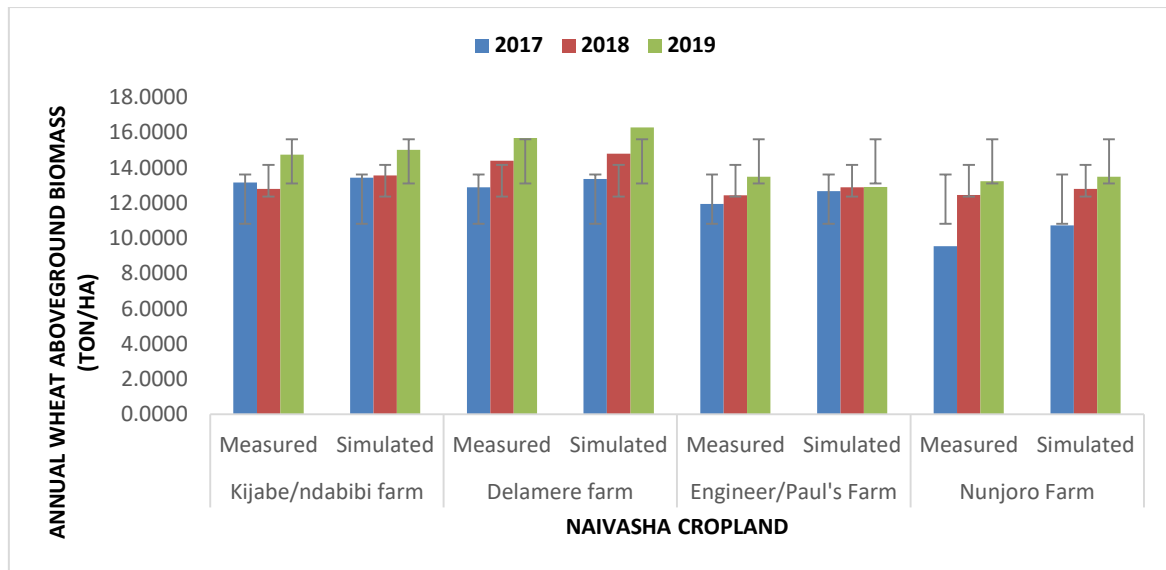


Figure 4.37: Comparison between observed and simulated annual aboveground biomass for Naivasha cropland from 2017 to 2019

Figure 4.37 shows the trend of observed and predicted biomass and grain yield at Kijabe/ndabibi, Delamere, Engineer/Mzee, and Nunjoro farms where for a period of three years (2017, 2018, and 2019). Annual yield production in Kijabe/Ndabibi and Delamere farms had the highest production in 2017 and 2019. In the previous year of 2017 had lower production and this may be attributed due to low rainfall hence low moisture storage level in the soil for plant growth. This indicates the variation of measured and predicted aboveground biomass (AGB) for wheat biomass, grain yield as cereals in Naivasha cropland. The wheat crop in the study was modelled since it felt under similar species to grass for livestock hay and human food production in cropland. The results show that the observed annual aboveground biomass of wheat is produced more in Delamere farm with close production to Kijabe/Ndabibi farm while at Engineer Paul's and Nunjoro producing less biomass. The production in 2019 for AGB was seen to have increased respectively probably owing to sufficient fall of rains during the season.

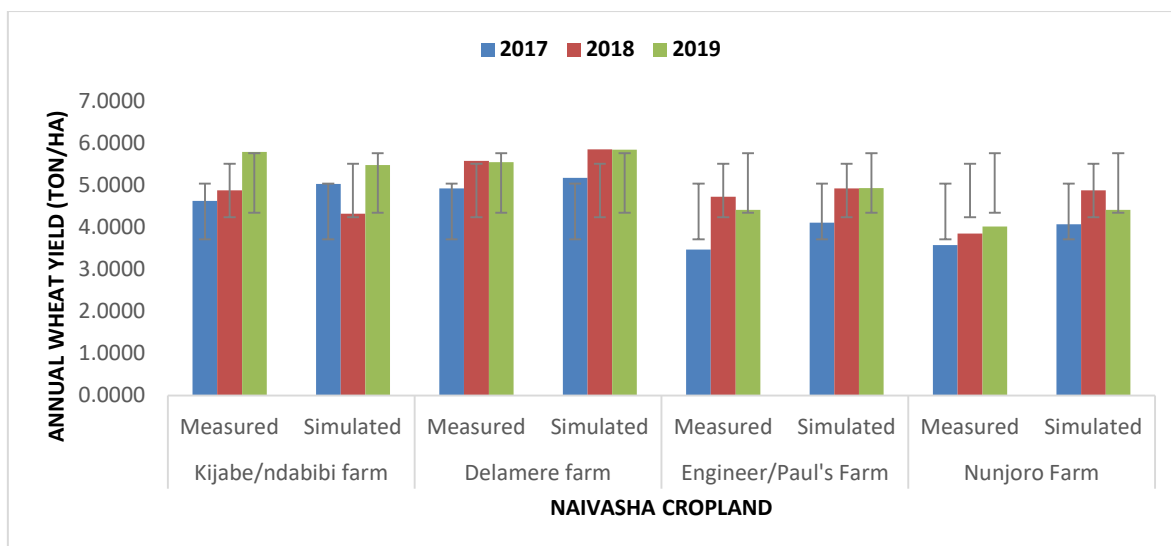


Figure 4.38: Comparison between observed and simulated annual wheat grain yield for Naivasha cropland from 2017 to 2019

From the croplands in Naivasha Sub-county, it depicts that the production of observed wheat and simulated annual aboveground biomass has almost similar trend for the three consecutive years since 2017 to 2019. The red bars represent the annual measured and simulated AGB for the period 2018 of wheat production in Naivasha cropland. The highest wheat production has been Delamere/minera farm followed by Kijabe/ndabibi farms, which show that the environmental conditions were favourable in the two growing areas.

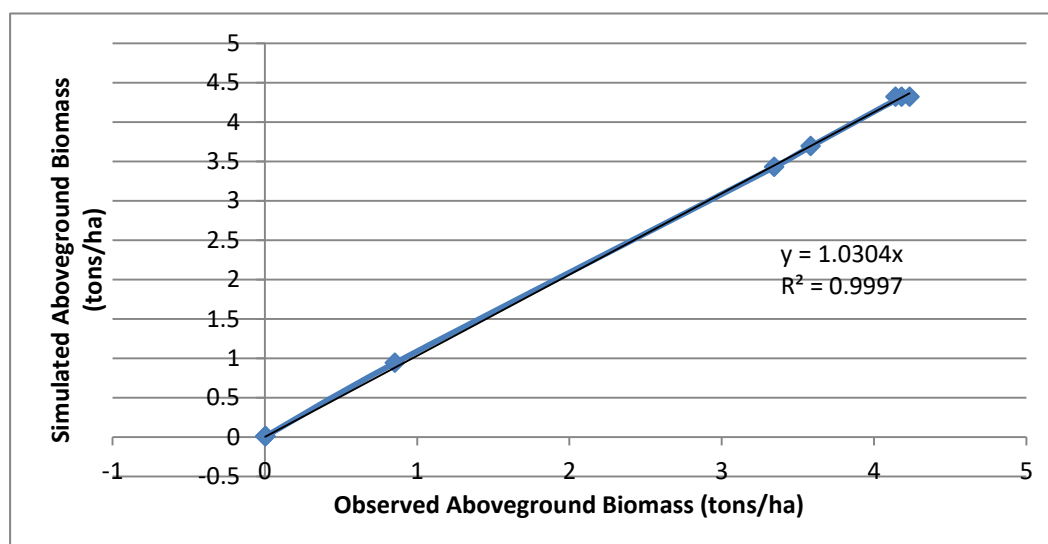


Figure 4.39: Measured and simulated aboveground biomass of wheat crop

Figure 4.39 shows the linear regression of model performance and this indicates that the correlation coefficient, R^2 is 0.9997 has close relationship between the measured and

predicted biomass. The findings were consistent with those of Jianguo *et al.* (2020), who studied the applicability of the APSIM Wheat Model in the Yangtze River Plain of China's Hubei Province and found positive correlations between the model's predicted and observed values for the time it takes wheat to grow from seeding to flowering and full maturity. While the model's performance during the growth period simulation was superior, the findings showed that the model's performance in simulating wheat grain yield and aboveground biomass was also satisfactory. For both wheat grain yield and biomass, the R^2 value was greater than 0.75. This suggests that APSIM perfectly predicted wheat production reasonably well.

Table 4.36: Statistical model evaluation performance of observed and simulated aboveground biomass of wheat

Depth (cm)	R^2	r	NSE	RMSE (Kg/ha)
Kijabe/Ndabibi farm	0.998	1.000	0.998	0.857
Delamere_Minera farm	0.997	1.000	0.997	0.075
Engineer/Paul's farm	0.999	1.000	0.999	0.342
Nunjoro farm	0.994	1.000	0.994	1.033
Mean	0.997	1.000	0.997	0.577

Table 4.37: Statistical model evaluation performance of observed and simulated grain yield of wheat

Depth (cm)	R^2	r	NSE	RMSE (Kg/ha)
Kijabe/Ndabibi farm	0.951	1.000	0.951	0.205
Delamere_Minera farm	0.994	1.000	0.994	0.480
Engineer/Paul's farm	0.974	1.000	0.974	0.787
Nunjoro farm	0.937	0.215	0.937	1.107
Mean	0.964	0.804	0.964	0.645

From figure 4.39, 4.40 and table 4.36, 4.37, it can be deduced that APSIM model was able to accurately simulate the biomass and grain yield reasonably well in response to extractable water content as indicated from the graphs. The model performance on biomass was found to be good for Kijabe/Ndabibi farm as described by $R^2 = 0.998$, $r = 1.000$, $NSE = 0.951$ and $RMSE = 0.857$ kg/ha. The performance for Delamere/Minera farm were $R^2 = 0.994$, $r = 1.000$, $NSE = 0.994$ and $RMSE = 0.075$ kg/ha and Engineer farm was $R^2 = 0.999$, $r = 1.000$,

NSE = 0.999 and RMSE = 0.342 kg/ha while Nunjoro farm was $R^2 = 0.994$, $r = 1.000$, NSE = 0.994 and RMSE = 1.033 kg/ha. The mean biomass performance was substantially good with $R^2 = 0.997$, $r = 1.000$, NSE = 0.997 and RMSE = 0.577 kg/ha. The goodness of fit was also assessed for wheat yield by calculating the mean where $R^2 = 0.964$, $r = 0.804$, NSE = 0.964 and RMSE = 0.645 kg/ha with R^2 and RMSE giving similar results. The results nearly concurred with those of Jianguo *et al.* carried out three wheat variety experiments in Wuhan, Jingmen, and Xiangyang, China and found that R^2 values of 0.72 - 0.87 for the wheat aboveground biomass and 0.75 - 0.78 for the grain yield were observed. There were statistically significant positive correlations between the calculated and measured values of wheat grain yield and aboveground biomass. The author also found that the average discrepancies between predicted and measured wheat grain production and aboveground biomass were less than 556 and 1323 kg ha⁻¹. 13.5%, 17.7%, and 19.8% were the NRMSE values for the simulated biomass and the observed data, respectively. So, in all three testing areas, the NRMSE values for wheat grain production and aboveground biomass were below 20%. From this study, it can be seen that the difference between observed and simulated biomass and yield from different Naivasha croplands were between 2017 and 2019 were relatively small meaning that the observed production was close to those predicted by APSIM. During this period, the simulated biomass and yield were higher than the observed biomass and grain yield, which was a clear indication, that APSIM over predicted production. As observed the R^2 and NSE have similar values because the original values were not significantly different.

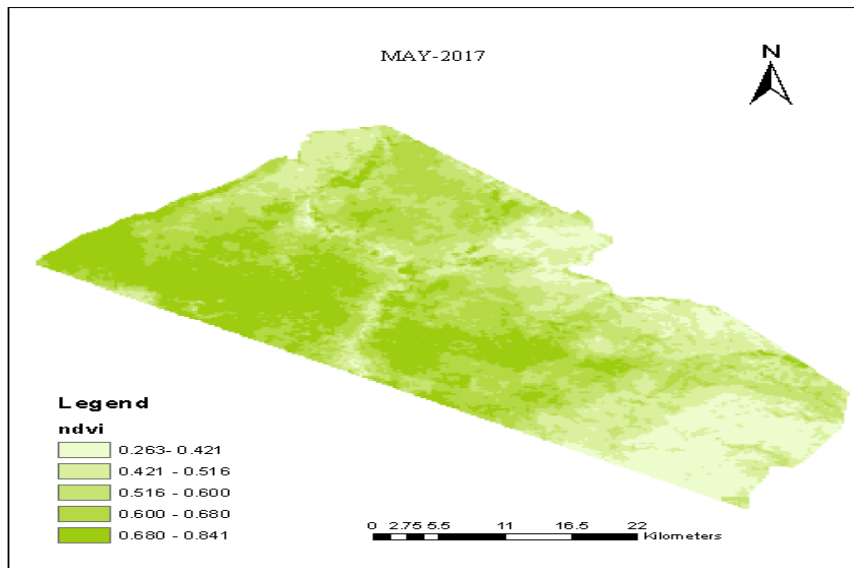
4.7.6 Model Sensitivity Analysis

Simlab 1.1 analysis of soil input parameters revealed that soil water conductivity and soil organic carbon amount are the most sensitive parameters for explaining variability in each of the model outputs of interest. In addition to the input parameters, hydraulic variables like saturated water content (APSIM's SAT), water holding capacity at upper limit (APSIM's DUL), and wilting point at lower limit (APSIM's LL15) influenced the model's results. Grossi *et al.* (2015) conducted an experiment and found that in DSSAT simulations, sorghum yield was more sensitive to precipitation, sunlight, and CO₂ concentrations. Consequently, canefw is most affected by the sun, rain, and temperature in computer simulations of agricultural systems.

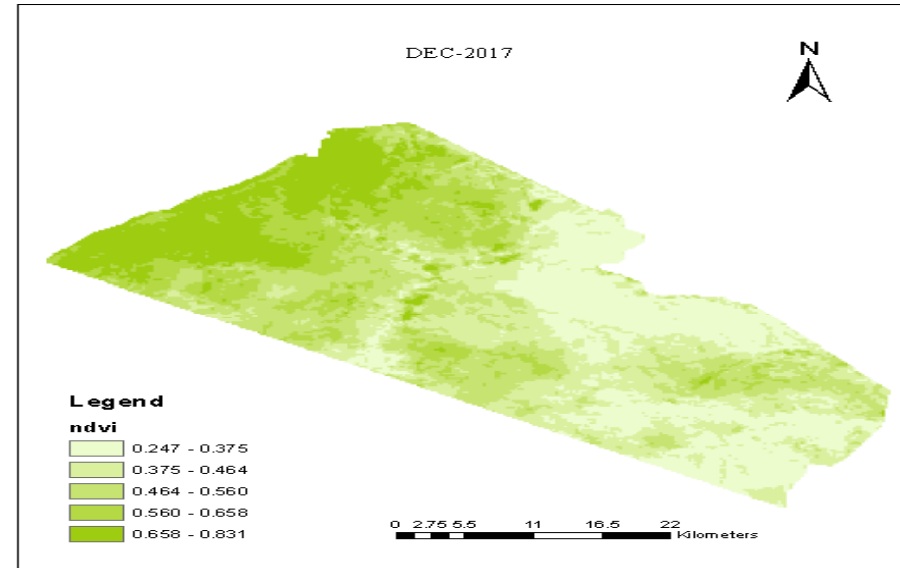
4.8 Normalized Difference Vegetation Index (NDVI)

Spatial monthly values of NDVI were derived from MODIS and PROBA-V imagery for the entire rangeland within the period of study (2017-2019). Much focus was based on sites

installed with 5TM-ECH₂O soil moisture, temperature stations and grass biomass clipping and measurements done within the periphery. The images displayed in Figure 4.40 and 4.44 are the sequential bi-seasonal images of (a) wet and (b) dry periods when site's aboveground biomass were clipped sampled, weighed and packed for oven drying in determination of dry matter content (biomass). It also indicates the range of NDVI values with transition in which vegetation greenness occurs for the period of 2017, 2018 and 2019. High NDVI value shows that there is high surface spectral reflectance due to greenness and high-density vegetation cover while low NDVI value indicates low or sparsely distributed vegetation cover with low density in greenness. The observed images shown that during the dry season, low vegetation greenness was realized and high vegetation greenness in wet season.



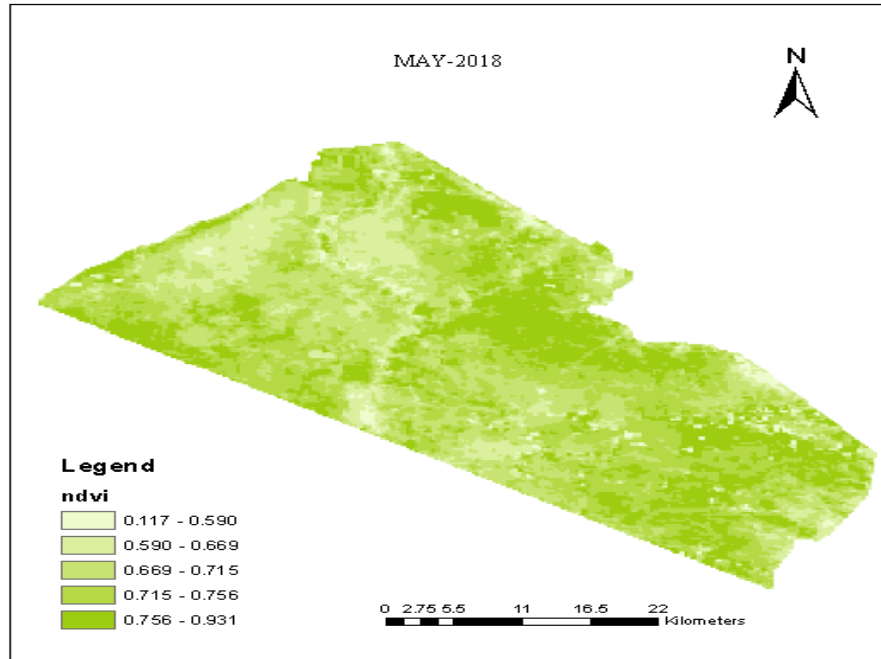
(a)



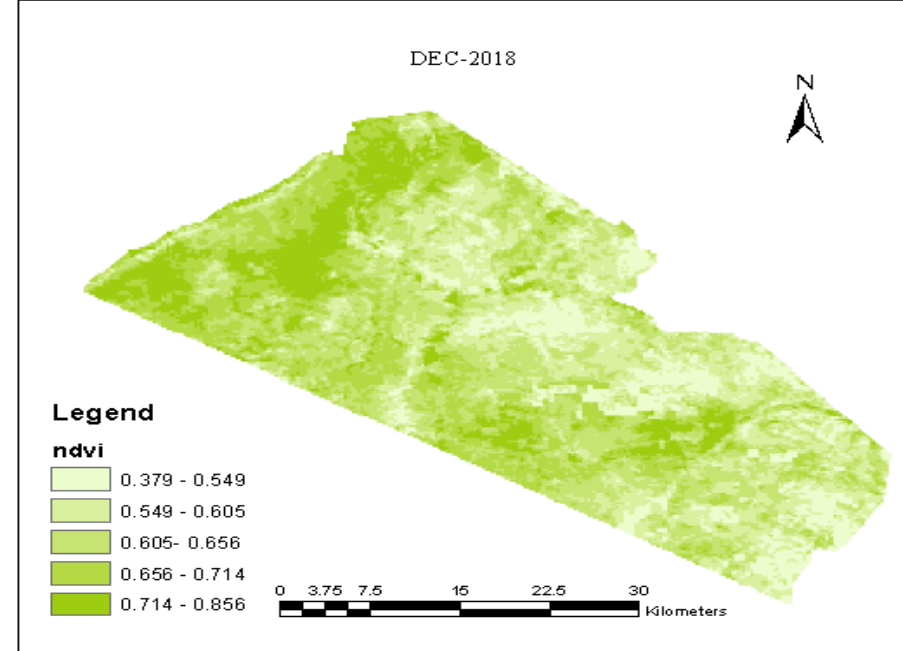
(b)

Figure 4.40: Vegetation NDVI trend from PROBA-V satellite imagery data for Maasai Mara Rangeland wet (a) and dry (b) season acquired on (May and Dec 2017)

Figure 4.41 indicates greenness within spatial segments in the month of May wet season with spectral reflectance ranged of between 0.263 and 0.841. During the dry season the greenness of vegetation particularly grass aboveground biomass spectral value ranged between 0.247 and 0.831 which shown that during the dry period the vegetation greenness was lower than during the wet season. This indicates that the bloomy vegetation cover was well dense during the wet season because of sufficient soil moisture useable by plants growth and development. As observed in May and December NDVI greenness on the upper left catchment of the rangeland ecosystem, the greenest vegetation is relatively high on May as compared to the December period.



(a)



(b)

Figure 4.41: Vegetation NDVI trend from PROBA-V satellite imagery data for Maasai Mara Rangeland wet (a) and dry (b) season acquired on (May and Dec 2018)

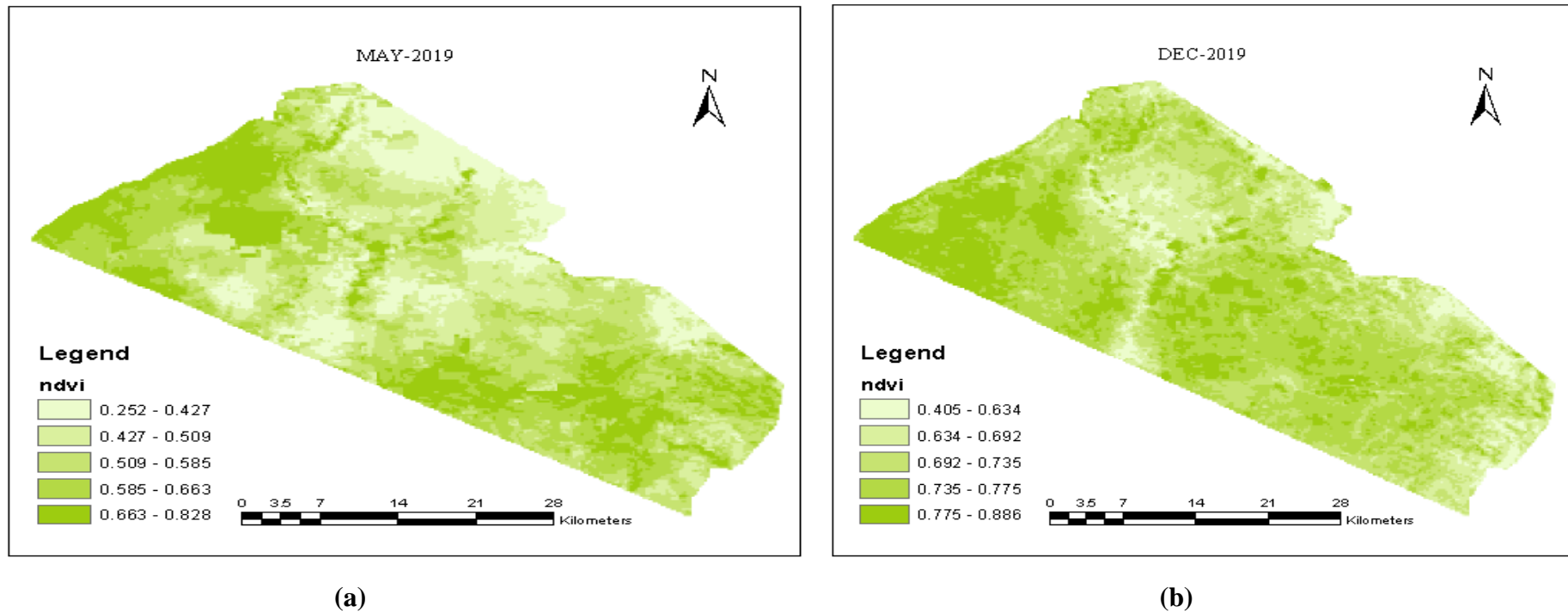


Figure 4.42: Vegetation NDVI trend from PROBA-V imagery satellite data for Maasai Mara Rangeland wet (a) and dry (b) season acquired on (May and Dec 2019)

From figure 4.41 and 4.42, it can be observed that vegetation NDVI trend derived from PROBA-V imagery satellite data for Maasai Mara Rangeland wet (May) and dry season (Dec) acquired on (May and Dec, 2017, 2018 and 2019). The spectral reflectance for greenness indicating blossom vegetation occurred within $0.663 \mu m$ to $0.828 \mu m$ during the wet season in 2019 while dry seasons ranged between $0.775 \mu m$ and $0.886 \mu m$ in December of the same year. This dense greenness in the period was due to high rainfall, which reflects high soil moisture content availability in the soil for vegetation growth and development where the net resultant effect was high biomass density. The NDVI ranged between 0.117 to 0.0668 in May and Dec 2019 respectively.

4.8.1 Naivasha Cropland Ecosystem

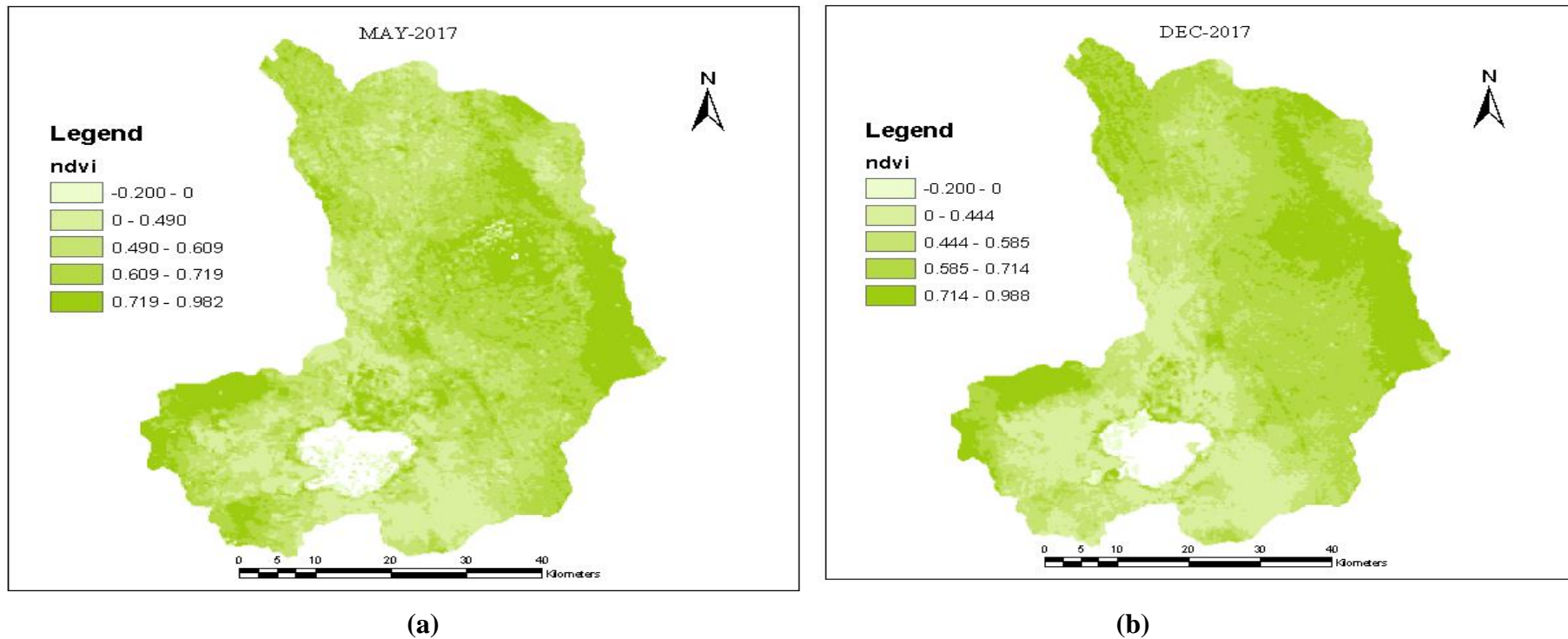
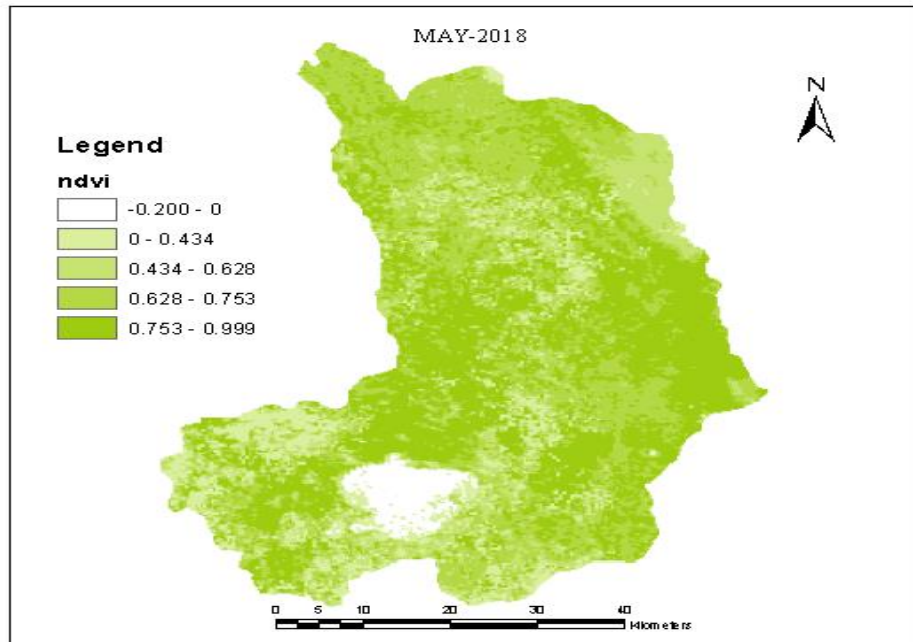
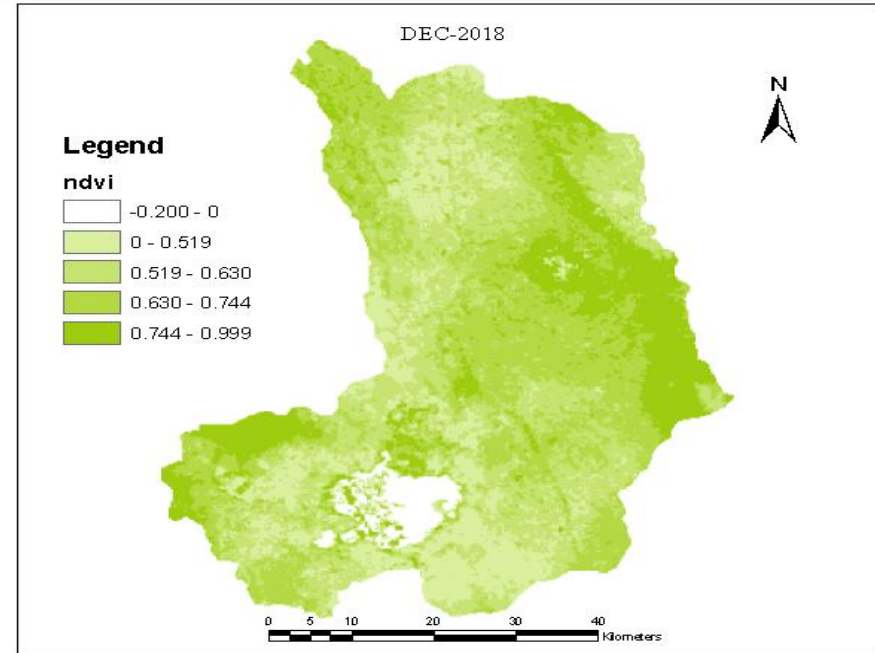


Figure 4.43: Vegetation NDVI trend derived from PROBA-V imagery satellite data for Naivasha cropland (a) wet (May) and (b) dry season (Dec) acquired on 2017.

From figure 4.43, 4.44 and 4.45, it can be observed that the NDVI for Naivasha cropland shows that during the month of May 2017, there was high NDVI as compared to December 2017. This may have been attributed to high rainfall frequency that occurred during the period. The NDVI values ranged from 0.609 to 0.982 μm for vegetation greenness during May period and 0.585 to 0.988 μm during the period of December. High NDVI was realized due to high reflectance of plants in red (R) to Near infrared (NIR) spectrum band caused by vegetation greenness. The highly dense vegetation depicts high NDVI values due to high reflectivity.

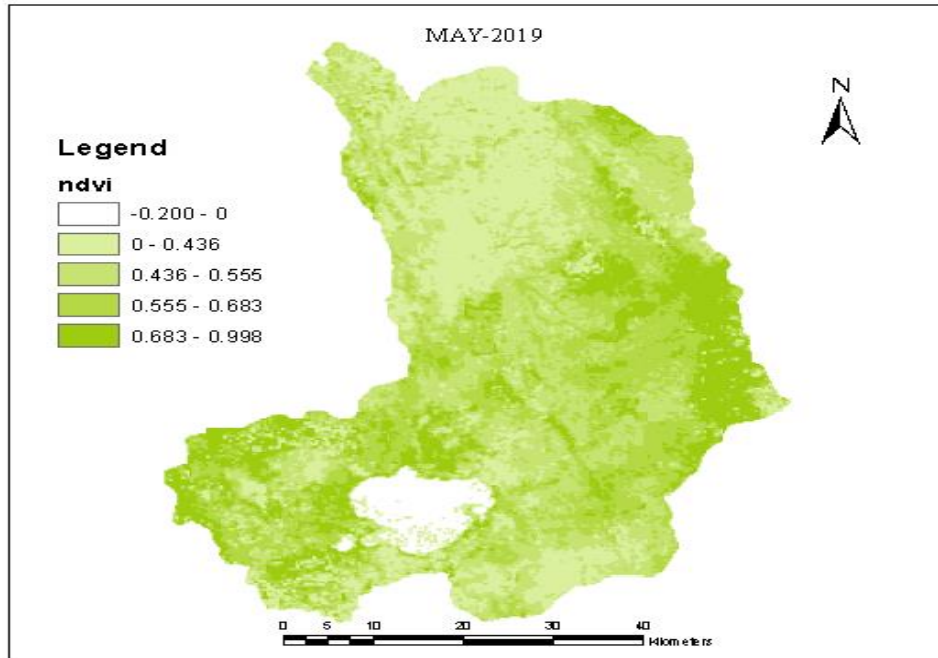


(a)

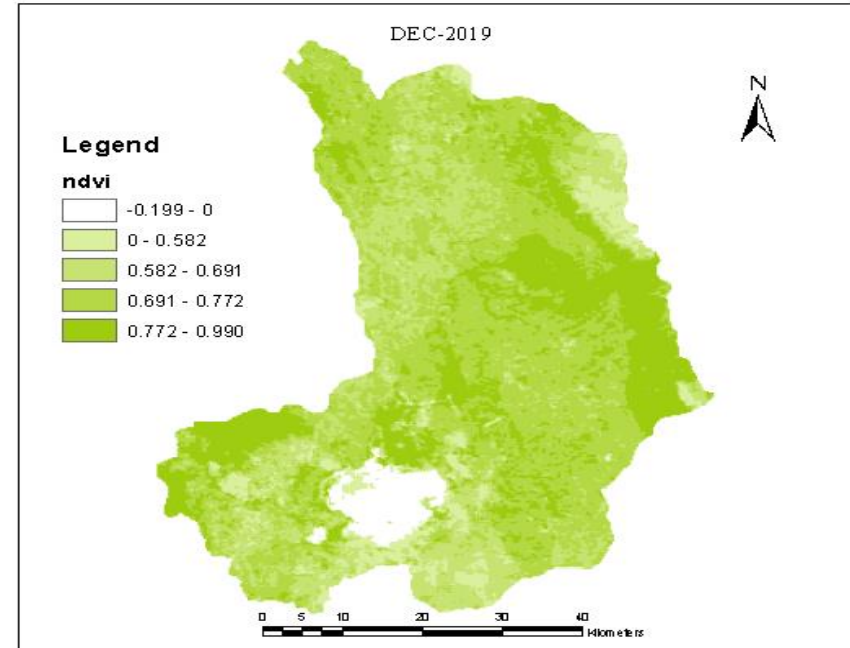


(b)

Figure 4.44: Vegetation NDVI trend derived from PROBA-V imagery satellite data for Naivasha cropland (a) wet (May) and (b) dry season (Dec) acquired on 2018.



(a)



(b)

Figure 4.45: Vegetation NDVI trend derived from PROBA-V imagery satellite data for Naivasha cropland (a) wet (May) and (b) dry season (Dec) acquired on 2019.

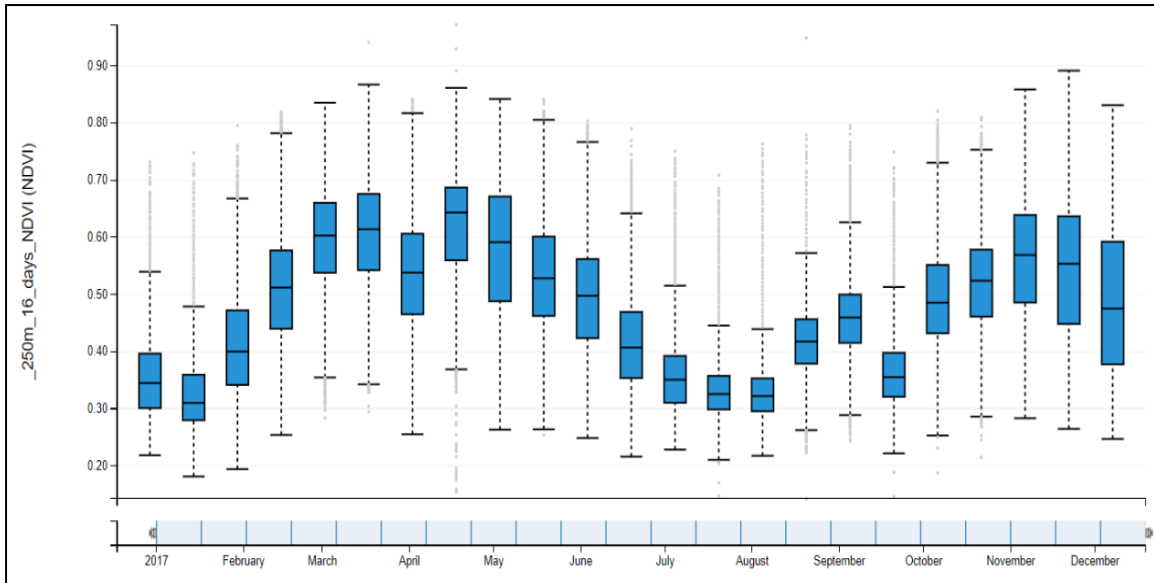


Figure 4.46: Graphical representation of NDVI trend between January – December in Naivasha cropland ecosystem during wet and dry season in 2017.

Figure 4.46 and 4.47 depict the graphical trend of NDVI of Naivasha Cropland between January and December of 2017. The trend indicates that between February and June, there was rise in NDVI value due to the greenness of vegetation and November and December. This shows that the commencement of planting season in Naivasha happens between that period and probably irrigated agriculture practiced in the second phase of cropping towards the end of the year (November and December). Similarly, the graph on figure 4.47 shows combined representation of spatial annual time series variation of NDVI during wet and dry seasons. This could be the reason why most land is gradually transforming from rain-fed to irrigated agriculture.

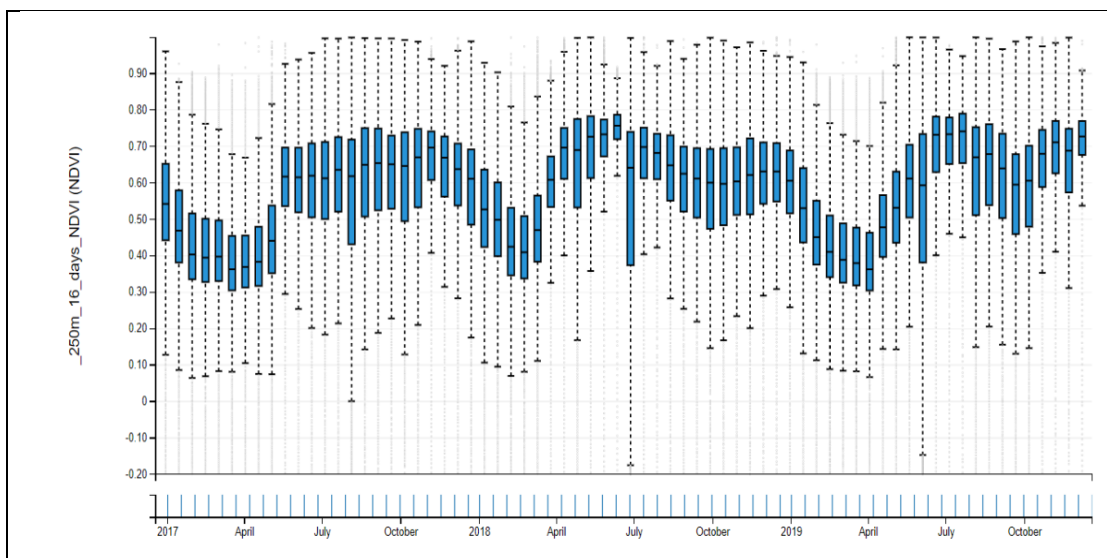


Figure 4.47: Graphical representation of NDVI trend of Naivasha Cropland ecosystem between January and December wet and dry season for the period 2017, 2018, and 2019

4.8.2 Time Series Analysis of Minimum and Maximum NDVI

Based on the study, the three years' period of 2017, 2018, and 2019 in figure 4.55, that maximum and minimum vegetation cover indicates homogenous trend of low vegetation cover in the dry season between the months of December, January, and February across the consecutive years. The maximum vegetation cover was observed in the month of March running through July, September, October, and November in 2018. The vegetation cover varied mainly on seasonal rainfall that fell due to the effect of East Africa intertropical convergence zone (ITCZ). During the rainy season, most of the rainfall events in 2017, 2018, and 2019 indicated that the maximum NDVI values were below 0.5 within the initial two months before the onset of the wet season. This was followed by increased NDVI values caused by greenness of vegetation cover between the range of 0.753 and 0.999 while there was a reduction in maximum NDVI values in the dry period ranged between 0 and 0.200 caused by decrease in rainfall followed by subsequent decline in vegetation greenness across the entire rangeland ecosystem.

4.8.3 Linear Correlation between Mean Monthly NDVI and Mean Maximum Monthly Rainfall

When measured at the proper spatial and temporal scale, there was a very strong and predictable correlation between seasonal precipitation and NDVI. All landmass types have a phenology that is highly attuned to the annual cycle of precipitation. Precipitation and normalized difference vegetation index (NDVI) values fluctuated widely over the MMNR rangeland ecosystem from 2017 to 2019. Although there is a strong relationship between NDVI and precipitation, it is not as strongly correlated with temperature over the course of a year. Analyses of the entire growing season reveal a direct relationship between the spatial pattern of average monthly or annual precipitation and the general temporal or spatial distribution of NDVI across the entire research region. Annual rainfall in 2018 was relatively high as compared to January 2017 and December 2019, characterized by aboveground biomass harvested in wet season of same period as compared to biomass harvested during wet, and dry season in 2017 (tables 4.33 to 4.35). During the dry season NDVI coefficient of variation analyses showed high instability or variability in 2017 erratic precipitation episodes.

4.8.4 Time Series Analyses of Mean Monthly Rainfall for 2017-2019 Period in Maasai Mara Rangeland Ecosystem

Almost the entirety of the period from 2017 to 2019 was marked by irregular rainfall variability in this region, with seasons of wet and dry spells (Figure 4.48). In 2018, there was an increase in precipitation of around 60 mm per month, according to a statistical time series

analysis of the mean monthly precipitation for the wet season (June, July, August, and September). Except for the year 2019, this made the soil moisture storage and retention potentially good for grass/vegetation or plant development virtually all year. Plant growth and biomass production are controlled by the seasonality of rain. Mean annual seasonal precipitation showed a rise in the west or south-western half of the region, mirroring the pattern of plant development in response to variations in rainfall. The amount of rain that falls during the wet season in different parts of Maasai Mara varies greatly. Some regions of the region, however, get a lot of rain, while the remainder of the downstream areas see relatively little precipitation.

4.8.5 Time Series Analyses of Maximum Mean Monthly Temperature

The research of mean monthly maximum temperature from 2017–2019 revealed a rise in maximum temperature larger than 26°C in virtually fully dry season, in addition to rainfall and vegetation change. Even while temperatures dropped from January to March, they rose gradually from July through October during the wet season (Figure 4.50). An abrupt drop in maximum temperature marked the beginning of the primary rainy season across virtually the entire year, especially at the end of the dry season in March or May. It is true that the maximum temperature can vary from season to season, however during the dry spell period; this is more so than during the rainy times (Appendix C.1).

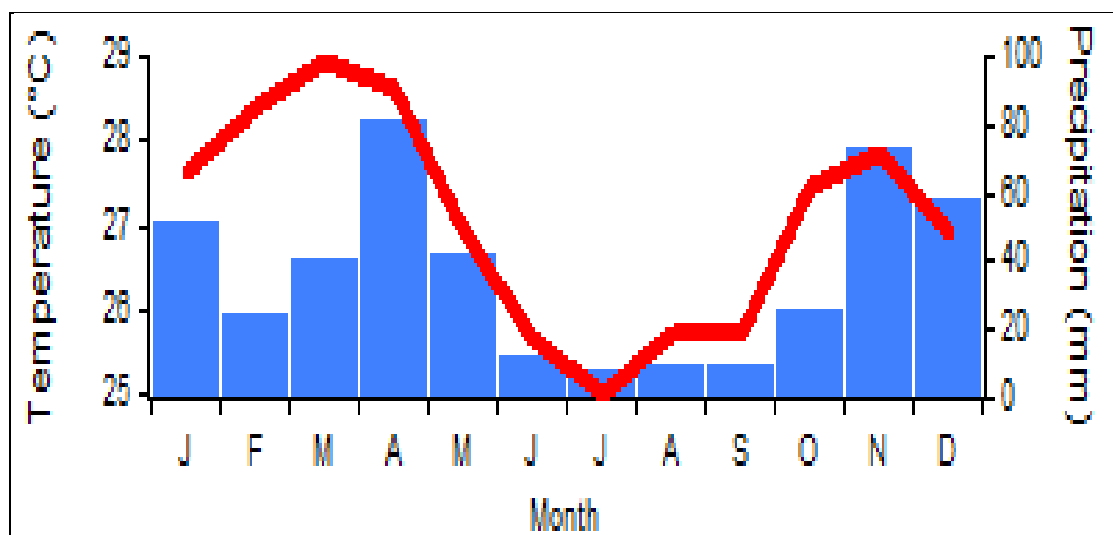


Figure 4.48: Annual precipitation and temperature during the seasons

4.8.6 Time Series Analyses of Mean Monthly NDVI for the 2017- 2019 Period

As observed from rainfall events, the erratic rainy season in dry season supported the soil store moisture that was utilized by vegetation such as shrubs, trees and grass growth in Maasai Mara rangeland and the mean monthly NDVI time series results indicates an increase of NDVI value after dry season (Figure 4.48). The spatial and temporal result of NDVI in the

regime depicted an increase of vegetation grass cover in Mara Main particularly in August, whereas there was a minimum vegetation cover in Mara Bridge in the month of November, December, January, and February in almost the whole three years.

4.8.7 Statistical Analysis of Total Aboveground Standing Biomass Quantities

The sites grass biomass in MMNR indicates that maximum NDVI value reflects the presence of maximum green biomass, while minimum value reflects minimum green biomass. The different between maximum and minimum NDVI values show that biomass production varies depending on whether the season is dry or wet. As observed from most quadrat site collection, generally, there was high vegetation cover in the wet season (March, April, May and July) than dry (January, February, short rains of August, September, October, November and December) from the period 2017 to 2019 as a result of good amount of rainfall in wet season for vegetation and grass growth. From the seasonal harvested AGB of dry matter in dry and wet season, observation made is that there is significant difference that exists in production between bi-seasons clipped aboveground biomass (Appendix B.10) as statistically shown in tables 4.41 and 4.42.

4.9 Land Use Land Cover Change in Maasai Mara National Reserve Rangeland and Naivasha Cropland Ecosystems

4.9.1 Maasai Mara National Reserve Rangeland Ecosystem

The LULC derived from MODIS imagery data for 2009 and 2019 are shown in the figures 4.49, 4.50, 4.51 and 4.52. In the study, maps were visualised based on the classes of each spatial coverage of land use and land cover. Generally, the major land use/covers in MMNR includes grassland, shrub-lands, rain-fed cropland, irrigated cropland, urban built-up bare land, water bodies, shrub-lands/natural grassland, forest cover (CEB), forest cover (CDB), forest cover (C - unknown), forest cover (OEB), forest cover (ODB) and forest cover (O-unknown) in the lower part of Maasai Mara catchment. Grasslands and shrub lands are mainly used for grazing of wildlife or as game reserves and encroachment of Maasai livestock herds. The figures 4.49 to 4.52 indicates the analysis of MODIS imagery based on land use/cover change in MMNR between 2009 and 2019 and the spatial extent of changes between 2017 and 2019 as indicated in table 4.43. From these derived maps, it clearly appears that MMNR is predominantly occupied by large percentage of grassland with 46.8% (717km²) in 2009, about 23.8% (365.4km²), 15.8% (273km²) of land being under closed forest with deciduous broadleaved respectively and natural grassland, as savannah, grasslands, or shrub lands, mostly used for grazing livestock and/or wildlife reserves. However, between 2009 and 2019, these rangelands have reduced by 3.38% (51.84km²) due

to encroached transformation of rain-fed cropland to irrigated cropland, whose area has increased from 0.82% (12.58km²) to 4.20% (64.44km²). Similarly, except for the grassland, shrub-land, forest cover, and water body, all the other land use/covers have undergone gradual change within the last decade.

Similar findings were established by Mwangi *et al.* (2017), who discovered that there are two systemic transitions (from closed forest to open forest and from open forest to small-scale agriculture) and that there is a trend (route) of deforestation from closed forest to small-scale agriculture, with open forest serving as a transitional land cover. These patterns suggest previously closed woods are being opened up (perhaps for timber and charcoal) and later cultivated. As farming spreads into the clearings, the surviving trees are logged. Between 1985 and 2003, the authors found that a shift in land tenure (from communal to private) was primarily responsible for the loss of MMNR rangeland to mechanized agriculture. Mechanized agriculture avoided profiting from rangelands during its expansion from 2003 to 2014, instead systematically going after profits from subsistence farmers. This indicated that tiny plots utilized for smallholder agriculture in the rangeland were merging into larger plots suitable for automated production. The natural vegetation has been declining due to opening of natural rangelands to agricultural practices that expanded from rain-fed to irrigated croplands including inadequate conservation policies and implementation. LULC maps (Figures 4.56 to 4.59) displays the base layer products for both Maasai Mara National Reserve rangeland followed subsequently by Naivasha cropland ecosystems.

Table 4.38: Description of land cover classes in Maasai Mara rangeland ecosystem

Class Code	Land Cover	Description
20	Shrub lands	These are areas characterized by a high percentage of shrub cover (2 – 5m high).
30	Grasslands	Mainly dominated by grasses (0-0.2m) and herbs (0.2-2m).
41	Rain-fed cropland	These are areas occupied by agricultural lands fed by rains during certain periods in a year.
42	Irrigated cropland	These are areas transformed from rain-fed agricultural practice to irrigated cropping system.
112	Urban/built up	Areas with upcoming commercial or residential (low and high-rise) premises, structures, and constructed materials.
114	Bare/sparse vegetation	Areas without vegetation or rare vegetation thriving.
116	Water bodies	These are areas covered by swamps, rivers, lakes, and open waters.
122	Shrubs/herbaceous cover	Area characterized by high percentage of shrubs mainly herbaceous cover.
124	Forest (evergreen broadleaved)	Are areas predominantly covered by evergreen broadleaved tree (> 5m high) with closed canopies (> 40% cover).
126	Forest (deciduous broadleaved)	Are areas predominantly covered by deciduous broadleaved trees (> 5m high) with closed canopies (> 40% cover).

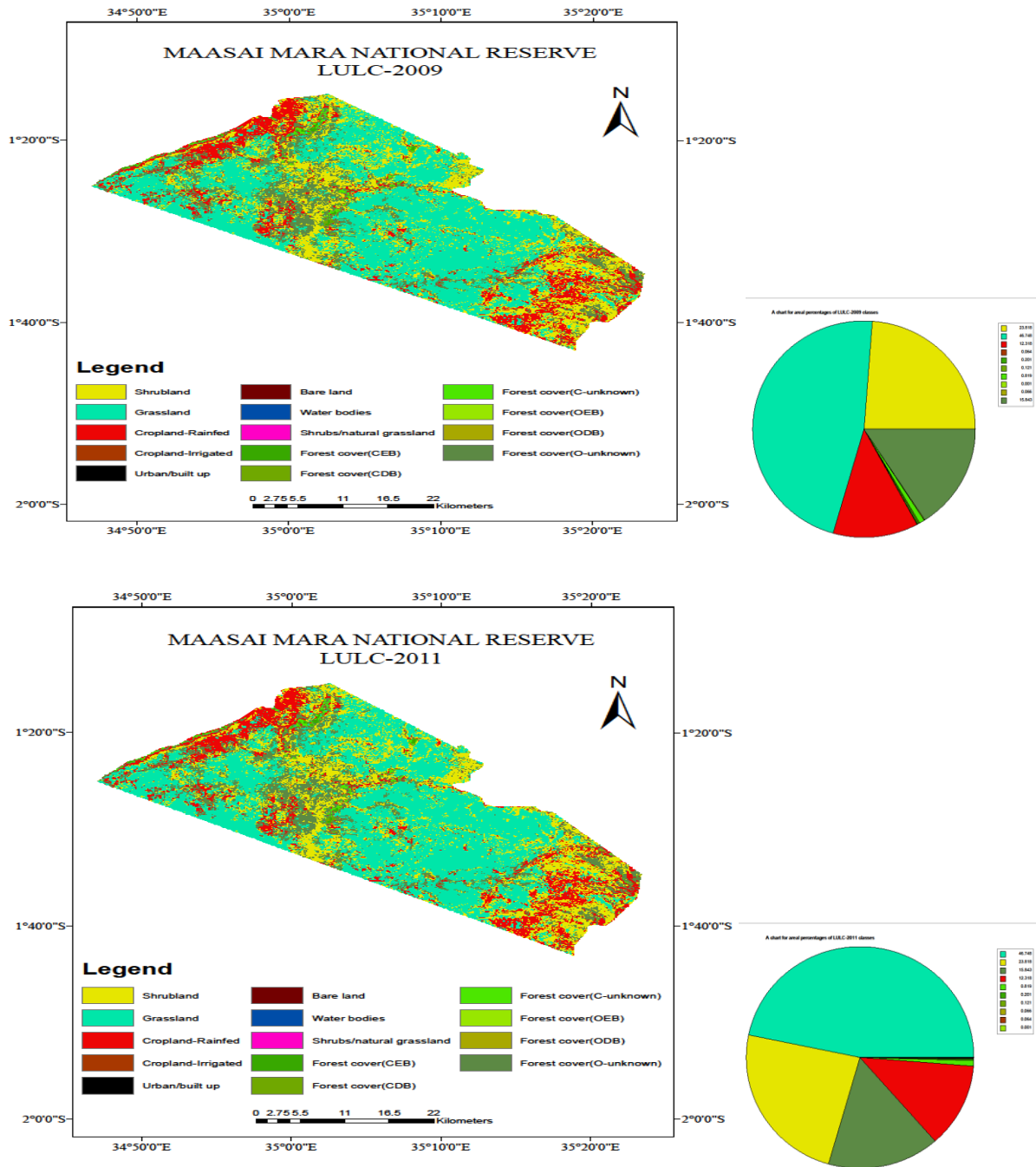


Figure 4.49: Land use/cover classification maps using MODIS imagery data of Maasai Mara National Reserve from January 2009 through December 2011

Figure 4.49 shows the LULC maps and respective proportion of cover occupied by each class between the year 2009 and 2011 of Maasai Mara National Reserve and rangeland ecosystem. The figure indicates that grassland occupies the largest proportion of the entire rangeland with 46.75%, which has remained constantly unchanged during the three-year period. Shrub-land with 23.82% has also remained unaltered in the same period and similarly the rest of the classes such as opened unknown forest cover (15.84%), rain-fed cropland (12.32%), forest cover closed unknown (0.82%) and irrigated cropland (0.06%) have been

maintained in the entire ecosystem. The rain-fed and irrigated croplands are practiced in conservancies and some sections of Mara Triangle where riparian Maasai community has encroached into the ecosystem for livelihood. Kariuki *et al.* (2018) conducted research and found that the primary land use varies with precipitation and land tenure, which in turn leads in different livelihood options for people. For instance, agriculture dominates the economy during wet years, and conservation efforts benefit from more widespread public backing of wildlife that attract tourists, such as rhinos, carnivores, and eland, may become extinct.

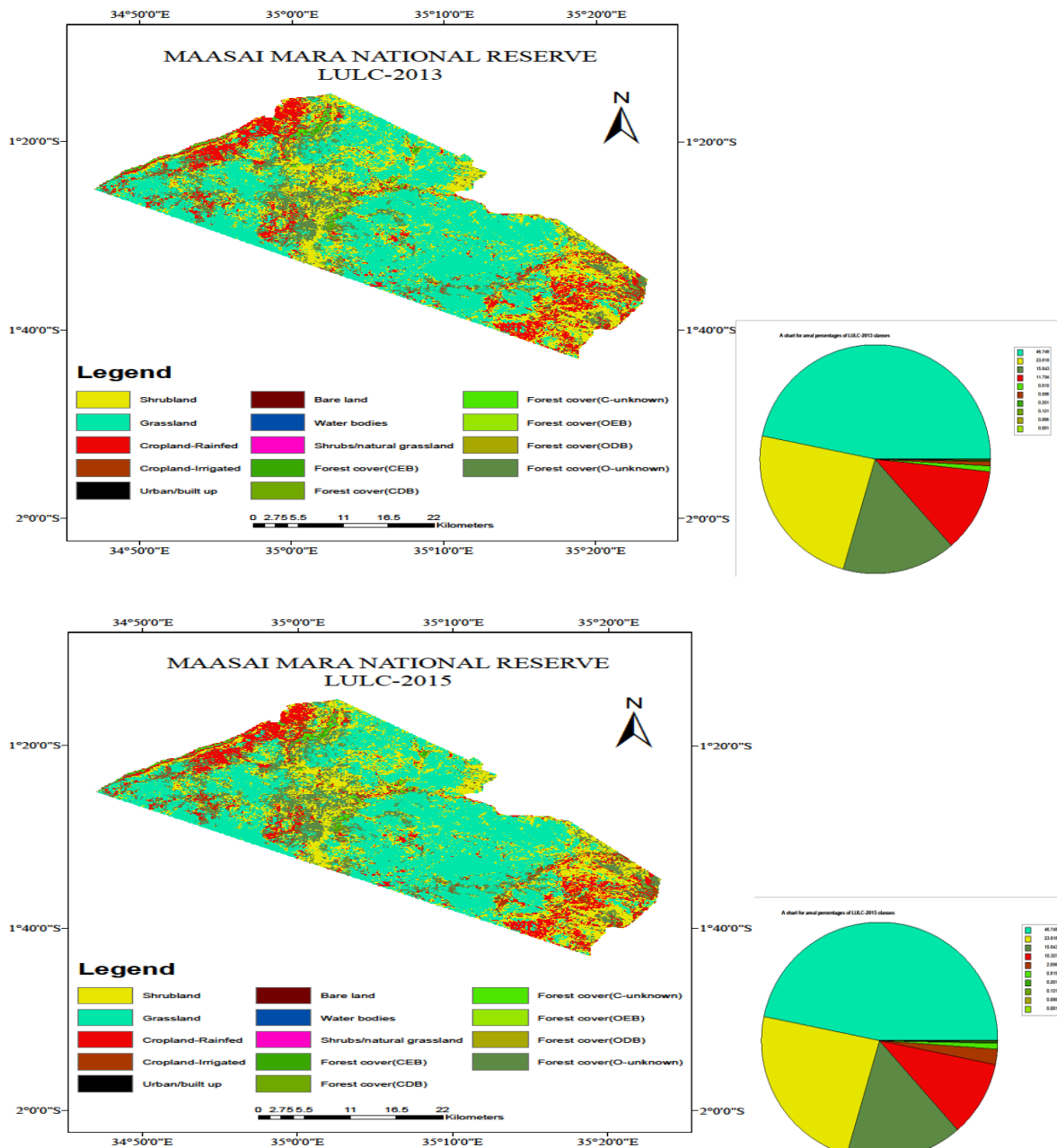


Figure 4.50: Land use/cover classification maps of Maasai Mara National Reserve from 2013 through 2015 using MODIS imagery data

The figure 4.50 shows a constant land use land cover class for grassland, shrubland, rainfed cropland and open unknown forest cover which had existed for the past five years since 2009 to 2012, however a decrease in land cover occurred between 2013 to 2015 for rainfed cropland from 12.32%, 11.79% to 10.33% and an increase of irrigated cropland from 0.588% in 2012 to 2.056% in 2015. This indicates the transformation of rainfed to irrigated cropland which signifies that some upcoming irrigation systems were being created in the area prompted by scarcity of rainfall. Research by Reid *et al.* (2003) found that wildlife populations in the Maasai Mara rangelands are expected to decrease by at least 40 percent, and that some species

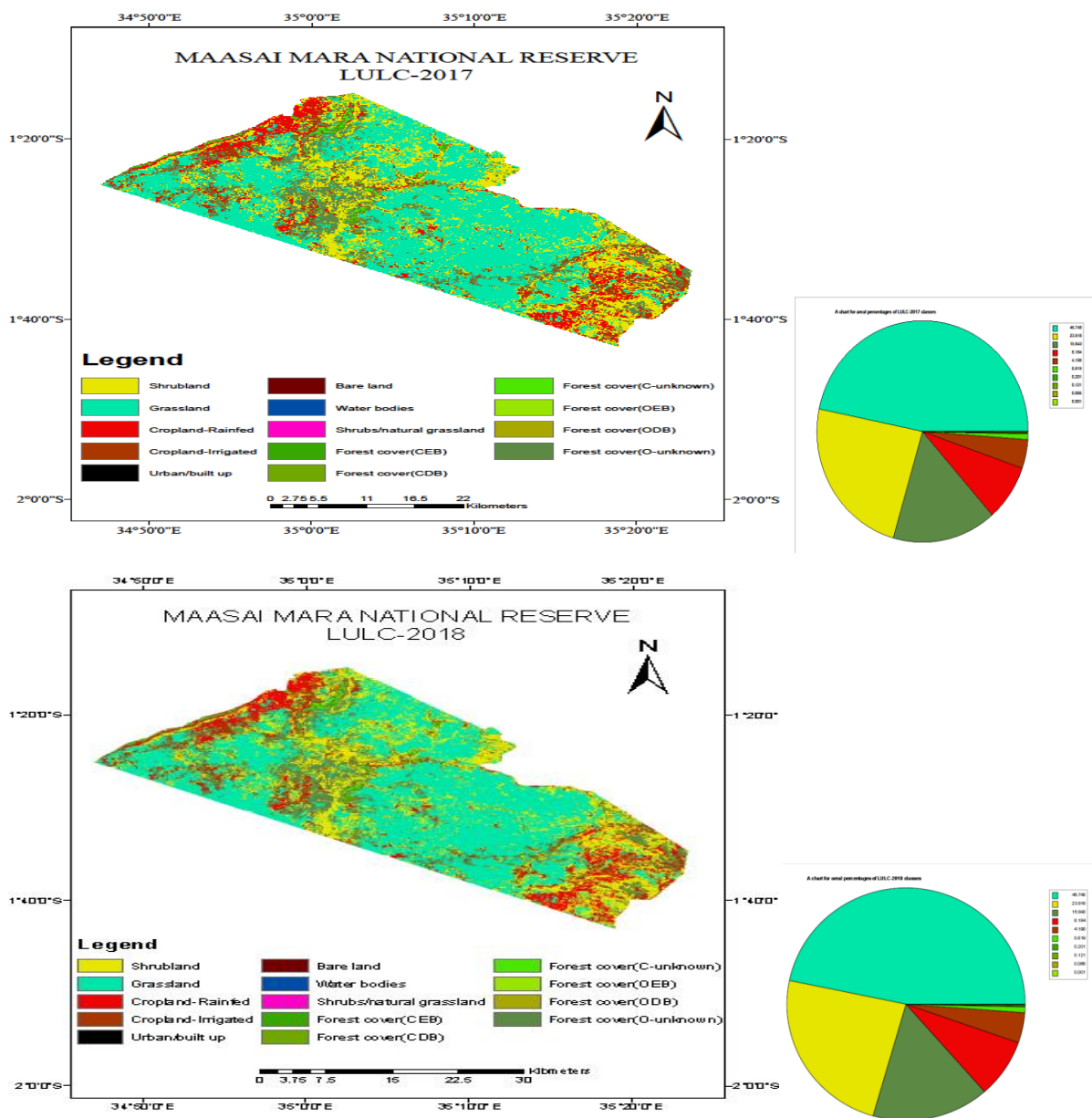


Figure 4.51: Land use/cover classification maps of Maasai Mara National Reserve in 2017 through 2018 from MODIS imagery data.

Figure 4.51 shows the land use land cover classes of MMNR rangeland and ecosystem for two year period between 2017 and 2018, the maps and charts indicates that grassland has continued to remain untransformed with 46.75% similar to shrubland with 23.82%. This also applies to other land cover classes and open unknown forest cover, closed unknown forest cover with rainfed and irrigated croplands occupying the same area for the last decade.

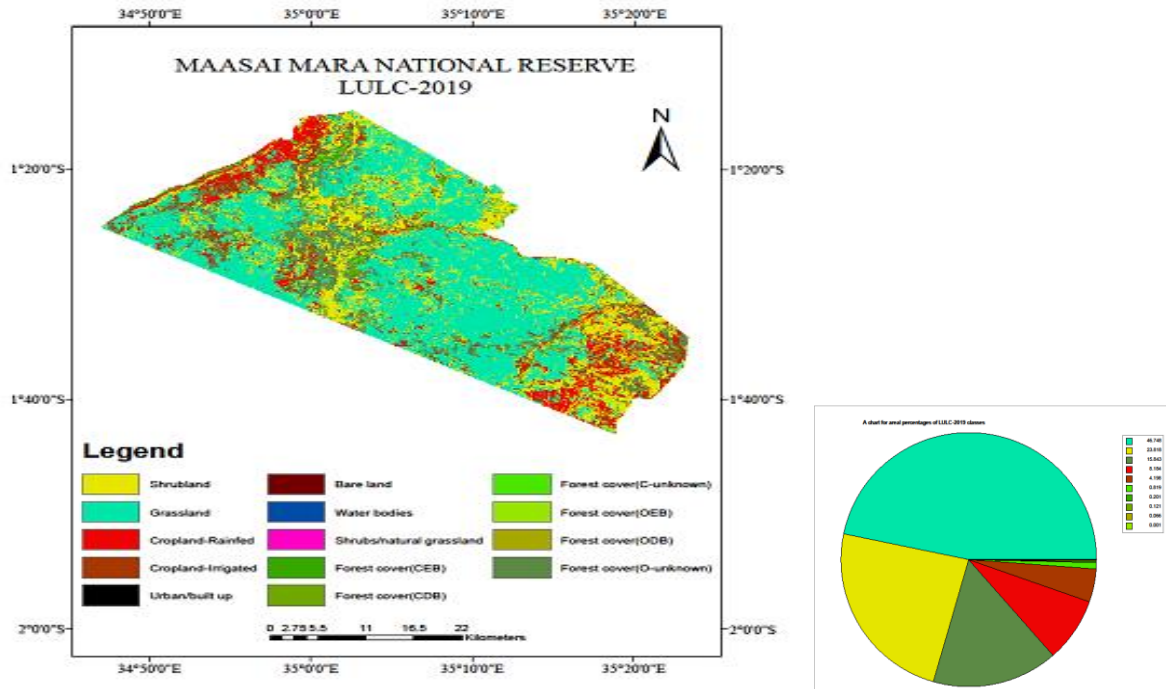


Figure 4.52: Land use Land cover classification representation in percent for Maasai Mara rangeland ecosystem in 2019.

Figure 4.52 shows the LULC classes for the period 2019 and it can be observed that the grassland occupies the largest proportion of land cover followed with shrubs that takes 46.75% and 23.82% respectively. Land use Land cover has remained unchanged of some classes for the last decade except in the rain-fed cropland, which decreased in 2013 to 2015 from 12.32% to 10.33% because of transformed water managed, or irrigated cropland. Due to short rains that were received in 2014, moving to irrigated cropland was probably the potential farming practices that were done in conservancies surrounding the MMNR ecosystem for food production. Most of the small-scale farmers alternatively shifted out of cultivation relying on rainfall and opted into venturing irrigation farming using water from excavated pans for storage of rainwater.

Mwangi *et al.* also discovered that the land surrounding the MMNR was utilized for grazing in their study. Between 1976 and 2014, the forest cover in the study area dropped from almost 20% to around 7%, primarily due to deforestation in the Mau Forest near the

Mara River's headwaters. The biggest shift is the gradual rise of small-scale agriculture and the reduction of forest cover. A similar expansion occurred in small-scale agriculture, which went from covering roughly 6.5% to 21% of the area during the same time span. In this case, the severity of the commission error throughout the intervals of 1976-1985 for the shift to small-scale agriculture from open forest is 72.9%.

Table 4.39: Maasai Mara National Reserve Land Use Land Cover classification between 2017- 2019 according to FAO land cover classes

OID	Class Name	Class Code	Count	Area cover (%)	Area cover (km²)
0	Shrub land	20	30162	23.818436	365.41
1	Grassland	30	59199	46.748478	717.20
2	Cropland, rain-fed	41	10364	12.31824	188.98
3	Cropland, irrigated	42	5316	0.063964	0.98
4	Urban/built up area	112	254	0.20058	3.08
5	Bare/sparse vegetation	114	153	0.120822	1.85
6	Water bodies	116	1037	0.818902	12.56
7	Shrubs/herbaceous cover	122	1	0.00079	0.01
8	Forest (closed, evergreen broadleaved)	124	84	0.066333	1.02
9	Forest (closed, deciduous broadleaved)	126	20063	15.84342	243.07

The total area of MMNR is 1534.174313km²

Table 4.39 shows the LULC classes for MMNR in area cover and its apparent that grassland dominates and occupies the greatest area of 717.20 km²(46.75%) of the total 1534.17km² followed by shrub-lands which are sparsely distributed within the entire rangeland catchment. Shrub-land occupies 365.42km² (23.82%) with shrubs of herbaceous original with least area cover of 0.01 km² (0.0008%). Closed deciduous broadleaved forest covers a substantive amount of cover, which was 243.07 (15.84%).

Table 4.40: Maasai Mara National Reserve Land Cover and Land Use Statistics for 2017-2019

Land cover and Land use within segments		Total Surface Area (ha)	Variance	SE	CV	RE
Shrubland	Direct Expansion	6,173,224,354	561,202,214	7491.343	6.483	
	Regression Estimation	1,325,579,518	120,507,229	3471.415	3.004	4.657
Grassland	Direct Expansion	7,900,112,700	446,334,051	6680.824	2.946	
	Regression Estimation	8,238,406,919	481,778,182	6941.024	3.060	0.926
Cropland, rainfed	Direct Expansion	174,363,929	34,189,005.8	1849.027	3.094	
	Regression estimation	153,308,604	26,896,246	1640.008	2.744	1.271
Cropland, irrigated	Direct Expansion	700.354	962.987	9.81319	3.162	
	Regression estimation	310.299	620.592	7.877764	2.538	1.552
Urban/builtup area	Direct Expansion	11,337.035	7,085.647	26.61888	2.735	
	Regression estimation	13,257.229	9,469.449	30.77247	3.162	0.748
Bare/sparse vegetation	Direct Expansion	10,994.903	3,435.9071	18.5362	3.162	
	Regression estimation	10,222.385	3,006.584	17.3395	2.958	1.143
Water bodies	Direct Expansion	631,354.068	157,838.517	125.6338	3.162	
	Regression estimation	596,111.817	141,931.39	119.135	2.999	1.112
Shrubs/herbaceous cover	Direct Expansion	0.170	0.284	125.6338	3.162	
	Regression estimation	0.0294	0.1469	0.1212	3.162	1.932
Forest(closed,evergreen broadleaved)	Direct Expansion	2,058.727	935.785	9.673598	3.060	

Forest(closed, deciduous broadleaved)	Regression estimation	2,058.726	935.785	9.673598	3.006	1.000
	Direct Expansion	57.299	6.6633	0.816258	0.979	
	Regression estimation	475.975	54.709	2.339012	3.043	0.122

V- Variance, SE – Standard Error, CV- Coefficient of Variation and RE – Relative Efficiency

Table 4.40 shows direct expansion area estimation and it can be observed that coefficient of variation in the relationship between the ground truth and satellite images ranged between 3.004 and 6.483 and its relative efficiency was 4.657. Transformation of rain-fed cropping in cropland occupies 188.983km² (12.32%) which may have declined due to increased irrigated cropland with 0.981km² (0.064%) and built-up area occupying 3.08km² (0.2%) in the entire area.

Table 4.41: Maasai Mara Rangeland Accuracy Assessment Report for Classification of MODIS images 2017, 2018, and 2019

Confusion Matrix based on Test and Training Area (TTA) mask, S - Shrubland, G- Grassland, Cr – Cropland rain-fed, Ci – Cropland irrigated, Bt – Urban/built up, Bsv – Bare/sparse vegetation, Wb – Water bodies, Shc–Shrubland/herbaceous cover, F_{CEBI} - Forest Cover (Closed, evergreen broadleaved), F_{CDBI} – Forest cover (Closed Deciduous Broadleaved).											
Class Producer's											
Users	S	GI	Cr	Ci	Bt	Bsv	Wb	Shc	F_{CEBI}	F_{CDBI}	Reference Totals
S	105	3	0	0	0	0	0	0	0	2	110
GI	4	166	1	0	0	0	0	0	0	0	171
Cr	1	5	50	0	0	0	0	1	0	0	57
Ci	0	0	0	4	0	0	0	1	0	0	5
Bt	0	0	0	0	14	0	0	0	0	0	14
BI	0	0	0	0	1	32	0	0	1	0	34
Wb	0	0	0	0	0	0	40	2	0	0	42
Sng	0	0	0	0	0	0	0	2	0	0	2
F_{CEBI}	0	0	0	0	1	0	0	0	21	0	22
F_{CDBI}	0	3	0	0	0	0	0	0	0	84	87
Classified Totals	110	177	51	4	16	32	40	6	22	86	518
Accuracy Assessment											
Producer's	95.5	93.8	98.0	100.0	87.5	100.0	100.0	100.0	95.5		97.7
User's	95.5	97.1	87.7	80.0	100.0	94.1	95.24	100.0	95.5		96.6
Kappa Class											
Overall Accuracy	95.22										
Kappa Index	0.94										

4.9.2 Naivasha Cropland Ecosystem

Table 4.42: Description of land cover classes in Naivasha Cropland

Code	Land Cover	Description
10	Arable land (cropland)	These are areas covered by growing crops (agricultural), ploughed fields, and horticultural farms.
20	Non-arable land	Are areas, which are less productive for crop production, infertile, and include either completely non-vegetated areas or areas under very low percent vegetation cover.
30	Land under water	These are areas covered by swamps, rivers, lakes, and open waters.
40	Urban Area	Areas with upcoming commercial or residential (low and high-rise) premises, structures, and constructed materials
50	Gazetted Forest	These are areas predominantly covered by tree (> 5m high) with closed canopies (> 40% cover).
60	Grassland	Are areas dominated by grasses (0-0.2m) and herbs (0.2-2m)

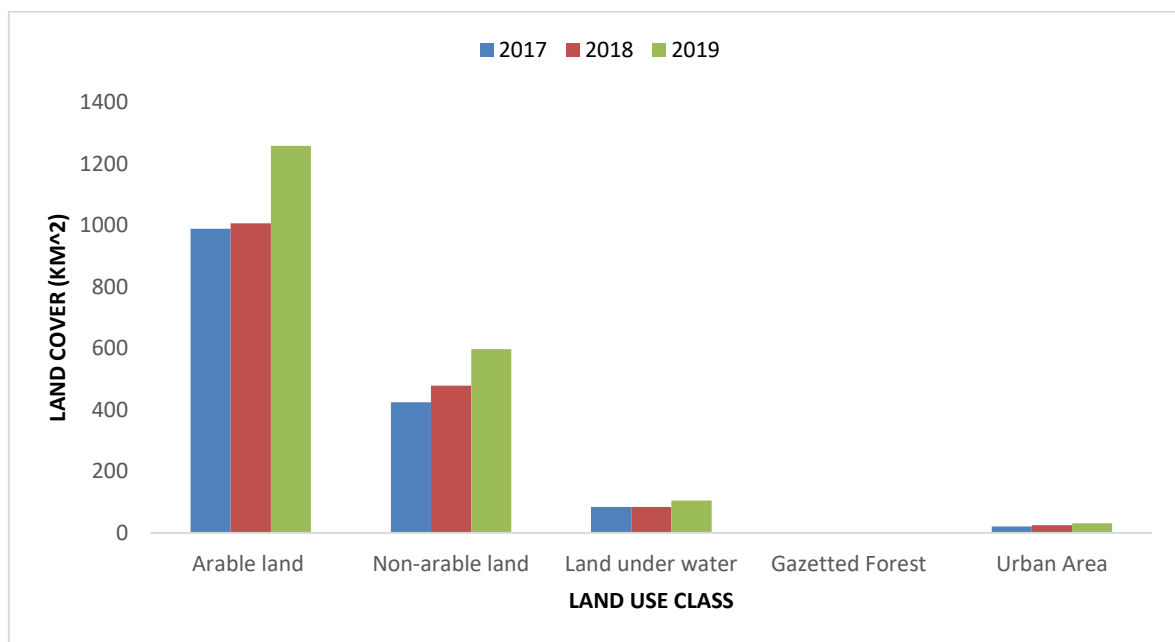


Figure 4.53: General Land use land cover distribution of Naivasha Sub-County

Figure 4.53 indicates that arable land occupies the largest area in Naivasha potentially good for crop production. The land cover has increasingly been rising in the consecutive years beginning 2017 to 2019. Land under water has also increased in 2019 despite homogeneity in 2017 and 2018. Gazetted forest has maintained its land cover in three consecutive years, however built-up area has slightly increased due to increased population, and this has risen from 2017, 2018 and 2019.

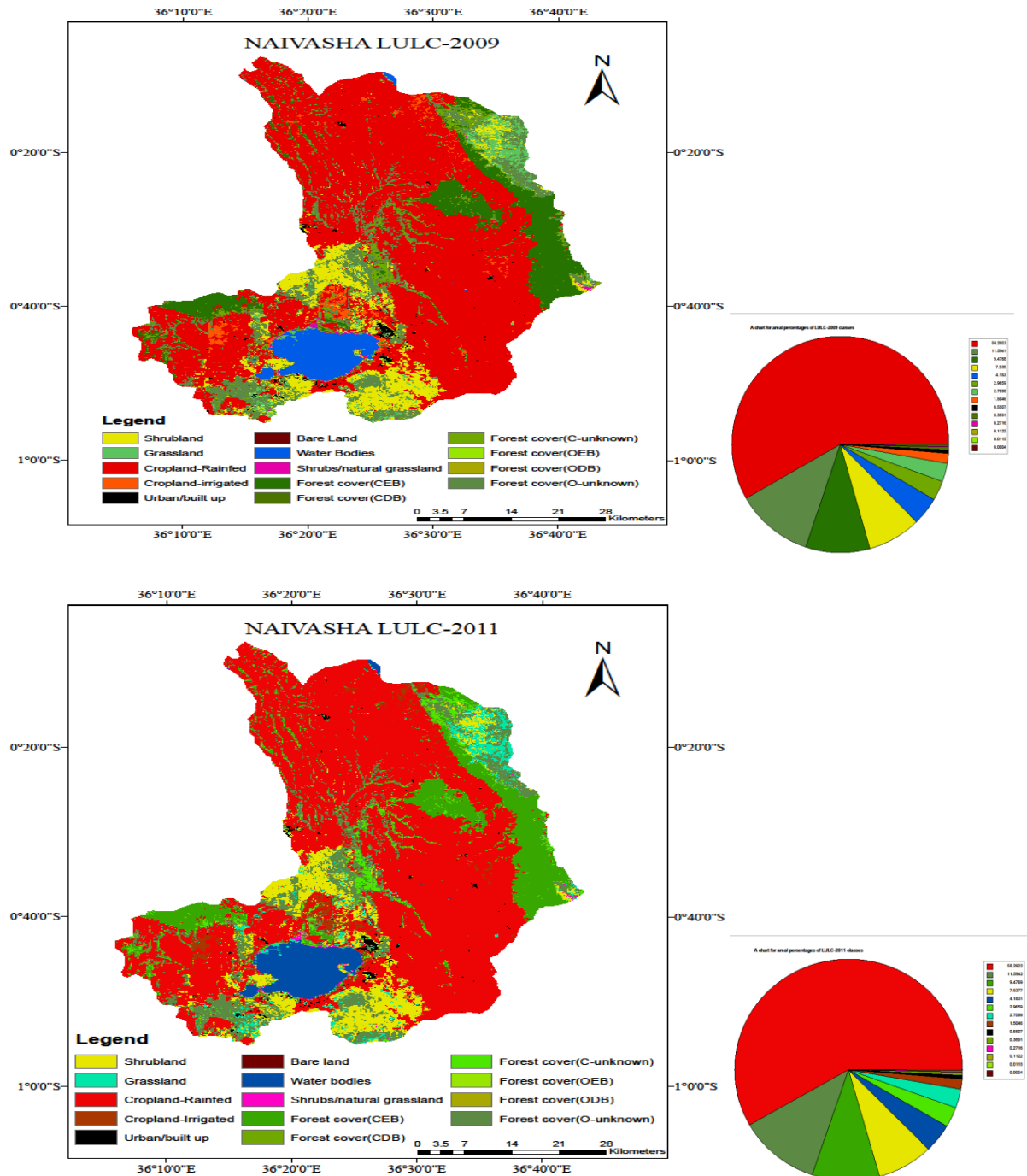


Figure 4.54: Land Use Land Cover Change for Naivasha Cropland in 2009 and 2011

Figure 4.54 shows the land use land cover distribution of Naivasha cropland individual classes as indicated in the maps and pie charts between 2009 and 2011. It can be noted that land use land cover has remained unaltered with rain-fed cropland occupying the largest area with 58.96% followed by closed unknown forest cover with 11.59%, deciduous forest cover of 9.48% and shrub-land with 7.94%. In comparison to transformation that took place within the period, it can be seen that extremely slight changes occurred within the period with slight decrease in rain-fed cropland by 0.0001%. The rest of the other land use remained unchanged during the three-year's period.

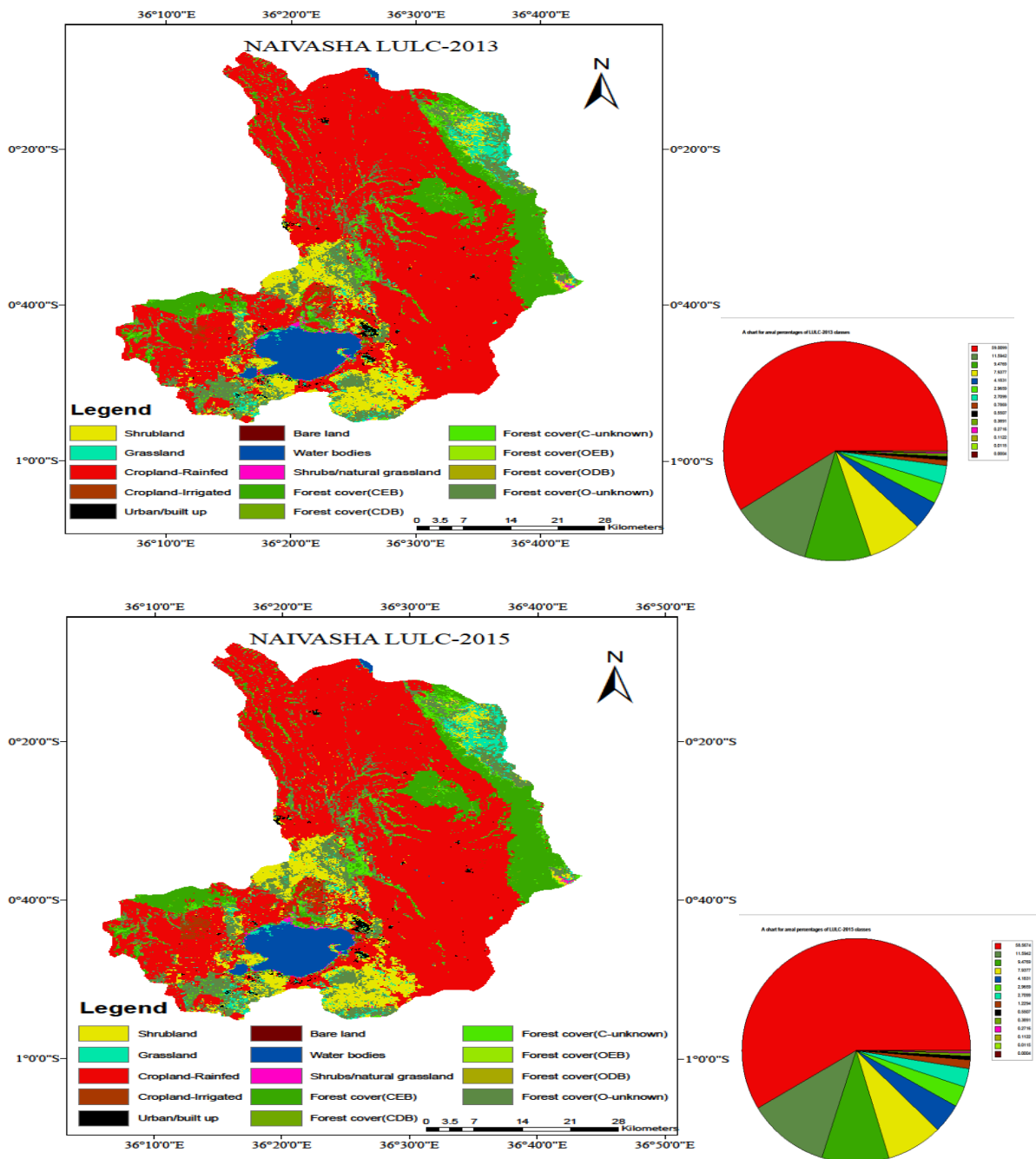


Figure 4.55: Land Use Land Cover Change for Naivasha Cropland in 2013 and 2015

Figure 4.55 shows that Land use cover in Naivasha cropland between 2013 and 2015 rain-fed cropland had decreased from 59.01% to 58.57% indicating a conversion of rain-fed to irrigated cropland (under water management) by 0.44% in the three-year land use transformation. An increase of irrigated land rose from 0.77% to 1.23% during the same period. The rest of the classes have remained unchanged in the entire ecosystem. The decline in land used as rain-fed cropland could probably be the shift caused by upcoming horticultural farms particularly floriculture.

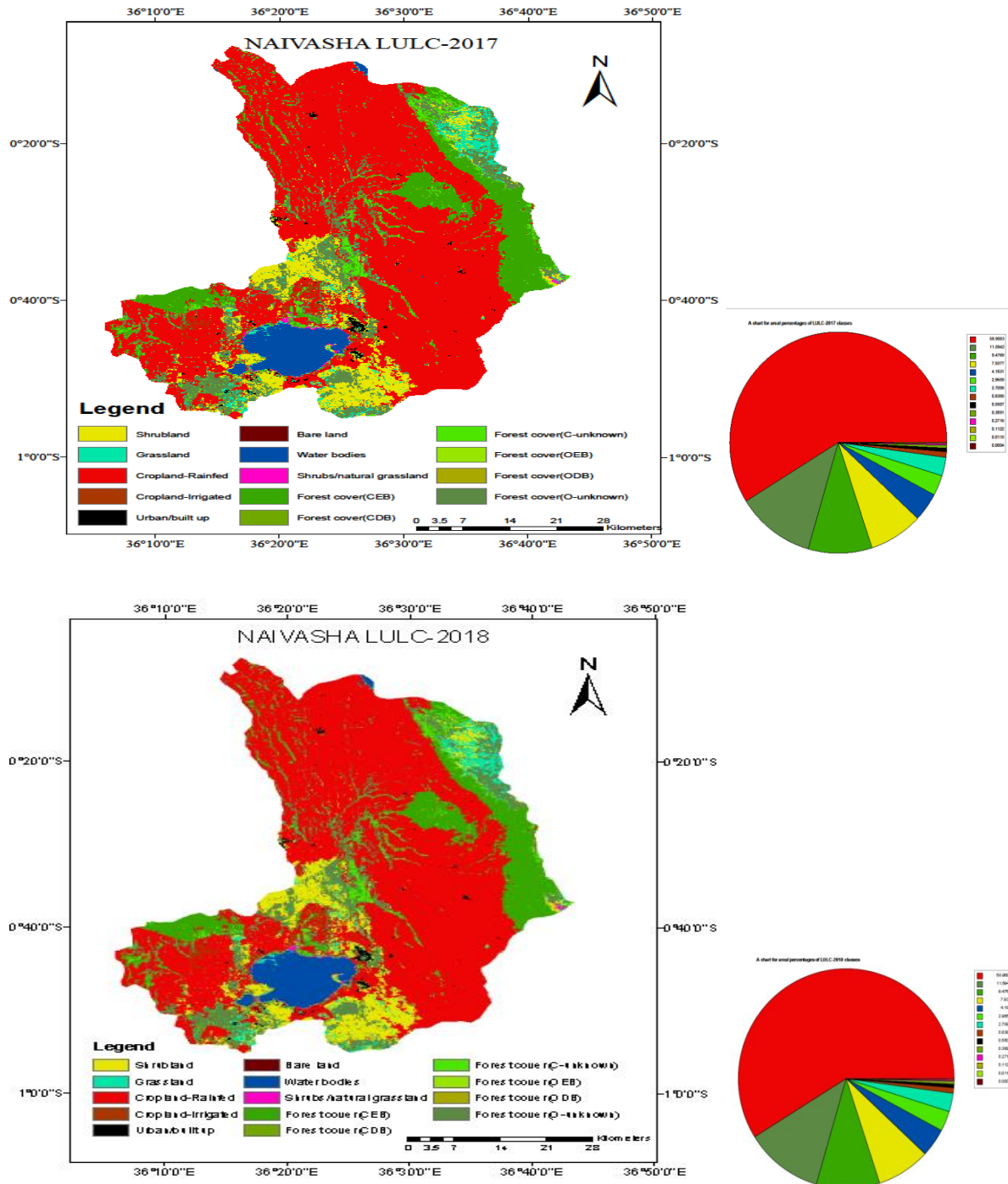


Figure 4.56: Land cover Land use changes for Naivasha cropland in 2017 and 2018

The figure 4.56 shows that rain-fed cropland occupies the greatest area cover with 58.96% followed by open unknown forest with 11.59%. It can be observed that all other classes remained unchanged during the period. Upcoming irrigation systems being transformed from rain-fed cropland in Naivasha cropland are slowly growing. The new upcoming floricultural farms with some built up structures such as green houses that require huge investments coupled with water scarcity. The rate of transformation in such area will gradually continue for many years to realize a change in land cover thus slight transformation could be observed. Majority of the land use land cover classes in Naivasha cropland remained unaltered with the slightest rise in rain-fed cropland from 58.57% to 58.97% in 2015-2017 while irrigated cropland decreased from 1.23% to 0.84% during the same period. In 2018 and 2019, there was no great change in land use land cover classes except a slight decrease in rain-fed cropland of 0.01% from 58.97 to 58.96% between 2017 and 2019. This probably may have been attributed by economic fluctuation leading to closure of most floricultural and other cropland farms worsened by Covid-19 pandemic, which retarded the growth and investments in cropland.

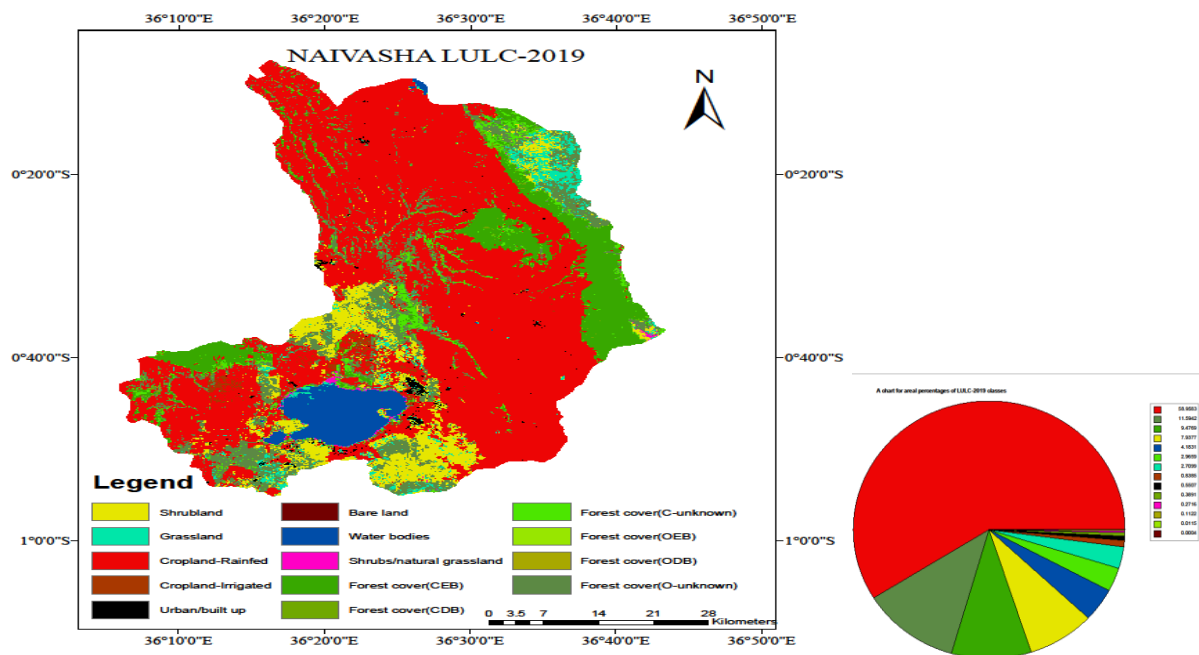


Figure 4.57: Land use land cover maps and percent representation of Naivasha Cropland ecosystem for the period 2019

Figure 4.57 indicates that in 2019 there was no change in almost land cover classes except the conversion of rain-fed to irrigated cropland. Water managed croplands have been the major developments in the area in Naivasha cropland, due to the rise of floral investments and upcoming built up area which has also been slowly growing. The state of art change in

land cover classes is a gradual phenomenon in the area because of huge implications of investments especially in shifting from rain-fed to irrigated cropland coupled with high-water demand for irrigation caused by scarcity in Naivasha Sub-County.

4.10 Estimation of Land Cover and Land Use Change

Level I and level II estimates of land cover and land use were generated by grouping together categories that were spatially and temporally similar. Agricultural climate zones, landform, water resources, terrain, and human activities all contributed to the catchment's varied land use. Most of the land was used for farming, as that was deemed the most economically significant human activity. Using a modified version of Anderson (1977), the taxonomic categorisation of various types of land cover was used as displayed as follows.

Table 4.43: Naivasha Land Use Land Cover classification between 2017 and 2019 according to FAO land cover classes

OID	Class Name	Code	Count	Area cover (%)	Area cover (km ²)
	Shrub-land	20	22010	7.937710	267.3785
1	Grassland	30	7514	2.709857	91.28042
2	Cropland, rain-fed	41	163482	8.958324	1985.987
3	Cropland, irrigated	42	2325	0.838491	28.24423
4	Urban/built up area	50	1527	0.550699	18.55007
5	Bare/sparse vegetation	60	1	0.000361	0.01216
6	Water bodies	80	11599	4.183076	140.9052
7	Shrubs/herbaceous cover	90	753	0.271563	9.147488
8	Forest(closed, evergreen broadleaved)	112	26278	9.476926	319.2264
9	Forest(closed, deciduous broadleaved)	114	1079	0.389132	13.10775
10	Forest (closed, mixed)	116	8224	2.965912	99.90553
11	Forest(open, evergreen broadleaved)	122	32	0.011541	0.388754
12	Forest(open, deciduous broadleaved)	124	311	0.112159	3.77803
13	Forest (open, mixed)	126	32149	11.59425	390.5476

The table 4.43 shows that the total catchment area is 3,368.45902 km² mainly covered by rain-fed cropland that occupies the greatest percent area of 58.96% (1985.99km²) and this indicates that between 2017 and 2019, rain-fed cropland cover was gradually transforming towards irrigated cropland with 0.84% (28.24km²) land cover. Other transition includes shrub-land cover of 7.94% (267.38km²) and grassland of 2.72% (91.28km²) which were found to be systematically transforming. Similarly, transition from mixed open forest (11.59% (390.55km²)) to mixed closed forest of 2.97% (99.91km²) was also found to be a dominant transition. The other transition area cover was open, deciduous broadleaved open forest occupying 0.11% (3.78km²) to closed, deciduous broadleaved forest covering 0.39% (13.11km²) with slight transition of closed evergreen broadleaved of 9.48% (319.23km²) and slight transition in water bodies to 4.18% (140.91km²) during the period. Observation made is that many transitions might in the years been found to be slightly transforming or stationary over the entire study period. With the infrastructure development, urban built up is gradually upcoming with 0.55% (18.55km²) transforming from all forms of land cover usually to horticultural farms. This suggests a trend (pathway) of conversion from closed forested area to large-scale horticultural farms including small-scale agriculture, with open forest as a transitional land cover. The observed reduction of various forms of forest due to deforestation was attributed to continuous encroachment to cropland area caused by a series of development in terms of urbanization, horticultural (green house) structures, and irrigated croplands.

4.10.1 Area Estimation through Direct Expansion

This section presents the land cover generated maps resulting from the classification of satellite images, accuracy assessment of maps, magnitude determination including rates, nature and geographic distribution of land cover changes. The derived thematic maps of land cover types in MMNR and Naivasha cropland were extracted from MODIS and Proba-V satellite images for the period of 2017, 2018, and 2019. The land cover in this cropland displayed includes rain-fed and irrigated agriculture, horticulture (flower farms), build-up land, bare land, grassland, water body, and forested land. The classification of croplands was divided into two major sub-classes, which appeared different as rain-fed and irrigated cropland with dissimilar spectral nature during classification process. The results obtained by direct expansion and regression estimation are shown in table 4.44.

Table 4.44: Naivasha Cropland Land Cover and Land Use statistics for 2017 - 2019

Land cover and Land use within segments		Total Surface Area (ha)	Variance	SE	CV	RE
Shrubland	Direct Expansion	130,936,377.80	43,645,459.26	1,765.65	3.459	
	Regression Estimation	105,458,799.00	28,949,474.3	1,437.99	2.817	1.508
Grassland	Direct Expansion	7,743,715.09	3,497,161.65	499.80	2.868	
	Regression Estimation	6,910,820.22	2,845,631.85	450.84	2.587	1.229
Cropland, rainfed	Direct Expansion	18,958,301,251.00	4,915,115,139	18,737.12	4.942	
	Regression estimation	5,536,558,091.00	767,443,696	7,403.88	1.953	6.405
Cropland, irrigated	Direct Expansion	718,750.06	205,357.16	121.11	2.246	
	Regression estimation	529,110.96	569,811.81	201.74	3.742	0.360
Urban/built-up	Direct Expansion	323,217.50	125,695.70	94.75	2.676	
	Regression estimation	228,232.97	245,789.36	132.50	3.742	0.511
Bare/sparse vegetation	Direct Expansion	0.2818	1.3149	0.0270	1.165	
	Regression estimation	0.0075	0.1056	0.0868	3.742	12.450
Water bodies	Direct Expansion	40,356,003.60	12,840,546.60	957.70	3.560	
	Regression estimation	42,544,875.80	14,181,625.30	1,006.47	3.742	0.905
Shrubs/herbaceous	Direct Expansion	45,684.2072.00	35,532.16	50.38	2.885	
	Regression estimation	59,768.9548.00	59,768.96	65.34	3.742	0.594
Forest (closed, evergreen broadleaved)	Direct expansion	284,388,090.70	72,389,695.83	2,273.92	3.731	

	Regression estimation	264,240,353.00	62,701,100.80	2,116.28	3.473	1.151
Forest (closed, deciduous broadleaved)	Direct expansion	163,406.76	69,324.08	70.37	2.812	
	Regression estimation	2,928,465.50	1,576,866.04	335.61	13.412	0.044
Forest (mixed)	Direct expansion	27063189.44	6532494.004	683.09	1.919	
	Regression estimation	26382578.10	6595644.53	686.38	3.599	0.990
Forest (open, evergreen broadleaved)	Direct expansion	62.16	87.02411912	2.49	3.359	
	Regression estimation	69.40	107.949766	2.78	3.742	0.806
Forest (open, deciduous broadleaved)	Direct expansion	8320.39	6852.088382	22.12	3.067	
	Regression estimation	10195.36	10195.3648	26.99	3.742	0.672
Forest (open, mixed)	Direct expansion	720,829,107.10	94314088.77	2595.52	3.481	
	Regression estimation	683,021,174.00	85377646.80	2469.50	3.312	1.105

From table 4.44, the best results of individual classes, were obtained for cropland, rain-fed with a coefficient of variation of 4.94% and a regression coefficient of 1.95% with relative efficiency of 6.4%. This may be because the structure of the landmass cover vegetation, consisting primarily of crops like forests (closed, evergreen broad leaves) and maize crops, gives a smooth texture and tone colour that gives a separate feature class under supervised categorization. Smaller leaves on other crops, like wheat plantations, resulted in a mottled structure and poor tone hue in satellite imagery, making it difficult to categorize the plants. The bare/sparse vegetation had the lowest reliability with a coefficient of variation of 1.165 and relative efficiency of 12.45%. This could be due to the mixed reflectance from ploughed grounds, quarrying and mixed cropping of beans/peas, barley, Lucerne, fodder trees and hay production (Appendix A.8 and B.16).

4.10.2 Other Land Use and Land Cover in Naivasha Cropland

Most parts of Naivasha croplands LULC has been commercialized for flowers (cropland, irrigated) instead of the normal farming systems for food security, however, crops such as wheat, maize, barley, fodder, and pasture are mainly practiced in most of the subsistence and private commercial farms. The cropland stations within Naivasha and their GPS co-ordinates were as follows; ITC_KEN_00003 – (-0.5998, 36.5666), Engineer/Mzee Paul Farm where entire mixed farming was practiced, however the farmers here are small scale. The other cropland was ITC_KEN_00009 – (-0.7538, 36.1909), Kijabe/Ndabibi farm and wheat growing in large scale was being done and within ITC_KEN_00011 – (-0.6847, 36.4109), Delamere farm, wheat and grass (Burma Rhodes)/Hay/Lucerne for commercial and feedstock for the dairy and beef production was also their major activity. The other croplands were ITC_KEN_00014 – (-0.64393, 36.4793) Nunjoro farm for Pasture production while ITC_KEN_00021 – (-0.7367, 36.4510) KWSTI where most of land is covered by shrubs because the institution main concern is the conservation of vegetation for wildlife management.

Table 4.45: Cropping systems in Naivasha cropland with Land Use Land Cover sizes

Location ID	Location Name	Latitude	Longitude	Cropping System	Sampled Area (ha)
00003	Engineer/Paul's farm	-0.5998	36.5666	Mixed Farming/wheat	0.8
00009	Kijabe/Ndabibi	-0.7538	36.1909	Wheat	1,000
00011	Delamere farm	-0.6847	36.4109	Grass/Hay wheat	10,000
00014	Nunjoro farm	-0.6439	36.4793	Pasture/wheat	500
00021	Kenya Wildlife Service Training Institute	-0.7367	36.4510	Shrub-land	2,500

4.10.3 Land Classification Accuracy Assessment

In the study, field surveys were used to assess the accuracy of ground truth for all land cover types to determine the reliability of the generated maps and improve the quality of data analysis. Publicly available satellite imagery Although the Copernicus hub was crucial in the development of reference data products for use in comparing land cover datasets, field verification was conducted through the previous performance of site visits that enabled actual

land cover comparison with land cover classifications dataset. The accuracy of the producer, the accuracy of the user, and the overall accuracy were evaluated in relation to each land cover category by comparing field verification data with the classified land cover data.

The Kappa index of agreement, a metric for quantifying the level of agreement between two maps with the same number of classes, was used to ensure accuracy. An error matrix is used to characterize these calculated accuracies, showing how the land cover measured in the field compares to the various classifications in the dataset. Based on the error matrices used to evaluate the categorization values, the producer and user accuracy varied from 80% to 100% for MMNR, and from 26.53% to 100% and 48.51% to 100% for Naivasha farmland, respectively. The accuracy of three of ten MODIS imaging maps (from 2017 and 2018, respectively) was assessed using reference data gathered from fieldwork in 2018 and 2019 in MMNR and Naivasha farmland.

Tables 4.46 and 4.51 display the overall accuracy of the MMNR and Naivasha cropland, which were 95.22% and 83.30%, respectively, with a Kappa of 0.94 and 0.81 for 14 - land cover classes. Maximum likelihood classification statistics and land use/cover maps were generated from MODIS and Proba-V images, as shown by the theme maps findings (MLC). Generally, values within these ranges are indicative of good representations of the real land use and land cover changes, hence they were utilized as the measure of actual agreement with the projected output.

Table 4.46: Naivasha Cropland Accuracy Assessment Report for Classification of MODIS image 2017, 2018, and 2019

Confusion Matrix based on Test and Training Area (TTA) mask, S - shrub land, G- Grassland, Cr – Cropland rain-fed, Ci – Cropland irrigated, Bt – Urban built up, Bl – Bare land, Wb – Water bodies, Sng – Shrubland/natural grassland, F_{CEB} - Forest Cover (CEB), F_{CDB} – Forest cover (CDB), F_{C-Unknown} – Forest cover (C-Unknown), F_{QEB} – Forest cover (QEB), F_{ODB} – Forest cover (ODB), F_{O-unknown} –Forest cover (O-unknown)															
User's	Class														Producer's
	S	GI	Cr	Ci	Bt	Bl	Wb	Sng	F_{CEB}	F_{CDB}	F_{C-unknown}	F_{QEB}	F_{ODB}	F_{O-Unknown}	Reference Totals
S	39	2	4	3	1	0	0	2	0	0	0	0	0	0	51
GI	2	24	0	3	1	0	1	1	0	0	0	0	0	2	34
Cr	1	2	49	28	9	2	0	0	0	4	0	0	1	4	101
Ci	0	0	0	13	0	0	0	0	0	0	0	0	0	0	13
Bt	0	0	0	0	25	0	0	0	0	0	0	0	0	0	25
Bl	0	0	0	0	0	1	0	0	0	0	0	0	0	0	1
Wb	0	0	0	0	0	0	42	0	0	0	0	0	0	0	42
Sng	0	0	0	0	0	0	0	14	0	0	0	0	0	0	14
F_{CEB}	0	0	0	0	0	0	0	0	55	0	2	0	0	0	59
F_{CDB}	0	0	0	0	0	0	0	0	0	25	1	0	0	0	26
F_{C-Unknown}	0	0	1	0	0	0	0	0	0	0	54	0	0	1	56

F_{QEB}	0	0	0	0	0	0	0	0	0	0	0	0	9	0	0	9
F_{ODB}	0	0	0	0	0	0	0	0	0	0	0	0	0	14	0	14
F_{O-Unknown}	0	3	0	2	0	0	1	1	0	2	0	1	2	100	112	
Classified Totals	42	31	54	49	36	3	44	18	55	33	58	10	17	107	64	
Accuracy Assessment																
User's	92.8	77.4	90.7	26.53	69.44	33.33	95.45	77.78	100.0	75.7	93.10	90.00	82.35	93.46		
	6	2	4						0	6						
Producer's	76.4	70.5	48.5	100.0	100.0	100.0	100.0	100.0	93.22	96.1	96.43	100.0	100.0	89.29		
	7	9	1	0	0	0	0	0		5		0	0			
Kappa Class																
Overall Performance						83.30										
Kappa Index						0.81										

Table 4.46 shows the error matrix for test and training mask for Naivasha cropland ecosystem, the accuracy assessment analysed indicates that irrigated cropland, built-up area, bare land, water bodies, and shrub-land/natural grassland were correctly classified in reference to the ground truth data. The overall accuracy was 83.30 and the Cohen's Kappa index was 0.81, which depicted satisfactory outcome on classification accuracy as determined. The users and producer's accuracy performance ranged between 26.53 to 100% accuracy and 48.51 to 100% accuracy respectively.

4.10.4 Common Characteristics of Rangeland and Cropland

Based on the rangeland ecosystem findings, MMNR being native grassland has existed over five decades is characterized by dominant native species of low water-demanding grasses, sparse shrubs, and trees along streams and river catchment. The main grass species includes a) pennisetum (b) purple needlegrass (c) ryegrass (d) stipa calamagrotis (e) harpachne and others (Appendix A.9). The radiation balance of a given area is likely to shift if natural vegetation is cleared to make way for agricultural use. Albedo increases, in theory, when land is devoid of vegetation for at least part of the year, because more of the sun's rays are reflected back into space. Decreased soil water-holding capacity is another negative effect on the environment. Soil compaction can lessen soil porosity as natural vegetation is cleared to make way for farming, lowering infiltration capacity and raising erosion hazards. Converting forested areas to farmland reduces occult precipitation in mountainous regions because monoculture croplands absorb less precipitation than do forests with several layers of vegetation (Holder, 2004). To be sure, local climate shifts due to changes in radiation and water balance result from the conversion of forestland to agricultural land. Soil moisture fluctuations appear to be more pronounced in forested areas after rainfall. This land use also results in the driest soil on average compared to the other vegetation types in the area.

4.11 Contribution of the Study to the Scientific World and the Economy

4.11.1 Contribution to Knowledge

The core contribution of the study is the meteorological, soil data obtained for this rangeland ecosystem through GIS, and remote sensing technology can form part of government databank for meteorological department and other research scientist. The study forms part of the underlying issues affecting the deterioration of this rangeland and it highlights the key area about the trend of soil moisture variability with the unfolding climate variability with its effect on biomass formation for increasing wildlife densities in Maasai Mara. MMNR being one of the economic hub and tourism attraction reserves that injects about 30% of Kenyan economy. The hub requires constant evaluation and monitoring of its

changing environmental behaviour for being a sole provider of biomass as feedstock to wildlife industry.

In addition, this research shows that GIS and RS techniques have made it possible for rangelands and croplands to be made available on digital platforms as a virtual ecosystem. For the best possible use of land and water, this allows hydrologists and other stakeholders to conduct a comprehensive scenario analysis. The models relative sensitivity analysis for APSIM and Hydrus-1D identified that the input parameters that influenced the predicted outcome were AGB and yield, soil moisture storage and retention, infiltration rate during precipitation events of high and low/erratic rainy seasons followed by dry season.

The study results can be utilized by government planners, hydrologist, environmentalist and stakeholders to mitigate against the negative effects of land degradation especially encroachment of livestock, expansion of conservancies and encroachment during dry seasons. Wildlife and livestock trampling causes soil matrix aggregation and disaggregation hence gradual compaction resulting from natural processes, climate variation, enhanced by off-road traffic of tourist during the rainy months of the year. This consequently encourage excess surface runoff, decreased soil moisture and subsequently decreased biomass production for maintenance of wildlife densities.

4.11.2 Contribution to Planning and Policy

The dwindling soil moisture storage and retention capacities may be due to the soil compaction caused by moving tourist traffic in-road and off-road, livestock and wildlife trampling and natural processes accelerated with the unfolding climate variability, however, such occurrence promotes excess runoff, diminished infiltration rate. To this effect most of the biomass growth retards owing to the diminished soil moisture levels within the bi-seasons of wet and dry periods. The blooming net primary productivity of biomass relies on the capability of soil potential to store and retain water for a reasonable period before recharge by another rainfall event.

The deficiency of adequate biomass caused by variability of soil moisture in this rangeland pose unforeseeable problem due to the pressure of carrying capacity caused by increasing wildlife population densities. In the study, anticipated growth of wildlife population over time and livestock encroachment highly dependence on the natural rangeland for biomass feeds. As observed without proper sustainability of this rangeland environment, the reserve may in future not be feasible for wildlife survival, and will forcefully become a migratory habitat for herbivores such zebra and wildebeest. The study will enable both National and Narok County government forge ways and options of planning and making decisions for proper ecosystem

management in sound and sustainable manner. The findings will also make the key stakeholders to review their management policies on land use, water resources conservation, biomass trends monitoring and evaluation including setting up modalities for systematic handling of the studied ecosystems in order to avert serious biomass/yield and water sources in the degraded catchment.

CHAPTER FIVE

CONCLUSIONS AND RECOMMENDATIONS

5.1 Conclusions

- i). In this study, the CRNS probe provided good estimates of spatial surface soil moisture for MMNR experimental site through comparison with 5TM-ECH₂O and gravimetric sampling in relation to rainfall events. Findings indicate that, the use of 5TM-ECH₂O probes, deeper soil layers showed higher amount of soil moisture. Most importantly, time series variation of volumetric water content of spatially distributed probes in wet season ranged between 0.11 and 0.32m³m⁻³ (0.16m³m⁻³) and in dry season ranged between 0.04 and 0.17m³m⁻³ (0.11m³m⁻³) across MMNR rangeland ecosystem respectively. Moreover, on Naivasha cropland, volumetric water content in wet season ranged between 0.13 to 0.37m³/m³ (0.22m³m⁻³) and dry season ranged between 0.06 to 0.22m³m⁻³ (0.14m³m⁻³) respectively. However, water retention shown that field capacity of soil water content at -3 bars ranged between 0.16cm³H₂O/cm³soil and 0.22cm³H₂O/cm³soil across the rangeland. Soil moisture in both ecosystems showed seasonal variation in response to cumulative rainfall patterns and an annual periodicity, revealing temporal variation throughout the study period that can be broken down into three distinct phases: a moisture-gaining phase, a moisture-losing phase, and a moisture-stable phase. This demonstrates the need for depth scaling when using the cosmic-ray neutron probe readings to infer root-zone soil moisture.
- ii). The estimated bulk density according to profile dropped by roughly 2.1% to 11.12% from upper layers (0-5cm) to deeper ones at the bottom, suggesting that the compacted soil layer at the bottom is likely linked to the pedological properties of the investigated soil profile (75–80 cm). Results showed that a well-calibrated APSIM model could be used to confidently simulate rangeland and agricultural environments, predicting biomass, grain yield, and yield-water content relationships based on meteorological factors, minimal soil, and cultivar characteristics for short-term simulations. APSIM proves to be an acceptable and reliable model that can be used as a research and decision tool to enhance production systems in croplands. Finally, data partitioning enabled the APSIM model perform accurately the simulation of above ground grass biomass (dry matter) in MMNR and subsequent use of Naivasha Cropland independent dataset for wheat biomass and yield validation. The selected Hydrus-1D and APSIM models were found capable of simulating hydrological processes in semi-arid region of MMNR and Naivasha cropland in Kenya.

This involved modelling the behaviour of rangeland biomass and cropland biomass and yields using ground based measurements, remote sensing, GIS, and ancillary data.

- iii). The significance of detecting and quantifying land cover through NDVI was to examine the impact of soil moisture trends on biomass production for a period of 3 to 10 years and evaluate the behaviour of biomass seasonality in rangeland and cropland ecosystems. The satellite time series analysis of 2017's, 2018's and 2019's from previous decade since 2009 indicates different vegetation coverage. The environmental degradation during periods of fluctuating rainfall coupled with expansion of settlements, that is, mechanized cultivation for commercial wheat production like in the northern loita plains. This may result in decline of biomass net primary productivity which drastic decline in wildlife population with subsequent drop in tourism as a revenue generator for both national and county governments.

The arable land (km²) in Naivasha cropland are Maiella (265.24km²) representing (21.1%), Biashara (264km²) corresponding to 20.1%, MaaiMahiu (222.64km²) (17.7%), Olkaria (221.6km²) (17.6%), Naivasha-East (106.4km²) (8.5%), Hellsgate (81.2km²) (6.5%), Viwandani (80.22km²) (63.4%) and Lakeview(16.6km²) (13.2%) due to climate variation at some seasons are rendered less productive in crop production. The Maiella and Biashara area are more productive than other arable land and Lake View is the least productive. The attributing factors to low production are management practices, soil conditions, and erratic rainfall that may supply inadequate soil moisture for cereal crops such as wheat, barley, and maize crop. Therefore, in analyzing and mapping the trends of LULC changes within MMNR rangeland and Naivasha cropland ecosystems provide a basis for proper guiding policies, management, strategic land use planning, and decision-making on resource protection.

5.2 Recommendations

Specific recommendations that have been drawn from this research for further studies are suggested as follows:

- i). This research used CRNS, 5TM-ECH₂O sensors and gravimetric technique to estimate soil moisture behaviour in rangeland ecosystem; therefore, further research should be conducted using different dielectric sensor such as Ground Penetrating Radar (GPR). It is therefore important to consider the number of calibrations carried out against the accuracy of the calibrated CRNS to have an accurate and valid estimate of soil moisture regimes. Therefore, multifactor experiments should be conducted to fully understand the climate-vegetation-soil interaction under different climate change scenarios.
- ii). Research should also be conducted by modelling the impact of soil heterogeneity and spatial variability of soil hydraulic characteristics in different layers of the soil profile in more

similar ecosystems using a different tool such as SWAT or VIC and other crop models to have a more comprehensive understanding of the systems hydrology and crop biomass and yield simulations. Moreover, a more secure installation of weather stations and spatial distribution of 5TM-ECH₂O soil moisture and temperature probe cables should be buried at least 30cm below the soil surface to provide realistic data and damages from hyenas and wildfire.

iii). In terms of Land Use Land Cover changes, ecosystems policies governing the conversion of grassland to either rain-fed or irrigated croplands for sustainable biomass production used for wildlife/livestock carrying capacities. Secondly, protection and conservation of MMNR from degradation by commercial wheat farming (agricultural and livestock) should instead be alternatively directed to venture into Naivasha arable cropland areas which instead can be favourable for wheat and livestock production. MMNR should be preserved for wildlife and tourism attraction. Croplands too require protection and conservation management for provision of future food security, therefore participatory approach of all stakeholders'(inter-government agencies and private sector), and research institutions should collaborate in the area of data gathering and analysis in order to fully access and utilize the best resources in the country's national reserves and croplands.

REFERENCES

- Albergel, C., de Rosnay, P., Gruhier, C., Munoz-Sabater, J., Hasenauer, S., Isaksen, L., Kerr, Y., & Wagner, W. (2012). Evaluation of remotely sensed and modelled soil moisture products using global ground-based in situ observations. *Journal of Remote Sensing of Environment*, 118, p. 215-226. ISSN 0034-4257.
- Alcamo, J., Dronin, N., Endejan, M., Golubev, G., & Kirilenko, A. (2007). A new assessment of climate change impact on food production shortfalls and water availability in Russia, *Journal of Global Environmental Change* 17, 429-444.
- Al-doski, J., Mansor, S.B., & Shafri, H.Z.M. (2013). Change detection process and techniques. *Civil and Environmental Research* 3: 37–45.
- Aliku, O. O., & Suarau, O. (2016). Establishing relationship between measured and predicted soil water characteristics using SOILWAT model in three agro-ecological zones of Nigeria. *Geoscience Model Development Discussions*, <https://doi.org/10.5194/gmd-2016-165>.
- Allen, J.D., & Hanuschak, G. A. (1988). The remote sensing applications program of the National Agricultural Statistic Service: 1980-1987, NASS Staff Report SRB-88-08, National Agricultural Statistics Service, Washington, DC.
- Allen, R.G., Smith, M., Pereira, L.S., & Perrier, A., (1994). “An Update for the Calculation of Reference Evapotranspiration”, ICID Bulletin.
- American Petroleum Institute (1996). *Estimation of infiltration and recharge for environmental site assessment*, Stephens and Associates, API Publication 4643.
- Anderson, J. R. (1977). Land use and land cover changes: A framework for monitoring. *Journal of Research by the Geological Survey*, 5: 143-153.
- Archontoulis, S.V., Miguez, F.E., & Moore, K.J. (2014). Evaluating APSIM maize, soil water, soil nitrogen, manure, and soil temperature modules in the Midwestern United States. *Journal of Agronomy*. 106:1025–1040.
<https://doi.org/10.2134/agronj2013.0421>.
- Arshad, M.A., Lowery, B., & Grossman, B. (1996). Physical tests for monitoring soil quality. In: J.W. Doran and A.J. Jones (eds.) *Methods for assessing soil quality*, *American society of soil Science journal*. Special. Publication. 49:123-142, SSSA, Madison, WI, USA.
- Ashraf, M.S., Izadi, B., & King, B. (1997). Transport of bromide under intermittent and continuous ponding conditions. *Journal of Environmental Quality*. 26:69-75.
- Atzberger, C., (2013). *Advances in Remote Sensing of Agriculture: Context Description*,

- Existing Operational Monitoring Systems and Major Information Needs, *Journal of Remote Sensing*, 5(2), 949-981.
- Ayu, I. W. (2013). Assessment of infiltration rate under different dry land types in Illerlive Sub district, Sumbuwa Bester. Indonasia. *Journal of Natural Science Research*, 3 (10):71-76.
- Baldyga, T. J. (2005). *Assessing land cover change impacts in Kenya's River Njoro watershed using remote sensing and hydrologic modelling* (Master's thesis). Laramie: University of Wyoming.
- Barger, N.N., Archer, S. R., Campbell, J.L., Huant, C., Morton, J.A., & Knapp, A.K. (2011). Woody plant proliferation in North American drylands: A synthesis of impacts on ecosystem carbon balance. *Journal of Geophysical Research, Biogeosciences* 116, G00K07
- Barr, A. G., King, K. M., Gillespie, T. J., den Hartog, G., & Neumann, H. H. (1994). A comparison of Bowen ratio and eddy correlation sensible and latent heat flux measurements above deciduous forest, Bound. -Lay. *Journal of Meteorology*, 71, 21-41.
- Bastiaanssen, W.G.M., Pelgrum, H, Menenti, M. & Feddes, R.A. (1996). *Estimation of surface resistance and Priestley-Taylor a-parameter at different scales*, In: Stewart *et al.* (1996) (eds.) *Scaling up in hydrology using remote sensing*, John Wiley & Sons, Chichester, p.255-262.
- Brady, N. C., & Weil, R. R. (2010). *"Elements of the Nature and Properties of Soils."* (Third Edition). Upper Saddle River, N.J: Prentice Hall.
- Behrman, J.A., Bryan, E., & Goh, A. (2014). *Gender, climate change, and group based approaches to adaptation*. In: Ringler C, Quisumbing AR, Bryan E, Meinzen-Dick R (eds) *Enhancing women's assets to manage risk under climate change. Potential for group based approaches*. IFPRI, Washington, DC, pp 3–8.
- Benedetti, R., Rossini, P & Taddei, R. (1994). Vegetation classification in the middle Mediterranean area by satellite data, *International Journal of Remote Sensing*, 15:583-596
- Berthelot, B., Dedieu, G., Cabot F., & Adam, S. (1997). "Estimation of surface reflectances and vegetation index using NOAA/AVHRR: Methods and results at global scale", *Communications for the 6th International Symposium on Physical Measurements and Signatures in Remote Sensing*, Val d'Isère, France, January. 17-21.

- Bestelmeyer, B.T., Brown, J. R., Havstad, K.M., Alexander, R., Chavez, G., & Herrick, J. (2003). Development and use of state-and-transition models for rangelands. *Journal of Range Management* 56: 114–126.
- Bell, J. E., Sherry, R., & Luo, Y. (2010). Changes in soil water dynamics due to variation in precipitation and temperature: An eco-hydrological analysis in a tallgrass prairie, *Water Resources Research.*, 46, W03523, <https://doi.org/10.1029/2009WR007908>.
- Ben-Hur, M., & S. Assouline. (2002). Tillage effects on water and salt distribution in a Vertisol during effluent irrigation and rainfall. *Journal of Agronomy*. 94:1295–1304.
- Blake, G.R., & Hartge, K.H. (1986): Bulk Density. *Methods of Soil Analysis, Part 1, American society of soil Science journal* 363-376, Madison, WI, USA.
- Bogena, H., Schulz, K., & Vereecken, H. (2006). Towards a Network of Observatories in Terrestrial Environmental Research. *Advances in Geosciences* 9, 109–114 (www.adv-geosci.net/9/109/2006/).
- Bogena, H. R., Huisman, J. A., Baatz, R., Hendriks Franssen, H.-J., & Vereecken, H. (2013). Accuracy of the cosmic-ray soil water content probe in humid forest ecosystems: The worst case scenario, *Water Resources Research.*, 49, 5778–5791, <https://doi.org/10.1002/wrcr.20463>.
- Bondeau, A., Smith, P. C., Zaehle, S., Schaphoff, S., Lucht, W., Cramer, W., Gerten, D., Lotze-Campen, H., Müller, C., Reichstein, M., & Smith, B. (2007). Modelling the role of agriculture for the 20th century global terrestrial carbon balance, *Global. Change Biology*. 13: 679-706.
- Boonman, J. G., (1993). East Africa's grasses and fodders: their ecology and husbandry. *Tasks for vegetation science*, 29. Springer.
- Bot, A., & Benites. J. (2005). *Importance of soil organic matter: Key to drought-resistance food production*. IAEA Tecdoc Series. Rome: Food and Agriculture Organization.
- Bouwer, H. (1986). *Intake rate: Cylinder infiltrometer*. p. 825–844. In A. Klute (ed.) *Methods of soil analysis. Part 1*. 2nd ed. SSSA Book Ser. 5. SSSA, Madison, WI.
- Brevik, E. C., Cerdà, A., Mataix-Solera, J., Pereg, L., Quinton, J. N., Six, J., & Van Oost, K. (2015): The interdisciplinary nature of SOIL, *SOIL*, 1, 117–129, <https://doi.org/10.5194/soil-1-117>.
- Briggs, J.M., & Knapp, A.K. (1995). Inter-annual variability in primary production in tall prairie: climate, soil moisture, topographic position, and fire as determinants of aboveground biomass. *American Journal of Botany* 82, 1024–1030.
- Brocca, L., Moramarco, T., Melone, F., Wagner, W., Hasenauer, S., & Hahn, S. (2012).

- Assimilation of surface - and root-zone ASCAT soil moisture products into rainfall-runoff modeling. *IEEE Transformative. GeoscienceRemote Sensing*. 50:2542–2555. <https://doi.org/10.1109/TGRS.2011.2177468>.
- Brocca, L., Melone, F., Moramarco, T., Wagner, W., Naeimi, V., Bartalis, Z., & Hasenauer, S. (2010a). Improving runoff prediction through the assimilation of the ASCAT soil moisture product, *Hydrological Earth System Science.*, 14, 1881–1893, <https://doi.org/10.5194/hess-14-1881-2010>.
- Brocca, L., Melone, F., Moramarco, T., & Morbidelli, R. (2012b). Spatial-temporal variability of soil moisture and its estimation across scales, *Water Resource Research.*, 46, W02516, <https://doi.org/10.1029/2009WR008016>.
- Brolsma, R. J., & Bierkens, M. F. P. (2007). Groundwater-soil water-vegetation dynamics in a temperate forest ecosystem along a slope, *Journal of water resources*. 43, W01414, <https://doi.org/10.1029/2005WR004696>.
- Bullied, W.J., & Entz, M.H. (1999). Soil water dynamics after alfalfa as influenced by crop termination technique. *Agronomy Journal* 91, 294–305.
- Bunce, R.G.H., Barr, C.J., & Fuller, R.M. (1992). *Integration of methods for detecting land use change, with special reference to Countryside Survey 1990*. In Whitby M C (ed.) *Land use change: the causes and consequences*. London, Her Majesty's Stationery office: 69-78.
- Carfagna, E. & Gallego, F.J. (2005). Using remote sensing for agricultural statistics. *International Statistical Review/Revue Internationale de Statistique*, 73(3): 389-404.
- Carmona, A.; & Nahuelhual, L. (2012). Combining land transitions and trajectories in assessing forest cover change. *Journal of Application Geography*. 32, 904–915.
- Chapin III, S.F., Matson, P.A., & Mooney, H.A. (2002). *Principles of Terrestrial Ecosystem Ecology*. Springer, New York.
- Chen, M., Willgoose, G.R., & Saco, P.M. (2014). Spatial prediction of temporal soil moisture dynamics using HYDRUS-1D. *Journal of Hydrologic Process*. 28, 171–185.
- Chong, D.L.S., Mougin, E., & Gastellu-Etchegorry, J. (1993). Relating the Global Vegetation Index to net primary productivity and actual evapo-transpiration over Africa. *International Journal of Remote Sensing* 14, 1517–1546.
- Cochran, W.G. (1977), *Sampling Techniques*, John Wiley & son.
- Cohen, J. A. (1960). Coefficient of agreement for nominal scales. *Educational and Psychological Measurement*, 20, 37-46.

- Congalton, R.G. (1991). A review of assessing the accuracy of classifications of remotely sensed data. *Remote Sensing of Environment*. 37: 35-46
- Comber, A.J., Fisher, P.F., & Wadsworth, R.A. (2006). What is land cover? *Environment and Planning and Design*, 32(2): 199-209.
- Cotter, J.J., & Tomczak, C. (1994). An image analysis system to develop area sampling frames for agricultural surveys. *Photogrammetric engineering and remote sensing*, 60(3): 299-306.
- Crow, W. T., Berg, A. A., Cosh, M. H., Loew, A., Mohanty, B. P., Panciera, R., de Rosnay, P., Ryu, D., & Walker, J. P. (2012). Upscaling sparse based soil moisture observations for the validation of coarse-resolution satellite soil moisture products, *Revised Geophysics.*, 50, RG2002, <https://doi.org/10.1029/2011RG000372>.
- Daly, E., Porporato, A., & Rodriguez-Iturbe, I. (2004). Coupled dynamics of photosynthesis, transpiration, and soil water balance. Part I: Upscaling from hour to daily level, *Journal of Hydrometeorology.*, 5,546–558, <https://doi.org/10.1175/1525-7541>.
- D’Asaro, E. A., Thomson, J., Shcherbina, A. Y., Harcourt, R. R., Cronin, M. F., Hemer, M.A., & Fox-Kemper, B. (2014). Quantifying upper ocean turbulence driven by surface waves. *Geophysical Resource Letters*. 2014, 41, 1–6.
- DeFries, R., & Eshleman, K. N. (2004). Land-use change and hydrologic processes: a major focus for the future. *Hydrological Processes* 18: 2183-2186.
- De Jong, T. (2011). *Water abstraction survey in Lake Naivasha basin, Kenya*. Wageningen University. B.Sc. Internship thesis. Wageningen.<ftp://ftp.itc.nl/pub/naivasha/Dejong.pdf>.
- Derner, J.D., Augustine, D.J., Ascough II, J.C., & Ahuja, L.R. (2012). Opportunities for increasing utility of models for rangeland management. *Rangeland Ecology Management*. 65, 623–631
- Desilets, D., Zreda, M., & Ferre, T. P.A. (2010). Nature's neutron probe: Land surface hydrology at elusive scale with cosmic rays, *Water Resource Research*, 46, W11505, <https://doi.org/10.1029/2009WR008726>.
- Dessu, S. B., & Melesse, A.M. (2012). Modeling the rainfall-runoff process of the Mara River basin using SWAT. *Hydrological Process* 26(26):403. <https://doi.org/10.1002/hyp.9205>
- Dessu, S.B., & Melesse, A.M. (2013). Evaluation and Comparison of Satellite and GCM Rainfall Estimates for the Mara River Basin, Kenya/Tanzania. *Handbook of Environmental Chemistry*. 25: 29-45.

- Dexter, A.R., & Bird, N.R.A. (2001). Methods for predicting the optimum and the range of soil water contents for tillage based on the water retention curve. *Soil Tillage Research*, 57:203-212, 2001.
- Didan, K. (2015). MOD13Q1 MODIS/Terra Vegetation Indices 16-Day L3 Global 250m SIN Grid V006. NASA EOSDIS Land Processes DAAC.
<https://doi.org/10.5067/MODIS/MOD13Q1.006>.
- Dirk, S.M., Carlson, D.A., Cherkauer, D.S., & Malik, P. (1999). Scale dependency of hydraulic conductivity in heterogeneous media. *Ground Water* 37:904–919.
- D’Odorico, P., Ridolfi, L., Porporato, A., & Rodriguez-Iturbe, I. (2000). Preferential states of seasonal soil moisture: The impact of climate fluctuations, *Water Resource. Research*, 36(8), 2209–2219.
- Dong, J., Ochsner, T. E., Zreda, M., Cosh, M. H., & Zou, C. B. (2014). Calibration and validation of the COSMOS rover for surface soil moisture measurement, *Vadose Zone Journal.*, 13, <https://doi.org/10.2136/vzj2013.08.0148>.
- Dorigo, W.A., Gruber, A., De Jeu, R.A.M., Wagner, W., Stacke, T., Loew, A., Albergel, C., Brocca, L., Chung, D., Parinussa, R.M., & Kidd, R. (2015). Evaluation of the ESA CCI soil moisture product using ground-based observations. *Remote Sensing Environment*.162:380–395. <https://doi.org/10.1016/j.rse.2014.07.023>.
- Drusch, M., Del Bello, U., & Carlier S. (2012). Sentinel-2: ESA's optical high-resolution mission for GMES operational services. *Remote Sensing Environment* 120: 25-36.
- Easton, Z. M., & Bock, E. M (2015). Hydrology Basics and the Hydrologic Cycle. VCE publication BSE-191.
- European Commission, Better regulation toolbox, appendix to the Better Regulation Guidelines, Strasbourg, 19.5.2015, SWD (2015) 111 final, COM (2015) 215 final, http://ec.europa.eu/smart-regulation/guidelines/docs/swd_br_guidelines_en.pdf.
- FAO. (1996). Multiple Frame Agricultural Surveys - Current surveys based on area and list sampling method (Vol. 1). *FAO Publication: Rome*.
- FAO (2015). The Global Forest Resources Assessment. *Food and Agriculture Organization, Rome*.
- FAO (1978). Wildlife management Kenya: Plans for rural incomes from wildlife in Kajiado district. AG/KEN/71/525 Technical Report 1. Rome: *Food and Agricultural Organization of the United Nations*.
- Feddes, R.A., Hoff, H., Bruen, M., Dawson, T., De Rosnay, P., Dirmeyer, P., Jackson, R. B., Kabat, P., Kleidon, A., Lilly, A., & Pitman, A. J. (2001). *Modelling Root Water*

- Uptake in Hydrological and Climate Models*. Bulletin of the American Meteorological Society 82 (12): 2797-2809. <https://doi.org/10.1175/1520-0477-082<2797:MRWUIH>2.3.CO;2>.
- Field, C.B., Chapin III, F.S., Chiariello, N.R., Holland, E.A., & Mooney, H.A. (1995a). *The Jasper Ridge CO₂ experiment: design and motivation*, p. 121-145. In: G. Koch and H. Mooney (eds.). Carbon dioxide and terrestrial ecosystems. Academic Press.
- Fischer, G., Van Velthuisen, H., & Nachtergaele, F. (2000). *Global agro-ecological zones assessment: methodology and results*. Interim report. Laxenburg, Austria: International Institute for Systems Analysis (IIASA), and Rome: FAO.
- Foody, G.M. (2002). Status of land cover classification accuracy assessment. *Remote Sensing of Environment*, 80, 185–201.
- Franch, B., Vermote, E.F., & Becker-Reshef, I. (2015). Improving the timeliness of winter wheat production forecast in the United States of America, Ukraine and China using MODIS data and NCAR Growing Degree Day information. *Remote Sensing of Environment* 161:131-148.
- Francois, M., Santandrea, S., Mellab, K., Vrancken, D., & Versluys, J. (2014). The PROBA-V mission: The space segment. *International journal of Remote Sensing*, 35, 2548 – 2564, <https://doi.org/10.1080/01431161.2014.883098>.
- Franz, T. (2014). *Stationary probe data calculations*. Lincoln, NE: Franz Hydrogeophysics Laboratory Group, University of Lincoln-Nebraska; p. 1–4.
- Franz, T. E., Zreda, M., Ferre, P. A., & Zweck, C. (2011). Understanding the spatiotemporal distribution of soil moisture in a southern Arizonan dry land, Abstract H52A-03 presented at 2011 Fall Meeting, AGU, San Francisco, California, 5–9 Dec.
- Franz, T., Wang, T., Avery, W., Finkenbiner, C., & Brocca, L. (2015). *Spatio-temporal characterization of soil moisture fields in agricultural areas using cosmic-ray neutron probes and data fusion*. EGU General Assembly; 2015 April 12–17; Vienna, Austria.
- Franz, T. E., Zreda, M., Rosolem, R., & Ferré, T. P. A. (2012a). Field validation of a cosmic-ray neutron sensor using a distributed sensor network, *Vadose Zone Journal.*, 11, <https://doi.org/10.2136/vzj2012.0046>.
- Franz, T. E., Zreda, M., Ferré, T. P. A., Rosolem, R., Zweck, C., Stillman, S., Zeng, X., & Shuttleworth, W. J. (2012b). Measurement depth of the cosmic ray soil moisture probe affected by hydrogen from various sources, *Water Resources Research.*, 48, W08515, <https://doi.org/10.1029/2012WR011871>.

- Foken, T. (2008). The Energy Balance Closure Problem: An Overview, *Ecological Applications*, 18, 1351–1367.
- Foken, T. (2015). A modified Bowen ratio method to determine sensible and latent heat fluxes. *Meteorologische Zeitschrift*, Vol. 10, No. 1, 71-80, <https://doi.org/10.1127/0941-2948/2001/0010-0071>.
- Fonseca, E. L. (2007): Estimativa da disponibilidade de forragem do bioma Campos Sulinos a partir de dados radiométricos orbitais: parametrização do submodelo espectral. *Ciência Rural*, v.37, p. 1668-1674.
- Fu, B.J., Chen, L.D., Ma, K.M., Zhou, H.F., & Wang, J. (2000). The relationships between land use and soil conditions in the hilly area of the Loess Plateau in northern Shaanxi, China. *Catena*. 36, 69–78.
- Fuchs (2015). Palmer Drought Severity Index (PSDI and sc PDSI). http://drought.unl.edu/Portals/0/docs/workshops/03222012_Kingston_Jamaica/Brian%20Fuchs-PDSI%20and%20scPDSI.pdf.
- Gabiri, G., Burghof, S. D., Iekkrüger, B., Leemhuis, C., Steinbach, S., & Näschen, K. (2018). Modeling spatial soil water dynamics in a tropical floodplain, East Africa. *Water*, 10, 191.
- Gallego, J., & Bamps, C. (2008). Using CORINE land cover and the point survey LUCAS for area estimation. *International Journal of Applied Earth Observation and Geoinformation*, 10(4): 467-475.
- Galvin, K.A., Reid, R.S., Behnke, R.H. Jr., & Hobbs, N.T. (2008). Fragmentation in Semi-Arid and Arid Landscapes: *Consequences for Human and Natural Systems*; Springer: Dordrecht, The Netherlands.
- Gao, X., Wu, P., Zhao, X., Wang, J., & Shi, Y. (2014): Effects of land use on soil moisture variations in a semi-arid catchment: Implications for land and agricultural water management, *Journal of Land Degradation Development*., 25, 163–172.
- Garcia-Ruiz, J. M. (2010): *The effects of land uses on soil erosion in Spain: A review*, *Catena*, 81, 1–11.
- Gee, G.W., & Bauder, J.W. (1979). Particle size analysis by hydrometer: A simplified method for routine textural analysis and a sensitivity test of measured parameters. *American Society of Soil Science. Journal*, 43:1004-1007.
- Gentine, P., Entekabi, D., Chehbouni, A., Boulet, G., & Duchemin, B. (2006). *Analysis of diurnal evaporative fraction behaviour*, Technical Paper, MIT Department of Civil and Environmental Engineering, Cambridge, USA, 4pp.

- Gerten, D., Schaphoff, S., & Lucht, W. (2007). Potential future changes in water limitations of the terrestrial biosphere, *Journal of Climate Change*, 80, 277–299, <https://doi.org/10.1007/s10584-006-9104-8>.
- Gibson, L. R. (2015). Growing degree - day calculation. <https://doi.org/agronomywww.agron.iastate.edu/Courses/agron212/Calculations/GDD.htm>
- Giglioli, N., & Saltelli, A. (2000). SimLab 1.1, Software for Sensitivity and Uncertainty Analysis, tool for sound modelling, *Joint Research Centre, European Commission, Institute for Systems Informatics and Safety*, Ispra, Italy.
- Giroto, M., Reichle, R.H., Rodell, M., Liu, Q., Mahanama, S., & De Lannoy, G.J.M. (2019). Multi-sensor assimilation of SMOS brightness temperature and GRACE terrestrial water storage observations for soil moisture and shallow groundwater estimation. *Remote Sensing Environment*. 227, 12-27.
- Goldewijk, K.K., Beusen, A., van Drecht, G., & de Vos, M. (2011). The HYDE 3.1 spatially explicit database of human-induced global land-use change over the past 12,000 years. *Global Ecology Biogeography*. 20, 73–86.
- Gomez-Plaza, A., Alvarez-Rogel, J., Albaladejo, J., & Castillo, V. M. (2000). Spatial patterns and temporal stability of soil moisture across a range of scales in a semi-arid environment, *Journal of Hydrologic Process*, 14, 1261–1277.
- Gornall, J., Betts, R., Burke, E., Clark, R., & Camp, J. (2010). Implications of climate change for agricultural productivity in the early twenty-first century. *Philos Trans R Society London B Biological Sciences* 365 (554): 2973-2989.
- Grayson, R. B., & Western, A.W. (1998). Towards areal estimation of soil water content from point measurements: Time and space stability of mean response, *Journal of Hydrology*., 207, 68–82.
- Grossi, M.C., Justino, F., Rodrigues, R.D.Á., & Andrade, C.L.T. (2015). Sensitivity of the sorghum yield to individual changes in climate parameters: *Modelling based approach*. *Bragantia*, 74, 341–349.
- Gupta, M., Grag, N.K., Joshi, H., & Sharma, M.P. (2012). Persistency and mobility of 2, 4- D in saturated soil zone under winter wheat crop in subtropical region of India. *Agriculture, Ecosystems and Environment*, 146, 60-72.
- Han, X., Franssen, H. J. H., Rosolem, R., Jin, R., Li, X., & Vereecken, H. (2015a). Correction of systematic model forcing bias of CLM using assimilation of cosmic ray Neutrons

- and land surface temperature: A study in the Heihe Catchment, China. *Hydrology and Earth System Sciences*, 19(1), 615–629. <https://doi.org/10.5194/hess-19 - 615>.
- Hauke, J., & Kossowski, T. (2011). Comparison of values of Pearson's and Spearman's correlation coefficients on the same sets of data. *Questiones Geographicae*, 30(2): 97-93
- Hawdon, A., McJannet, D., & Wallace, J. (2014). Calibration and correction procedures for cosmic-ray neutron soil moisture probes located across Australia, *Water Resource Research*, 50, 5029–5043, <https://doi.org/10.1002/2013WR015138>.
- He, L., Asseng, S., Zhao, G., Wu, D., Yang, X., & Zhuang, W. (2015). Agricultural and Forest Meteorology Impacts of recent climate warming, cultivar changes, and crop management on winter wheat phenology across the Loess Plateau of China. *Agriculture for Meteorologist*. 200: 135-143.
- Lamprey, R H., & Reid, R. S. (2004). Expansion of human settlement in Kenya's Maasai Mara: what future for pastoralism and wildlife? *Journal of Biogeography* 31, 997–1032, © 2004 Blackwell Publishing Ltd.
- Herrero, M., Ringler, C., Van de Steeg, J., Koo, J., & Notenbaert, A. (2010). Climate variability and climate change and their impacts on Kenya's agricultural sector. ILRI, Nairobi. Kenya:1-56.
- Hodnett, M. G., & Bell, J. P. (1986). Soil moisture investigations of groundwater recharge through black cotton soils in Madhya Pradesh, India, *Hydrological Science Journal*, 31(3), 361–381.
- Holzworth, D. P., Huth, N. I., Devoil, P. G., Zurcher, E. J., Herrmann, N. I., McLean, G., & Keating, B.A.(2014). APSIM-evolution towards a new generation of agricultural systems simulation. *Environmental Modelling Software*, 62, 327–350.
- Homewood, K., Lambin, E. F., Coast, E., Kariuki, A., Kikula, I., Kivulia, J., Said, M., Serneels, S., & Thompson, M. (2001). Long-term changes in Serengeti-Mara wildebeest and land cover: Pastoralism, population, or policies? *Proceedings of National Academic Science*. USA 98, 12544–12549.
- Honar, M. R. S., Seyed, A. G., & Alireza, G. (2011). Evaluation of water flow and infiltration using HYDRUS model in sprinkler irrigation system. *2nd International Conference on Environmental Engineering and Applications IPCBEE* vol.17 (2011) IACSIT Press.
- Honari, M., Ashrafzadeh, A., Khaledian, M., Vazifedoust, M., & Mailhol, J.C. (2017). Comparison of HYDRUS-3D soil moisture simulations of subsurface drip irrigation

- with experimental observations in the south of France. *Journal of Irrigation and Drainage Engineering*. 143, 1–8.
- Hornbuckle, B., Irvin, S., Franz, T., Rosolem, R., & Zweck, C. (2012). The potential of the COSMOS network to be a source of new soil moisture information for SMOS and SMAP, in: Proc. IEEE Int. *Geoscience Remote Sensing. Symposium*. 22–27 July 2012, Munich, Germany, 1243–1246.
- Howard, P.J.A., & Howard, D.M. (1990). Use of organic carbon and loss-on-ignition to estimate soil organic matter in different soil types and horizons. *Biology and Fertility of Soils*. 9:306-310.
- Huete, A., Dedan, K., Miura, T., Rodriguez, E. P., Gao, X., & Ferreira, L.G. (2002). Overview of the Radiometric and Biophysical Performance of the MODIS Vegetation Indices. *Remote Sensing of Environment* 83(1-2):195-213, [https://doi.org/10.1016/S0034-4257\(02\)00096-2](https://doi.org/10.1016/S0034-4257(02)00096-2)
- Hunt, L.A., & Boote, K.J. (1998). Data for model operation, calibration, and evaluation. In: G.Y. Tsuji, G. Hoogenboom, and P.K. Thornton, editors, *Understanding options for agricultural production*. Kluwer Academic Publication. Dordrecht, the Netherlands.
- Huntington, T. G. (2007). *Available water capacity and soil organic matter*. In: Encyclopedia of Soil Science, second edition. Taylor and Francis: pp 139– 43.
- Huyghe, C., De Vlieghe, A., van Gils, B., & Peeters, A. (2014a). Grasslands and herbivore production in Europe and effects of common policies. Collection Synthèse, Quae, 320 p, <http://www.quae.com/fr/r3371.html>
- Intergovernmental Panel on Climate Change [IPCC]. (2013). *Summary for Policymakers Climate Change 2013: The Physical Science Basis*. Contribution of Working Group I to the Fifth Assessment Report of the Intergovernmental Panel on Climate Change ed T F Stocker, D Qin, G-K Plattner, M Tignor, S K Allen, J Boschung, A Nauels, Y Xia, V Bex and P M Midgley (Cambridge University Press), p. 116.
- Jalloh, A., Nelson, G.C., Thomas, T.S., Zougmore, R., & Roy-Macauley, H. (eds) (2013). West African agriculture and climate change: a comprehensive analysis IFPRI Research Monograph. *International Food Policy Research Institute (IFPRI)*, Washington, DC. <https://doi.org/10.2499/9780896292048>.
- Jianguo, M., Zhao, P., Zhou, Y., Li, F., Ling, X., Deng, N., & Peng, S. (2020). The Adaptability of APSIM-Wheat Model in the Middle and Lower Reaches of the Yangtze River Plain of China: A Case Study of Winter Wheat in Hubei Province. *Journal of Agronomy*. 10, 981; <https://doi.org/10.3390/agronomy10070981>.

- Mthandi, J., Kahimba, F. C., Tarimo, A. K. P. R., Baandah, A., Salim, M.W., & Lowole. (2014). Modification, calibration and validation of APSIM to suit maize (Zeamays L.) production system: A case of Nkango irrigation scheme in Malawi. *American Journal of Agriculture and Forestry*. Special Issue: *Journal of Agriculture Ecosystem and Environment*. Vol. 2, No. 6-1, pp. 1-11, <https://doi.org/10.11648/j.ajaf.s.2014020601.11>.
- Jones, H. G. (1992). *Plants and Microclimate: A Quantitative Approach to Environmental Plant Physiology*, 2nd edition, Cambridge University Press.
- Kalma, J., McVicar, T., & McCabe, M. (2008). Estimating land surface evaporation: A review of methods using remotely sensed surface temperature data. *Surveys Geophysical*, 29, 421–469.
- Kariuki, J., Rebecca, W., Simon, M., & Rob. (2018). Rangeland livelihood strategies under varying climate regimes: Model insights from southern Kenya. *Journal of Land Management* 7, 47; 1-22, <https://doi.org/10.3390/land7020047>.
- Karkanis, P., Au, K., & Schaalje, G. (1991). Comparison of four measurement schedules for determination of soil particle-size distribution by the hydrometer method. *Can Agricultural Engineering* 33:211–216.
- Keating, B.A., Carberry, P.S., Hammer, G. L., Probert, M.E., Robertson, M.J., Holzworth, D., Bristow, K.L., Asseng, S., Chapman, S., McCown, R.L., Freebairn, D.M., & Smith, C.J. (2003). An overview of APSIM, a model designed for farming systems simulation. *European Journal of Agronomy* 18 (3-4), 267-288.
- Khan, R. M. (2013). *Problem solving and data analysis using minitab: A clear and easy guide to six sigma methodology* (1sted.). Wiley.
- Knapp, A. K., Beier, C., Briske, D. D., Classen, A. T., Luo, Y., Reichstein, M., Smith, M. D., Smith, S. D., Bell, J. E., Fay, P. A., Heisler, J. L., Leavitt, S. W., Sherry, R., Smith, B., & Weng, E.(2008). Consequences of more extreme precipitation regimes for terrestrial ecosystems. *Bioscience*, 58(9), 811-821, <https://doi.org/10.1641/B580908>.
- Konikow, L. F., & Bredehoeft, J. D. (1992). Ground-water models cannot be validated. *Advances in Water Resources* 15(1): 75- 83.
- Köhli, M., Schrön, M., Zreda, M., Schmidt, U., Dietrich, P., & Zacharias, S. (2015). Footprint characteristics revised for field-scale soil moisture monitoring with cosmic-ray neutrons. *Water Resources Research*, 51, 5772–5790.
- Koorevaar, P., Menelik, G., & Dirksen, C. (1983). *Elements of soil physics*. Elsevier Science, Amsterdam.

- Laio, F., Porporato, A., Ridolfi, L., & Rodriguez-Iturbe, I. (2001a). Plants in water-controlled ecosystems: active role in hydrological processes and response to water stress. II. Probabilistic soil moisture dynamics. *Advanced Water Resources*. 24(7), 707-723.
- Laio, F., Porporato, A., Fernandez-illescas, C.P. & Rodriguez-Iturbe, I. (2001b). Plants in water-controlled ecosystems: active role in hydrological processes and response to water stress. IV. Discussion of real cases. *Advanced Water Resources*. 24(7), 745-762.
- Reid, R., Lamprey, H., & Robin, S. (2004). Expansion of human settlement in Kenya's Maasai Mara: what future for pastoralism and wildlife? *Journal of Biogeography*. 31, 6 997-1032, <https://doi.org/doi: 10.1111/j.1365-2699.2004. 01062.x>
- Latham, J.S. (1981-83). Final report of a pilot project on the utilization of Remote Sensing and Field data for the production of Agricultural statistics on crop acreage. *Unpublished internal report, FAO*.
- Lenhart, T., Eckhardt, K., Fohrer, N., & Frede, H.G. (2002). Comparison of two different approaches of sensitivity analysis. *Physical. Chemical. Earth*, 27, 645–654.
- Leuning, R., van Gorsel, E., Massman, W.J., & Isaac, P.R., (2012). Reflections on the surface energy imbalance problem. *Journal of Agricultural. Forest Meteorology*. 156 (0), 65–74.
- Liang, X., Lettenmaier, D. P., Wood, E. F., & Burges, S. J. (1994). A simple hydrologically based model of land surface water and energy fluxes for general circulation models, *Journal of Geophysical Research and Atmosphere*, 14415–14428.
- Liang, X., Lettenmaier, D. P., & Wood, E. F. (1996). One-dimensional statistical dynamic representation of sub-grid spatial variability of precipitation in the two-layer variable infiltration capacity model, *Journal of Geophysical Research and Atmosphere*, 101, 21403–21422, <https://doi.org/10.1029/96JD01448>.
- Liang, W. L., Kosugi, K., & Mizuyama, T. (2007). Heterogeneous soil water dynamics around a tree growing on a steep hillslope. *Vadose Zone Journal*, 6(4), 879-889.
- Liu, J.P., Song, M., Horton, R.M., & Hu, Y. (2013). Reducing spread in climate model projections of a September ice-free. *Proceedings of National Academy of Science.*, 110, 12571-12576, <https://doi.org/10.1073/pnas.1219716110>.
- Liu, Q., Noriyuki, Y., Kiyoshi, O., & Hemanta, H. (2012). “Automatic Soil Water Retention Test System with Volume Change Measurement for Sandy and Silty Soils.” *Soils and Foundations* 52, 368–80, <https://doi.org/10.1016/j.sandf.2012.02.012>.

- Li, W., Huang, H.Z., Zhang, Z.N., & Wu, G.L., (2011). Effects of grazing on the soil properties and C and N storage in relation to biomass allocation in an alpine meadow. *Journal of Plant Nutrition and Soil Science*. 11, 27–39.
- Ludwig, J.A., Wilcox, B.P., Breshears, D.D., Tongway, D.J., & Imeson, A.C. (2005). Vegetation patches and runoff-erosion as interacting ecohydrological processes in semiarid landscapes, *Ecology*, 86 (2), 288–297.
- Luo, Z., Wang, E., Sun, O.J., Smith, C.J., & Probert, M.E. (2011). Modeling long-term soil carbon dynamics and sequestration potential in semi-arid agro-ecosystems. *Agriculture. for Meteorologist*. 151 (12), 1529 – 1544.
- Ma, L.R., Ahuja, S.A., Saseendran, R.W., Malone, T.R., Green, B.T., Nolan, P.N.S., Bartling, G.N., Flerchinger, K.J., Boote, G., & Hoogenboom. (2011). *A protocol for parameterization and calibration of RZWQM2 in field research*. In: L.R. Ahuja and L. Ma, editors, *Methods of introducing system models into agricultural research*. SSSA Book Service. SSSA, Madison, WI. p. 1–64.
- Madana, M. (2002). *Improving land use survey method using high-resolution satellite imagery*. International Institute for Geo Information Science and Earth Observation (ITC) (M.Sc. Thesis).
- Malek, K., Stockle, C., Chinnayakanahalli, K., Nelson, R., Liu, M., & Rajagopalan, K. (2017). VIC-CropSyst: A regional-scale modeling platform to simulate the nexus of climate, hydrology, cropping systems, and human decisions. *Geoscientific Model Development*, 10, 3059–3084. <https://doi.org/10.5194/gmd-2016-294>
- Mao, D., & Cherkauer, K.A. (2009). Impacts of land use change on hydrologic responses in the Great Lakes region. *Journal of Hydrology*. 374, 71–82.
- Maselli, F. (2001). Definition of spatially variable spectral end-members by locally calibrated multivariate regression analyses. *Remote Sensing of Environment*, 75, pp. 29–38.
- Ma, S., Lardy, R., Graux, A.-I., Ben Touhami, H., Klumpp, K., Martin, R., & Bellocchi, G. (2015). Regional-scale analysis of carbon and water cycles on managed grassland systems. *Environmental Modelling Software* 72, 356–371.
- Mati, B.M., Mutie, S., Gadain, H., Home, P., & Mtaló, F. (2008). Impacts of land-use/cover change on the hydrology of the transboundary mara river, Kenya/Tanzania. *Lakes Reservoirs Resource Management* 13:169–177.
- Mbatha, K.R., & Ward, D. (2010). The effects of grazing, fire, nitrogen and water availability on nutritional quality of grass in semi-arid savanna, South Africa. *Journal of Arid Environment*. 2010; 74(10):1294–1301. <https://doi.org/10.1016/j.jaridenv.2010.06.004>.

- McCown, R. L., Hammer, G.L., Hargreaves, J. N. G., Holzworth, D. P. & Freebairn, D. M. (1996). APSIM: a novel software system for model development, model testing and simulation in agricultural systems research. *Agricultural Systems*, 50, 255 – 271.
- McGraw, S.A., Vivoni, P., Mascaró, G., & Franz, T. E. (2015). Closing the water balance with cosmic-ray soil moisture measurements and assessing their spatial variability within two semiarid watersheds. *Journal of Hydrology and Earth System Sciences Discussions*. 12, 6: 5343-5388.
- Melillo, J.M., Steudler, P.A., Aber, J.D., Newkirk, K., Lux, H., Bowles, F.P., Catricala, C., Magill, A., Ahrens, T., & Morrisseau, S. (2002). Soil warming and carbon cycle feedbacks to the climate system, *Science*, 298, 2173–2176, <https://doi.org/10.1126/science.1074153>.
- Mellander, P. E., Bishop, K., & Lundmark, T. (2004). The influence of soil temperature on transpiration: A plot scale manipulation in a young Scots pine stand, *Forest Ecological Management.*, 195, 15–28, <https://doi.org/10.1016/j.foreco.02.051>.
- Mello, C.R., Oliveira, G.C., Resck, D.V.S., Lima, J.M., & Dias Júnior, M.S. (2002). Estimativa da capacidade de campo baseada no ponto de inflexão da curva característica. *Ci. Agro technology*, 26:836-841.
- Meroni, M. F., Dominique, B., Riad, D., Mustapha, H., Myriam, H., Josh, L., & Olivier, L. (2015). Testing VGT data continuity between SPOT and PROBA-V missions for operational yield forecasting in North African countries. *European Union*, 1-28, <https://doi.org/10.2788/920806>.
- Merz, B., & Plate, E. J. (1997). An analysis of the effect of spatial variability of soil and soil moisture on runoff, *Water Resource. Research.*, 33, 2909–2922.
- Mishra, A.K., & Singh, V.P. (2010) A Review of Drought Concepts. *Journal of Hydrology*, 391, 202-216. <https://doi.org/10.1016/j.jhydrol.2010.07.012>.
- Mora, C., Caldwell, I.R., Caldwell, J.M., Fisher, M.R., Genco, B.M., & Running, S.W. (2015). Suitable days for plant growth disappear under projected climate change: potential human and biotic vulnerability. *PLoS Biology*. <http://dx.doi.org/10.1371/journal.pbio.1002167>.
- Morgan, J.A., LeCain, D.R., & Pendall, E. (2015). C4 grasses prosper as carbon dioxide eliminates desiccation in warmed semi-arid grassland. *Nature* 476:202–205. <https://doi.org/10.1038/nature10274>

- Mulinge, E., Gicheru, P., Muriithi, F., & Kihui, E. (2015). “Economics of land degradation and improvement in Kenya,” A Global Assessment for Sustainable Development, 1 – 686. <https://doi.org/10.1007/978-3-319-19168-3>.
- Muneepeerakul, C.P., Miralles-Wilhelm, F., Tamea, S., Rinaldo, A., & Rodriguez-Iturbe, I. (2008). Coupled hydrologic and vegetation dynamics in wetland ecosystems. *Water Resource Research*, 44, W07421.
- Mwangi, H.M., Julich, S., Patil, S.D., McDonald, M.A., & Feger, K.H. (2016). Relative contribution of land use change and climate variability on discharge of Upper Mara River, Kenya. *Journal of Hydrological* 5, 244–260.
- Mwangi, H.,Lariu, M., Julich, P., Patil,S., Sopan, D.,Mcdonald, Morag, A. F., & Karl-einz. (2017). Characterizing the Intensity and Dynamics of Land-Use Change in the Mara River Basin, East Africa. 9, 8; <https://doi.org/10.3390/f9010008>.
- Nelson, D.W., & Sommers, L.E. (1996). Total carbon, organic carbon, and organic matter. In: Sparks, D.L., editors, *Methods of Soil Analysis*. SSSA Book Ser. 5. SSSA, Madison. p. 961–1010.
- Nemani, P. R., & Running, S. W. (1989). Estimation of regional surface resistance to evapotranspiration from NDVI and thermal IR AVHRR data. *Journal of Applied Meteorology*, 28: 276- 284.
- Nemani, R. (2003). Climate-driven increases in global terrestrial net primary production from 1982 to 1999, *Science*, 300, 1560–1563.
- Niaghi, A.R. (2019). New Approach to Improve the Soil Water Balance Method for Evapotranspiration Estimation, 11, 2478; <https://doi.org/10.3390/w11122478>.
- Nikole, F. (2014). *Impacts of climate change on livestock production in South Eastern Australia*
- Njoku, E.G., Jackson, T.J., Lakshmi, V., Chan, T.K., & Nghiem, S.V. (2003). Soil moisture retrieval from AMSR-E. *IEEE Transactions Geoscience and Remote Sensing* 41:215–229.
- Niu, C. Y., Musa, A., & Liu, Y. (2015). Analysis of soil moisture condition under different land uses in the arid region of Horqin sandy land, northern China. *Journal of Solid Earth*, 6, 4: 1157–1167.
- O'Connor, T.G., Haines, L.M., & Snyman, H.A. (2001). Influence of precipitation and species composition on phytomass of a semi-arid African grassland. *Journal of Ecology* 89, 850 –860.
- O'Geen, A. T. (2010). Research connects soil hydrology and stream water chemistry in

- California oak woodlands. *California Agriculture* 64, 78-84.
- Oguike, P. C., & Onwuka, B. M. (2018). Moisture characteristics of soils of different land use systems in Ubakala Umuahia, Abia State, Nigeria. *International Journal of Scientific and Research Publications*, Volume 8, Issue 4, April 2018 ISSN 2250-3153, <https://doi.org/10.29322/IJSRP.8.4.2018.p7604>.
- Ogutu, J.O., Piepho, H. P., Dublin, H.T., Bhola, N., & Reid, R.S. (2009). Dynamics of Mara-Serengeti ungulates in relation to land use changes. *Journal of Zoology*. 278, 1–14.
- Olson, R.J., Johnson, K.R., Zheng, D.L., & Scurlock, J.M.O (2000). *Global and Regional Ecosystem Modeling: Databases of Model Drivers and Validation Measurements*. ORNL Technical Memorandum TM-2001/196. Oak Ridge National Laboratory, Oak Ridge, Tennessee.
- Ongoma, V., & Chen, H. (2017). Temporal and spatial variability of temperature and precipitation over East Africa from 1951 to 2010. *Meteorology of Atmospheric Physics* 129:131–144. <https://doi.org/10.1007/s00703-016-0462-0>.
- Ontitism, S. M., Ondabu, N., & Ouda, J. (2000). The performance and composition of ley grasses and legumes, sweet potatoes and fodder trees. In: Wamae L, Murithi F, Wasike W (eds) *Proceedings of the 7th KARI biennial scientific conference held on 13th–17th November 2000, Nairobi*, pp 389–392.
- Peterson, A., Helgason, M., Warren, D. I., & Andrew, M. (2016). Estimating field-scale rootzone soil moisture using the cosmic-ray neutron probe. *Hydrology of Earth System Science* 20, 1373–1385.
- Piao, S.L, Ciais, P., & Friedlingstein, P. (2008). Net carbon dioxide losses of northern ecosystems in response to autumn warming. *Nature*, 451, 49–52.
- Piao, S.L., Fang, J.Y., Zhou, L.M., Zhu, B., Tan, K., & Tao, S. (2005). Changes in vegetation net primary productivity from 1982 to 1999 in China, *Global Biogeochemical Cycles*, 19, GB2027, <https://doi.org/10.1029/2004GB002274>.
- Pauwels, V. R. N., & Samson, R. (2006). Comparison of different methods to measure and model actual evapotranspiration rates for a wet sloping grassland, *Journal of Agricultural Water Management*. 82, 1 – 24, <https://doi.org/10.1016/j.agwat.2005.06.001>.
- Peng, C., Xicheng, T., Meng, G., & Yayu, Y. (2013). *Virtual Reality in Smart City*. In F. Bian *et al.* (Eds.) GRMSE 2013, Part I, CCIS 398 (107–118). Springer-Verlag Berlin Heidelberg.
- Perlman, H. (2016). *The Water Cycle* - USGS Water Science School,

<https://water.usgs.gov/edu/watercycle.html>.

- Perry, C.R., Chhikara, R.S., & Spears, F.M (1979). Modeling of stratum variance for use in sample allocation in agricultural area frame surveys. ASA Section on Survey Research Methods.
- Plisnier, P.D., Serneels, S., & Lambin, E.F. (2000). Impact of ENSO on East African Ecosystems: A Multivariate Analysis Based on Climate and Remote Sensing Data. *Global Ecology of Biogeography* 9, 481–497.
- Plummer S., Chen, J., Dedieu, G. & Simon, M. (2003). GLOBCARBON Detailed Processing Model GLBC-ESL-DPM-V1.3, 202 pp.
- Porporato, A., D’odorico, P., Laio, F., Ridolfi, L., & Rodriguez-Iturbe, I. (2002). Ecohydrology of water-controlled ecosystems. *Advanced Water Resources* 25:1335–1348.
- Porporato, A., Laio,F., Ridolfi, L., & Rodriguez-Iturbe, I. (2001). Plants in water-controlled ecosystems: Active role in hydrologic processes and response to water stress: III. Vegetation water stress, *Advanced Water Resources*, 24, 725–744.
- Rahman, H., & Dedieu, G. (1994). SMAC: a simplified method for the atmospheric correction of satellite measurements in the solar spectrum. *Remote Sensing*, 15(1), 123-143.
- Riazanoff, S. (2004) “SPOT 123-4-5 *Geometry Handbook*”, Reference GAEL-P135-DOC-001, Issue 1, Revision 4, Date 20.08.2004.
- Reed, D.E., Ewers, B.E., & Pendall, E. (2014). Impact of mountain pine beetle induced mortality on forest carbon and water fluxes. *Environmental Research Letters* 9 (10), 105004.
- Reed, D.E., Ewers, B.E., Pendall, E., Frank, J., & Kelly, R. (2016). Bark beetle-induced tree mortality alters stand energy budgets due to water budget changes. *Theories of Application Climatology*. 1–13.
- REGLAP (2012). *Key Statistics on the Drylands of Kenya, Uganda and Ethiopia*, REGLAP Secretariat, October 2012. Nairobi: REGLAP Secretariat.
- Reid, R.S., Rainy, M., Ogutu, J., Kruska, R.L., Kimani, K., Nyabenge, M., McCartney, Njuguna, E., Wilson, C.J., & Lamprey, R. (2003). People, wildlife and livestock in the Mara ecosystem: The Mara Count 2002. *International Livestock Research Institute, Nairobi*.

- Reynolds, S.G. (1970). The gravimetric method of soil moisture determination, Part III: An examination of factors influencing soil moisture variability. *Journal of Hydrology*, 11:288–300. [https://doi.org/10.1016/0022-1694\(70\)90068-5](https://doi.org/10.1016/0022-1694(70)90068-5).
- Ridolfi, L., D’Odorico, P., Porporato, A., & Rodriguez-Iturbe, I. (2000). Impact of climate variability on the vegetation water stress, *Journal of Geophysics Research*, 105, 18,013–18,025.
- Ridolfi, L., D’Odorico, P., & Laio, F. (2007). Vegetation dynamics induced by phreatophyte-aquifer interaction, *Journal of Theoretical Biology*, 248, 301–310.
- Rivera Villarreyes, C. A., Baroni, G., & Oswald, S. E. (2011). Integral quantification of seasonal soil moisture changes in farmland by cosmic-ray neutrons, *Hydrology of Earth System Science*, 15, 3843–3859, <https://doi.org/10.5194/hess-15-3843>.
- Rivera Villarreyes, C. A., Baroni, G., & Oswald S. E. (2014). In-verse modeling of cosmic-ray soil moisture for field scale soil hydraulic parameters, *European Journal of Soil Science*, 65, 876–886, <https://doi.org/10.1111/ejss.12162>.
- Rockström, J. (2003). Resilience building and water demand management for drought mitigation. *Physics and Chemistry of the Earth, Parts A/B/C* 28(20–27): 869-877.
- Rodriguez-Iturbe, I. (2000). Ecohydrology: a hydrologic perspective of climate-soil-vegetation dynamics, *Water Resources Research*, 36, 3–9.
- Rodriguez-Iturbe, I., Porporato, A., Laio, F. & Ridolfi, L. (2001). Plants in water-controlled ecosystems: Active role in hydrologic processes and response to water stress: I. Scope and general outline, *Advanced Water Resources*, 24, 695–705.
- Rodriguez-Iturbe, I., Porporato, A., Ridolfi, L., Isham, V., & Cox, D.R. (1999). Probabilistic modelling of water balance at a point: The role of climate, soil and vegetation, *Proceedings of Roy Society London, Service. A*, 455, 3789-3805.
- Roger Blench & Florian Sommer (2015). *Understanding Rangeland Biodiversity*. Printed by Chameleon Press, SW18 4SG ISBN 0 85003 432 9.
- Rosolem, R., Hoar, T., Arellano, A., Anderson, J., Shuttleworth, W., Zeng, X., & Franz, T. (2014). Translating aboveground cosmic-ray neutron intensity to high-frequency soil moisture profiles at sub-kilometer scale. *Hydrology of Earth System Science*. 18 (11), 4363–4379. <http://dx.doi.org/10.5194/hess-18 - 4363>.
- Roudier, P., Sultan, S., Quirion, P., & Berg, A. (2011). The impact of future climate change on West African crop yields: what does the recent literature say? *Global Environmental Change* 21 1073–83.

- Running, S.W., Ramakrishna, N.R., Heinsch, F.A., Zahao, M., Reeves, M., & Hashimoto, H. (2004). A continuous satellite-derived measure of global terrestrial primary production. *BioScience* 54:547-560.
- Sala, O.E., Medina, J.A., & Schulze, E.D. (1996). 'Biodiversity and ecosystem function in grasslands' in Mooney, H.A., Medina, J.A., Sala, O.E., and Schulze, E-D. (eds.) *Functional roles of biodiversity: a global perspective*. New York: John Wiley.
- Sala, O. (2001). Productivity of temperate grasslands, p.285-300. In: J. Roy, B. Saugier, and H.A. Mooney (eds.). *Terrestrial Global Productivity*. San Diego, CA, USA: Academic Press.
- Saltelli, A., Guimarães Pereira, Â., Van der Sluijs, J.P., & Funtowicz, S. (2013). 'What do I make of your latinorum? Sensitivity auditing of mathematical modelling', *International Journal of Foresight and Innovation Policy*, (9), 2/3/4, 213–234.
- Saltelli, A., & Funtowicz, S. (2014). "When all models are wrong: More stringent quality criteria are needed for models used at the science-policy interface." *Issues in Science and Technology* 17: 108126.
- Sandholt, I., Rasmussen, K., & Andersen, J.(2000). A simple interpretation of the surface temperature/vegetation index space for assessment of surface moisture status. *Remote Sensing. Environment.*, 79, 213–224.
- Saxton, K. E., & Rawls, W. J. (2006). Soil water characteristic estimates by texture and organic matter for hydrologic solutions. *Journal of American Society of Soil Science* 70:1569 – 1578.
- Scholes, R.J., & Archer, S.R.(1997). Tree-Glass Interactions in Savannas. *Annual Revolution of Ecological System*. 28, 517–544.
- Schuman, G.E., Janzen, H.H., & Herrick, J.E. (2002). Soil carbon dynamics and potential carbon sequestration by rangelands. *Environmental Pollution* 116: 391–396.
- Seidel, S.J., Palosuo, T., Thorburn, P., & Wallach, D. (2018). Towards improved calibration of crop models-where are we now and where should we go? *European Journal of Agronomy*. 94, 25–35.
- Seneviratne, R. W., Young, M. G., Beltranena, E., Goonewardene, L. A., Newkirk, R. W., & Zijlstra, R. T. (2010). The nutritional value of expeller pressed canola meal for grower finisher pigs. *Journal of Animal. Science*. 88 (6): 2073-2083, <https://doi.org/10.2527/jas.2009-2437>.
- Serneels, S., & Lambin, F.E.(2001). Proximate causes of land-use change in Narok District, Kenya: A spatial statistical model. *Agricultural Ecosystem Environment*. 85, 65–84.

- Shan, L., & Chen, G.L., (1993). *Theory and practice of dry land farming on the loess plateau*. Chinese Science Press, pp. 256–280 (in Chinese).
- Sharma, M.L., Gander, G.A., & Hunt, C.G. (1980). Spatial variability of infiltration in a watershed. *Journal of Hydrology*. 45:101–122.
- Sheffield, J., Goteti, G., Wen, F., & Wood, E.F. (2004). A simulated soil moisture based drought analysis for the United States. *Journal of Geophysical Research*. 109, D24108.
- Shi, T., Guan, D., Wang, A., Wu, J., Jin, C., & Han, S. (2008). Comparison of three models to estimate evapotranspiration for a temperate mixed forest. *Hydrological Processes*, 22, 3431– 3443, <https://doi.org/10.1002/hyp.6922>.
- Shuttleworth, J., Rosolem, R., Zreda, M., & Franz, T.E., (2013). The Cosmic-ray Soil Moisture Interaction Code (COSMIC) for use in data assimilation. *Hydrology and Earth System Sciences*, 17(8): 3205-3217.
- Šimůnek, J., & de Vos, J. A. (1999). *Inverse optimization, calibration, and validation of simulation models at the field scale*. In Modelling of Transport Process in Soils at Various Scales in Time and Space, 431-445. J. Feyen and K. Wiyono, eds. Wageningen, The Netherlands: Wageningen Perspective.
- Šimunek, J., & van Genuchten, M.T. (1999). Using the HYDRUS-1D and HYDRUS-2D codes for estimating unsaturated soil hydraulic and solute transport parameters. In Characterization and Measurement of the Hydraulic Properties of Unsaturated Porous Media; van Genuchten, M.T., Leij, F.J., Wu, L., Eds.; *University of California: Riverside, CA, USA*, pp. 1523–1536.
- Šimůnek, J., & Hopmans, J. W. (2002). *Parameter optimization and nonlinear fitting*. In Methods of Soil Analysis: Part 1. Physical Methods, 139-157. J. H. Dane and G. C. Topp, eds. 3rd ed. Madison, Wiscost. SSSA.
- Simunek, J., van Genuchten, M. T. & Sejna, M. (2008). Development and applications of the HYDRUS and STANMOD software packages and related codes, *Vadose Zone Journal.*, 7(2), 587–600, <https://doi.org/10.2136/Vzj2007.0077>.
- Simunek J., van Genuchten, M.T. & Sejna, M.(2012a). HYDRUS technical manual: The HYDRUS software package for simulating the two- and three- dimensional movement of water, heat and multiple solutes in variably-saturated porous media. *Technical manual*. 2.0.
- Smith, P., Lanigan, G., Kutsch, W.L., Buchmann, N., Eugster, W., Aubinet, M., Ceschia, E., Beziat, P., Yeluripati, J.B., Osborne, B., Moors, E.J., Brut A., Wattenbach, M.,

- Saunders, M., & Jones, M., (2010). Measurements necessary for assessing the net ecosystem carbon budget of croplands. *Agricultural Ecosystem Environment*, 139, 302-315.
- Smith, S. D., Charlet, T. N., Zitzer, S. F., Abella, S. R., Vanier, C. H., & Huxman, T. E. (2014). Long- term response of a Mojave Desert winter annual plant community to a whole ecosystem atmospheric CO₂ manipulation (FACE). *Global Change Biology* 20:879–892.
- Soil Survey Staff. (2014). *Keys to soil taxonomy*, 12th edition. USDA Natural Resources Conservation Service.
- Steduto, P., Hsiao, T.C., Raes, D., & Fereres, E. (2009). AquaCrop - The FAO crop model to simulate yield response to water: I. Concepts and underlying principles. *Journal of Agronomy*. 101:426–437.
- Stehfest, E., Heistermann, M., Priess, J.A., Ojima, D.S., & Alcamo, J. (2007). Simulation of global crop production with the ecosystem model Data Center, *Ecological Model*. 209, 203–219.
- Sterckx, S., Benhadj, I., Duhoux, G., Livens, S., Dierckx, W., Goor, E., Adriaensen, S., Heyns, W., Van Hoof, K., Strackx, G., Nackaerts, K., Reusen, I., Van Achteren, T., Dries, J., Van Roey, T., Mellab, K., Duca, R., & Zender, J. (2014). “The PROBA-V Mission: Image Processing and Calibration.” *International Journal of Remote Sensing* 35 (7): 2565–2588.
- Stockdale, T. N., Alves, O., Boer, G., Deque, M., Ding, Y., Kumar, A., & Kumar, K. (2010). Understanding and Predicting Seasonal-to-Inter-Annual Climate Variability - The Producer Perspective. *Procedia Environmental Sciences*, 1:5, 55-80, <https://doi.org/10.1016/j.proenv.2010.09.006>.
- Stockle, C.O., Nelson, R.L., Higgins, S., Brunner, J., Grove, G., Boydston, R.A., Whiting, M., & Kruger, C. (2010). Assessment of climate change impact on eastern Washington *Climatic Change*, <https://doi.org/10.1007/s10584-010-9851-4>.
- Desai, S. A., Cook, B., Saliendra, N., & Mackay, D. (2009). Contrasting carbon dioxide fluxes between a drying shrub wetland in Northern Wisconsin, USA, and nearby forests. *Biogeosciences* 6 (6), 1115–1126.
- Sultan, B., Roudier, P., Quirion, P., Alhassane, A., Muller, B., Dingkuhn, M., Ciais, P., Guimberteau, M., Traore, S., & Baron, C. (2013). Assessing climate change impacts on sorghum and millet yields in the Sudanian and Sahelian savannas of West Africa. *Environmental Research Letters*, 8(1): 014040.

- Swarowsky, A. (2011). Catchment-scale soil water dynamics in a Mediterranean-type oak woodland. *Journal of Vadose Zone*, 10, 800-815.
- Takagi, K., & Lin, H.S. (2011). Temporal dynamics of soil moisture spatial variability in the Shale Hills critical zone observatory. *Vadose Zone Journal*. 10:832–842. <https://doi.org/10.2136/vzj2010.0134>.
- Tamiru, L., & Fekadu, H. (2019). Effects of Climate Change Variability on Agricultural Productivity. *International Journal of Environmental Science Natural Resources*. 17(1): 555953. <https://doi.org/10.19080/IJESNR.2019.17.555953>.
- Tan G.X., & Shibasaki, R. (2003). Global estimation of crop productivity and the impacts of global warming by GIS and EPIC integration, *Ecological. Model*. 168, 357–370.
- Thomas, A.R.C., Bond, A.J., & Hiscock, K.M., (2013). A multi-criterion based review of models that predict environmental impacts of land use-change for perennial energy crops on water, carbon and nitrogen cycling. *GCB Bioenergy* 5, 227–242.
- Thuillier, G., Hersé, M., Labs, D., Foujols, T., Peetermans, W., Gillotay, D., Simon, P.C., & Mandel, H. (2003). The solar spectral irradiance from 200 to 2400 nm as measured by the SOLSPEC spectrometer from the ATLAS and EURECA missions. *Sol. Physical.*, 214, 1 – 22, <https://doi.org/10.1023/A:1024048429145>.
- Tinet, A.J., Chanzy, A., Braud, I., Crevoisier, D., & Lafolie, F. (2015). Development and Evaluation of an Efficient Soil-Atmosphere Model (FHAVeT) based on the Ross fast solution of the Richards equation for bare soil conditions. *Hydrology of Earth System Science*, 2015, 19, 969–980.
- Touhami, I., Andreu, J. M., Chirino, E., Sanchez, J. R., Moutahir, H., Pulido-Bosch, A., Martinez, S., & Bellot, J. (2013). Recharge estimation of a small karstic aquifer in a semiarid Mediterranean region (southeastern Spain) using a hydrological model. *Hydrological Processes* 27:165-174 <https://doi.org/10.1002/hyp.9200>.
- Trenberth, K.E. (2011). Changes in precipitation with climate change. *Climate Research*, 47(1): 123.
- Ursulino, B. S., Gico L. M., Suzana, M., Coutinho, A. P., Rabelo, C., Victor, H., Dos, S. A., Diego C., Villar, G., Ana, C., Dos, S. N., Severino, M., Lassabatere, L., & Angulo-J, R. (2019). Modelling soil water dynamics from soil hydraulic parameters estimated by an alternative method in a tropical experimental basin. *Water*; 11, 1007; <https://doi.org/10.3390/w11051007>.
- Van Genuchten, M. Th., & Nielsen, D. R. (1985). On describing and predicting the hydraulic properties on unsaturated soils, *Annales Geophysicae.*, 3(5), 615-628.

- Van Genuchten, M.T., Leij, F.J., & Yates, S.R. (1991). The RETC Code for Quantifying the Hydraulic Functions of Unsaturated Soils. EPA Report, 600/2-91/065, USA Salinity Laboratory, USDA.
- Vather, T., Everson, C., Mengistu, M., & Franz, T. (2018). Cosmic ray neutrons provide an innovative technique for estimating intermediate scale soil moisture. *South African Journal of Science*. 2018; 114(7/8), Art. #2017-0422, 9 pages.
<http://dx.doi.org/10.17159/sajs.2018/20170422>.
- Veenendaal, E. M., Kolle, O. L., & Jon. (2004). Seasonal variation in energy fluxes and carbon dioxide exchange for a broad-leaved semi-arid savanna (Mopane woodland) in Southern Africa, *Global Change Biology* (2004) 10, 318-328,
<https://doi.org/10.1046/j.1529-8817.2003.00699.x>.
- Vereecken, H., Kamai, T., Harter, T., Kasteel, R., Hopmans, J., & Vanderborght, J. (2007). Explaining soil moisture variability as a function of mean soil moisture: A stochastic unsaturated flow perspective, *Geophysical Research Letters*., 34, L22402,
<https://doi.org/10.1029/2007GL031813>.
- Waithaka, J. (2004). Maasai Mara - an ecosystem under siege: an African case study on the societal dimension of rangeland conservation, *African Journal of Range and Forage Science*, 21:2, 79-88, <https://doi.org/10.2989/10220110409485838>.
- Ward, R.C., & Robinson, M. (1990). *Principles of Hydrology*. McGraw-Hill Book Company.
- Webb, E. K., Pearman, G. I., & Leuning, R. (1980). Correction of flux measurements for density effects due to heat and water vapour transfer, *Q. J. Roy. Meteorological Society*, 106, 85 –100, <https://doi.org/10.1002/qj.49710644707>.
- Western, A.W., & Blöschl, G. (1999). On the spatial scaling of soil moisture. *Journal of Hydrology*; 217:203-24.
- Western, A.W., Grayson, R.B., Blöschl, G., Willgoose, G., & McMahon, T. A. (1999). Observed spatial organization of soil moisture and relation to terrain indices, *Water Resource Research*, 35(3), 797–810.
- Western, D., Groom, R., & Worden, J. (2009). The impact of subdivision and sedentarization of pastoral lands on wildlife in an African savanna ecosystem. *Biological Conservation*. 200 142, 2538–2546.
- Western, D., & Nightingale, D.L.M. (2003). *Environmental change and the vulnerability of pastoralists to drought: A Case Study of the Maasai in Amboseli, Kenya*; Cambridge University Press.
- Wigton, W., Srivastava, A., Zekaria, S., Mudeir, Y., Mossa, Y., Tadesse, G., Yigezu, B.,

- Tariku, A., Beyene, H., & Abdi, J. (2009). Agricultural Statistical Methodology in Ethiopia. *Central Statistical Agency (Ethiopia) Publication: Addis Ababa.*
- Wilson, K. B., Baldocchi, D. D., & Hanson, P. J. (2011). Leaf age affects the seasonal pattern of photosynthetic capacity and net ecosystem exchange of carbon in a deciduous forest. <https://doi.org/10.1046/j.0016-8025.2001.00706.x>.
- World Meteorological Organization (WMO): (2009). *Instruments and Observing Methods – WMO Field intercomparison of rain intensity gauges*, Report No. 99.
- Wu, G., Liu, Y., Dong, B., Liang, X., Duan, A., Bao, Q., & Yu, J. (2012). Revisiting Asian monsoon formation and change associated with Tibetan Plateau forcing: I. Formation. *Journal of Climate Dynamics* 39:1169 – 1181, <https://doi.org/10.1007/s00382-012-1334-z>.
- Wu, P., Gao, X., Zhao, X., Wang, J., & Shi, Y. (2014). Effects of land use on soil moisture variations in a semi-arid catchment: implications for land and agricultural water management. *Journal of land degradation and development*. 25: 163 – 172 (2014), <https://doi.org/10.1002/ldr.1156>.
- Xingwu D., Rong, L., Feng, D., & Zhang, G. (2017). Soil moisture variation in a farmed dry-hot valley catchment evaluated by a redundancy analysis approach. *Journal of water*. 9, 92, <https://doi.org/10.3390/w9020092>.
- Yang, W., Seager, R., Cane, M.A., & Lyon, B. (2015). The annual cycle of East African precipitation. *Journal of Climatology*. 28:2385–2404. <https://doi.org/10.1175/JCLI-D-14-00484.1>.
- Yu, Y., Wei, W., Chen, L. D., Jia, F. Y., Yang, L., Zhang, H. D., & Feng, T. J. (2015). Responses of vertical soil moisture to rainfall pulses and land uses in a typical loess hilly area, China, *Solid Earth*, 6, 595–608, <https://doi.org/10.5194/se-6-595-2015>.
- Zhao, R. J., Zhang, Y. L., & Fang, L. R. (1980). The Xinanjiang model Hydrological Forecasting *Proceedings Oxford Symposium*, IASH, Oxford.
- Zreda, M., Desilets, D., Ferre, T.P.A., & Scott, R.L. (2008). Measuring soil moisture content non-invasively at intermediate spatial scale using cosmic-ray neutrons. *Geophysical Research Letters*., 35, L21402:1–L21402:5.
- Zreda, M., Shuttleworth, W. J., Zeng, X., Zweck, C., Desilets, D., Franz, T., & Rosolem, R. (2012). COSMOS: the COsmic-ray Soil Moisture Observing System, *Hydrology Earth System Science*., 16, 4079–4099, <https://doi.org/10.5194/hess-16-4079-2012>.

APPENDICES

Appendices A: Plates

Appendix A.1: Installed Cosmic-Ray Neutron Sensor at Maasai Mara National Reserve



Appendix A.2: Installed 5TM-ECH₂O (Soil Moisture, Soil Temperature Capacitance Sensors) profiles and Data Download at Maasai Mara Field Sites



Appendix A.3: Bulk Soil Samples Excavated from Experimental Sites for Analysis



Appendix A.4: Field Core Ring Samples at Laboratory for Weight Measurements and Oven Drying



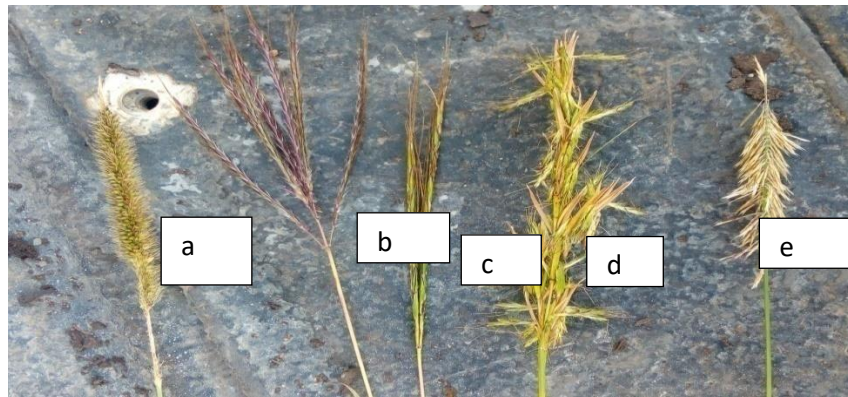
Appendix A.5: Quadrat Aboveground Grass Biomass Harvesting via 50cm by 50cm Sample Metal Frame and Laboratory Oven Drying



Appendix A.6: Characteristics of Standing Grass Biomass Over Wet and Dry Season



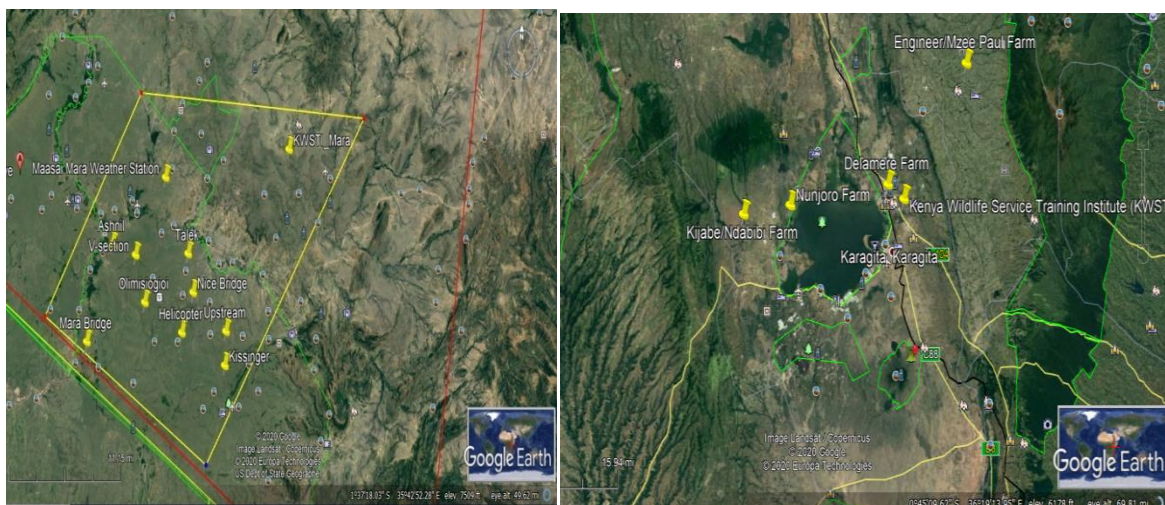
Appendix A.7: Dominant Grass Species (a) Pennisetum (b) Purple Needlegrass (c) Ryegrass (d) Stipa Calamagrotis (e) Harpachne Mara Natural Grassland Ecosystem



Appendix A.8: Wheat Farms and Hay Production at Kijabe/Ndabibi Cropland on 28/5/2018



Appendix A.9: Spatial Distribution of 5TM-ECH₂O Soil Moisture, Soil Temperature Stations in Maasai Mara Rangeland and Naivasha Cropland Ecosystem



Appendices B: Tables

Appendix B.1: Gravimetric Soil Samples Cored from 24 Sampling Points at six Sample Profiles making (144 Samples)

from 0-5cm, 5-10cm, 10-15cm, 15-20cm, 20-25cm and 25-30cm Soil Depths.

Sampling Point_ID	Ring Distance	Angle Deg	Profile Depth (cm)	Foil wgt (g)	Sample wet wgt + Core ring (g)	Oven dry wgt (g) + Core ring (g)	Mass of water content (g)	Core ring +Foil after oven dry soil (g)	Mass of oven – dry soil samples (g)	Core diameter (cm)	Core ring height (cm)	Core ring volume (cm ³)
C300	75m	300	20	0.51	261.58	247.49	14.09	96.01	95.50	5.06	5.1	102.50
C300	75m	300	25	0.51	268.58	239.78	28.80	96.15	95.64	5.05	5.1	102.50
C300	75m	300	30	0.49	269.42	234.42	35.00	98.09	97.60	5.05	5.1	102.50
D0, D360	175m	0	5	0.49	244.88	230.63	14.25	96.10	95.61	5.70	4.05	81.40
D0	175m	0	10	0.46	260.02	245.77	14.25	105.51	105.05	5.65	4.05	81.40
D0	175m	0	15	0.52	272.59	258.18	14.41	115.03	114.51	5.65	4.05	81.40
D0	175m	0	20	0.50	268.63	252.51	16.12	112.40	111.90	5.70	4.00	80.40
D0	175m	0	25	0.55	278.16	255.45	22.71	108.83	108.28	5.65	4.02	80.80
D0	175m	0	30	0.53	285.76	244.52	41.24	108.13	107.60	5.70	4.05	81.40
D60	175m	60	5	0.51	230.37	218.47	11.90	114.93	114.42	5.65	4.05	81.40
D60	175m	60	10	0.53	229.56	213.94	15.62	96.82	96.29	5.71	4.05	81.40

D60	175m	60	15	0.51	247.80	229.37	18.43	110.25	109.74	5.65	4.05	81.40
D60	175m	60	20	0.49	280.40	247.63	32.77	115.48	114.99	5.65	4.05	81.40
D60	175m	60	25	0.48	276.46	240.10	36.36	112.22	111.74	5.65	4.05	81.40
D60	175m	60	30	0.48	264.45	222.09	42.36	95.29	94.81	5.70	4.05	81.40
<hr/>												
D120	175m	120	5	0.50	223.29	209.48	13.81	113.34	112.84	5.65	4.05	81.40
D120	175m	120	10	0.52	212.60	197.65	14.95	97.98	97.46	5.70	4.05	81.40
D120	175m	120	15	0.50	276.38	246.30	30.08	110.01	109.51	5.70	4.05	81.40
D120	175m	120	20	0.49	271.92	239.74	32.18	112.11	111.62	5.65	4.05	81.40
D120	175m	120	25	0.50	267.73	229.75	37.98	108.95	108.45	5.65	4.10	82.41
D120	175m	120	30	0.53	273.72	233.08	40.64	110.61	110.08	5.65	4.05	81.40
<hr/>												
D180	175m	180	5	0.52	208.28	194.32	13.96	96.26	95.74	5.70	4.10	82.41
D180	175m	180	10	0.56	240.5	219.32	21.18	111.77	111.21	5.68	4.05	81.40
D180	175m	180	15	0.60	254.79	222.29	32.50	111.89	111.29	5.61	4.05	81.40
D180	175m	180	20	0.53	272.65	226.42	46.23	111.61	111.08	5.65	4.05	81.40
D180	175m	180	25	0.56	288.50	239.67	48.83	128.44	127.88	5.65	4.10	82.41
D180	175m	180	30	0.56	282.15	240.11	42.04	114.59	114.03	5.65	4.06	81.60
<hr/>												
D240	175m	240	5	0.47	227.33	212.27	15.06	92.86	92.39	5.05	5.10	102.50
D240	175m	240	10	0.48	241.3	223.92	17.38	97.35	96.87	5.05	5.10	102.50

D240	175m	240	15	0.47	248.96	218.55	30.41	92.81	92.34	5.02	5.09	102.30
D240	175m	240	20	0.46	249.38	220.80	28.58	92.95	92.49	5.05	5.09	102.30
D240	175m	240	25	0.48	260.18	224.99	35.19	93.75	93.27	5.00	5.09	102.30
D240	175m	240	30	0.52	263.77	228.16	35.61	93.03	92.51	5.05	5.05	101.50
D300	175m	300	5	0.48	228.18	211.35	16.83	98.15	97.67	5.05	5.10	102.50
D300	175m	300	10	0.56	230.14	202.88	27.26	96.35	95.79	5.05	5.05	101.50
D300	175m	300	15	0.51	259.28	223.24	36.04	95.06	94.55	5.08	5.10	102.50
D300	175m	300	20	0.44	253.62	214.07	39.55	95.71	95.27	5.05	5.10	102.50
D300	175m	300	25	0.47	246.86	209.82	37.04	90.95	90.48	5.05	5.10	102.50
D300	175m	300	30	0.49	250.35	214.85	35.50	93.99	93.50	5.00	5.06	101.70

Appendix B.2: Gravimetric and Volumetric Water Content of Maasai Mara Soil Samples

Sampling Point_ID	Ring Distance	Angle Deg	Profile Depth (cm)	Mass of oven dry soil (g)	Mass of water content (g)	Volume of soil (cm ³)	Bulk density (g/cm ³)	Gravimetric water content (%)	Volumetric water content (cm ³ /cm ³)
C300	75m	300	20	95.50	13.58	102.50	0.932	14	0.13
C300	75m	300	25	95.64	28.29	102.50	0.933	30	0.28
C300	75m	300	30	97.60	34.51	102.50	0.952	35	0.34

D0, D360	175m	0, 360	5	95.61	13.76	81.40	1.175	14	0.17
D0	175m	0, 360	10	105.05	13.79	81.40	1.291	13	0.17
D0	175m	0, 360	15	114.51	13.89	81.40	1.407	12	0.17
D0	175m	0, 360	20	111.90	15.62	80.40	1.392	14	0.19
D0	175m	0, 360	25	108.28	22.16	80.80	1.340	20	0.27
D0	175m	0, 360	30	107.60	40.71	81.40	1.322	38	0.50
D60	175m	60	5	114.42	11.39	81.40	1.406	10	0.14
D60	175m	60	10	96.29	15.09	81.40	1.183	16	0.19
D60	175m	60	15	109.74	17.92	81.40	1.348	16	0.22
D60	175m	60	20	114.99	32.28	81.40	1.413	28	0.40
D60	175m	60	25	111.74	35.88	81.40	1.373	32	0.44
D60	175m	60	30	94.81	41.88	81.40	1.165	44	0.51
D120	175m	120	5	112.84	13.31	81.40	1.386	12	0.16
D120	175m	120	10	97.46	14.43	81.40	1.197	15	0.18
D120	175m	120	15	109.51	29.58	81.40	1.345	27	0.36
D120	175m	120	20	111.62	31.69	81.40	1.371	28	0.39
D120	175m	120	25	108.45	37.48	82.41	1.316	35	0.45
D120	175m	120	30	110.08	40.11	81.40	1.352	36	0.49

D180	175m	180	5	95.74	13.44	82.41	1.162	14	0.16
D180	175m	180	10	111.21	20.62	81.40	1.366	19	0.25
D180	175m	180	15	111.29	31.90	81.40	1.367	29	0.39
D180	175m	180	20	111.08	45.70	81.40	1.365	41	0.56
D180	175m	180	25	127.88	48.27	82.41	1.552	38	0.59
D180	175m	180	30	114.03	41.48	81.60	1.397	36	0.51
<hr/>									
D240	175m	240	5	92.39	14.59	102.50	0.901	16	0.14
D240	175m	240	10	96.87	16.90	102.50	0.945	17	0.16
D240	175m	240	15	92.34	29.94	102.30	0.903	32	0.29
D240	175m	240	20	92.49	28.12	102.30	0.904	30	0.27
D240	175m	240	25	93.27	34.71	102.30	0.912	37	0.34
D240	175m	240	30	92.51	35.09	101.50	0.911	38	0.35
<hr/>									
D300	175m	300	5	97.67	16.35	102.50	0.953	17	0.16
D300	175m	300	10	95.79	26.70	101.50	0.944	28	0.26
D300	175m	300	15	94.55	35.53	102.50	0.922	38	0.35
D300	175m	300	20	95.27	39.11	102.50	0.929	41	0.38
D300	175m	300	25	90.48	36.57	102.50	0.883	40	0.36
D300	175m	300	30	93.50	35.01	101.70	0.919	37	0.34

Table 4.12: Analysis of Variance (ANOVA) on Spatial Distribution of Volumetric Water Content with Depth at 10 M Concentric Distance to CRNS in Maasai Mara Rangeland Ecosystem (Main Station)

Source	Sum of squares (SS)	Degrees of freedom (df)	Mean squares (MS)	P value	CI (%)	SD	F statistics	LSD
Between Groups	0.716	5	0.077	≤0.05	95	0.104	7.135	0.428
Within Groups	0.063	30	0.011					
Total		35						

P value - Significant at the 0.05 probability level, F – F ratio, CI – Confidence interval level (%), SD – Standard deviation,

LSD, least significant difference between means.

Mean Square of Profile (MSP) - 0.077, Mean Square Error (MSE) – 0.0108, Sum of Square Error (SSE) – 0.2688

Source	Sum of squares (SS)	Degrees of freedom (df)	Mean squares (MS)	P value	CI (%)	SD	F statistics	LSD
Between Groups	0.548	5	0.011	≤0.05	95	0.210	2.015	0.493
Within Groups	0.062	30	0.033					
Total		35						

P value - Significant at the 0.05 probability level, F – F ratio, CI – Confidence interval level (%), SD – Standard deviation,

LSD, least significant difference between means

Mean Square of Profile (MSP) - 0.088, Mean Square Error (MSE) – 0.044, Sum of Square Error (SSE) – 0.044

Source	Sum of squares (SS)	Degrees of freedom (df)	Mean squares (MS)	P value	CI (%)	SD	F statistics	LSD
Between Groups	0.557	5	0.087	≤0.05	95	0.246	1.436	0.578
Within Groups	0.063	30	0.060					
Total		35						

P value - Significant at the 0.05 probability level, F – F ratio, CI – Confidence interval level (%), SD – Standard deviation, LSD, least significant difference between means.

Mean Square of Profile (MSP) - 0.087, Mean Square Error (MSE) – 0.060, Sum of Square Error (SSE) – 0.044

Source	Sum of squares (SS)	Degrees of freedom (df)	Mean squares (MS)	P value	CI (%)	SD	F statistics	LSD
Between Groups	0.632	5	0.082	≤0.05	95	0.341	0.704	0.802
Within Groups	0.106	30	0.116					
Total		35						

P value - Significant at the 0.05 probability level, F – F ratio, CI – Confidence interval level (%), SD – Standard deviation, LSD, least significant difference between means

Mean Square of Profile (MSP) - 0.082, Mean Square Error (MSE) – 0.116, Sum of Square Error (SSE) – 0.116

Appendix B.3: Soil Textural Classes within the Main Weather Station

**SOIL TEXTURE ANALYSIS (HYDROMETER METHOD) – Mara Main station –
Concentric measurements within the CRNS distance from 10m, 25m, 50m, 75m, 150m
and 175m across soil layers.**

KEY:	SC – Sandy Clay, SCL – Sandy Clay Loam, SL – Sandy Loam, C - Clay					
Sample	Soil	Lab.	Sand %	Clay %	Silt %	Texture
Description	Depth(cm)	No./2018				Grade
A0	2.5	3605	72	18	10	SL
A60	2.5	3606	76	18	6	SL
A120	2.5	3607	76	18	6	SL
A180	2.5	3608	82	16	2	SL
A240	2.5	3609	74	16	10	SL
A300	2.5	3610	80	12	8	SL
Mean	2.5		77	16	7	SL
A0	12.5	3611	70	22	8	SCL
A60	12.5	3612	64	32	4	SCL
A120	12.5	3613	72	24	4	SCL
A180	12.5	3614	64	28	8	SCL
A240	12.5	3615	64	24	12	SCL
A300	12.5	3616	68	22	10	SCL
Mean	12.5		67	25	8	SCL
A0	22.5	3617	52	40	8	SC
A60	22.5	3618	58	38	4	SC
A120	22.5	3619	54	40	6	SC
A180	22.5	3620	56	42	2	SC
A240	22.5	3621	56	40	4	SC
A300	22.5	3622	56	36	8	SC
Mean	22.5		56	39	5	SC
B0	2.5	3623	74	16	10	SL
B60	2.5	3624	76	12	12	SL
B120	2.5	3625	74	18	8	SL
B180	2.5	3626	78	16	6	SL
B240	2.5	3627	76	16	8	SL

B300	2.5	3628	72	18	10	SL
Mean	2.5		75	16	9	SL
B0	12.5	3629	70	18	12	SL
B60	12.5	3630	72	18	10	SL
B120	12.5	3631	68	24	8	SCL
B180	12.5	3632	76	16	8	SL
B240	12.5	3633	74	16	10	SL
B300	12.5	3634	78	14	8	SL
Mean	12.5		73	18	9	SL
B0	22.5	3635	74	18	8	SL
B60	22.5	3636	58	36	6	SL
B120	22.5	3637	58	36	6	SL
B180	22.5	3638	62	32	6	SL
B240	22.5	3639	60	30	10	SL
B300	22.5	3640	60	36	4	SL
Mean	22.5		62	31	7	SCL
C0	2.5	3641	64	28	8	SCL
C60	2.5	3642	74	14	12	SL
C120	2.5	3643	76	16	8	SL
C180	2.5	3644	72	14	14	SL
C240	2.5	3645	78	14	8	SL
C300	2.5	3646	76	12	12	SL
Mean	2.5		74	16	10	SL
C0	12.5	3647	80	16	4	SL
C60	12.5	3648	76	16	8	SL
C120	12.5	3649	74	22	4	SCL
C180	12.5	3650	66	24	10	SCL
C240	12.5	3651	70	24	6	SCL
C300	12.5	3652	68	16	16	SL
Mean	12.5		72	20	8	SL
C0	22.5	3653	76	22	2	SCL
C60	22.5	3654	70	30	0	SCL
C120	22.5	3655	64	24	12	SCL

C180	22.5	3656	66	24	10	SCL
C240	22.5	3657	58	36	6	SC
C300	22.5	3658	66	30	4	SCL
Mean	22.5		67	27	6	SCL
D0	2.5	3659	70	18	12	SL
D60	2.5	3660	68	18	14	SL
D120	2.5	3661	66	22	12	SCL
D180	2.5	3662	70	18	12	SL
D240	2.5	3663	70	18	12	SL
D300	2.5	3664	64	26	10	SL
Mean	2.5		68	20	12	SL
D0	12.5	3665	72	18	10	SL
D60	12.5	3666	60	30	10	SCL
D120	12.5	3667	64	28	8	SCL
D180	12.5	3668	60	32	8	SCL
D240	12.5	3669	56	38	6	SC
D300	12.5	3670	52	44	4	SC
Mean	12.5		61	31	8	SCL
D0	22.5	3671	72	18	10	SL
D60	22.5	3672	60	34	6	SCL
D120	22.5	3673	56	38	6	SC
D180	22.5	3674	56	40	4	SC
D240	22.5	3675	60	36	4	SC
D300	22.5	3676	54	42	4	SC
Mean			60	34	6	SCL

Appendix B.4: Soil Texture Classification of within CRNS footprint and 5TM-ECH₂O sensor stations in Maasai Mara National Reserve

Orientation	Distance from CRS (m)	Soil Depth (cm)	Sand%	Clay%	Silt%	Textural
						Class
Ring A	10	P1 (0-5)	77	16	7	SL
		P2 (10-15)	67	25	8	SCL

		P3 (20-25)	56	39	5	SC
Ring B	25	P1 (0-5)	75	16	9	SL
		P2 (10-15)	73	18	9	SL
		P3 (20-25)	62	31	7	SCL
Ring C	75	P1 (0-5)	74	16	10	SL
		P2 (10-15)	72	20	8	SL
		P3 (20-25)	67	27	6	SCL
Ring D	175	P1 (0-5)	68	20	12	SL
		P2 (10-15)	61	31	8	SCL
		P3 (20-25)	60	34	6	SCL

SOIL TEXTURE ANALYSIS (HYDROMETER METHOD) – 5TM-ECH₂O stations spatially distributed within the catchment

KEY:SC – Sandy Clay, SCL – Sandy Clay Loam, SL – Sandy Loam, C - Clay

Sample Description	Soil Depth(cm)	Lab.No./2018	Sand %	Silt %	Clay %	Texture Grade
Mara Main stn	5	3677	70	22	8	SCL
„	10	3678	72	22	6	SCL
„	20	3679	58	36	6	SC
„	40	3680	54	42	4	SC
„	80	3681	52	38	10	SC
V-Section	5	3682	64	22	14	SCL
„	10	3683	60	24	16	SCL
„	20	3684	52	38	10	SC
„	40	3685	56	38	6	SC
„	80	3686	54	36	10	SC
Talek	5	3682	68	24	8	SCL
„	10	3683	66	30	4	SCL
„	20	3684	60	36	4	SC
„	40	3685	58	36	6	SC

„	80	3686	56	36	8	SC
Up-Stream	5	3687	60	28	12	SCL
„	10	3688	56	36	8	SC
„	20	3689	58	38	4	SC
„	40	3690	56	40	4	SC
„	80	3691	52	40	8	SC
Helicopter	5	3692	76	16	8	SL
„	10	3693	78	18	4	SL
„	20	3694	66	30	4	SCL
„	40	3695	66	34	0	SCL
„	80	3696	72	26	2	SCL
Nice Bridge	5	3697	72	22	6	SCL
„	10	3698	70	24	6	SCL
„	20	3699	66	28	6	SCL
„	40	3700	64	28	8	SCL
„	80	3701	68	26	6	SCL
Olimisigioi	5	3702	64	28	8	SCL
„	10	3703	60	32	8	SCL
„	20	3704	38	46	16	C
„	40	3705	64	32	4	SCL
„	80	3706	54	42	4	SC
Mara Bridge	5	3707	68	22	10	SCL
„	10	3708	76	16	8	SL
„	20	3709	62	24	14	SCL
„	40	3710	64	24	12	SCL
„	80	3711	60	26	14	SCL
Kissingen	5	6124	80	14	6	SL

”	10	6125	78	14	8	SL
”	20	6126	68	26	6	SCL
”	40	6127	70	26	4	SCL
”	80	6128	62	30	8	SCL
Ashnil	5	6129	78	14	8	SL
”	10	6130	72	22	6	SCL
”	20	6131	64	32	4	SCL
”	40	6132	66	32	2	SCL
”	80	6133	54	38	8	SC

Appendix B.5: Soil Bulk Density of Maasai Mara National Reserve Ecosystem Sites

Sample Location	Soil Dep th (cm)	Ring No.	Lab No. /20 18	Bulk Density (g cm ⁻³)	Remarks
Mara Main	5	2	614 9	1.40	F
Mara Main	10	5	615 0	1.45	F
Mara Main	20	11	615 1	1.34	F
Mara Main	40	14	615 2	1.19	F
Mara Main	80	8	615 3	1.25	F
Kissinger	5	1	615 4	1.52	F
Kissinger	10	4	615 5	1.62	F
Kissinger	20	7	615 6	1.71	F
Kissinger	40	13	615	1.72	F

				7				
Kissinger	80	22		615	1.52	F		
				8				
Ashnil	5	3		615	1.64	F		
				9				
Ashnil	10	6		616	1.55	F		
				0				
Ashnil	20	15		616	1.63	F		
				1				
Ashnil	40	X120		616	1.55	F		
				2				
Ashnil	80	16		616	1.22	F		
				3				

Source	Sum of squares (SS)	Degrees of freedom (df)	Mean squares (MS)	P value	CI (%)	SD	F statistics	LSD
Between Groups	2.024	9	0.140	≤0.05	95	1.250	0.090	4.321
Within Groups	0.066	40	1.563					
Total		49						

P value - Significant at the 0.05 probability level, F – F ratio, CI – Confidence interval level (%), SD – Standard deviation, LSD, least significant difference between means.

Mean Square of Profile (MSP) - 0.140, Mean Square Error (MSE) – 1.563, Sum of Square Error (SSE) – 0.695

Sample Location	Soil Depth (cm)	Ring No.	Lab No./2018	Bulk Density (g cm ⁻³)	Remarks
Helicopter	5	21	2761	1.37	F
Helicopter	10	7	2762	1.11	NF
Helicopter	20	19	2763	1.33	NF
Helicopter	40	11	2764	1.13	F

Helicopter	80	5	2765	1.10	NF
V- section	5	13	2766	1.24	F
V- section	10	17	2767	1.20	F
V- section	20	23	2768	1.15	F
V- section	40	2	2769	0.93	NF
V- section	80	9	2770	1.28	F
Up-stream	5	1	2771	1.17	F
Up-stream	10	3	2772	1.27	F
Up-stream	20	16	2773	1.12	F
Up-stream	40	15	2774	1.21	F
Up-stream	80	14	2775	1.16	F
Talek	5	6	2776	0.98	NF
Talek	10	18	2777	1.10	F
Talek	20	20	2778	1.75	F
Talek	40	12	2779	1.35	F
Talek	80	4	2780	1.19	F
Nice-Bridge	5	22	2781	1.18	F
Nice-Bridge	10	8	2782	1.29	F
Nice-Bridge	20	24	2783	1.27	F
Nice-Bridge	40	10	2784	1.09	F
Nice-Bridge	80	8	2785	1.12	F
Mara-bridge	5	4	2786	1.16	F
Mara-bridge	10	2	2787	1.18	F
Mara-bridge	20	3	2788	1.07	F
Mara-bridge	40	12	2789	1.26	F
Mara-bridge	80	10	2790	1.14	NF
Olimisigioi	5	15	2791	0.84	NF
Olimisigioi	10	14	2792	1.13	NF
Olimisigioi	20	7	2793	1.00	F
Olimisigioi	40	13	2794	1.22	F
Olimisigioi	80	16	2795	1.35	F

Full – F, Not Full – NF

Appendix B.6: Soil Particle Density of Maasai Mara Rangeland Sites

Sample Description/lab. No.	Mara main(6134)		Mara main(6135)		Mara main(6136)		Mara main (6137)		Mara main(6138)	
Soil depth (cm)	5		10		20		40		80	
	1	2	1	2	1	2	1	2	1	2
Pyknometer No.										
Density of water	0.9973	0.9973	0.9973	0.9973	0.9973	0.9973	0.9973	0.9973	0.9973	0.9973
Wt. Pyknometer (wa)	33.23	33.3	40.14	28.75	33.62	33.3	28.32	33.00	33.25	33.36
Wt. pyknometer + soil(ws)	43.84	42.12	58.47	47.91	42.83	42.16	47.01	45.65	45.27	46.10
Wt. pycnometer + soil + water (wsw)	90.93	89.2	102.81	94.89	90.42	89.06	93.79	92.30	91.07	92.14
Pycnometer + water(ww)	84.74	83.87	92.04	83.95	84.78	83.8	83.13	84.84	83.66	84.59
Particle density(g.cm ⁻³)	2.39	2.52	2.42	2.32	2.57	2.45	2.32	2.43	2.60	2.45
Average density(g.cm⁻³)	2.46		2.37		2.51		2.38		2.53	

Sample Description/lab. No.	Kissinger (6139)		Kissinger (6140)		Kissinger (6141)		Kissinger (6142)		Kissinger (6143)	
Soil depth (cm)	5		10		20		40		80	
	1	2	1	2	1	2	1	2	1	2
Pyknometer No.										
Density of water	0.9973	0.9973	0.9973	0.9973	0.9973	0.9973	0.9973	0.9973	0.9973	0.9973
Wt. Pyknometer (wa)	33.62	33.26	33.38	33.34	33.30	33.34	33.40	33.30	32.97	33.4
Wt. pyknometer + soil(ws)	44.43	45.30	45.4	45.82	45.4	42.1	48.1	42.12	48.13	45.27
Wt. pycnometer + soil + water (wsw)	90.41	90.53	91.56	92.05	91.55	89.03	93.07	89.20	93.36	90.68

Pycnometer + water(ww)	83.86	83.65	84.34	84.90	84.33	83.77	84.31	83.87	84.34	83.57
Particle density(g.cm ⁻³)	2.53	2.33	2.5	2.34	2.47	2.50	2.47	2.52	2.46	2.49
Average density(g.cm⁻³)	2.53		2.42		2.49		2.50		2.48	

Sample Description/lab. No.	Ashnil (6144)		Ashnil (6145)		Ashnil (6146)		Ashnil (6147)		Ashnil (6148)	
Soil depth (cm)	5		10		20		40		80	
	1	2	1	2	1	2	1	2	1	2
Pyknometer No.										
Density of water	0.9973	0.9973	0.9973	0.9973	0.9973	0.9973	0.9973	0.9973	0.9973	0.9973
Wt. Pyknometer (wa)	33.34	33.32	33.30	33.34	33.31	33.25	33.31	33.30	33.40	33.30
Wt. pyknometer + soil(ws)	44.1	42.12	44.77	45.18	46.0	45.27	44.24	45.71	44.12	43.28
Wt. pycnometer + soil + water (wsw)	91.01	90.00	91.10	91.40	92.27	91.07	90.8	91.84	92.08	91.46
Pycnometer + water(ww)	84.63	84.73	84.20	84.30	84.92	83.66	84.34	84.46	85.60	85.55
Particle density(g.cm ⁻³)	2.45	2.49	2.51	2.49	2.37	2.60	2.44	2.46	2.52	2.45
Average density(g.cm⁻³)	2.47		2.50		2.49		2.45		2.49	

Sample Description/lab. No.	Nicebridge (3773)		Nicebridge (3774)		Nicebridge (3775)		Nicebridge (3776)		Nicebridge (3777)	
Soil depth (cm)	5		10		20		40		80	
	1	2	1	2	1	2	1	2	1	2
Pyknometer No.										
Density of water	0.9973	0.9973	0.9973	0.9973	0.9973	0.9973	0.9973	0.9973	0.9973	0.9973
Wt. Pyknometer (wa)	33.41	27.86	33.449	45.503	33.436	42.696	33.424	42.549	33.468	42.697

Wt. pyknometer + soil(ws)	47.53	40.23	45.166	56.705	44.158	55.251	48.144	53.946	48.424	58.731
Wt. pycnometer + soil + water (wsw)	93.08	84.10	91.99	99.775	91.21	100.394	93.282	100.02	93.946	102.259
Pycnometer + water(ww)	84.96	76.713	84.94	93.104	85.00	93.165	84.979	92.983	84.892	93.117
Particle density(g.cm ⁻³)	2.35	2.48	2.50	2.47	2.37	2.35	2.29	2.61	2.53	2.32
Average density(g.cm⁻³)	2.41		2.49		2.36		2.45		2.42	

Sample Description/lab. No.	Talek (3778)		Talek (3779)		Talek (3780)		Talek(3781)		Talek (3782)	
Soil depth (cm)	5		10		20		40		80	
	1	2	1	2	1	2	1	2	1	2
Pyknometer No.										
Density of water	0.9973	0.9973	0.9973	0.9973	0.9973	0.9973	0.9973	0.9973	0.9973	0.9973
Wt. Pyknometer (wa)	33.23	42.32	33.27	42.36	33.25	42.38	33.53	42.61	33.3	42.38
Wt. pyknometer + soil(ws)	43.45	55.30	48.83	61.43	45.81	53.58	44.81	54.44	46.59	59.87
Wt. pycnometer + soil + water (wsw)	90.61	100.52	94.18	104.48	92.00	99.35	92.07	99.75	93.65	101.11
Pycnometer + water(ww)	84.65	92.74	84.69	92.74	84.61	92.73	85.08	93.21	84.65	92.14
Particle density(g.cm ⁻³)	2.39	2.49	2.56	2.59	2.42	2.44	2.62	2.23	3.09	2.05
Average density(g.cm⁻³)	2.44		2.58		2.43		2.43		2.57	

Sample Description/lab. No.	Marabridge (3788)		Marabridge (3789)		Marabridge (3790)		Marabridge (3791)		Marabridge (3792)	
	Soil depth (cm) 5		10		20		40		80	
	1	2	1	2	1	2	1	2	1	2
Pyknometer No.										
Density of water	0.9973	0.9973	0.9973	0.9973	0.9973	0.9973	0.9973	0.9973	0.9973	0.9973
Wt. Pyknometer (wa)	33.36	42.49	33.34	42.47	33.37	42.47	33.37	42.47	33.35	42.36
Wt. pyknometer + soil(ws)	44.76	55.89	48.39	56.97	45.09	55.88	48.43	56.40	46.00	57.71
Wt. pycnometer + soil + water (wsw)	91.63	101.03	93.23	101.56	90.42	100.7	93.06	100.94	92.03	101.73
Pycnometer + water(ww)	84.79	92.98	84.45	92.89	83.94	92.58	84.78	92.81	84.63	92.16
Particle density(g.cm ⁻³)	2.49	2.50	2.39	2.48	2.23	2.53	2.22	2.40	2.40	2.65
Average density(g.cm⁻³)	2.50		2.44		2.38		2.31		2.53	

Sample Description/lab. No.	Helicopter (3793)		Helicopter (3794)		Helicopter (3795)		Helicopter (3796)		Helicopter (3797)	
	Soil depth (cm) 5		10		20		40		80	
	1	2	1	2	1	2	1	2	1	2
Pyknometer No.										
Density of water	0.9973	0.9973	0.9973	0.9973	0.9973	0.9973	0.9973	0.9973	0.9973	0.9973
Wt. Pyknometer (wa)	33.36	42.43	33.3	42.41	33.36	42.42	33.33	42.42	33.34	42.40
Wt. pyknometer + soil(ws)	46.10	57.38	46.08	56.30	46.17	56.04	45.66	54.05	45.42	55.40
Wt. pycnometer + soil + water (wsw)	92.41	101.89	91.36	101.01	91.72	100.66	91.56	99.47	91.59	100.08

Pycnometer + water(ww)	84.59	92.78	83.89	92.57	84.45	92.91	84.62	92.85	84.64	92.81
Particle density(g.cm ⁻³)	2.58	2.55	2.40	2.54	2.31	2.31	2.28	2.32	2.35	2.26
Average density(g.cm⁻³)	2.57		2.47		2.31		2.30		2.31	

Sample Description/lab. No.	V-section (3798)		V-section (3799)		V-section (3800)		V-section (3801)		V-section (3802)	
Soil depth (cm)	5		10		20		40		80	
	1	2	1	2	1	2	1	2	1	2
Pyknometer No.										
Density of water	0.997	0.9973	0.9973	0.9973	0.9973	0.9973	0.9973	0.9973	0.9973	0.9973
	3									
Wt. Pyknometer (wa)	33.31	42.41	33.25	42.90	33.34	42.42	33.32	42.41	33.63	42.80
Wt. pyknometer + soil(ws)	44.43	54.97	45.27	54.20	45.46	55.61	47.30	54.81	44.43	52.02
Wt. pycnometer + soil + water (wsw)	90.71	100.09	91.07	99.78	91.76	100.51	92.20	100.20	90.56	98.40
Pycnometer + water(ww)	84.58	92.95	83.66	92.90	84.84	92.95	84.44	92.82	83.89	92.84
Particle density(g.cm ⁻³)	2.21	2.31	2.60	2.55	2.32	2.34	2.24	2.38	2.61	2.51
Average density(g.cm⁻³)	2.27		2.57		2.33		2.31		2.56	

Sample Description/lab. No.	Olimisiogioi	Olimisiogioi (3804)	Olimisiogioi (3805)	Olimisiogioi (3806)	Olimisiogioi (3807)
------------------------------------	---------------------	----------------------------	----------------------------	----------------------------	----------------------------

(3803)										
Soil depth (cm)	5		10		20		40		80	
Pyknometer No.	1	2	1	2	1	2	1	2	1	2
Density of water	0.997	0.9973	0.9973	0.9973	0.9973	0.9973	0.9973	0.9973	0.9973	0.9973
	3									
Wt. Pyknometer (wa)	33.33	42.46	33.30	42.37	33.3	42.41	33.34	42.49	33.45	42.60
Wt. pyknometer + soil(ws)	47.97	56.53	43.71	55.15	42.12	52.08	44.33	55.60	51.21	59.96
Wt. pycnometer + soil + water (wsw)	92.14	100.84	90.45	100.50	88.98	98.34	90.87	100.41	94.95	103.32
Pycnometer + water(ww)	83.92	92.86	84.69	92.84	83.87	92.73	84.77	92.82	85.07	93.20
Particle density(g.cm ⁻³)	2.27	2.30	2.23	2.49	2.37	2.38	2.24	2.37	2.25	2.39
Average density(g.cm⁻³)	2.29		2.36		2.37		2.30		2.32	

Sample Description/lab. No.	Upstream (3808)		Upstream (3809)		Upstream (3810)		Upstream (3811)		Upstream (3812)	
Soil depth (cm)	5		10		20		40		80	
Pyknometer No.	1	2	1	2	1	2	1	2	1	2
Density of water	0.9973	0.9973	0.9973	0.9973	0.9973	0.9973	0.9973	0.9973	0.9973	0.9973
Wt. Pyknometer (wa)	33.41	42.56	33.37	42.57	33.34	42.45	33.34	42.52	33.55	42.40
Wt. pyknometer + soil(ws)	48.81	58.91	45.81	58.58	50.35	59.51	48.50	55.69	51.43	55.40

Wt. pycnometer + soil + water (wsw)	93.11	102.56	92.33	102.49	95.03	102.96	93.51	101.10	94.68	100.08
Pycnometer + water(ww)	84.31	93.28	85.04	93.31	85.01	93.14	84.93	93.20	84.45	92.81
Particle density(g.cm ⁻³)	2.33	2.31	2.41	2.34	2.43	2.35	2.30	2.49	2.33	2.26
Average density(g.cm⁻³)	2.32		2.37		2.39		2.40		2.30	

Particle density

Source	Sum of squares (SS)	Degrees of freedom (df)	Mean squares (MS)	P value	CI (%)	SD	F statistics	LSD
Between Groups	0.376	9	0.011	≤0.05	95	0.332	0.104	1.146
Within Groups	0.025	40	0.110					
Total		49						

P value - Significant at 0.05 probability level, F – F ratio, CI – Confidence interval level (%), SD – Standard deviation, LSD, least significant difference between means,

Mean Square of Profile (MSP) - 0.011, Mean Square Error (MSE) – 0.033, Sum of Square Error (SSE) – 0.247

Appendix B.7: Total Organic Carbon Concentration of Main Mara Meteorological Station and 5TM-ECH₂O Probe sites

Soil Sample ID	Sample reference Station ECH₂O Soil Moisture Main Location	Soil Depth (cm)	Total Organic Carbon (%)	Class
2705	Talek	5	2.28	Adequate
2706	Talek	10	1.84	Moderate
2707	Talek	20	1.75	Moderate
2708	Talek	45	1.16	Low
2709	Talek	80	0.98	Low
2710	Mara Bridge	5	1.81	Moderate
2711	Mara Bridge	10	1.62	Moderate
2712	Mara Bridge	20	1.31	Moderate
2713	Mara Bridge	45	1.10	Low
2714	Mara Bridge	80	0.92	Low
2715	Olimesiogioi	5	2.30	Moderate
	Olimesiogioi	10	2.13	Moderate
	Olimesiogioi	20	1.86	Moderate
2716	Olimesiogioi	45	1.20	Low
2717	Olimesiogioi	80	0.64	Low
2718	Upstream	5	1.85	Moderate
2719	Upstream	10	1.62	Moderate
2720	Upstream	20	1.41	Moderate
2721	Upstream	45	0.92	Low
2722	Upstream	80	0.53	Low
2723	Nice bridge	5	2.29	Moderate
2724	Nice bridge	10	1.98	Moderate
2725	Nice bridge	20	1.72	Moderate
2726	Nice bridge	45	0.92	Low
2727	Nice bridge	80	0.46	Low
2728	Helicopter	5	1.85	Moderate
2729	Helicopter	10	1.66	Moderate
2730	Helicopter	20	1.34	Moderate

2731	Helicopter	45	0.80	Low
2732	Helicopter	80	0.52	Low
2733	V-section	5	1.95	Moderate
2734	V-section	10	1.64	Moderate
2735	V-section	20	1.26	Moderate
2736	V-section	45	0.99	Low
2737	V-section	80	0.74	Low
2738	Mara Main 5TM- ECH ₂ O	5	2.25	Moderate
2739	Mara Main 5TM- ECH ₂ O	10	2.00	Moderate
2740	Mara Main 5TM- ECH ₂ O	20	1.49	Moderate
2741	Mara Main 5TM- ECH ₂ O	40	1.26	Low
2742	Mara Main 5TM- ECH ₂ O	80	1.04	Low
6114	Kissinger	5	2.39	Moderate
6115	Kissinger	10	1.95	Moderate
6116	Kissinger	20	1.58	Moderate
6117	Kissinger	40	0.82	Low
6118	Kissinger	80	0.42	Low
6119	Ashnil	5	2.11	Moderate
6120	Ashnil	10	1.81	Moderate
6121	Ashnil	20	1.47	Moderate
6122	Ashnil	40	1.11	Low
6123	Ashnil	80	0.42	Low

Appendix B.7a: Analysis of variance of sites total organic carbon concentration

Source	Sum of squares (SS)	Degrees of freedom (df)	Mean squares (MS)	P value	CI (%)	SD	F statistics	LSD
Between Groups	14.523	9	0.121	≤0.05	95	1.294	0.072	4.473
Within Groups	12.687	40	1.675					
Total		49						

P value - Significant at the 0.05 probability level, F – F ratio, CI – Confidence interval level (%), SD – Standard deviation, LSD, least significant difference between means.

Mean Square of Profile (MSP) - 0.121, Mean Square Error (MSE) – 1.675, Sum of Square Error (SSE) – 0.745

Appendix B.8: Infiltration test – Maasai Mara Meta Plains – Main Weather Station

Elapsed time (mins)	Height of receding water from reference point (cm)		Inner/Outer ring – 30/55cm, Height - 25cm		
	Before Filling	After Filling	Infiltration during the period Depth (cm)	Accumulated Infiltration (cm)	Average infiltration rate (cm/hr)
0		10.0	0.0	0.0	0.0
2		12.7	2.7	2.7	81.0
5		13.7	1.0	3.7	44.4
7		13.9	0.2	3.9	33.4
9		14.0	0.1	4.0	26.7
11		14.4	0.4	4.4	24.0
13		14.7	0.3	4.7	21.7
15		14.9	0.2	4.9	19.6
17		15.0	0.1	5.0	17.7
19		15.1	0.1	5.1	16.1
24		15.5	0.4	5.5	13.8
29		16.0	0.5	6.0	12.4
34		16.3	0.3	6.3	11.1
39		16.7	0.4	6.7	10.3
44		17.4	0.3	7.0	9.6
49		17.7	0.3	7.3	8.9
59		18.2	0.5	7.8	7.9
69		18.7	0.5	8.3	7.2
79		19.2	0.5	8.8	6.7
89		19.8	0.6	9.4	6.3
99		20.3	0.5	9.9	6.0
109		20.9	0.6	10.5	5.8

119	21.5	0.6	11.1	5.6
129	22.1	0.6	11.7	5.4

Elapsed time (mins)	Height of receding water from reference point (cm)		Inner/Outer ring – 30/55cm, – 25cm Infiltration during the period		Height Average infiltration rate (cm/hr)
	Before filling	After filling	Depth (cm)	Accumulated Infiltration (cm)	
0		10.0	0.0	0.0	0.0
2		9.3	0.7	0.7	21.0
5		8.9	0.4	1.1	13.2
7		9.2	0.3	1.4	12.0
9		9.0	0.2	1.6	10.7
11		8.8	0.2	1.8	9.8
13		8.5	0.3	2.1	9.7
15		7.9	0.6	2.7	10.8
17		7.2	0.7	3.4	12.0
19		7.0	0.5	3.9	12.3
24		6.5	0.5	4.4	11.0
29		6.0	0.5	4.9	10.1
34		5.9	0.9	5.8	10.2
39		5.6	0.3	6.1	9.4
44		5.2	0.4	6.5	8.9
49		4.9	0.3	6.8	8.3
59		4.5	0.4	7.2	7.3
69		4.0	0.5	7.7	6.7
79		3.7	0.3	8.0	6.1
89		3.4	0.3	8.3	5.6
99		3.2	0.2	8.5	5.2
109		3.0	0.2	8.7	4.8
119		0.0	0.0	8.7	4.4
129		0.0	0.0	8.7	4.1

Appendix B.9: Spatial soil water characteristics at various soil depth and soil water retention

Table 4.23: Spatial soil water characteristics at 15-20 cm soil depth and soil water retention

Site_ID	Soil Depths (cm)	%Sand	%Clay	%Silt	FC (m³/m³)	WP (m³/m³)	Saturation (m³/m³)	Infiltration rate (m/hr)	Avail Water (m³/m³)	Bulk Density (g/cm³)	Textural Class
Mara-main	20	58	36	6	0.289	0.199	0.489	0.167	0.090	1.355	SC
V-section	20	52	38	10	0.307	0.209	0.496	0.162	0.098	1.336	SC
Talek	20	60	36	4	0.286	0.199	0.487	0.163	0.087	1.359	SC
Upstream	20	58	38	4	0.296	0.208	0.492	0.147	0.088	1.347	SC
Helicopter	20	66	30	4	0.257	0.173	0.473	0.242	0.093	1.352	SCL
Kissinger	20	68	26	6	0.241	0.157	0.463	0.348	0.084	1.422	SCL
Nice Bridge	20	66	28	6	0.250	0.165	0.469	0.291	0.085	1.408	SCL
Olimisigioi	20	38	46	16	0.368	0.253	0.517	0.145	0.115	1.281	C
Ashnil	20	64	32	4	0.266	0.182	0.478	0.208	0.084	1.384	SCL
Mara Bridge	20	62	24	14	0.242	0.147	0.463	0.453	0.095	1.423	SCL
Average	20	58	35	8	0.286	0.195	0.487	0.179	0.091	1.360	SC

Table 4.24: Spatial soil water characteristics at 35-40 cm soil depth and soil water retention

Site_ID	Soil Depths (cm)	%Sand	%Clay	%Silt	FC (m ³ /m ³)	WP (m ³ /m ³)	Saturation (m ³ /m ³)	Infiltration rate (m/hr)	Avail Water (m ³ /m ³)	Bulk Density (g/cm ³)	Textural Class
Mara-main	40	54	42	4	0.318	0.227	0.500	0.127	0.091	1.325	SC
V-section	40	56	38	6	0.300	0.209	0.493	0.152	0.091	1.344	SC
Talek	40	58	36	6	0.289	0.199	0.489	0.167	0.090	1.355	SC
Upstream	40	56	40	4	0.307	0.218	0.496	0.136	0.089	1.336	SC
Helicopter	40	66	34	2	0.271	0.191	0.480	0.174	0.080	1.379	SCL
Kissinger	40	70	26	4	0.239	0.157	0.462	0.343	0.082	1.426	SCL
Nice Bridge	40	64	28	8	0.253	0.165	0.470	0.297	0.088	1.404	SCL
Olimisigioi	40	64	32	4	0.266	0.182	0.478	0.208	0.084	1.384	SCL
Ashnil	40	66	32	2	0.264	0.182	0.476	0.204	0.082	1.388	SCL
Mara Bridge	40	64	24	12	0.239	0.147	0.462	0.445	0.092	1.426	SCL
Average	40	60	34	6	0.279	0.190	0.484	0.188	0.089	1.368	SCL

Table 4.25: Spatial soil water characteristics at 75-80 cm soil depth and soil water retention

Site_ID	Soil Depths (cm)	%Sand	%Clay	%Silt	FC (m³/m³)	WP (m³/m³)	Saturatio n (m³/m³)	Infiltration rate (m/hr)	Avail Water (m³/m³)	Bulk Density (g/cm³)	Textural Class
Mara-main	80	52	38	10	0.307	0.209	0.496	0.162	0.098	1.336	SC
V-section	80	54	36	10	0.296	0.199	0.491	0.178	0.096	1.348	SC
Talek	80	56	36	8	0.292	0.199	0.490	0.172	0.093	1.352	SC
Upstream	80	52	40	8	0.314	0.218	0.499	0.145	0.096	1.328	SC
Helicopter	80	72	26	2	0.236	0.157	0.460	0.337	0.079	1.430	SCL
Kissinger	80	62	30	8	0.262	0.173	0.476	0.253	0.089	1.390	SCL
Nice Bridge	80	68	26	6	0.241	0.157	0.463	0.348	0.084	1.422	SCL
Olimisigioi	80	54	42	4	0.318	0.227	0.500	0.127	0.091	1.325	SC
Ashnil	80	54	38	8	0.303	0.209	0.494	0.157	0.094	1.340	SC
Mara Bridge	80	60	26	14	0.251	0.155	0.469	0.376	0.096	1.407	SCL
Average	80	59	34	8	0.280	0.190	0.485	0.190	0.075	1.366	SCL

Appendix B 10: Biomass water equivalent (BWE) used in the calibration of cosmic ray neutron sensor

Sample Number	Bearing Degrees (0 N)	Distance (m)	Sample Area (m ²)	Biomass Wet Weight in Bag (g)	Biomass Dry Weight in Bag (g)	Khaki Bag Weight (g)	Biomass Wet Weight (g)	Biomass Dry Weight (g)	Vegetation Water Percent (%)	Standing Wet Biomass (kg/m ²)	Standing Dry Biomass (kg/m ²)	Biomass Water Equivalent, BWE (kg/m ² = mm of H ₂ O)
1	0	10	0.25	462.00	226.54	12.02	449.98	214.52	52.33	1.80	0.86	1.37
2	120	10	0.25	445.00	176.92	12.50	432.50	164.42	61.98	1.73	0.66	1.40
3	240	10	0.25	368.00	160.20	10.38	357.62	149.82	58.11	1.43	0.60	1.13
4	60	25	0.25	462.00	226.54	12.02	449.98	214.52	52.33	1.80	0.86	1.37
5	180	25	0.25	414.00	165.00	10.59	403.41	154.41	61.72	1.61	0.62	1.30
6	300	25	0.25	524.00	245.63	10.62	513.38	235.01	54.22	2.05	0.94	1.58
7	0	75	0.25	381.00	202.24	10.67	370.33	191.57	48.27	1.48	0.77	1.09
8	120	75	0.25	463.00	151.00	11.25	451.75	139.75	69.06	1.81	0.56	1.52
9	240	75	0.25	535.00	267.27	12.50	522.50	254.77	51.24	2.09	1.02	1.57
10	60	175	0.25	416.00	228.35	11.42	404.58	216.93	46.38	1.62	0.87	1.18
11	180	175	0.25	400.00	219.86	10.59	389.41	209.27	46.26	1.56	0.84	1.13
12	300	175	0.25	450.00	172.97	10.73	439.27	162.24	63.07	1.76	0.65	1.43
												1.34

Appendix B.11: Measured Above Ground Biomass in Maasai Mara National Reserve

Table 4.90: Observed Biomass, Kissinger, 12/12/2017_Dry season

Sample ID	Coordinates		Quadrat Area size (m)	Area in m ²	Wet wgt (Kg)	Dry wgt (Kg)	Projected biomass in tons/hac	Biomass in Kg/m ²
	Latitudes	Longitudes						
A	-1.558890	35.236623	0.5m x 0.5m	0.25	0.236	0.097	3.880	0.388
B	-1.558888	35.236670	0.5m x 0.5m	0.25	0.249	0.098	3.920	0.392
C	-1.558828	35.236678	0.5m x 0.5m	0.25	0.182	0.084	3.360	0.336
D	-1.558898	35.236559	0.5m x 0.5m	0.25	0.153	0.082	3.280	0.328
E	-1.558717	35.236668	0.5m x 0.5m	0.25	0.123	0.090	3.600	0.360
F	-1.558600	35.236640	0.5m x 0.5m	0.25	0.198	0.098	3.920	0.392
Mean					0.190	0.092	3.66	0.366
Mean 0.366kg/m²								

Table 4.91: Observed Biomass, Kissinger, 05/05/2018_Wet season

Sample ID	Coordinates		Quadrat Area size (m)	Area in m ²	Wet wgt (Kg)	Dry wgt (Kg)	Projected biomass in tons/hac	Biomass in Kg/m ²
	Latitudes	Longitudes						
A	-1.558890	35.236623	0.5m x 0.5m	0.25	0.366	0.137	5.480	0.548
B	-1.558888	35.236670	0.5m x 0.5m	0.25	0.424	0.189	7.560	0.756
C	-1.558828	35.236678	0.5m x 0.5m	0.25	0.316	0.128	5.120	0.512
D	-1.558898	35.236559	0.5m x 0.5m	0.25	0.300	0.119	4.760	0.476
E	-1.558717	35.236668	0.5m x 0.5m	0.25	0.350	0.188	7.520	0.752
F	-1.558600	35.236640	0.5m x 0.5m	0.25	0.363	0.122	4.880	0.488
Mean					0.353	0.147	5.89	0.589
Mean 0.589kg/m²								

Table 4.92: Observed Biomass, Ashnil, 12/12/2017_Dry season

Sample ID	Coordinates		Quadrat Area size (m)	Area in m ²	Wet wgt (Kg)	Dry wgt (Kg)	Projected biomass in tons/hac	Biomass in Kg/m ²
	Latitudes	Longitudes						
A	-1.452340	35.072132	0.5m x 0.5m	0.25	0.225	0.094	3.760	0.376
B	-1.452387	35.072171	0.5m x 0.5m	0.25	0.275	0.102	4.080	0.408
C	-1.452429	35.072187	0.5m x 0.5m	0.25	0.186	0.089	3.560	0.356
D	-1.452395	35.071170	0.5m x 0.5m	0.25	0.232	0.099	3.960	0.396
E	-1.452316	35.072266	0.5m x 0.5m	0.25	0.124	0.087	3.480	0.348
F	-1.452401	35.072242	0.5m x 0.5m	0.25	0.146	0.085	3.400	0.340
Mean					0.198	0.093	3.710	0.371
Mean = 0.371kg/m²								

Table 4.93: Observed Biomass, Ashnil, 05/05/2018_Wet season

Sample ID	Coordinates		Quadrat Area size (m)	Area in m ²	Wet wgt (Kg)	Dry wgt (Kg)	Projected biomass in tons/hac	Biomass in Kg/m ²
	Latitudes	Longitudes						
A	-1.452340	35.072132	0.5m x 0.5m	0.25	0.492	0.153	6.120	0.612
B	-1.452387	35.072171	0.5m x 0.5m	0.25	0.399	0.110	4.400	0.440
C	-1.452429	35.072187	0.5m x 0.5m	0.25	0.386	0.095	3.800	0.380
D	-1.452395	35.071170	0.5m x 0.5m	0.25	0.381	0.095	3.800	0.380
E	-1.452316	35.072266	0.5m x 0.5m	0.25	0.351	0.130	5.200	0.520
F	-1.452401	35.072242	0.5m x 0.5m	0.25	0.392	0.073	2.920	0.292
Mean					0.400	0.109	4.370	0.437
Mean = 0.437kg/m²								

Table4.94: Observed Biomass, Mara Bridge, 12/12/2017_Dry Season

Sample ID	Coordinates		Quadrat Area size (m)	Area in m ²	Wet wgt (Kg)	Dry wgt (Kg)	Projected biomass in tons/hac	Biomass in Kg/m ²
	Latitudes	Longitudes						
A	-1.538332	35.036152	0.5m x 0.5m	0.25	0.126	0.064	2.560	0.256
B	-1.538384	35.036156	0.5m x 0.5m	0.25	0.174	0.052	2.080	0.208
C	-1.538427	35.036168	0.5m x 0.5m	0.25	0.187	0.072	2.880	0.288
D	-1.538398	35.036186	0.5m x 0.5m	0.25	0.139	0.068	2.720	0.272
E	-1.538417	35.036178	0.5m x 0.5m	0.25	0.121	0.066	2.640	0.264
F	-1.538401	35.036241	0.5m x 0.5m	0.25	0.143	0.074	2.960	0.296
Mean					0.143	0.066	2.640	0.264
Mean 0.264kg/m²								

Table 4.95: Observed Biomass, Mara Bridge, 05/05/2018_Wet season

Sample ID	Coordinates		Quadrat Area size (m)	Area in m ²	Wet wgt (Kg)	Dry wgt (Kg)	Projected biomass in tons/hac	Biomass in Kg/m ²	Standard Error
	Latitudes	Longitudes							
A	-1.538332	35.036152	0.5m x 0.5m	0.25	0.345	0.063	2.520	0.252	± 0.056
B	-1.538384	35.036156	0.5m x 0.5m	0.25	0.296	0.068	2.720	0.272	± 0.036
C	-1.538427	35.036168	0.5m x 0.5m	0.25	0.392	0.073	2.920	0.292	± 0.016
D	-1.538398	35.036186	0.5m x 0.5m	0.25	0.373	0.083	3.320	0.332	± 0.024
E	-1.538417	35.036178	0.5m x 0.5m	0.25	0.338	0.080	3.200	0.320	± 0.012
F	-1.538401	35.036241	0.5m x 0.5m	0.25	0.329	0.095	3.800	0.380	± 0.072
Mean					0.346	0.077	3.080	0.308	
Mean 0.308kg/m²									

Table 7.0: Observed Biomass, Helicopter, 12/12/2017_Dry season

Sample ID	Coordinates		Quadrat Area size (m)	Area in m ²	Wet wgt (Kg)	Dry wgt (Kg)	Projected biomass in tons/hac	Biomass in Kg/m ²
	Latitudes	Longitudes						
A	-1.530420	35.174223	0.5m x 0.5m	0.25	0.232	0.104	4.160	0.416
B	-1.530482	35.174290	0.5m x 0.5m	0.25	0.194	0.097	3.880	0.388
C	-1.530329	35.174233	0.5m x 0.5m	0.25	0.186	0.099	3.960	0.396
D	-1.530498	35.174267	0.5m x 0.5m	0.25	0.107	0.092	3.680	0.368
E	-1.530317	35.174228	0.5m x 0.5m	0.25	0.126	0.089	3.560	0.356
F	-1.530402	35.174289	0.5m x 0.5m	0.25	0.184	0.102	4.080	0.408
Mean					0.172	0.097	3.89	0.389
Mean = 0.389kg/m²								

Table 7.1: Observed Biomass, Helicopter, 05/05/2018_Wet season

Sample ID	Coordinates		Quadrat	Area in m ²	Wet wgt (Kg)	Dry wgt (Kg)	Projected biomass in tons/hac	Biomass in Kg/m ²
	Latitudes	Longitudes	Area size (m)					
A	-1.530420	35.174223	0.5m x 0.5m	0.25	1.932	0.109	4.360	0.436
B	-1.530482	35.174290	0.5m x 0.5m	0.25	1.894	0.103	4.120	0.412
C	-1.530329	35.174233	0.5m x 0.5m	0.25	1.886	0.105	4.200	0.420
D	-1.530498	35.174267	0.5m x 0.5m	0.25	1.907	0.104	4.160	0.416
E	-1.530317	35.174228	0.5m x 0.5m	0.25	1.426	0.098	3.920	0.392
F	-1.530402	35.174289	0.5m x 0.5m	0.25	1.564	0.101	4.040	0.404
Mean					1.768	0.103	4.133	0.413
Mean = 0.413kg/m²								

Table 7.2: Observed Biomass, Olimisigioi, 12/12/2017_Dry season

Sample ID	Coordinates		Quadrat Area size (m)	Area in m ²	Wet wgt (Kg)	Dry wgt (Kg)	Projected biomass in tons/hac	Biomass in Kg/m ²
	Latitudes	Longitudes						
A	-1.503840	35.120073	0.5m x 0.5m	0.25	0.125	0.090	3.600	0.360
B	-1.503788	35.120070	0.5m x 0.5m	0.25	0.175	0.092	3.680	0.368
C	-1.503828	35.120088	0.5m x 0.5m	0.25	0.186	0.085	3.400	0.340
D	-1.503898	35.120072	0.5m x 0.5m	0.25	0.132	0.089	3.560	0.356
E	-1.503917	35.120068	0.5m x 0.5m	0.25	0.124	0.098	3.920	0.392
F	-1.503901	35.120040	0.5m x 0.5m	0.25	0.146	0.094	3.760	0.376
Mean					0.148	0.091	3.650	0.365
Mean 0.365kg/m²								

Table 7.3: Observed Biomass, Olimisigioi, 05/05/2018_Wet season

Sample ID	Coordinates		Quadrat Area size (m)	Area in m ²	Wet wgt (Kg)	Dry wgt (Kg)	Projected biomass in tons/hac	Biomass in Kg/m ²
	Latitudes	Longitudes						
A	-1.503840	35.120073	0.5m x 0.5m	0.25	1.625	0.101	4.040	0.404
B	-1.503788	35.120070	0.5m x 0.5m	0.25	1.675	0.103	4.120	0.412
C	-1.503828	35.120088	0.5m x 0.5m	0.25	1.486	0.098	3.920	0.392
D	-1.503898	35.120072	0.5m x 0.5m	0.25	1.932	0.104	4.160	0.416
E	-1.503917	35.120068	0.5m x 0.5m	0.25	1.324	0.093	3.720	0.372
F	-1.503901	35.120040	0.5m x 0.5m	0.25	1.346	0.097	3.880	0.388
Mean					1.565	0.099	3.970	0.397
Mean biomass = 0.397kg/m²								

Table 7.4: Observed Biomass, Talek, 12/12/2017_Dry season

Sample ID	Coordinates		Quadrat Area size (m)	Area in m ²	Wet wgt (Kg)	Dry wgt (Kg)	Projected biomass in tons/hac	Biomass in Kg/m ²
	Latitudes	Longitudes						
A	- 1.461173	35.182764	0.5m x 0.5m	0.25	0.226	0.096	3.840	0.384
B	-.461188	35.182770	0.5m x 0.5m	0.25	0.202	0.101	4.040	0.404
C	-1.461136	35.182778	0.5m x 0.5m	0.25	0.104	0.084	3.360	0.336
D	-1.461199	35.182772	0.5m x 0.5m	0.25	0.152	0.077	3.080	0.308
E	-1.461127	35.182768	0.5m x 0.5m	0.25	0.101	0.086	3.440	0.344
F	-1.461104	35.182746	0.5m x 0.5m	0.25	0.104	0.091	3.640	0.364
Mean					0.148	0.089	3.570	0.357
Mean 0.357kg/m²								

Table 7.5: Observed Biomass, Talek, 05/05/2018_Wet season

Sample ID	Coordinates		Quadrat Area size (m)	Area in m ²	Wet wgt (Kg)	Dry wgt (Kg)	Projected biomass in tons/hac	Biomass in Kg/m ²	Standard Error
	Latitudes	Longitudes							
A	- 1.461173	35.182764	0.5m x 0.5m	0.25	1.826	0.105	4.200	0.420	± 0.027
B	-1.461188	35.182770	0.5m x 0.5m	0.25	1.502	0.107	4.280	0.428	± 0.047
C	-1.461136	35.182778	0.5m x 0.5m	0.25	1.804	0.103	4.120	0.412	± 0.021
D	-1.461199	35.182772	0.5m x 0.5m	0.25	1.952	0.097	3.880	0.388	± 0.049
E	-1.461127	35.182768	0.5m x 0.5m	0.25	2.701	0.102	4.080	0.408	± 0.013
F	-1.461104	35.182746	0.5m x 0.5m	0.25	1.804	0.104	4.160	0.416	± 0.007
Mean					1.932	0.103	4.12	0.412	
Mean 0.412kg/m²									

Table 7.6: Observed Biomass, Upstream, 12/12/2017_Dry season

Sample ID	Coordinates		Quadrat Area size (m)	Area in m ²	Wet wgt (Kg)	Dry wgt (Kg)	Projected biomass in tons/hac	Biomass in Kg/m ²
	Latitudes	Longitudes						
A	-1.529190	35.238243	0.5m x 0.5m	0.25	0.126	0.093	3.720	0.372
B	-1.529189	35.238274	0.5m x 0.5m	0.25	0.102	0.086	3.440	0.344
C	-1.529128	35.238288	0.5m x 0.5m	0.25	0.104	0.074	2.960	0.296
D	-1.529098	35.238270	0.5m x 0.5m	0.25	0.152	0.089	3.560	0.356
E	-1.529217	35.238268	0.5m x 0.5m	0.25	0.201	0.094	3.760	0.376
F	-1.529106	35.238149	0.5m x 0.5m	0.25	0.204	0.095	3.800	0.380
Mean					0.148	0.089	3.54	0.354
Mean 0.354kg/m²								

Table 7.7: Observed Biomass, Upstream, 05/05/2018_Wet season

Sample ID	Coordinates		Quadrat Area size (m)	Area in m ²	Wet wgt (Kg)	Dry wgt (Kg)	Projected biomass in tons/hac	Biomass in Kg/m ²
	Latitudes	Longitudes						
A	-1.529196	35.238287	0.5m x 0.5m	0.25	1.826	0.106	4.240	0.424
B	-1.529218	35.238245	0.5m x 0.5m	0.25	1.502	0.097	3.880	0.388
C	-1.529108	35.238268	0.5m x 0.5m	0.25	1.804	0.104	4.160	0.416
D	-1.529107	35.238272	0.5m x 0.5m	0.25	1.952	0.109	4.360	0.436
E	-1.529199	35.238270	0.5m x 0.5m	0.25	2.701	0.114	4.560	0.456
F	-1.529106	35.238159	0.5m x 0.5m	0.25	1.804	0.105	4.200	0.420
Mean					1.932	0.106	4.23	0.423
Mean 0.423kg/m²								

Table 7.8: Observed Biomass, V-section, 12/12/2017_Dry season

Sample ID	Coordinates		Quadrat Area size (m)	Area in m ²	Wet wgt (Kg)	Dry wgt (Kg)	Projected biomass in tons/hac	Biomass in Kg/m ²
	Latitudes	Longitudes						
A	-1.462422	35.106108	0.5m x 0.5m	0.25	0.186	0.088	3.520	0.352
B	-1.462498	35.106175	0.5m x 0.5m	0.25	0.193	0.091	3.640	0.364
C	-1.462448	35.106184	0.5m x 0.5m	0.25	0.274	0.098	3.920	0.392
D	-1.462368	35.106172	0.5m x 0.5m	0.25	0.192	0.087	3.480	0.348
E	-1.462457	35.106168	0.5m x 0.5m	0.25	0.102	0.079	3.160	0.316
F	-1.462470	35.106149	0.5m x 0.5m	0.25	0.143	0.089	3.560	0.356
Mean					0.182	0.089	3.55	0.355
Mean 0.355kg/m²								

Table 7.9: Observed Biomass, V-section, 05/05/2018_Wet season

Sample ID	Coordinates		Quadrat Area size (m)	Area in m ²	Wet wgt (Kg)	Dry wgt (Kg)	Projected biomass in tons/hac	Biomass in Kg/m ²
	Latitudes	Longitudes						
A	-1.462422	35.106108	0.5m x 0.5m	0.25	1.886	0.103	4.120	0.412
B	-1.462498	35.106175	0.5m x 0.5m	0.25	1.693	0.106	4.240	0.424
C	-1.462448	35.106184	0.5m x 0.5m	0.25	1.974	0.108	4.320	0.432
D	-1.462368	35.106172	0.5m x 0.5m	0.25	1.892	0.102	4.080	0.408
E	-1.462457	35.106168	0.5m x 0.5m	0.25	1.902	0.098	3.920	0.392
F	-1.462470	35.106149	0.5m x 0.5m	0.25	1.843	0.100	4.000	0.400
Mean					1.865	0.103	4.11	0.411
Mean 0.411kg/m²								

Table 7.91: Observed Biomass, Nice-Bridge, 12/12/2017_Dry season

Sample ID	Coordinates		Quadrat Area size (m)	Area in m ²	Wet wgt (Kg)	Dry wgt (Kg)	Projected biomass in tons/hac	Biomass in Kg/m ²
	Latitudes	Longitudes						
A	-1.495192	35.149133	0.5m x 0.5m	0.25	0.136	0.092	3.680	0.368
B	-1.495198	35.149170	0.5m x 0.5m	0.25	0.189	0.094	3.760	0.376
C	-1.495096	35.149188	0.5m x 0.5m	0.25	0.184	0.089	3.560	0.356
D	-1.495292	35.143170	0.5m x 0.5m	0.25	0.174	0.090	3.600	0.360
E	-1.493317	35.149268	0.5m x 0.5m	0.25	0.198	0.088	3.520	0.352
F	-1.493406	35.149240	0.5m x 0.5m	0.25	0.228	0.096	3.840	0.384
Average					0.185	0.092	3.600	0.360
Mean biomass = 0.366kg/m²								

Table 7.92: Observed Biomass, Nice-Bridge, 05/05/2018_Wet season

Sample ID	Coordinates		Quadrat Area size (m)	Area in m ²	Wet wgt (Kg)	Dry wgt (Kg)	Projected biomass in tons/hac	Biomass in Kg/m ²
	Latitudes	Longitudes						
A	-1.495192	35.149133	0.5m x 0.5m	0.25	1.636	0.101	4.040	0.404
B	-1.495198	35.149170	0.5m x 0.5m	0.25	1.788	0.104	4.160	0.416
C	-1.495096	35.149188	0.5m x 0.5m	0.25	1.784	0.103	4.120	0.412
D	-1.495292	35.143170	0.5m x 0.5m	0.25	1.874	0.105	4.200	0.420
E	-1.493317	35.149268	0.5m x 0.5m	0.25	1.798	0.102	4.080	0.408
F	-1.493406	35.149240	0.5m x 0.5m	0.25	1.928	0.106	4.240	0.424
Mean					1.801	0.104	4.140	0.414
Mean biomass = 0.414kg/m²								

Appendix B.12: Evaluation of APSIM Model performance over dry and wet season

Quadrat 1-10 (Averaged Standing Grass Biomass) (tons/ha) – Dry Season	Measured (o)	Simulated (s)	(s-o)	(s-o)²	(s-mean o)	(s-mean o)²	(o-mean o)	(o-mean o)²	(s-mean s)	(s-mean s)²	(o-mean o) (s-mean s)
Mara Main	3.28	3.39	0.11	0.0121	-0.119	0.0142	-0.229	0.052	-0.206	0.0424	-0.023
Kissinger	3.66	3.70	0.04	0.0016	0.191	0.0365	0.151	0.023	0.104	0.0108	0.047
Ashnil	3.71	3.80	0.09	0.0081	0.291	0.0847	0.201	0.040	0.204	0.0416	-0.003
Mara Bridge	3.89	3.92	0.03	0.0009	0.411	0.1689	0.381	0.145	0.324	0.1050	0.057
Helicopter	3.57	3.67	0.10	0.0100	0.161	0.0259	0.061	0.004	0.074	0.0055	-0.013
Olimisiogioi	3.60	3.78	0.18	0.0324	0.271	0.0734	0.091	0.008	0.184	0.0339	-0.093
Talek	3.55	3.57	0.02	0.0004	0.061	0.0037	0.041	0.002	-0.026	0.0007	0.067
Upstream	3.54	3.76	0.22	0.0484	0.251	0.0630	0.031	0.001	0.164	0.0269	-0.133
V-section	3.65	3.69	0.04	0.0016	0.181	0.0328	0.141	0.020	0.094	0.0088	0.047
Nicegridge	2.64	2.68	0.04	0.0016	-0.829	0.6872	-0.869	0.755	-0.916	0.8391	0.047
Summation	35.09	35.96	0.87	0.1171	0.870	1.1903	0.000	1.050	0.000	1.1146	0.000
n	10										
Mean o	3.509				NSE	r	RMSE	R²			

Mean s		3.596		Optimum	0	1	1	1			
$\frac{100}{(\text{mean } o)}$	2.850			Summation	0.889	0.000	0.012	0.889			

Quadrat 1-10 (Averaged Standing Grass Biomass) (tons/ha) – Wet Season	Measured (o)	Simulated (s)	(s-o)	(s-o)²	(s-mean o)	(s-mean o)²	(o-mean o)	(s-mean s)	(o-mean o)²	(s-mean s)²	(o-mean o) (s-mean s)
Mara Main	6.54	6.78	0.24	0.059	0.32	5.401	2.08	4.329	2.33	5.420	4.8438
Kissinger	5.89	5.75	-0.14	0.019	0.29	1.662	1.43	2.037	1.29	1.672	1.8455
Ashnil	4.87	4.25	-0.13	0.016	-0.21	0.046	-0.09	0.007	-0.21	0.044	0.0181
Mara Bridge	3.08	4.13	0.00	0.000	-0.33	0.106	-0.33	0.106	-0.32	0.104	0.1050
Helicopter	4.13	4.13	0.01	0.000	-0.33	0.106	-0.34	0.115	-0.32	0.103	0.1092
Olimisiogioi	3.97	4.15	0.01	0.000	-0.31	0.098	-0.32	0.102	-0.31	0.095	0.0986
Talek	4.12	4.15	0.04	0.001	-0.31	0.095	-0.35	0.120	-0.30	0.092	0.1051

Upstream	4.23	4.28	0.04	0.002	-0.18	0.033	-0.23	0.051	-0.18	0.031	0.0400
V-section	4.11	3.92	-0.06	0.003	-0.54	0.294	-0.49	0.236	-0.54	0.290	0.2617
Nicebridge	4.14	3.02	-0.06	0.004	-1.44	2.082	-1.38	1.903	-1.44	2.071	1.9849
Summation	44.59	44.55	-0.04	0.106	-0.04	9.923	0.00	9.007	0.00	9.922	9.4118
n	10										
Mean o	4.46				NSE	r	RMSE	R²			
Mean s		4.46		Optimum	0	1	1	1			
$\frac{100}{(\text{mean } o)}$	22.42			Summation	0.988	0	0.1029	0.988			

Appendix B.13: Naivasha Cropland Monthly Rainfall at Delamere Manera Farm

Year/Month	Jan	Feb	Mar	April	May	June	July	Aug	Sep	Oct	Nov	Dec	Mean Annual rainfall
2010	127.5	80	237	148.5	213	59	0	68	66	81.3	61.5	12	1154
2011	31.5	36.5	122	85.5	93.5	137	47	142	39	92.8	107.5	6	980
2012	5	18	7	160.5	293	37.5	59	48.5	94	86.5	59	138	1006
2013	30.5	6	62	460	16	77	24	0	45	41	146.5	122.6	1031
2014	26	113	103	18.5	17	23	80.5	37.5	53	17	63	83.5	635
2015	0	16	0	241	87	102	56	47	64	36	173	134.5	957
2016	60	25	35	80	176	82	69	23	114	23	86	0	773
2017	0	15	10	84.5	106.5	8	63	134.5	78.5	112.5	88	0	701
2018	37	0	157	261.5	298.5	88	40.5	29	2.5	62	56	85.5	1118
2019	10	37	21	66.5	78.5	150	65	0	20.5	86.5	165	172	872
Mean	33	35	75	101	138	76	50	53	58	64	101	79	

Appendix B.14: Major land cover classes of Naivasha Cropland

Land Cover Class	(Area Covered (Km²) and % cover		
Period	2017	2018	2019
Arable land	987.89 (65%)	1006.317 (63%)	1257.896 (63%)
Non-arable land	423.76	477.84	597.304

Land under water	84	84	105
Gazetted Forest	1.2	1.6	2
Urban Area	20.3	24.8	31
Total Area (Km²)	1517.15	1594.557	1993.2

Appendix B.15: Naivasha Sub-County Agro-Ecological Zones based on land potential by wards using Area Sampling

Land Potential Wards	Maaimahiu	Olkaria	Lakeview	Naivasha East	Viwanda ni	Biashara	Maiella	Hells Gate	Total
Arable land (km²)	222.64	221.6	16.6	106.4	80.22	264	265.236	81.2	1257.896
Non-arable land (km²)	360.36	3	16.6	10	24.78	10	162.564	10	597.304
Land under water (km²)	0	105	0	0	0	0	0	0	105
Gazetted forest area (km²)	2	0	0	0	0	0	0	0	2
Urban area (km²)	6	2	6	4	4	2	1	6	31
Altitude (m.a.s.l)	1520-2660	1900-2000	1900-2100	2000-2700	1900-2000	2000-2300	1900-2700	1900-2200	-
Rainfall range (mm p.a)	-	600-1000mm	750-1000mm	750-1000mm	750-1000mm	600-1000mm	800-1055mm	750-1000mm	-
Temperature range oC	12-25	15-25	15-25	12-25	15-25	12-25	12-25	15-25	-
High Potential (Ha)	0	0	0	80.4	0	64	50	0	194.40

Medium potential (Ha)	166	160	16.6	26	80.22	150	177	60.2	836.02
Low Potential (Ha)	56	162.2	0	0	0	50	38	21	327.2
Main Agro-Ecological zones (specify)	UH3,LH3,LH4,LH5,UM4,UM5,UM6	LH4,LH5,UM5,UM6	LH4,UM5,UM6	LH3	LH4,UM5,UM6	UH2,UH3,LH3,LH4,LH5,UM6	UH2,UH3,LH4,LH5,UM5,UM6	LH4,LH5,UM5,UM6	-
Soil types	Sandy Loam	Sandy loam	Sandy Loam	Sandy Loam	Sandy Loam	Sandy Loam	Sandy Loam	Sandy Loam	-
Livelihoods	Crop farming, livestock keeping, quarrying, business	Crop farming, livestock keeping, quarrying, business	Crop farming, livestock keeping, quarrying, business -	Crop farming, livestock keeping, quarrying, business	Crop farming, livestock keeping, quarrying, business	Crop farming, livestock keeping, quarrying, business	Crop farming, business employ ment	Crop farming, livestock keeping, quarryin, business	-

Appendix B.16: Chemical Properties of selected farms in Naivasha Sub-county

Kijabe/Ndabibi Farm

Fertility Results	Units	Value	Class
Soil pH		6.65	Near neutral
*Total Nitrogen %	%	0.15	Low
*Total organic carbon %	%	1.42	Moderate
Phosphorous	ppm	50	Adequate
Potassium	ppm	3.00	High
Calcium	ppm	4.00	Adequate
Magnesium	ppm	3.45	High
Manganese	%	0.65	Adequate
Copper	Ppm	1.70	Adequate
Iron	Ppm	155	Adequate
Zinc	Ppm	11.8	Adequate
Sodium	%	0.80	Adequate

Delamere/Minera Farm

Parameter	Unit	Result	Guide Low	Guide High	Symbol	Current	Last three analysis	Method
pH(H ₂ O)		8.49	6.50	7.50	pH	8.49	7.3	Potentiometric
*EC(Salts)	mS/cm	231	-	<800	EC(S)	231	503	Potentiometric
*Phosphorus (Oslen)	ppm	30.4	20.0	50.0	P(O)	30.4	-	Colorimetric
*Potassium	ppm	1450	253	1260	K	1450	1560	Spectroscopy
Calcium	Ppm	3870	3890	4860	Ca	1870	3410	Spectroscopy
Magnesium	Ppm	430	389	778	Mg	430	402	Spectroscopy
Sulphur	ppm	60.5	10.0	50.0	S	60.5	4.65	Spectroscopy
Sodium	ppm	1110	-	<559	Na	1110	172	Spectroscopy
Iron	ppm	159	60.0	350	Fe	159	146	Spectroscopy
Manganese	ppm	250	20.0	200	Mn	250	95.1	Spectroscopy
Boron	ppm	1.29	0.80	2.00	B	1.29	1.57	Spectroscopy
Copper	ppm	1.54	1.50	10.0	Cu	1.54	1.1	Spectroscopy
Zinc	ppm	10.9	2.00	20.0	Zn	10.9	10	Spectroscopy
*C.E.C	Meq/100g	32.4	15.0	30.0		32.4	26.2	Calculated
*Total Nitrogen	%	0.20	0.20	0.50	N	0.20	-	Colorimetric
*Organic Matter	%	3.59	3.00	8.00	OM	3.59	-	Colorimetric

*C/N ratio		10.4	10.0	25.0	CN	10.4	-	-
*PERCENTAGES AND RATIOS								
Calcium	%	59.7	60	75	Ca%	59.7	64.99	
Potassium	%	11.5	2	10	K%	11.5	15.29	
Magnesium	%	11.1	10	20	Mg%	11.1	12.77	
Sodium (ESP)	%	14.9	0	7.5	Na%	14.9	2.85	
Other bases	%	2.91	3	10	OB%	2.91	4.1	
Hydrogen	%	0.00	10	15	H%	0.00	0	
Total		100						
Ca:Mg ratio	%	5.40	4	7	CaMg	5.40	5.09	

Appendix B.17: General trends of Pasture and Fodder Conservation in Naivasha between 2013 and 2019

Year	Silage in Tonnes	Hay Bales	Standing Hay (Ha)	Homemade Ratio (Tonnes)	Beans/Peas Husks	Maize stovers (tonnes)	Wheat stovers (bales)
2013	420	5,120	9,720	32,200	0	340	2,900
2014	560	5,470	9,800	34,000	0	380	3,400
2015	580	5,800	10,000	35,000	0	400	3,800
2016	1,280	130,250	4,500	42,000	280	9,120	56,000
2017	880	90,150	3,000	32,000	170	8,170	60,000
2018	2,640	270,450	2,500	30,000	1,240	15,140	120,000
2019	2,746	289,652	2,700	31,200	1,352	16,503	129,600

Appendix B.18: General wheat crop production and acreage in Naivasha Sub County

WARD	Acreage (Ha)	Production (Tons)	Area in m²	Production in Kg	Production in Kg/m²
Maiella	2220 (99.5%)	6030	22,200,000	6,030,000	0.272
Maaimahiu	10 (0.448%)	0	10,000,000	0	0
Biashara	1 (0.045%)	0.001	10,000	1	0.0001
Total	2231	6,030	22,310,000	6,030,001	0.2721

Appendix B.19: Observed and Predicted wheat production in Naivasha Crop

Observed annual wheat production - Kijabe/Ndabibi farm

Year	Biomass (kg/ha)	Biomass (ton/ha)	Yield (kg/ha)	Yield (ton/ha)
2017	13177.0	13.1770	4630.0	4.6300
2018	12805.3	12.8053	4887.7	4.8877
2019	14758.1	14.7581	5800.6	5.8006
Mean	13580.1	13.5801	5106.1	5.1061

Observed annual wheat production - Delamere Minera farm

Year	Biomass (kg/ha)	Biomass (ton/ha)	Yield (kg/ha)	Yield (ton/ha)
2017	12889.5	12.8895	49301	4.9301
2018	14409.9	14.4099	55844	5.5844
2019	15697.0	15.6970	55523	5.5523
Mean	14335.5	14.3355	53556	5.3556

Observed annual wheat harvest - Nunjoro farm

Year	Biomass (kg/ha)	Biomass (ton/ha)	Yield (kg/ha)	Yield (ton/ha)
2017	11941.5	11.9415	3471.2	3.4712
2018	12450.0	12.4500	4729.4	4.7294
2019	13501.4	13.5014	4419.6	4.4196
Mean	12631.0	12.6310	4206.7	4.2067

Annual wheat production - **Engineer/Mzee Paul's farm**

Year	Biomass (kg/ha)	Biomass (ton/ha)	Yield (kg/ha)	Yield (ton/ha)
2017	9545.8	9.5458	3583.2	3.5832
2018	12452.3	12.4523	3858.1	3.8581
2019	13248.3	13.2483	4023.3	4.0233
Mean	11748.8	11.7488	3821.5	3.8215

Simulation results of wheat biomass and yield

Predicted annual wheat harvest production - Kijabe/Ndabibi farm

Year	Biomass (kg/ha)	Yield (kg/ha)	Grain Protein (%)	Grain size (g)	Extractable soil water (mm)
2017	13445.1	5040.1	16.417	0.041	326.700
2018	13575.9	4329.3	10.896	0.029	294.760
2019	15023.0	5489.4	12.505	0.032	334.322
Mean	14014.7	4952.9	13.273	0.034	318.594

Predicted annual wheat harvest production - Delamere Minera farm

Year	Biomass (kg/ha)	Yield (kg/ha)	Grain Protein (%)	Grain size (g)	Extractable soil water (mm)
2017	13375.5	5183.3	12.700	0.041	388.513
2018	14813.4	5861.1	13.419	0.036	293.308
2019	16298.0	5854.6	16.419	0.041	357.570
Mean	14.8290	5633.0	14.179	0.039	346.464

Predicted annual wheat harvest production - Engineer/Mzee Paul's farm

Year	Biomass (kg/ha)	Yield (kg/ha)	Grain Protein (%)	Grain size (g)	Extractable soil water (mm)
2017	12678.1	4114.5	11.138	0.028	294.913
2018	12899.5	4930.1	12.563	0.033	339.042
2019	12907.9	4938.6	16.020	0.033	268.325
Mean	12828.5	4661.1	13.240	0.031	300.760

Predicted annual wheat harvest - Nunjoro farm

Year	Biomass (kg/ha)	Yield (kg/ha)	Grain Protein (%)	Grain size (g)	Extractable soil water (mm)
2017	10728.2	4073.9	15.632	0.041	514.277
2018	12805.3	4887.7	16.078	0.041	286.493
2019	13501.4	4419.6	11.127	0.030	294.913
Mean	12345.0	4460.4	14.279	0.037	365.228

Appendix B.20: Evaluation of APSIM Model Wheat Crop Performance - Aboveground Biomass (tons/ha) – Growing Season 2017, 2018 and 2019

	Observed (o)	Simulated (s)	(s-o)	(s-o) ²	(s-mean o)	(s-mean o) ²	(o-mean o)	(s-mean s)	(o-mean o) ²	(s-mean s) ²	(o-mean o) (s-mean s)
Kijabe/Ndabibi Farm	13.1770	13.4451	0.2681	0.0719	0.1350	0.0182	0.4031	0.6296	0.1625	0.3964	0.2538
	12.8053	13.5759	0.7706	0.5938	0.2667	0.0711	0.5039	0.4279	0.2539	0.1831	0.2156
	14.7581	15.2030	0.4449	0.1979	1.6229	2.6337	1.1780	1.1283	1.3876	1.2731	1.329
Summation	40.7404	42.224	1.4836	0.8636	1.4836	2.6519	1.78E-15	1.78E-15	2.1505	1.9183	1.9694
n	3										
Mean o	13.5801				NSE	r	RMSE (ton/ha)	R²			
Mean s		14.0747			0	1	1	1			
$\frac{100}{(\text{mean } o)}$	7.364				0.956	1.00	0.1345	0.998			
					Summation						

Wheat Grain Yield) (tons/ha) 2017, 2018 and 2019

	Measured (o)	Simulated (s)	(s-o)	(s-o) ²	(s-mean o)	(s-mean o) ²	(o-mean o)	(s-mean s)	(o-mean o) ²	(s-mean s) ²	(o-mean o) (s-mean s)
Kijabe/Ndabibi Farm	4.6300	5.0401	0.4101	0.1682	-0.0660	0.004	-0.476	0.087	0.227	0.008	0.0017
	4.8877	4.3293	-0.5584	0.3118	-0.7768	0.603	-0.218	-0.624	0.048	0.389	0.0186
	5.8006	5.4894	-0.3112	0.0968	0.3833	0.147	0.695	0.537	0.482	0.288	0.1388
Summation											
N	3										
Mean o	5.1061				NSE	r	RMSE (ton/ha)	R²			
Mean s		4.9529			0	1	1	1			
$\frac{100}{(mean o)}$	19.584				Summation Optimum						
					5.93 (0.593)	0.987	-0.060	0.927			

Wheat Aboveground Biomass (tons/ha) – Growing Season 2017, 2018 and 2019

	Measured (o)	Simulated (s)	(s-o)	(s-o) ²	(s-mean o)	(s-mean o) ²	(o-mean o)	(s-mean s)	(o-mean o) ²	(s-mean s) ²	(o-mean o) (s-mean s)
Delamere/Minera Farm	12.8995	13.3755	0.476	0.2266	-0.9600	0.9215	-1.4360	-1.4535	2.0620	2.1126	4.3561
	14.4099	14.8134	0.4035	0.1628	0.4779	0.2284	0.0744	-0.0156	0.0055	0.0002	0.0000
	15.6970	16.2980	0.6010	0.3612	1.9625	3.8515	1.3615	1.4690	1.8538	2.1581	4.0006
Summation	43.0064	44.4869	1.4805	0.7506	1.4805	5.0015	0.0000	0.0000	3.9213	4.2709	8.3567
N	3										
Mean o	14.3355				NSE	r	RMSE (ton/ha)	R²			
Mean s		14.8290			Optimum	0	1	1	1		
$\frac{100}{(mean\ o)}$	6.9757				Summation	0.956	1.00	0.1345	0.998		

Wheat Grain Yield) (tons/ha) - Annual Harvest 2017, 2018 and 2019

	Measured (o)	Simulated (s)	(s-o)	(s-o) ²	(s-mean o)	(s-mean o) ²	(o-mean o)	(s-mean s)	(o-mean o) ²	(s-mean s) ²	(o-mean o) (s-mean s)
Delamere farm	4.9301	5.1833	0.2532	0.0641	-0.1723	0.0297	-0.4255	-0.4497	0.1811	0.2022	0.0366
	5.5844	5.8611	0.2767	0.0766	0.5055	0.2555	0.2288	0.2281	0.0523	0.0520	0.0027
	5.5523	5.8546	0.3023	0.0914	0.4990	0.2490	0.1967	0.2216	0.0387	0.0491	0.0019
Summation	16.0668	16.899	0.8322	0.0774	0.8322	0.5342	0.0000	0.0000	0.2721	0.3034	0.0412
N	3										
Mean o	5.3556				NSE	r	RMSE (ton/ha)	R²			
Mean s		5.6330		Optimum	1	1	1	1			
$\frac{100}{(\text{mean } o)}$	18.6720			Summation	0.927	0.987	-0.060	0.927			

Wheat Aboveground Biomass) (tons/ha) – Growing Season 2017, 2018 and 2019

	Measured (o)	Simulated (s)	(s-o)	(s-o) ²	(s-mean o)	(s-mean o) ²	(o-mean o)	(s-mean s)	(o-mean o) ²	(s-mean s) ²	(o-mean o) (s-mean s)
Engineer/ Mzee Paul Farm	11.9415	12.6781	0.7366	0.5426	0.0471	0.0022	0.6895	0.1504	0.4754	0.0226	0.0108
	12.4500	12.8995	0.4500	0.2021	0.2685	0.0721	-0.1810	0.071	0.0327	0.0050	0.0002
	13.5014	12.9079	-0.5935	0.3522	0.2769	0.0767	0.8704	0.0794	0.7577	0.0063	0.0048
Summation	37.8929	38.4855	0.5926	1.0969	0.5926	0.1510	0.0000	0.0000	1.2658	0.0340	0.0157
n	3										
Mean o	12.6310				NSE	r	RMSE (ton/ha)	R²			
Mean s		12.8285			Optimum	1	1	1	1		
$\frac{100}{(mean\ o)}$	7.9171				Summation	0.956	1.00	0.1345	0.998		

Wheat Grain Yield) (tons/ha) 2017, 2018 and 2019

	Measured (o)	Simulated (s)	(s-o)	(s-o) ²	(s-mean o)	(s-mean o) ²	(o-mean o)	(s-mean s)	(o-mean o) ²	(s-mean s) ²	(o-mean o) (s-mean s)
Engineer/ Mzee Paul Farm	3.4712	4.1145	0.6433	0.4138	-0.0922	0.00851	-0.7355	-0.5466	0.5410	0.2987	0.1616
	4.7294	4.9301	0.2007	0.0403	0.7234	0.52326	0.5227	0.2690	0.2732	0.0724	0.0198
	4.4196	4.938.6	0.5190	0.2694	0.7319	0.53563	0.2129	0.2775	0.0453	0.0770	0.0035
Summation	12.6202	13.9832	1.363	0.7235	1.3630	1.06740	0.0000	0.0000	0.8595	0.4481	0.1849
n	3										
Mean o	4.2067				NSE	r	RMSE (ton/ha)	R²			
Mean s		4.6611			Optimum	1	1	1			
$\frac{100}{(mean\ o)}$	23.7714				Summation	0.927	0.987	-0.060	0.927		

Wheat Aboveground Biomass) (tons/ha) – Growing Season 2017, 2018 and 2019

	Measured (o)	Simulated (s)	(s-o)	(s-o) ²	(s-mean o)	(s-mean o) ²	(o-mean o)	(s-mean s)	(o-mean o) ²	(s-mean s) ²	(o-mean o) (s-mean s)
Nunjoro Farm	9.5458	10.728	1.1824	1.3981	-1.0206	1.0416	-2.2030	-1.617	4.853	2.6139	12.6860
	12.4523	12.805	0.353	0.1246	1.0565	1.1162	0.7035	0.460	0.495	0.2119	0.1049
	13.2483	13.502	0.2531	0.0641	1.7526	3.0716	1.4995	1.156	2.249	1.3373	3.0070
Summation	35.2464	37.035	1.7885	1.5867	1.7885	1.7431	0.0000	0.0000	7.5966	4.1632	15.7979
n	3										
Mean o	11.7488				NSE	r	RMSE (ton/ha)	R²			
Mean s			12.345	Optimum	1	1	1	1			
$\frac{100}{(\text{mean } o)}$	8.5115			Summation	0.956	1.00	0.1345	0.998			

Quadrat (Wheat Grain Yield) (tons/ha)	Measured (o)	Simulated (s)	(s-o)	(s-o) ²	(s-mean o)	(s-mean o) ²	(o-mean o)	(s-mean s)	(o-mean o) ²	(s-mean s) ²	(o-mean o) (s-mean s)
Nunjoro Farm	3.5832	4.0739	0.4907	0.2408	0.2524	0.06369	-0.2383	-0.3865	0.05680	0.1493	0.0085
	3.8581	4.8877	1.0296	1.0601	1.0662	1.13671	0.0366	0.4273	0.00134	0.1826	0.0002
	4.0233	4.4196	0.3963	0.1571	0.5981	0.35768	0.2018	-0.0408	0.04071	0.0017	0.0001
Summation	11.4646	13.381	1.9166	1.4579	1.9166	1.55808	0.0000	0.0000	0.0988	0.3336	0.0088
n	3										
Mean o	3.8215				NSE	r	RMSE (ton/ha)	R²			
Mean s		4.4604		Optimum	1	1	1	1			
$\frac{100}{(mean\ o)}$	26.1675			Summation	0.927	0.987	-0.060	0.927			

Appendix B.21: Land Cover Classification Segmentation in Area size

L2_KEN_LCC_09_Clip.tif.vat, 9/24/2020, Page 1

OID	Value	Count	AREA (Km²)
0	20	30162	23.818436
1	30	59199	46.748478
2	41	15599	12.318274
3	42	81	0.063964
4	112	254	0.20058
5	114	153	0.120822
6	116	1037	0.818902
7	122	1	0.00079
8	124	84	0.066333
9	126	20063	15.843422

L2_KEN_LCC_11_Clip1.tif.vat, 9/24/2020, Page 1

OID	Value	Count	AREA (Km²)
0	20	30162	23.818436
1	30	59199	46.748478
2	41	15599	12.318274
3	42	81	0.063964
4	112	254	0.20058
5	114	153	0.120822
6	116	1037	0.818902
7	122	1	0.00079
8	124	84	0.066333
9	126	20063	15.843422

OID	Value	Count	AREA (Km²)
0	20	22010	7.93771
1	30	7514	2.709857
2	41	162398	58.567389
3	42	3409	1.229425
4	50	1527	0.550699
5	60	1	0.000361
6	80	11599	4.183076
7	90	753	p
8	112	26278	9.476926
9	114	1079	0.389132
10	116	8224	2.965912
11	122	32	0.011541
12	124	311	0.112159
13	126	32149	11.59425

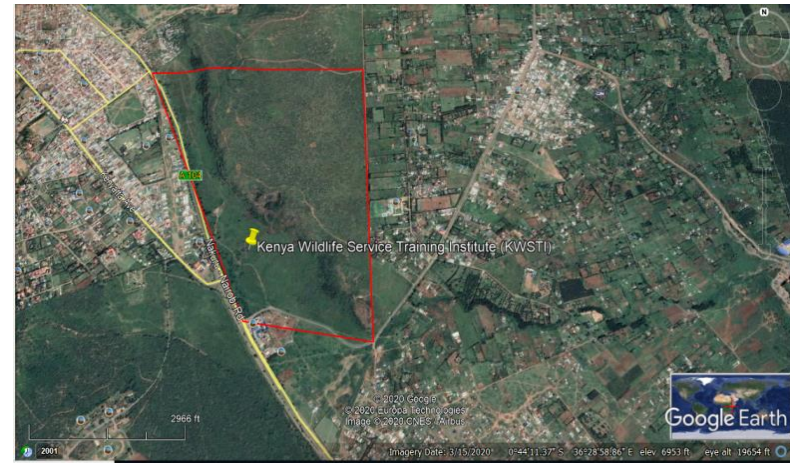
OID	Value	Count	AREA (Km²)
0	20	30162	23.818436
1	30	59199	46.748478
2	41	10364	8.184281
3	42	5316	4.197958
4	112	254	0.20058
5	114	153	0.120822
6	116	1037	0.818902
7	122	1	0.00079
8	124	84	0.066333
9	126	20063	15.843422

OID	Value	Count	AREA (Km²)
0	20	30162	23.818436
1	30	59199	46.748478
2	41	10364	8.184281
3	42	5316	4.197958
4	112	254	0.20058
5	114	153	0.120822
6	116	1037	0.818902
7	122	1	0.00079
8	124	84	0.066333
9	126	20063	15.843422

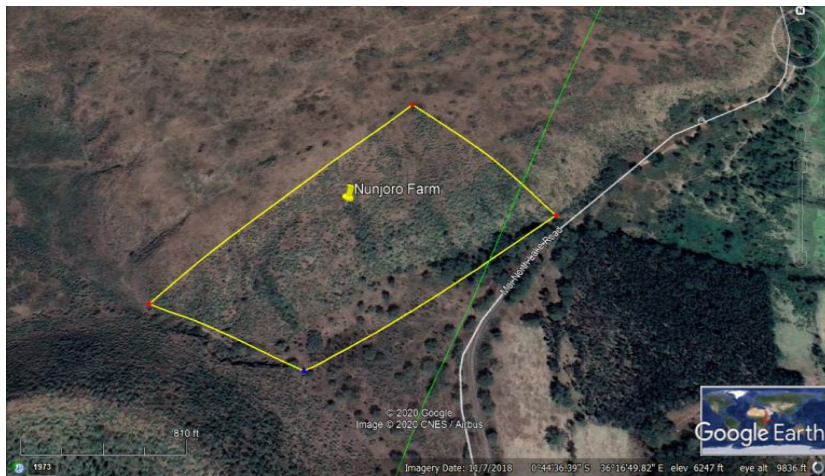
Appendix B.21: Naivasha Cropland Land use Land Covers Segmentation of (a) Kijabe/Ndabibi farm (b) Kenya Wildlife Service Training Institute (c) Nunjoro farm (d) Delamere/Minera farm



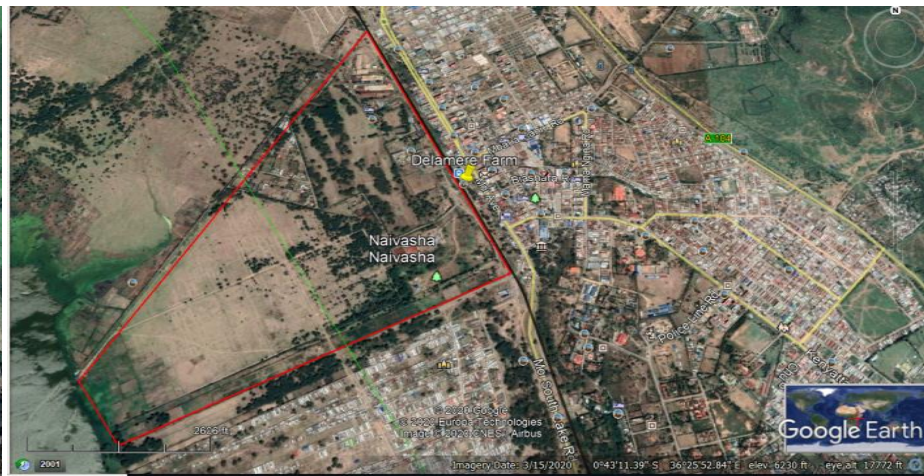
(a)



(b)



(c)

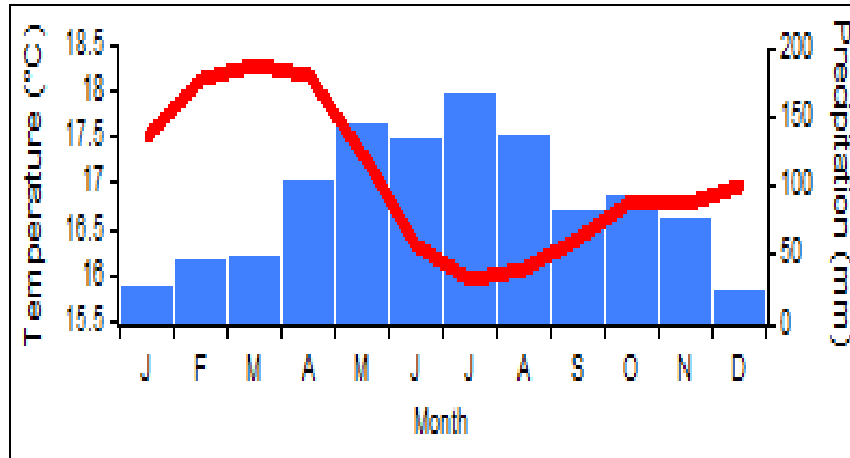


(d)

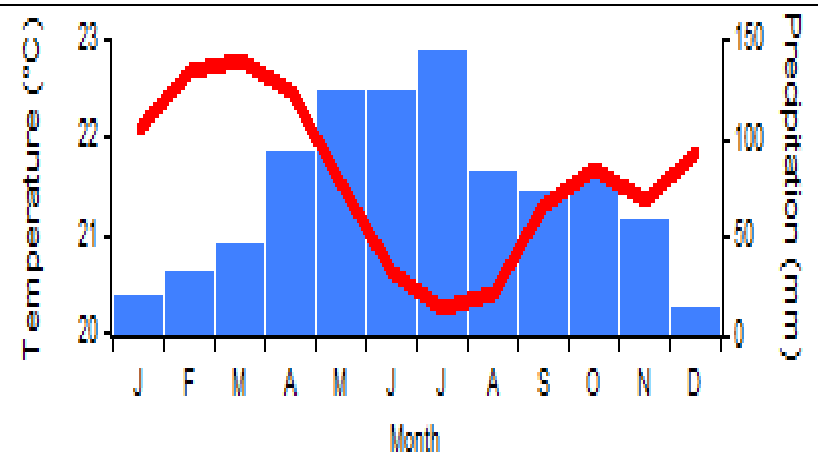
Appendices C: Graphs

Appendix C.1: Monthly Trend of Precipitation and Temperature of Maasai Mara National Reserve Sites

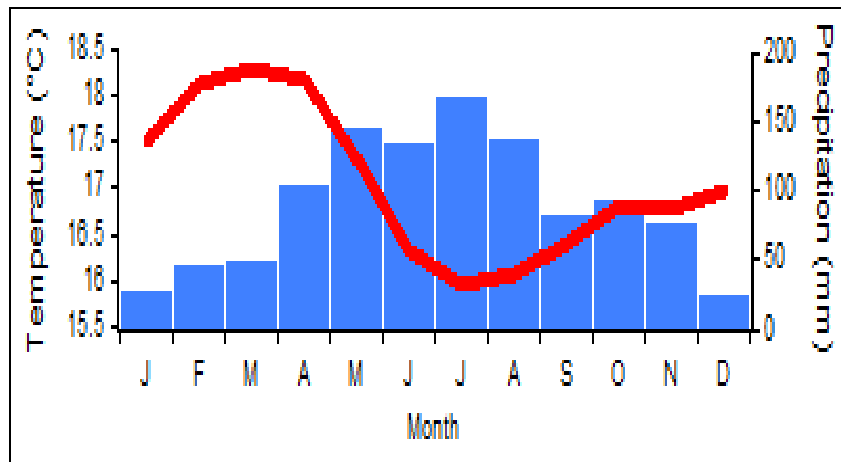
Mara Main Station



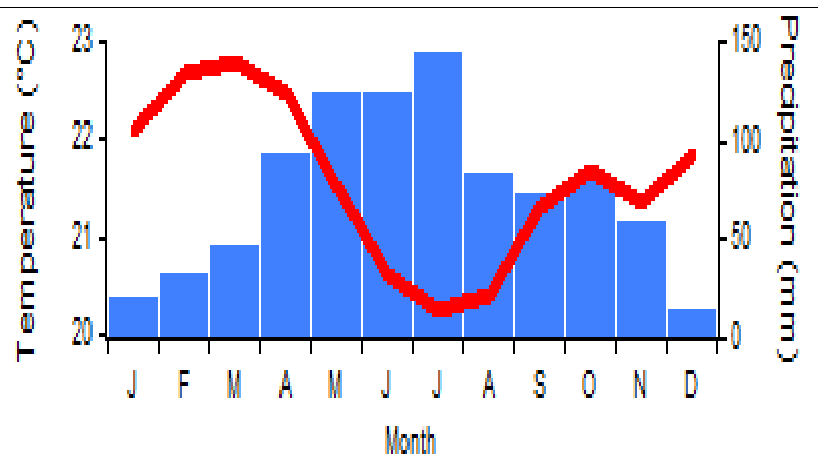
Kissinger



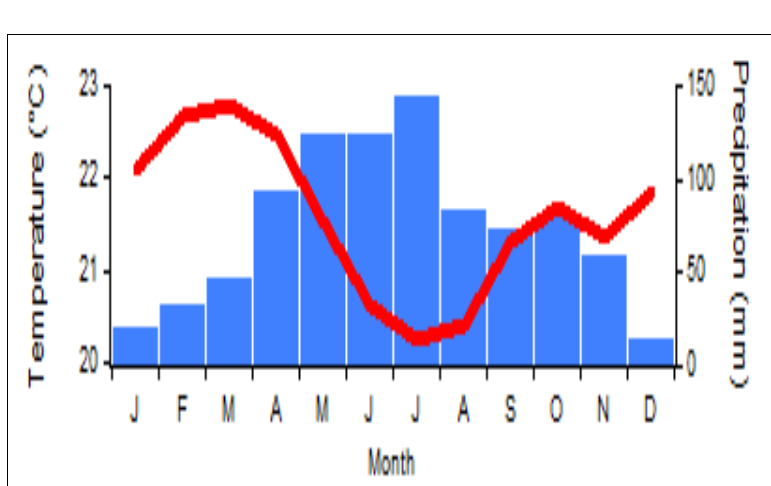
Ashnil station



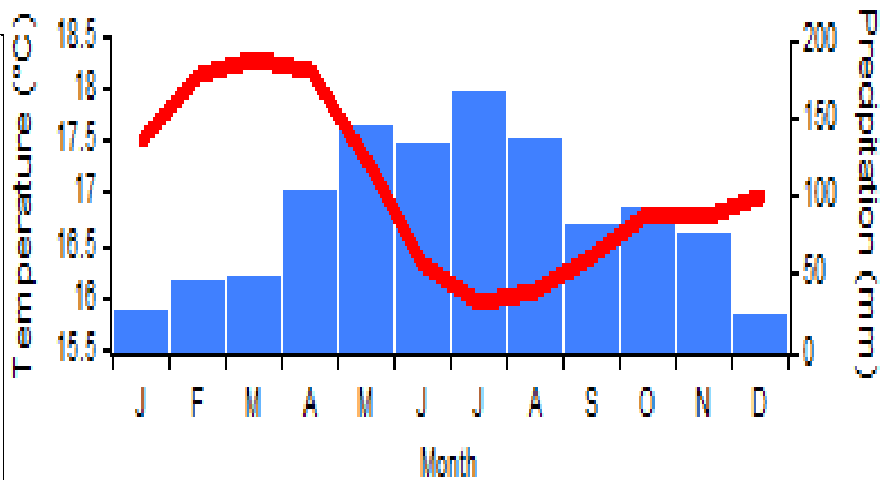
Mara Bridge



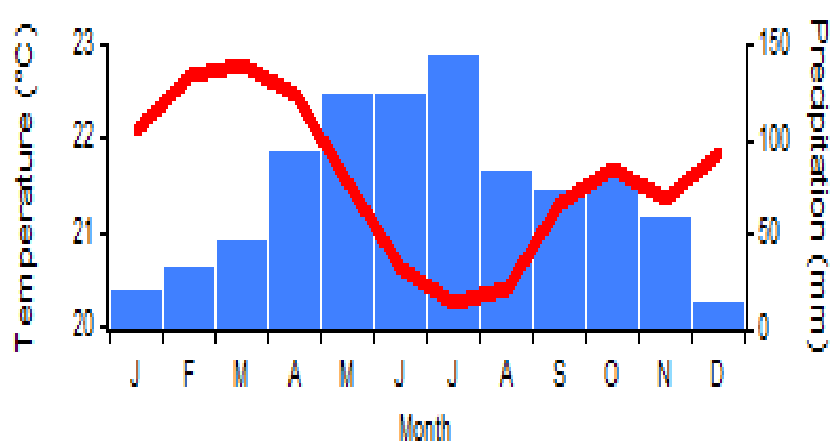
Helicopter



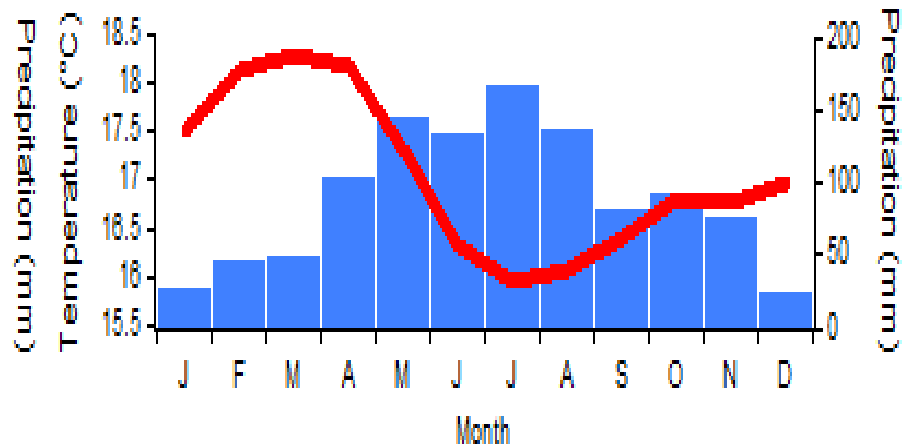
Olimisiogioi



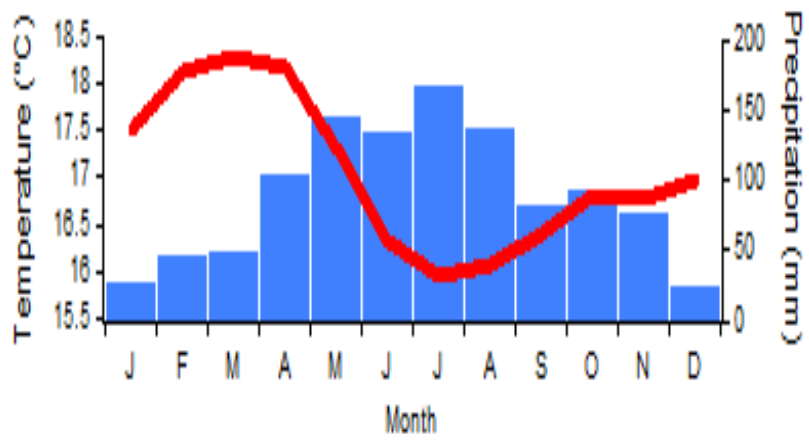
Talek



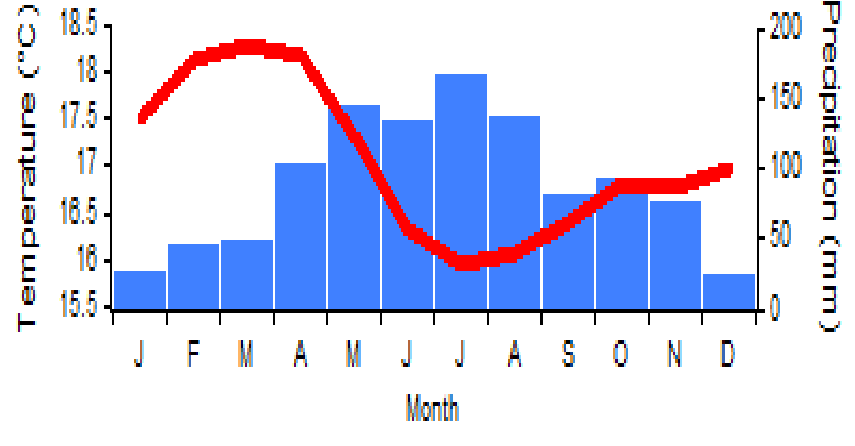
Upstream



V-section

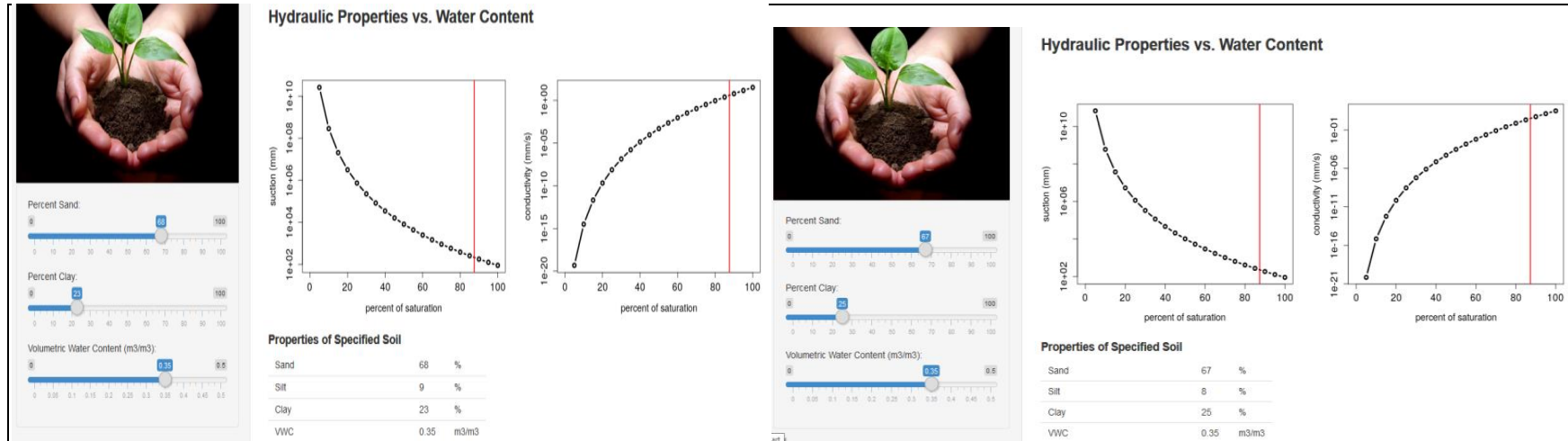


Nice Bridge

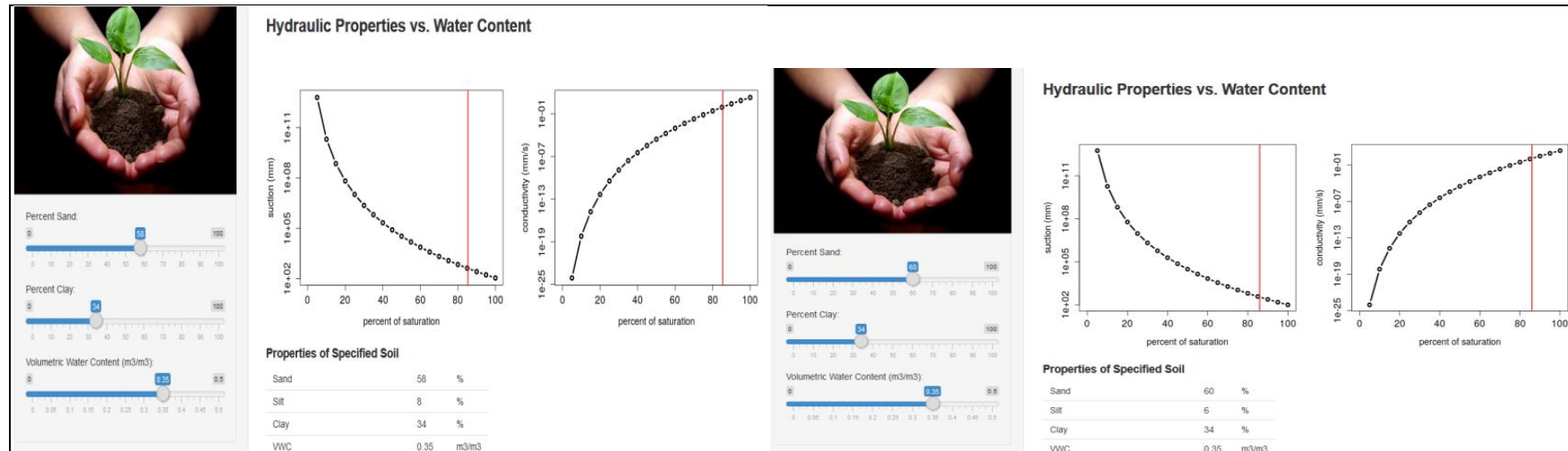


Appendix C.2: Soil Water Content against Hydraulic Properties

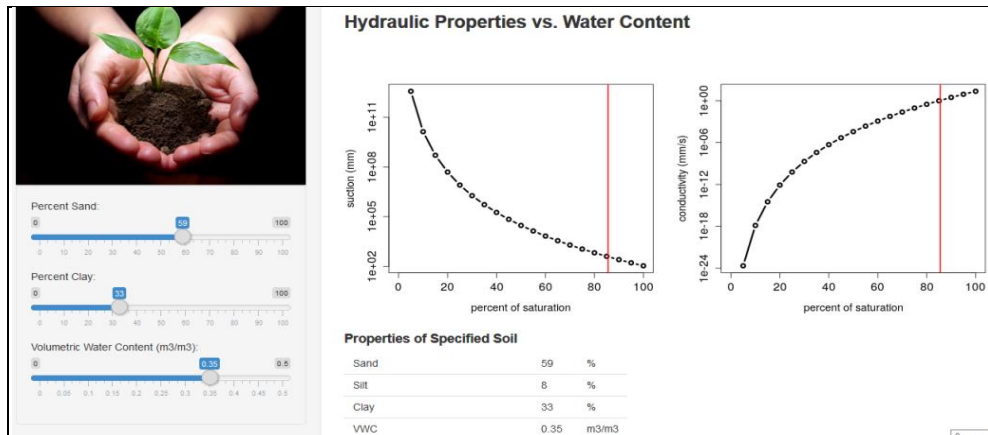
At 5cm



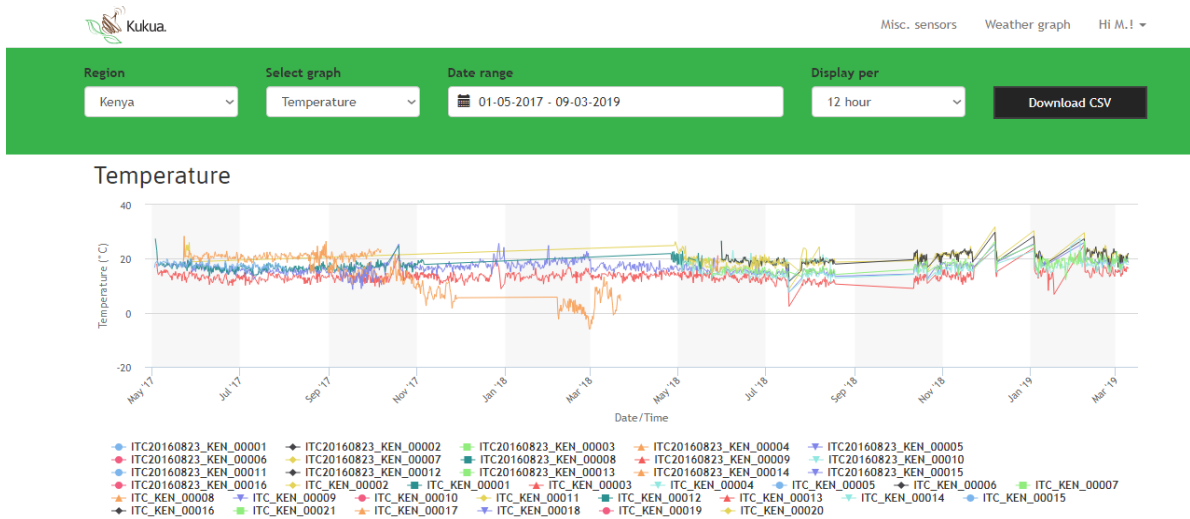
At 20cm



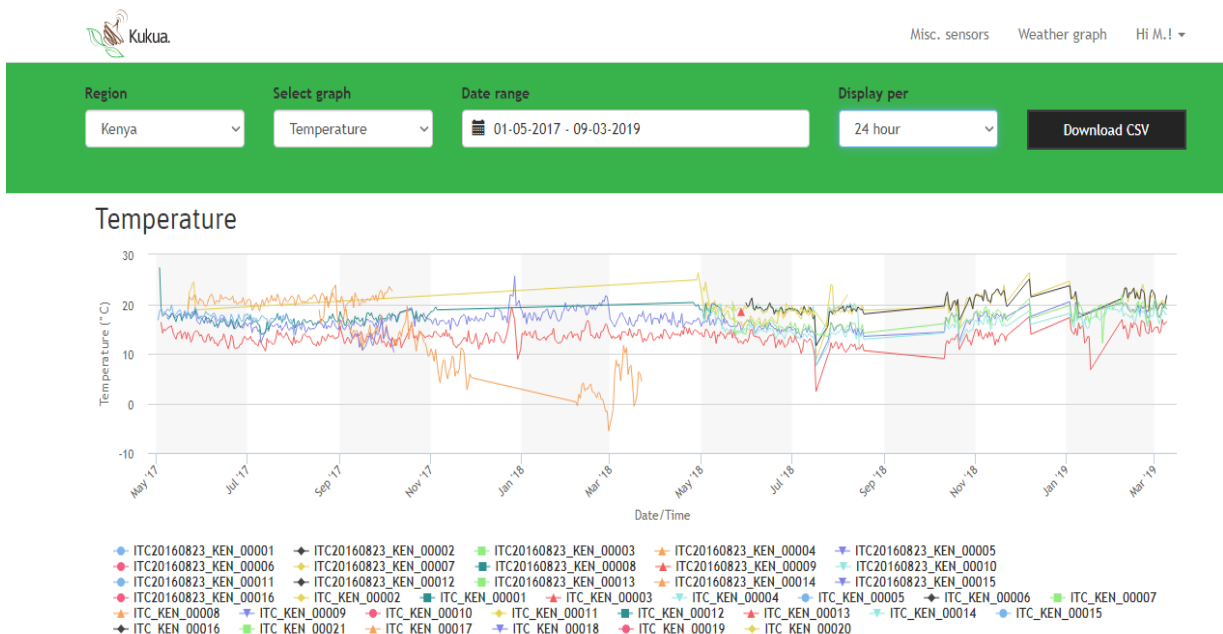
At 80cm



Appendix C.3: Naivasha Climate Variables by Bowen's Ratio Half-Day (12 hours) parameters dataset_2017_2019




Daily – Time Step Parameters Dataset_2017_2019




Appendices D: Research Permit

Appendix D.1: NACOSTI Research Permit


REPUBLIC OF KENYA
National Commission for Science, Technology and Innovation

Ref No: 257221

RESEARCH LICENSE




This is to Certify that Mr. Charles Kapkwang of Egerton University, has been licensed to conduct research in Narok on the topic: **EFFECTS OF SOIL MOISTURE VARIABILITY ON BIOMASS PRODUCTION USING SELECTED MODELS - CASE OF MAA SAI MARA RANGELAND AND NAIVASHA CROPLAND ECOSYSTEMS, KENYA** for the period ending: **15/October/2020.**

Licensee No: NACOSTI/19/2140

Applicant Identification Number: 257221

Director General
NATIONAL COMMISSION FOR SCIENCE, TECHNOLOGY & INNOVATION

Verification QR Code



NOTE: This is a computer generated License. To verify the authenticity of this document Scan the QR Code using QR scanner application.

Appendices E: List of Publications



Journal of Engineering Research and Reports

20(12): 64-90, 2021; Article no.JERR.72533
ISSN: 2582-2926

Evaluation of Spatio-Temporal Soil Moisture Variability in Semi-Arid Rangeland Ecosystem, Maasai Mara National Reserve, Kenya

Charles C. Kapkwang^{1,2*}, Japheth O. Onyando², Peter M. Kundu² and Joost Hoedjes³

¹Department of Agricultural Biosystems and Economics, University of Kabanga, P.O. Box 2030 - 20200, Kericho, Kenya.

²Department of Agricultural Engineering, Egerton University, P.O. Box 536 - 20115, Egerton, Kenya.

³Department of Water Resource and Earth Observation Science, University of Twente, Netherlands.

Authors' contributions

This work was carried out in collaboration among all authors. All authors read and approved the final manuscript.

Article information

DOI: 10.9734/JERR/2021A201217421

Editorial:

(1) Dr. Heba Abdallah Mohamed Abdallah, National Research Centre, Egypt.

Revised:

(1) Nooshin Sajjadi, Islamic Azad University, Iran.

(2) Lupupa Kachenga, Eden University, Zambia.

Complete Peer review History: <https://www.scitecresearch.com/review-history/72533>

Received 16 June 2021

Accepted 23 August 2021

Published 02 September 2021

Original Research Article

ABSTRACT

Aim: To evaluate the spatio-temporal soil moisture storage and retention capacities in semi-arid rangeland ecosystem, Maasai Mara National Reserve (MMNR), Kenya
Study Design: Randomized complete block design (RCBD) of reference Cosmic Ray Neutron Sensor (CRNS) station, ten-(10) spatially distributed (soil moisture and temperature capacitance) probes (STM-ECH₂O) sites.
Place and Duration of Study: Kenya, MMNR, the oldest natural semi-arid rangeland ecosystem and globally unique for the great wildebeest migration, between May 2017 and April 2019.
Methodology: Soil moisture (SM) variation data was collected using (CRNS) at spatial and point-scale STM-ECH₂O probes, and gravimetric water content from (10) spatially distributed stations. Both CRNS and STM-ECH₂O probes were used to monitor near-real time moisture levels at different soil layers ranging between 0-5cm, 5-10cm, 15-20cm, 35-40cm, and 75-80cm. Soil physical and chemical properties were laboratory analyzed. Calibration and validation datasets

were obtained from 5TM-ECH₂O probe and gravimetric soil samples extracted from respective layers and sites.

Results: The pedological characteristics of the investigated ecosystem soil profile indicate decreased bulk density by 2.1% to 11.12% from upper layers (0-5cm) to deeper layers at (75-80 cm). Across the rangeland, 70% of soil textural classes were sandy clay loam (SCL) with higher clay percent and 30% sandy clay (SC) and soil porosity varied between 30.1% and 51% in the ecosystem. Moreover, volumetric water content (VWC) of spatially distributed 5TM-ECH₂O probes ranged between 0.11m³m⁻³ and 0.32m³m⁻³ during wet season with mean VWC of 0.16m³m⁻³, however, the VWC ranged between 0.04 m³m⁻³ and 0.17m³m⁻³ during the dry season with a mean volume of 0.11m³m⁻³ across the rangeland ecosystem.

Conclusion: In this study, SM exhibited an annual periodicity of seasonal variation of spatial and temporal moisture partitioned as moisture gaining, losing, and a moisture stable period. This probably could be a consequence of increased movement of water to deeper layers caused by high precipitation and less evaporative demand caused by lower temperatures. The calibrated CRNS probe provided good estimates of spatial soil moisture variation when calibrated with 5TM-ECH₂O and gravimetric sampling in relation to precipitation events and that deeper soil layers showed higher amount of soil moisture than shallow layers. The findings of the study will provide better formulation of the ecosystem vegetation management policies, conservation and planning for sustainable wildlife tourism industry.

Keywords: Soil moisture; variability; storage; capacities; rangeland; ecosystem.



Seasonal Vegetation Response to Climate Variability on Land use Land Cover Changes using In-Situ and Satellite Imagery Observation Data for Semi-Arid Maasai Mara National Reserve Rangeland Ecosystem, Kenya

Charles C. Kapkwang ^{a,b*}, Japheth O. Onyando ^b, Peter M. Kundu ^b and Joost Hoedjes ^c

^a Department of Agricultural Bio Systems and Economics, University of Kabanga, P.O Box 2030-20200, Kericho, Kenya.
^b Department of Agricultural Engineering, Egerton University, P.O Box 536-20115, Egerton, Kenya.
^c Department of Water Resource and Earth Observation Science, University of Twente, Netherlands.

Authors' contributions

This work was carried out in collaboration among all authors. Author CCK designed the study, performed the statistical analysis, wrote the protocol, and wrote the first draft of the manuscript. Authors JOO, PMK and JH managed the analyses of the study and the literature searches. All authors read and approved the final manuscript.

Article Information

DOI: 10.9734/JERR/2021/21517461

Editorial:
(1) Prof. Tian-Quan Yun, South China University of Technology, China.
Reviewers:
(1) Abdelkhalik Ibrahim Alestal, Islamic University, Palestine.
(2) Badr-Eddine Boudriki Semlali, Abdelmalek Essaâdi University, Morocco.
Complete Peer review History: <https://www.scribd.com/document/75161>

Original Research Article

Received 01 September 2021
Accepted 04 November 2021
Published 15 November 2021

ABSTRACT

Monitoring vegetation response through enhanced change detection by remote sensing and geographical information systems has tremendously improved real time information on surface features. Over the last few decades biomass monitoring at large scale has been made possible from information and metrics derived from satellite sensors. Maasai Mara National Reserve has been utilized in many decades as Kenyan natural grassland for wildlife grazing without periodic assessment of biomass production as affected by impact of climate variability yet it's a tourism hub and one Kenyan economic contributor. This research evaluates the use of high spatial resolution satellite imagery such as the Moderate Resolution Imaging Spectro-radiometer or the Project for On-Board Autonomy-Vegetation and latest SENTINEL-2 for deriving the Normalized Difference Vegetation Index values in relations to in-situ measurements of biomass production between 2009 and 2019 in Mara, Kenya. Area frame sampling of biomass per unit area in Kg ha⁻¹ clipped from 50cm by 50cm quadrats were used in destructive sampling. The reserve grassland area coverage was estimated to be 717.203km² (46.75%) where the in-situ total above ground grass biomass projected in dry season was 35.094 tonha⁻¹. This was approximated as 2,516,952.208 tonnes per the season reserve cover while in wet season, 42.123 tonha⁻¹ was approximated as 3,021,074.197 tonnes. The error matrices developed to assess the accuracies of the ecosystem classification indicated values that ranged between 80-100% and 87.5-100% for producer's and user's accuracy respectively. 3 out of 7 satellite imagery maps (2017, 2018, and 2019) were assessed for accuracy using reference data collected during fieldwork in 2018 and 2019 in ecosystem. The overall accuracy was 95.22% with Kappa index of 0.94 for 14 land cover classes shown in table 7. From the findings, potential factors influencing vegetation growth in different climatic regions are varied and complex. It can be noted that climate variability influence vegetation response in spatial scale to supply sustainable quality vegetation/pasture for wildlife feeds and ecosystem development. Vegetation mapping and monitoring of ecosystem behavior help stakeholders with information of vegetation characteristics Decision policy formulation and wildlife planning.

Keywords: Remote sensing; geographical information systems; NDVI; monitoring; rangeland ecosystem.